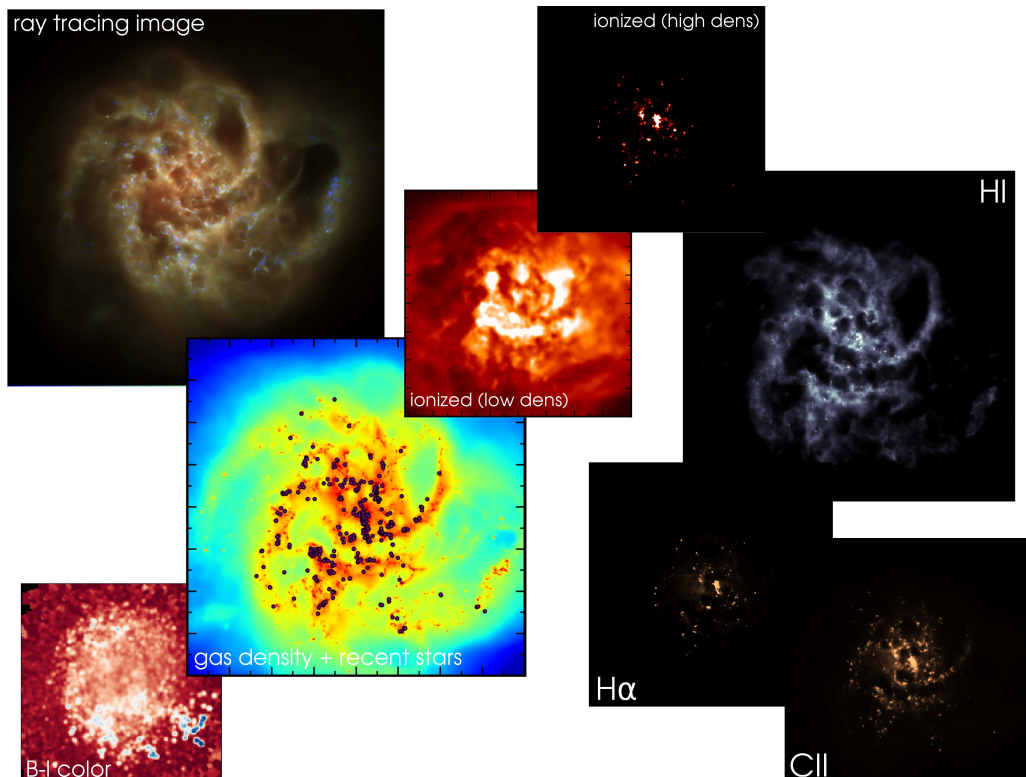UNIVERSITEIT
GENT

# Stervormingsmodes en populatiegradiënten
# in gesimuleerde dwerggalaxieën

## Star-formation modes and population gradients
## in simulated dwarf galaxies

# Joeri Schroyen



ray tracing image

ionized (high dens)

HI

ionized (low dens)

gas density + recent stars

B-I color

Hα

CII

Universiteit Gent
Faculteit Wetenschappen
Vakgroep Fysica & Sterrenkunde

Promotor: Prof. Dr. Sven De Rijcke

Universiteit Gent
Faculteit Wetenschappen

Vakgroep Fysica & Sterrenkunde
Krijgslaan 281, S9, B-9000 Gent, België

Tel.: +32-9-264.47.96
Fax.: +32-9-264.49.89

*Figuur voorpagina: Voorstellingen van verschillende aspecten van een dwerggalaxie-model (Z4refrot_HR), zoals aangeduid op de beelden.*

Proefschrift tot het behalen van de graad van
Doctor in de Sterrenkunde
Academiejaar 2013-2014

# Dankwoord

Lang geleden, lijkt het wel, ben ik begonnen aan dit avontuur... met een in extremis toch nog succesvolle masterthesis in handen, maar niettemin wat onzekerheid in de knieën *of dat ik dat hier wel zou kunnen.* De eerste voorzichtige stapjes werden gezet - een masterthesis waar ik aan kon verderwerken, mijn allereerste conferentie, het wennen aan jezelf te kunnen onderhouden met te studeren - en het vertrouwen begon langzaam maar gestaag te groeien. Een eerste talk op een conferentie, een eerste publicatie, af en toe geciteerd worden... *hm, misschien zou dat hier toch nog wel eens kunnen lukken...* En plots zijn we hier, op het moment dat u het dankwoord van mijn thesis leest, met voor mij (letterlijk en figuurlijk) nieuwe werelden die zijn opengegaan, fijne en interessante jaren achter de rug, en vele ervaringen rijker.

Zonder Sven en Sander zou er hier ongetwijfeld bitter weinig te lezen geweest zijn, dus de eerste lading bedankingen gaat hun richting uit, voor, respectievelijk, de astronomische zingeving van mijn leven de laatste 4-5 jaar, en de computationele voetsporen waarin ik gretig heb kunnen treden. Haast even noemenswaardig zijn onze system-goeroe Gerbrand, en onze rots in de administratieve branding Inge, voor het vlot laten lopen van alle hardware, software en paperware. De leuke en vlotte sfeer op kantoor, tenslotte, was de verdienste van iedereen die de laatste jaren residentie heeft genomen in de vakgroep in de S9, en met name mijn bureaugenoten doorheen de jaren: Mina, Annelies, Robbert, Ilse, Joris, en Jacopo.

Persoonlijke dankwoorden gaan nog uit naar VTI Hasselt, voor de vele momenten van sport en ontspanning, en mijn ouders en mijn broer voor alle steun. Maar de meest persoonlijke aller bedankingen is voor Mina, voor alles wat hier al geschreven staat, en alles wat hier niét geschreven staat. Blagodarya, lyubov moya!

*Gent, september 2013*
*Joeri Schroyen*

# Contents

# 1

# Introduction

Today we *largely* understand the *large scale* evolution of the Universe, through the ΛCDM cosmological model that describes the age, expansion history, and the global contents of the Universe (dark energy, cold dark matter, baryonic matter). However, we remain to have embarrasingly *little* knowledge of the *small scale* physics involved in forming and evolving the baryonic structure (gas, stars and dust) of galaxies - which actually happens to be the only component that we can directly observe and measure (Figure 1.1). Questions as to how, when, where, and why gas starts forming stars and stops forming stars, and how the produced elements are recycled in the interstellar medium, are fundamental issues in galaxy formation and evolution... though unfortunately, they still await to be thoroughly answered.

*Enter "dwarf galaxies".* Dwarf galaxies are often considered to be the ideal "galactic laboratories" to gain insight into many astrophysical processes. Their obvious main feature is that they are a relatively small type of galaxies - about 1/10 of the Milky Way's size as a rough guideline. Their relatively shallow gravitational potential makes them very sensitive to the different (astro)physical processes that affect galaxy evolution and that try to counteract gravity. Hence we can use these galaxies to try to understand and answer the very fundamental questions we still have about star formation and galaxy formation in general. Furthermore, their modest dimensions allow simulations to achieve much higher resolution and physical detail than for any other type of galaxy, and their close proximity to Us in the Galaxy makes that some of the most detailed galactic observations available are of our satellite dwarf galaxies.

However, besides their practical and experimental use, they are also very interesting objects to study in their own right. In the ΛCDM model it is widely adopted that galaxies,
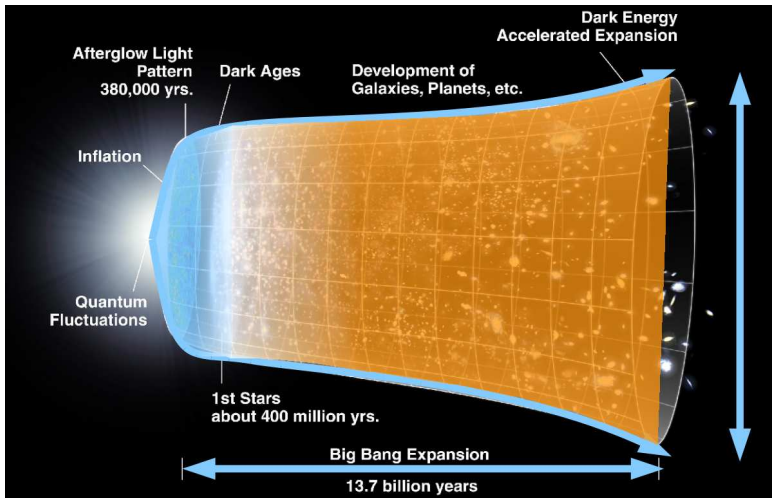
**Figure 1.1:** Schematic representation of the evolution of the Universe. Indicated in blue are the known, large scale properties of the Universe: the initial components, the expansion history, and current size and age. Orange indicates the unknown, small scale processes which transform the baryonic content of the Universe from the primordial ingredients into galaxies. Image credit: NASA/WMAP Science Team.

and any structures in general, have formed according to a bottom-up hierarchical scenario. Dwarf galaxies, the most numerous type of galaxies in the Universe, are therefore bestowed with the cosmological honour of being the first galactic objects that formed, and through merging provided the basic "building blocks" with which all other galaxies are formed. They are therefore also of great cosmological and theoretical importance. Any ambitious theory about structure formation should be able to account for the dwarf galaxy population, and studying their specific properties will also learn us essential information about the specific properties and evolution of the other types of galaxies that they form. To provide the reader with a broad context about dwarf galaxies in this introductory chapter, we will first take a dive into history in Section 1.1, then give an overview of the current state and inventory of dwarf galaxies in Section 1.2, and the current theory on their nature, evolution and origin in Section 1.3. Briefly giving the reader a better idea here of what is generally considered to be a dwarf galaxy, before continuing, is not that straightforward, since very strict quantitative criteria are not readily available or agreed upon. The general idea is that one speaks of a dwarf galaxy when

- its absolute V-band magnitude is higher than -18 mag,
- its total stellar mass is lower than $10^{10}\,\mathrm{M}_\odot$,
- it has physical dimensions of the order of a few kiloparsec.

When going all the way down the luminosity ladder, the lower limits, however, are much more ambiguous. There is a small zoo of galactic (sub)categories at the faint end (ultra-faint dwarfs, hobbit galaxies, faint fuzzies,...) all the way down to globular clusters, but

any further subdivision not only depends on reaching a consensus in the astronomical society (which can be a daunting task in itself), but also on the technical limitations of the instruments and detectors to observe these faint objects.

## 1.1    A brief history of dwarf galaxies

It seems worthwhile to first take a small dive into the history of observations and theories about dwarf galaxies. This trip to the astronomical past logically starts with the "Very First Dwarf" - the first dwarf galaxy ever observed. Or at least we would like it to... However, doing so entails a certain degree of ambiguity, especially concerning what exactly is meant by "observing".

Let us therefore first interpret this quite literally as "the first dwarf galaxy that was *seen* by humans", without necessarily being recognized as such, or being the subject of any kind of astronomical study (in the scientific form in which it has been performed during the last couple of hundred years). In this category we can confidently nominate the Small Magellanic Cloud (SMC, see Figure 1.2), an irregular dwarf galaxy which is visible only with the aid of the naked eye and a clear night in the southern hemisphere, together with its aptly named bigger brother, the Large Magellanic Cloud (LMC). Except for the local civilizations, who had undoubtedly noticed them on the sky above their heads (and attributed them many mythical properties), the first "northerners" that gazed upon them and left reports of their observations are the Persian astronomer Al-Sufi (964), the Italian discoverer Amerigo Vespucci (1503), and his Portuguese colleague Fernão de Magalhães (1519-22). The latter also contributed his name to the objects, albeit centuries after his death (under the late-medieval sailors they were long know as the "Cape Clouds", and have since been known under a variety of alternative names before the current name became widespread). For a long time the Magellanic Clouds also held the title of the closest galactic objects, until the Saggitarius dwarf galaxy obtained it when discovered in 1994.

When we focus on the more professional form of observing, in the more scientific era of astronomy, we should start with NGC205 / Messier 110 (Figure 1.3), a satellite of Andromeda. The very first *official* observation is from Charles Messier (1730-1817), who depicted it in 1773 on a drawing of Andromeda as "Petite Nébuleuse (plus faible)", though he himself never included it in his famous list. Soon after, in 1783, NGC205 was discovered completely independently (because the previous observations were not openly published) by Caroline Herschel. This time the publicity was not skipped, and in 1785 Caroline's brother William Herschel described and published her discovery. More than a century later, in 1888, John Dreyer gave the "nebula" a place in the New General Catalog, and was assigned number 205. Almost another century later, in 1967, the dwarf galaxy is also finally added to the Messier list, under impulse of Kenneth Glyn Jones as a tribute to the original discoverer - wherein it got assigned the current last number, 110. During the era of these discoveries, at the end of the 18th century, there was not much more known about these objects than the mere fact that *they were there...* Further knowledge about

**Figure 1.2:** The small and large Magellanic Clouds, the two most prominent "blobs" on the left side of the image, together with our own Milky Way on the southern hemisphere. Image credit: ESO.

them was at least as vague as the spots of light these objects themselves made on the night sky. They were categorized, along with a whole zoo of other observed objects, under the name "nebulae", although it was far from clear what all these nebulae consisted of. Were they luminous gas or dust particles, or individual stars... And it was even less clear *where* these objects resided. Only much later it would become apparent that these nebula-catalogs (Messier, IC, NGC) consist of a great variety of objects, from planetary nebula and emitting gas clouds to full-blown galaxies, both dwarfs and giants. In these issues the SMC was an invaluable tool to gain more insight into the nature and the dimensions of these objects, due to its proximity and good visibility. John Frederick William Herschel (1792-1871) describes in 1847 in detail his observations of the SMC, in which he discerns a bar-shape, and discovers dozens of small, individual nebulae and star clusters that reside in the SMC. This "nebula" therefore indisputably consisted of individual stars and emitting gas clouds, but it took quite a while still before people started getting an idea of its true size and position relative to us, in the Milky Way. The opinions again were divided, and were roughly split up in two camps: according to one the SMC was a *part of* the Milky Way, an overdensity of gas and stars somewhere in the outer regions - according to the other a fully self-contained entity that existed *outside of* the Milky Way, but might still feel its gravitational influence. The latter might seem like the self-evident option, but only a century ago the notion that anything at all existed outside of the Milky Way was not evident at all, which also fueled the "great debate" between Harlow Shapley and Heber Curtis about the nature of spiral nebulae and the size of the Universe in general (26th of April, 1920).

The SMC, that also got its place in the New General Catalog in 1888 as NGC292, remained the subject of intensive study during the decades following Herschel's observations, and
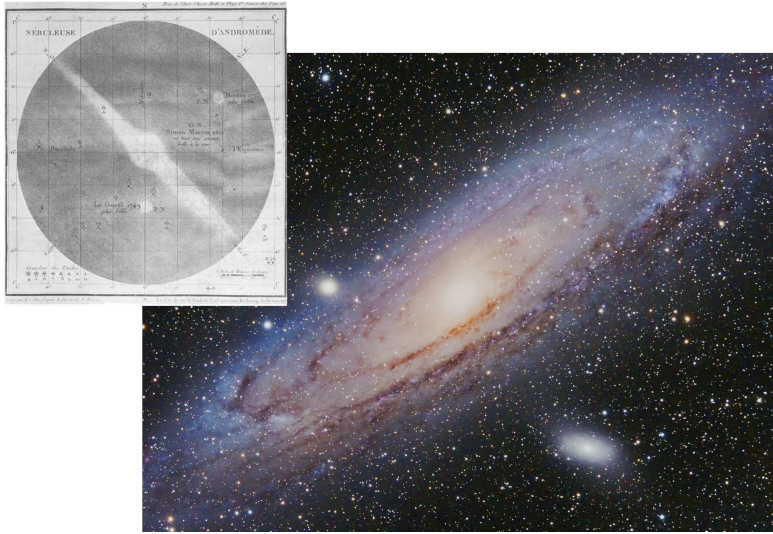
**Figure 1.3:** The "First Dwarf" NGC205 as a separate, bright blob at the lower right side of Andromeda on the large picture, and the Andromeda system as drawn by Charles Messier in 1773 in the small inset, with NGC205 indicated as "Petite Nébuleuse (plus faible)". Photograph credit: Terry Hancock (http://www.flickr.com/photos/terryhancock/7770860404/)

still is today. A first breakthrough came in 1912, with the discovery of the now famous relation between the period and the luminosity of a class of variable stars, the Cepheids, by Henrietta Swan Leavitt (1868-1921) from observations of the SMC (see the left part of Figure 1.5). She was one of the former "computers" at the Harvard College Observatory: the often laborious and repetitive calculations and other tasks, inherent to astronomical observations and categorizations, were at that time often assigned to women, who were specifically hired for this work. This is justifiably considered as one of the - literally - groundbreaking discoveries in astronomy, because it gave astronomers a tool for (relative) distance measuring in the Universe, on a scale that reached far beyond the range of parallax measurements. A second breakthrough followed only two years later, in 1913, when Ejnar Hertzsprung (1873-1967) measured the distance to local Cepheids using their parallax, and compared them with the Cepheids in the SMC discovered by Leavitt. These ingredients made it possible for the very first time to get a well-founded estimate of the distance to the SMC, or any other extragalactic object for that matter, by calibrating the absolute distance with the local Cepheids, and the result was: 1 kilo-parsec (kpc). Comparing this to the current value of 61kpc this seems quite off, but it was already a big step in the right direction - although not yet sufficient to place the Magellanic Clouds outside of the Milky Way with any degree of certainty. In 1925 a new actor appeared on stage, namely NGC6822 (Figure 1.4), another irregular dwarf galaxy. Part of the astronomical legacy of Edwin Hubble (1889-1953) is the calculation of the distance to NGC6822 with the aid of 11 Cepheids discovered by him, that place the object at 214 kpc away from us (current value

500 kpc). This made the NGC6822 dwarf galaxy in one blow "The first object definitely assigned to a region outside of the Galactic system", and ended "the great debate" as well as the plausibility of Shapley's value of 100 kpc for the size of the Universe. Through Hubble's work, and more importantly (as he eagerly admitted himself) through the work of Leavitt that formed the basis for it, yet again a new world was unveiled to humanity, changing its vision on the Universe.

The lid of a big pot of fresh, unexploited astronomical phenomena was lifted, and in the years after, new observations and discoveries followed each other in rapid succession. In 1928, Walter Baade (1893-1960) used deep, long-exposure photographic plates to resolve nearby galaxies into individual stars, and estimated from the brightness of the brightest stars that the distance of IC1613 (discovered in 1906 by Max Wolf) is similar to that of NGC6822 (current value for IC1613: 700 kpc). Shapley himself, the "loser" of the "great debate" did not stay behind, and discovered two extended, faint stellar concentrations, at the real edge of the observable for the state of the astronomical technique at the time (exposure of 23 hours with a 60-inch telescope). These were the Sculptor and Fornax dwarf galaxies, respectively named after the constellations they appear to reside in. One year later, Baade and Hubble succeeded to assign these objects a distance, by using the 100-inch telescope on Mount Wilson (right side of Figure 1.5), and the by then well-tested Cepheid method: Sculptor is placed at 84 kpc, Fornax at 187 kpc (current values 90 kpc and 140 kpc). This meant that both these "dwarf extragalactic nebulae" were part of what, by then, was already known as the "Local Group", then consisted of "five dwarfs
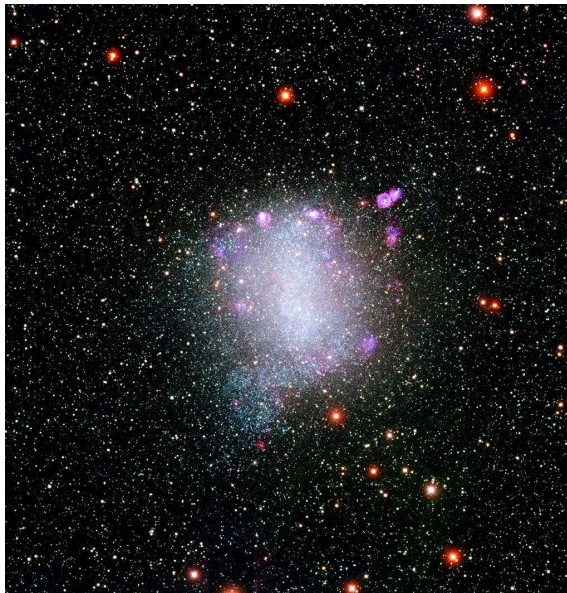


**Figure 1.4:** NGC6822, "the first object definitely assigned to a region outside of the Galactic system" - Edwin Hubble, 1925. Image credit: Local Group Galaxies Survey Team, NOAO, AURA, NSF.

among eleven recognized members". This made astronomers reconsider the faint end of the extragalactic luminosity function, which was first assumed to be symmetric, although of course only the bright end was known with any degree of confidence at the time. The suspicion rose that proportionally many more dwarf systems exist than giant systems, predominantly in the Local Group, but perhaps also in other galaxy groups and clusters in general. Over time the share of the faint end continuously increased in the Local Group, mostly thanks to the 100-inch telescope that was built on Mount Wilson in 1917 (right side of Figure 1.5). In 1944 Baade reported on two new members: NGC147 and NGC185, both dwarf systems that were presumed to be satellites of Andromeda. In the same year Baade also succeeded in resolving the previously mentioned "First Dwarf" NGC205 into individual stars for the very first time, confirming that this was also a mini-companion of Andromeda. The flame had obviously lit the fuse and, with the occasional intervals, the discoveries followed one another in continuous succession, even to the present day. Since the brightest galaxies are naturally the easiest to spot, and the sensitivity of the telescopes and equipment continuously improved, the discoveries were of subsequently fainter and fainter objects. The last decade is marked by the discoveries of a dozen or so extremely diffuse stellar systems around the Milky Way and Andromeda, by using very sensitive and/or accurate observations such as the famous Sloan Digital Sky Survey (SDSS) (see Belokurov 2013) - examples are Ursa Major I and II, Bootes I, Leo IV, Andromeda IX to XIII... These are often called "ultra-faint dwarfs" (Ufd), and in terms of luminosity and stellar mass are often surpassed by massive globular clusters. They have luminosities of the order of only $10^4$ solar luminosities, but total derived masses of several $10^6$ solar masses, giving them an incredibly high mass-luminosity ratio and indicating these systems are highly dominated by dark matter (Simon & Geha, 2007).

Since we started with the Very First Dwarf, it seems fitting to try to close this historical section with the Very Last Dwarf, in order to end up in the present again. This title is however a challenge trophy that doesn't stay in the same hands for too long, since new
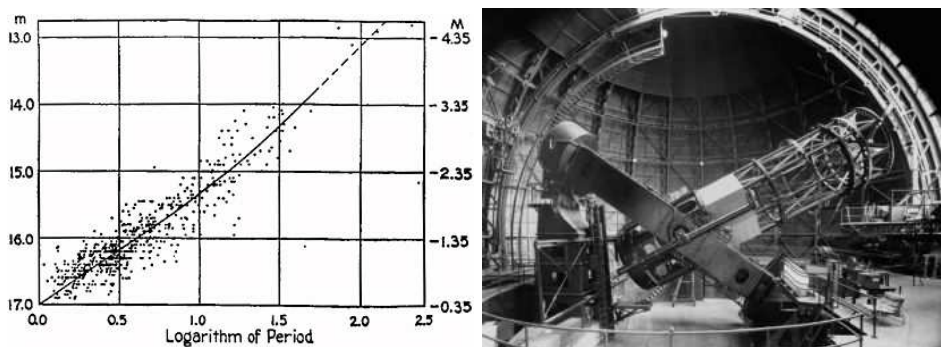


**Figure 1.5:** Two important tools for the discovery and understanding of dwarf galaxies during the course of history. Left: the relation between the periodicity and luminosity of Cepheids by Henrietta Swan Leavitt. Right: the 100-inch telescope on Mount Wilson. Photograph credit: Mount Wilson Observatory.

discoveries of ever fainter objects are made all the time. One of the most recent additions to our little club is Leo T, discovered in 2007 and slowly falling towards the Milky Way from a distance of 420 kpc (Irwin *et al.*, 2007). It fits nicely into the recent trends of discoveries, being of the Ufd type with a luminosity of $4 \times 10^4 \, L_\odot$ and a mass-to-light ratio of 140, making it a very dark matter dominated dwarf.

## 1.2  An inventory

Currently, the counter for the Local Group stopped somewhere around 44 dwarf galaxies, of different breeds and plumages. The majority of them resides in a more or less bound orbit around one of the "Three Great Ones" of our group (Milky Way, Andromeda, M33), with a few exceptions that have a more unbound behaviour. To this we can also add a collection of possible members, of which the membership is either suspected or disputed, see Figure 1.6.

Although in the previous section we only focused on the dwarfs in the Local Group, which was justified in the historical context, they are of course also found elsewhere. Considering that we find ourselves in an ordinary middle-class neighbourhood in an run-of-the-mill part of the Galaxy, they should even be everywhere, and make up the majority of galaxies in the Universe (current estimates are around 7 trillion). Unfortunately, their low brightnesses can sometimes prevent them from being detected if they are too far away, and resolved observations are only possible in the closest galaxy clusters and groups, with the current technology. The ultra-faint dwarfs at the lower end of the luminosity function are sometimes even hardly detectable in our own group. In time the upcoming E-ELT is
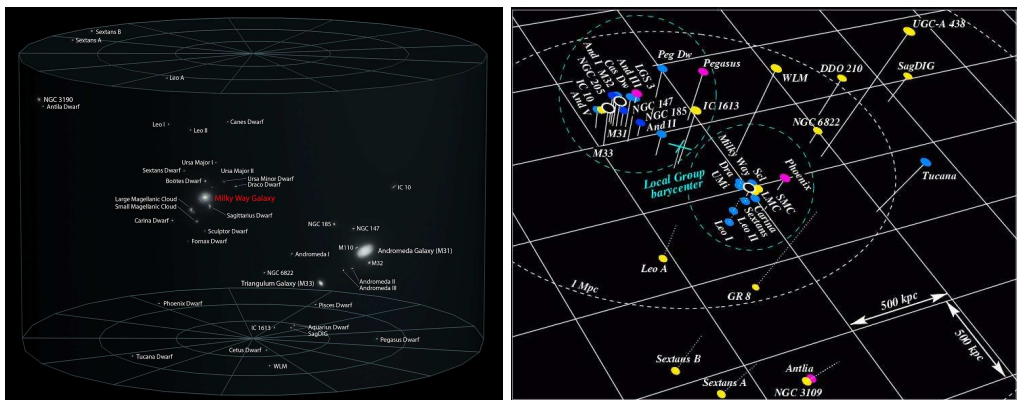


**Figure 1.6:** Visualizations of the Local Group, with most of its members shown. Left: a more realistic depiction of all the galaxies with their true optical appearances (credit: Andrew Z. Colvin, http://en.wikipedia.org/wiki/Local_Group). Right: a more schematic depiction with simple markers, where the galactic type is indicated by the color of the marker (yellow=dIrr - blue=dE/dSph - pink=dT) (credit: Grebel 1999).

the next candidate to try to expand our view in these matters.

From what we *can* see of dwarf galaxies, a few things become apparent. In the part of the Universe where we can observe them, they indeed seem to form the numerical majority among galaxy types (see Figure 1.8), indicating their cosmological importance in the evolution of structure in the Universe. There are also several noticeably different *kinds* of dwarf galaxies around, among which the main distinction is generally made between *star-forming + gas-rich* (late type) and *quiescent + gas-less* (early-type) dwarfs. Further, more specific categories are (see Figure 1.7, Mateo 1998 and Tolstoy *et al.* 2009 for an overview on dwarf galaxy properties):

- dwarf irregulars (dIrr): irregular of shape, often significantly rotating gas and stars (rotationally supported), and containing an ample supply of gas with which they are actively forming stars continuously throughout their galactic body (Dolphin *et al.*, 2005; Weisz *et al.*, 2008),

- blue compact dwarfs (BCD): actively forming stars, concentrated, low stellar rotation (Koleva et. al in prep.), steep solid-body rotation profile of the neutral gas though low specific angular momentum (van Zee *et al.*, 2001); exhibiting a strong, very localized, and possibly very short-lived star formation event or "starburst" from a present supply of gas, that is easily tenfold of the average "nominal" star formation rate (SFR) of dIrrs (making it of the order of $0.1M_\odot$/year, Hunter & Elmegreen 2004) - although the classification criteria vary significantly between authors. Their metallicities can be extremely low - down to 1/30 of the solar value (Kunth *et al.*, 1988),
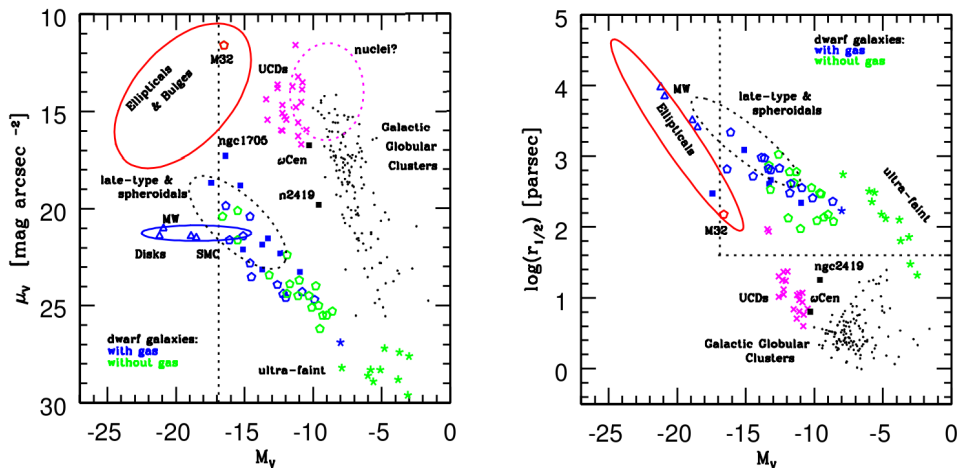


**Figure 1.7:** Overview plots from Tolstoy *et al.* (2009) to distinguish between different galaxy types, showing scaling relations of central surface brightness (left) and half-light radius (right) versus V-band magnitude. Dotted straight lines indicate the "classical" limits for what should be considered a dwarf galaxy.

- dwarf ellipticals (dE): very regular of shape with elliptical isophotes, usually not rotationally supported, for the most part devoid of gas or any kind of interstellar medium and therefore currently not actively forming stars anymore (though with a large range of possible star formation histories, Dolphin *et al.* 2005), not very strongly dark-matter dominated (mass-to-light ratio - M/L - around 5)

- dwarf spheroidals (dSph): very regular and fairly round of shape, often collected into one category with the dEs, but generally more diffuse, less massive, fainter, and are dark-matter dominated (M/L between 10 and 100)

- transition type dwarfs (dT): dwarf galaxies with properties somewhere in between the star-forming/gas-rich types (dIrr, BCD) and quiescent/gas-less types (dE, dSph) - for instance a fairly regular elliptical appearance, but with some supply of gas around or low-level star formation present (Koleva *et al.*, 2013),

- ultra-faint dwarfs (Ufd): extension of the dwarf galaxies as a class to very low luminosities, sometimes surpassed by massive globular clusters in terms of stellar masses and luminosities, usually devoid of gas and star formation, formed mostly in a single star formation episode, highly dark-matter dominated (M/L can reach 1000 and more) (Simon & Geha, 2007),

- ultra-compact dwarfs (UCD): somewhere between early type galaxies and globular clusters, relatively regular, but highly concentrated with very steeply declining radial surface brightness profiles - these are generally believed to be of a *different* origin then most other dwarf galaxies, most likely galactic bulges or nuclei that survived a bigger galaxy being stripped in a strong interaction (Mieske *et al.*, 2008),

- tidal dwarfs (dTidal): a highly debated type of dwarf galaxy, also of a *different* formation scenario, without a noticeable dark matter halo - which is supposedly formed as a byproduct of strong tidal interactions between big galaxies, where stellar clusters are formed in the tidal debris that can sometimes reach to the dwarf-galaxy-range (Duc *et al.*, 2007).

Furthermore, different dwarf galaxy types appear to show a distinctively different spatial distribution within groups or clusters, as exemplified by the Local Group in the right panel of Figure 1.6. The early-type quiescent, gas-less dEs and dSphs, which are sometimes coined as the "red and dead" dwarf galaxies, are predominantly found in the vicinity of giant galaxies (in groups) or in the central regions with high densities (in clusters), preferentially on radial orbits. Late-type star-forming/gas-rich dIrrs and BCDs, which are blue and have young stellar populations, are systematically found much further away from giant galaxies, in regions with much lower densities, and presumably on much more tangential orbits. This connection between the galaxy type and the preferred environment is what is know as the "morphology-density relation", which exists for both dwarf and giant galaxies, and is an important link in theories on dwarf galaxy formation and evolution. It provides insightful clues on the mechanisms of structure formation, and reversely any

theory or model of structure formation in the Universe needs to be able to explain and reproduce it (see the next section). Since many theories include mechanisms for late-type dwarfs to be converted into early-types at *some* point in their evolution, the morphology-density relation also provides us with a tool to assess how "relaxed" or evolved a galaxy cluster is, by the relative numbers of both classes of dwarfs. For examples, we turn to Figure 1.8. The more late-type dwarf galaxies a cluster has, and the further from the center they are orbiting, the less relaxed the cluster is (e.g. the Virgo cluster, Binggeli *et al.* 1993), since it indicates the dwarf galaxies have fallen into the cluster relatively recent. On the other hand, the more early-type dwarf galaxies there are in a cluster, and the closer their orbits are to the center, the more relaxed the cluster is (e.g. the Coma cluster, Forman & Jones 1982), since this would mean the dwarfs fell into the cluster a long time ago.

## 1.3 Theory

After the previous overview of the current state of the discovered dwarf galaxies, we will now give an overview of the currently accepted theories about the nature, the origin, and the evolution of dwarf galaxies.

### 1.3.1 Nature

One of the main conceptions on the nature of dwarf galaxies is that they are not simply scaled-down versions of giant galaxies, they feature several fundamentally distinctive fea-
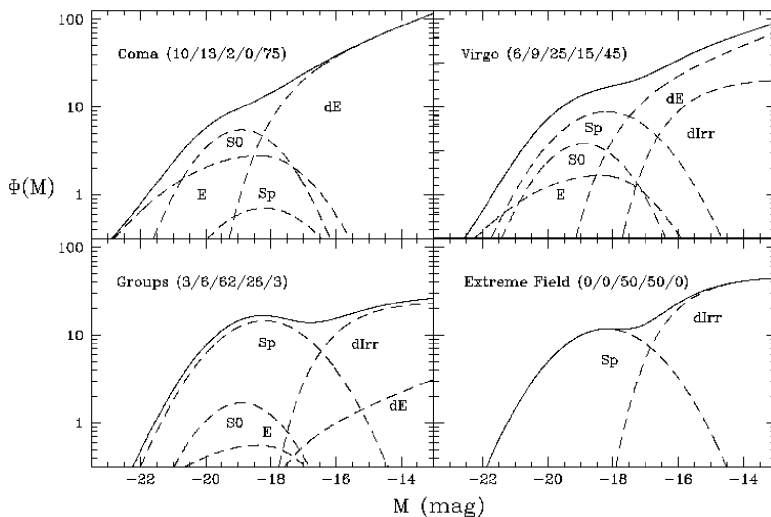


**Figure 1.8:** Luminosity functions of four different galaxy environments, indicating the contribution of different types of galaxies. Image credit: Helmut Jerjen, http://burro.astr.cwru.edu/Academics/Astr222/Galaxies/Intro/properties.html.

tures, which are all in some way connected to the fact that they have very *shallow potential wells.*

As already mentioned earlier in this introductory chapter, dwarf galaxies have a very high mass-to-light ratio (M/L). Having a high total mass compared to the total amount of luminous matter is an indication of a large amount of dark matter in the dwarf galaxy. Elliptical galaxies and dEs on average have a M/L of 5, dSphs are generally speaking somewhere between 10 and 100, and Ufds can even reach values of up to 1000 and more (Mateo, 1998; Wilkinson *et al.*, 2004; Simon & Geha, 2007; Tolstoy *et al.*, 2009). The trend is clear, the fainter the galaxy is, the more dark-matter-dominated it will be on average. In dwarf galaxies the stellar body, while for human eyes the main component of a galaxy, is of little dynamical importance. The total stellar mass is so small with respect to the total mass, that it does not greatly affect the potential well. The stars can actually be seen as a sort of "test particles" which, through their dynamical properties, reveal the underlying gravitational potential, which is mostly determined by the invisible but dominant dark matter halo.

Dwarf galaxies are also very diffuse systems, and generally it holds that the fainter a galaxy is, the more diffuse it will be - as opposed to giants. As a class, dwarf galaxies can be characterised by a surface brightness profile that exponentially declines with radius, where giant ellipticals usually show a much steeper De Vaucouleurs profile. Since this is a quite universal feature among the most common categories of dwarf galaxies (early types and late types), this hints to at least some evolutionary connection between the categories.

Furthermore, dwarf galaxies are also significantly more metal-poor than giant galaxies, where the term "metals" means all elements heavier than hydrogen and helium, the components of the primordial gas out of which the first stars formed. These elements are necessarily formed inside stars or as a byproduct of star formation (e.g. supernovae), through subsequent chains of nuclear reactions, and enrich the environment. Giant galaxies have average metallicities above that of our sun, while dwarf galaxies usually don't get higher than 1/3 of this, and often much lower.

All these features can actually be summarized in a single phrase: dwarf galaxies are quite *inefficient* star formation factories - a property which boils down to a natural outcome of its shallow potential well. The relatively weak gravitational forces make the system not very resilient against opposing forces, such as hydrodynamical pressures in the gas. Gas is therefore very inefficient at collapsing and reaching the necessary conditions for forming stars, so that only a small fraction of the matter is converted into luminous matter. This makes that proportionally much less stars are formed compared to the total matter, giving them a high M/L, and makes the formed stellar body relatively diffuse. When stars do form, they will eject their synthesized materials into the environment through feedback and supernovae which are powerful enough (compared to the gravity) to expel a significant amount of these metals out of the galaxy, unavailable for future star formation.

## 1.3.2    Evolution

Considering all the types and sub-types, the evolution of dwarf galaxies as a class can quickly become a complex issue. We can, however, start from an obviously simple point of view: since dwarf galaxies currently contain stars, they must have all contained gas at some point in their evolution to form these with. All dwarf galaxies we observe now, including the gas-poor dEs/dSphs must have been gas-rich before, and at some point must have strongly resembled dIrrs, or at least some common, gas-rich ancestor. Lots of these "primordial dwarfs" have however lost the majority of their gas reservoir during the course of their evolution, to star formation, other galaxies, or the intergalactic medium (IGM) - in some cases very gradually, in others quite drastically.

### 1.3.2.1    Internal gas removal

The most straightforward way to lose gas is to simply use it to form stars with, eventually depleting the full reservoir. A second most straightforward way is practically the opposite, though both are connected: a dwarf galaxy could blow its own gas content away into intergalactic space, through the stellar feedback from supernovae following a period of intense star formation (Yoshii & Arimoto, 1987). The out-of-control nuclear fusion in an exploding star injects enormous amounts of materials and energy into the ISM, creating an bubble of hot, thin gas that expands through the ISM with a strong shockwave. Combining many of these might accelerate the gas to above the escape velocity, making the gas unbound and escape the potential.

These are actually the two limiting cases, the majority of dwarf galaxies will exhibit behaviour somewhere in between: a gas content that might temporarily become dispersed enough by supernovae to shut down star formation, but that remains bound and available for future star formation when it collapses again over time. Which limit it most tends towards is mostly determined by the total mass of the galaxy, but also by other parameters such as the amount of angular momentum, and the metallicity of the gas. Stronger gravitational forces better contain the supernova forces, and more massive dwarfs will therefore convert their gas more efficiently into stars, while less massive dwarfs will have more difficulties to make the gas collapse densely enough again after a star formation event. Conservation of angular momentum will pose a centrifugal barrier in rotating dwarf galaxies that significantly decreases how efficiently gas collapses into the potential, moderating any possible strong starburst occurring. More metal-rich gas will be able to cool more efficiently through all the extra emission lines these higher elements provide to radiate energy away, decreasing the hydrodynamical pressures and making the gas collapse much easier, while metal-poor gas will have much more difficulties to achieve this. This continuous struggle between gravity and all opposite forces and "star formation pressures" makes for a whole spectrum of possible star formation histories, because most of these forces are roughly of the same order in the dwarf galaxy regime.

### 1.3.2.2   External gas removal

Many external processes can also play a role in the removal of gas from a dwarf galaxy. These mostly involve interactions of the dwarf galaxy as a whole with other "entities" in the Universe, be it other galaxies, large or small, the IGM, or cosmic radiation fields.

Interactions with other galaxies are almost inevitable and often plentiful, only few dwarf galaxies would be able to spend most of their life isolated from the rest of the galaxy-population of the Universe. The rate of interaction can vary strongly, however, depending on what type of interacting galaxy and at which point in cosmological history we are looking. Although they are the numerically dominant kind of galaxy, in cosmologically recent times interactions between dwarfs are rather rare due to their small dimensions and large separations. However, they are not impossible (as evidenced by the interacting Magellanic system, Besla *et al.* 2012), and in earlier cosmological times when the Universe was much smaller and denser things were undoubtedly different, since in the hierarchical scheme of structure formation the larger galaxies are created by mergers of smaller ones (see Section 1.3.3). Interactions with larger galaxies are much more likely, since their gravitational influence reaches much further, and most dwarf galaxies are in some orbit around massive galaxies. The strength and consequences of the interactions depend on how closely and with what relative velocities both galaxies approach eachother, and can produce a diversity of phenomena. This can go from partial gas loss that leaves ghostly trails which can wrap around the host galaxy several times (Martínez-Delgado *et al.*, 2008), over dynamically disturbed dark matter halos and stellar bodies that could lose much of their angular momentum (tidal stirring/stripping Mayer *et al.* 2001a,b or galaxy harassment Moore *et al.* 1996, 1998), to complete dwarf galaxies disrupted into huge tidal arms, indicating their imminent demise and assimilation into the host galaxy (galactic cannibalism, Ostriker & Tremaine 1975; Ostriker & Hausman 1977).

Dwarf galaxies will also interact with the intergalactic medium (IGM), a very hot and rarefied gas component that permeates the space between galaxies in clusters and groups. Although its density is very low, compared to bound gas in a galaxy, the IGM can have a strong influence on the much denser gas content of galaxies that move through it, and even completely strip them of their gas. In the so-called "ram-pressure stripping" process (Gunn & Gott, 1972; Lin & Faber, 1983; Mayer *et al.*, 2006; Boselli *et al.*, 2008), the IGM piles up at the front side of the dwarf galaxy which is plowing its way through this on its orbit, becomes denser and starts exerting a one-sided pressure on the bound gas of the galaxy. If the dwarf galaxy is moving fast enough, this is able to push away part of the bound gas, with the aid of hydrodynamical instabilities such as the Kelvin-Helmholtz effect (Valcke *et al.*, 2010; Roediger *et al.*, 2013), or even completely separate the gas content from the rest of the galaxy - while stars and dark matter are practically unaffected. On relatively short timescales of the order of 100 Myr or even less, a dwarf galaxy can leave most of its gas content behind on its way into the cluster.

### 1.3.2.3   Combination internal and external processes

Until now this has been an overview of *individual* processes, internal and external ones, that all might have the capability to unload a dwarf galaxy of the majority of its gas, and could therefore be a candidate-mechanism to convert gas-rich galaxies into gas-poor ones. The reality for the life of an actual dwarf galaxy is, however, usually not so unilateral. Often it will be a *combination* of the abovementioned mechanisms, and there is always an *interplay* between internal and external processes. For instance, gas which is only temporarily expelled from the central regions of a dwarf galaxy after a period of intense star formation, but remains bound to the galaxy and could re-collapse to feed star formation, can be permanently removed from the potential by a relatively mild gravitational interaction with another galaxy (starvation/strangulation, Larson *et al.* 1980; Balogh *et al.* 2000; Kawata & Mulchaey 2008).

Worth mentioning here is that dwarf galaxies can also experience interactions with different types of radiation fields that exist in the Universe, from cosmic rays, newly formed stars, UV background from reionization... None of these are usually energetic enough to independently expel gas from a dwarf galaxy, but they can assist the other mechanisms described above. An extra heat source can make the gas expand, so that it becomes more diffuse and more loosely bound, which will cause all gas-removing processes to become much more effective

In summary: due to their low mass, dwarf galaxies are susceptible to a variety of internal and external processes and disturbances, that significantly affect their ISM. This network of "interplaying interactions" undoubtedly holds the potential to transform gas-rich into gas-poor dwarf galaxies, in an appropriate manner that can explain the occurences of all the different dwarf galaxy types observed today.

### 1.3.3   Origin

After talking about the evolution of dwarf galaxies, a few words on the current theories about their origin.

In the context of the Λ-CDM cosmological paradigm (where the majority of the Universe is made up of dark energy and cold dark matter), there is a wide consensus on the so-called "hierarchical structure formation scenario". This dictates that after the decoupling of matter and radiation, when baryonic matter became free to collapse into to already existing dark matter halos, statistically speaking the smallest structures formed earliest, merged over time, and gradually formed larger structures. Therefore dwarf galaxies, or their common gas-rich ancestor (the "primordial" dwarf), were the first *galactic* objects to be formed in the Universe. The ones that managed to avoid too drastic interactions during their evolution formed the current dwarf galaxy populations, the other ones merged repeatedly and went on to form ever larger and larger galaxies. As mentioned in the previous section (1.3.2), these interactions between dwarfs were more abundant in the young and much smaller Universe than today. The currently more abundant practice of dwarf galaxies being assimilated by large galaxies can be seen as the continuation of the

hierarchical scenario.

Dwarf galaxies are therefore sometimes coined to be "galactic building blocks" of galaxy formation.

## 1.4   Modeling

However interesting dwarf galaxies might be in both cosmological and experimental contexts, observationally we of course only see a "snapshot" of a galaxy at a specific point in its evolution. This snapshot can provide us with a great deal of information on the galaxy's past evolution (through e.g. its stellar populations), but these are often characterized by large uncertainties and/or relatively low time resolutions. Furthermore there is also the unfortunate fact that not all components or aspects of a galaxy can be traced back through time equally well when using observations, and some even not at all (e.g. gas evolution).

So to really experiment in these so-called galactic laboratories we have to resort to modeling, and build virtual representations of dwarf galaxies to investigate and compare with observations. Galaxy modeling comes in many forms and levels of detail: from simple semi-analytic models consisting of only a few equations that empirically describe the evolution of a few global quantities, to full-fledged galaxy simulations that attempt to self-consistently form and evolve galaxies in their entirety with all relevant astrophysical components and processes taken in to account. The modeling of dwarf galaxies in this PhD research falls under the latter category, and is performed in the form of N-Body/SPH simulations using a modified version of the freely available GADGET-2 simulation code.

### 1.4.1   Particles

A central concept in modeling using simulations, is to divide whatever physical system is under investigation into a finite amount of fundamental elements such as particles or cells. In a galactic context the former "particle approximation" seems to be quite justified to represent the stellar component... but this approximation can also be done for the gaseous component, which is actually to be seen as a continuous medium, and even for the dark matter content of which we currently don't even understand what it consists of. The precise details of the "particle"-concept differ, however, for the different astrophysical components - Sections 1.4.4 and 2.3.2 elaborate further on this, while Figure 1.9 gives a schematic representation.

### 1.4.2   Resolution

When dividing a system into particles, the first question raised is: how many of them should we take? Or, how large or massive should the elemental units of the system be? This seems like a straightforward issue to handle, basically looking for the most advantageous trade-off between computational cost and spatial detail. However, the chosen resolution
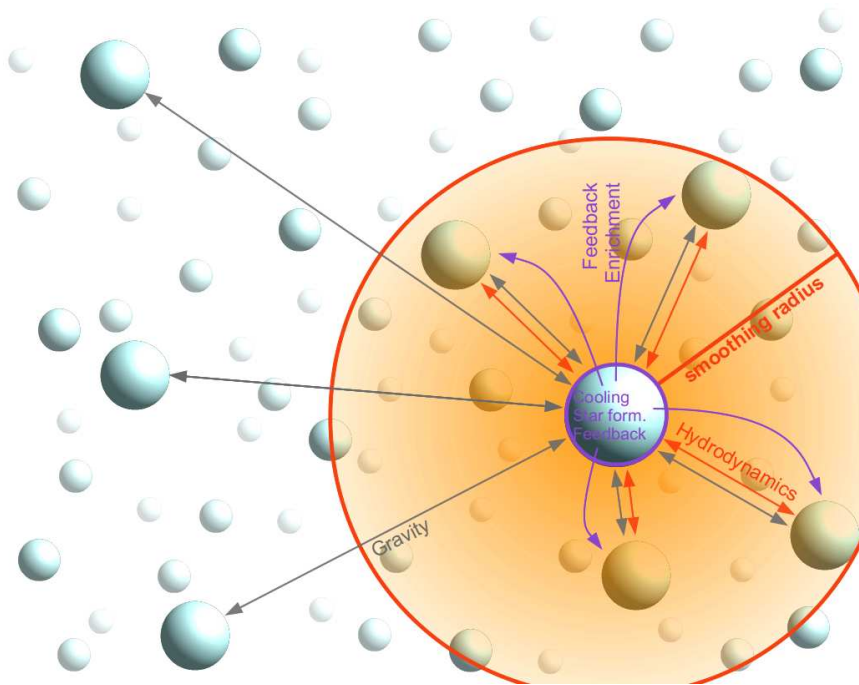
**Figure 1.9:** Schematical representation of the particle concept, and the on-grid and sub-grid processes that could be acting on a single particle in the N-Body/SPH simulations of dwarf galaxies used in this PhD research. The on-grid physics are comprised of gravity (indicated as grey arrows), which is in principle calculated for all particles, and hydrodynamics (orange arrows) which is only calculated for particles within the primary particle's sphere of influence (orange circle). The strength of the influence declines with distance, which is indicated by the color gradient in the orange circle. The sub-grid physical processes that go on inside a simulation particle are comprised of radiative cooling (and heating), star formation, and stellar feedback. Of course this last one only applies to star particles, and consists of the expulsion of (enriched) matter and supernova energy over the neighbouring gas particles. These are both spread out within the area that used to be the original gas particle's sphere of influence, also according to the same smoothing kernel function.

will invoke a deeper separation in the different physics that are taken into account in the simulation.

## 1.4.3 Physics

Once a resolution is chosen for a simulation, it will mark the distinction between so-called "on-grid" and "sub-grid" physical processes. This can be understood as the "resolved" and "unresolved" physics.

#### 1.4.3.1   On-grid physics

Physical processes such as gravity and hydrodynamics have a relatively scalable character, and can be described purely as fundamental interactions between individual simulation particles (see Figure 1.9). The more practical details on implementing these two processes are discussed in Section 2.3.2.

#### 1.4.3.2   Sub-grid physics

Other physical processes like star formation, however, are not scalable. These take place on specific spatial scales, which are currently still far below any feasible full-galaxy-simulation scale due to computational limits. These non-resolved processes can still partly contain interactions between individual simulation particles, but also contain a form of "internal evolution" which is added to the particles (see Figure 1.9). These additional prescriptions are based on theoretical assumptions and models about the composition of a particle and what goes on inside it. All the actual *astro*physical processes that we need to include to have self-consistent simulations of galaxy formation and evolution are of this form, and their implementations are discussed in more detail in Section 2.2.

### 1.4.4   Simulation methods

The simulation method of choice in this PhD research is a so-called N-Body/SPH method, specifically GADGET-2, that implements the on-grid gravitational (N-Body) and hydrodynamical (SPH) forces. It is modified and extended with additional prescriptions and functionalities to enable all the necessary sub-grid astrophysical processes, to form a galaxy inside a simulation. Details on all implementations can be found in Chapter 2.

#### 1.4.4.1   N-Body

Both stars and dark matter mainly interact with each other through gravity, and are basically treated as point masses without any size in the N-Body method. Ideally, the gravitational force on a particle is the result of summing the gravitational forces it experiences from each individual particle. In the reality of computational limitations this is done with sophisticated approximation schemes to avoid having to explicitly calculate every one of these forces. N-Body codes are therefore in essence very simple, only having to calculate gravity between particles, but with the right calculation schemes behind it, they can be made very accurate and very efficient for simulating a self-gravitating system.

#### 1.4.4.2   Smoothed Particle Hydrodynamics (SPH)

Gas, however, requires a more complex particle-concept if one wants to combine it with the other components in the simulations. In the SPH method, the gas is functionally speaking represented as particles, making it highly compatible with gravitational N-Body methods, but as the name suggests they are also given the notion of a spatial extent. They can be seen as anchor points in a continuous medium, which have a limited area of influence

in which they interact hydrodynamically with other anchor points (see Figure 1.9). The strength of the interaction falls off with distance according to a specific function, the smoothing kernel, which reaches zero at a specific radius (smoothing length). The most important feature, however, is that the area of influence is set for each particle individually by the local density of gas particles - having a small smoothing length (= high resolution) in dense environments and vice versa. SPH is therefore able to adapt its spatial resolution to local conditions, and can efficiently and automatically cope with a large range of densities and scales in a single simulation. This flexibility and computational efficiency, together with its intuitive concept and compatibility with standard N-Body techniques are the main reasons to choose the SPH method for full-galaxy simulations. More extensive descriptions of the SPH method can be found in Section 2.3.2.

### 1.4.4.3   Problems and alternatives

The SPH method is not without flaws, however, when used to simulate an interstellar medium. Shocks, discontinuities, or contact layers between different media of any kind are usually a major issue to simulate correctly with SPH, since it will inherently tend to smooth these out. SPH can therefore not capture their full effect on the gas, and is not very well suited to simulate all kinds of hydrodynamical instabilities (e.g. Kelvin-Helmholtz, Rayleigh-Taylor).

An alternative to the particle-based (Lagrangian) approach is a so-called mesh-based (Eulerian) approach. Here it is not the simulated matter, but the (fixed) spatial volume itself which is divided into cells by a grid. These cells keep track of the matter that flows in and out of it through its boundaries, and they can be refined when necessary by splitting them up into smaller cells. These types of simulation codes, called Adaptive Mesh Refinement (AMR), are superior at capturing discontinuities and hydrodynamical instabilities, but bring about their own problems. They are computationally more intensive, can not easily handle large density contrasts due to the large number of grid levels needed (i.e. less flexible), and by construction have a fixed-size spatial domain that might turn out to be too small.

Capturing these hydrodynamical instabilities is mainly important in the context of galaxy simulations when the ISM of the simulated galaxy is interacting with an environment. For example, during ram pressure stripping (described in Section 1.3.2) Kelvin-Helmholtz instabilities will arise on the boundaries between the high density ISM and the low density IGM, and they are the dominant processes that will mix and disrupt the dense ISM in the galaxy. Capturing shocks on the other hand are important when modeling very explosive events such as individual supernovae. AMR codes, capturing all these phenomena much better than SPH, are practically mandatory in these situations. However, the dwarf galaxy simulations in this PhD research are predestined to evolve in isolation, and the computational limitations on resolution make that supernova feedback in our simulations comes from whole stellar populations, which is given in a very smoothed "SPH-way" (see Section 2.2.3). Perfectly resolving all hydrodynamical instabilities and shocks is therefore of lesser importance, and the flexibility, efficiency, and intuitiveness of SPH is preferred

over the benefits provided by AMR.

## 1.5   Thesis overview

This thesis manuscript is structured as follows:

- Chapter 2 gives a comprehensive summary on all aspects of the N-Body/SPH dwarf galaxy models that have been used for this research, and provides guidelines for aspiring simulators on how to set them up.

- Chapters 3 and 4 are integral representations of the research on these dwarf galaxy models that has been published in two articles in *Monthly Notices of the Royal Astronomical Society* during the course of this PhD project. Evidently this research does not always employ *all* the functionalities of the models, since these were developed alongside the research.

- Chapter 5 concludes the main body of research of this PhD project with an account of the latest, not yet published results on the dwarf galaxy models, now using their *full* capabilities as outlined in Chapter 2. This mainly revolves around the usage of the full scheme of radiative cooling and heating, and the possibilities derived from this.

Lastly, an concise summary of the entire PhD work is given in Chapters 6 and 7, respectively in English and in Dutch, as well as an outlook on possible future research in Chapter 8. Appendices are provided with useful codes and scripts to analyze and visualize dwarf galaxy models.

# 2

# How to cook a numerical dwarf galaxy model

This first chapter is an attempt at giving a self-contained and detailed overview/manual for how to cook up a self-consistent N-Body/SPH dwarf galaxy model - *Ghent style*.

First of all, we do not aim specifically at simulating either late-type (gas rich and starforming) dwarfs or early-type (gas-less, no star formation) dwarfs: their classification mostly depends on when during their star-formation evolution they are observed, a view which is also advocated in Koleva *et al.* (2013) in the context of observations. Within this unified picture, a meaningful comparison of our simulations with observations of both early-type and late-type dwarf galaxies is permissible. In isolated dwarf galaxy models, free of any external influences, stellar feedback alone is unable to unbound the gas from the potential well, so they retain at least part of their gas reservoirs throughout the simulations. In Schroyen *et al.* (2011), Chapter 3 in this thesis, we show that high-angular-momentum dwarf galaxies foster continuous star formation and are dwarf-irregular-like (dIrr) while low-angular-momentum dwarf galaxies have long quiescent periods in between centralized star-formation events. During these lulls, these dwarfs would be classified as dwarf spheroidals (dSph) or dwarf ellipticals (dE) (although containing gas for future star formation), while during a star formation event it would appear as a bursty dwarf galaxy that is at least qualitatively reminiscent of a blue compact dwarf (BCD).

For this PhD research we intentionally chose to use dwarf galaxy models in *isolation*, and not give them a more cosmologically funded formation history. This is done to have total control over all parameters, to be able to unambiguously evaluate their effects, and in this way probe their fundamental behaviour under idealized conditions. Because of this choice, we will never try throughout this thesis to compare individual model evolutions one-to-one with those of observed dwarf galaxies, or search in our range of models for the

best match to a specific dwarf galaxy. If a good match could be found, it would not give more useful insight or information about the dwarf galaxy besides the statement that the model's evolution is *one of the many possible ways* that such an object could have been formed. Considering the isolated setup and the inherent stochasticity of the system, it is even highly unlikely that the simulated star formation history would be any proxy at all for the actual star formation history that the dwarf galaxy might have experienced, especially at the earliest epochs. We will focus on comparing mean properties of our models with observed dwarf galaxies to learn about their evolution.

In the remainder of this chapter, we will

1. Discuss the basic ingredients that are used in our models for their initial setup, in all their forms: presenting all the available options for all components, while discussing which option or combination of options to select in what situation and why (Section 2.1).

2. Explain the astrophysical recipes that are employed, on top of a background of gravitational and hydrodynamical physics, to turn these raw initial ingredients into a simulated dwarf galaxy - by treating the gas as a self-consistent interstellar medium (ISM) that radiatively cools/heats, forms stars, and gets heated and enriched by supernovae (Section 2.2).

3. Present the cookware that we used/modified/developed to generate and implement all the above, and do all the necessary calculations (Section 2.3).

These dwarf galaxy models and simulation codes were (and still are) a work in progress, and are developed and extended *alongside* the scientific research we do with them. This chapter tries to give a complete and concise overview of the *current* status of our models, as of at the end of this PhD research, meaning that the results of our published research during the past years that we present in Chapters 3 (Schroyen *et al.*, 2011) and 4 (Schroyen *et al.*, 2013) do not always use the full capabilities of the models as they are described here. At the beginning of each of these chapters we briefly state which specific setup and options are used for the models at hand, to indicate at which point in the development process the research took place. In Chapter 5 we present the results of our latest simulations, which are using the *full* capabilities of the models.

Note: these models are very much the product of a group effort. Many of the basic elements of our dwarf galaxy models were already solidly in place before my time (Valcke *et al.*, 2008), and other elements were modified, extended, and added by/in cooperation with others (e.g. Cloet-Osselaer *et al.*, 2012; Vandenbroucke *et al.*, 2013; De Rijcke *et al.*, 2013). I therefore cannot - and should not - claim total intellectual ownership over them in the presentation of this particular PhD research... To give a clear view on my own contributions to the dwarf galaxy models, in this overview chapter, markings in the title of the sections/subsections indicate whether I

- † created this particular element in the models,

- ◎ made a significant contribution to it,

- \* made minor contributions to,

- relied on someone else's diligent labour.

## 2.1   Ingredients

In order to cook something interesting, one needs proper and tasteful ingredients to start with. The basic spherically symmetric initial setup for our dwarf galaxy models consist of (see also Figure 2.1)

- a dark matter halo with a density profile and a matching orbital velocity distribution (Section 2.1.1),

- a superimposed gas cloud, set to a fixed initial temperature of $10^4$K, initial metallicity of $10^{-4}Z_\odot$ and with the gas particles initially at rest. It can also be given an initial density profile, initial random motions, and an initial rotation profile (Sections 2.1.2, 2.1.3 and 2.1.4).

The relative masses of both components comply to the cosmological parameters $\Omega_m = 0.2383$ (total matter density) and $\Omega_{dm} = 0.1967$ (dark matter density) from Spergel *et al.* (2007), while the total average density over the initial simulation volume is equal to

$$\rho_{tot} = 5.55 \times \frac{3h^2 100^2}{8\pi G}[\Omega_m(1+z)^3 + 1 - \Omega_m] \tag{2.1}$$

where $h = 0.71$ (Spergel *et al.*, 2007), $G$ is the gravitational constant, and $z$ is the redshift. The factor 5.55 results from the Tolman model for a spherical overdensity of matter in the Universe, the rest of the expression is the average density of the Universe in function of redshift. When a total mass for the model is taken, the masses and initial average densities of the individual components are determined, and at the same time also the initial radius of the spherical volume that they occupy. The exact spatial distribution of the mass within this radius is however still to be determined at will (Sections 2.1.1 and 2.1.2).

The simulations generally start at redshift 4.3, a value where dwarf-galaxy-sized halos will on average be formed according to the results of a query to the milli-Millenium simulation (Springel *et al.*, 2005; Valcke *et al.*, 2008). Since at that redshift, and even higher ones, massive galaxies are already observed, our most recent simulations in Chapter 5 start from a much higher redshift of 12. The gas cools (Section 2.2.1), collapses into the gravitational potential well of the dark matter, and is able to form the stellar body of the simulated dwarf galaxy through a self-consistent description of star formation (Section 2.2.2), feedback (Section 2.2.3) and metal enrichment (Section 2.2.4). Further specific information and details on these models are given in Table 2.1 and in the rest of this section. The actual initial condition files (containing positions, velocities,... for all the particles) are created by random sampling of the chosen density profiles.

**Table 2.1:** Details of the basic spherical setup for our dwarf galaxy models. Columns indicate: (1) model number, (2) total dark matter mass [$10^6\,\mathrm{M_\odot}$], (3) cutoff radius for the dark matter halo [kpc], (4) Kuz'min Kutuzov parameter [kpc], (5) NFW characteristic radius [kpc], (6) NFW characteristic density [$10^7\,\mathrm{M_\odot/kpc^3}$], (7) total initial gas mass [$10^6\,\mathrm{M_\odot}$], (8) cutoff radius for the gas halo [kpc], (9) pseudo-isothermal scale radius [kpc], (10) pseudo-isothermal characteristic density [$10^7\,\mathrm{M_\odot/kpc^3}$].

| nr | $M_{DM,i}$ | $r_{cut}$ | $r_{KK}$ | $r_{NFW}$ | $\rho_{nfw}$ | $M_{g,i}$ | $r_{cut}$ | $r_{p-i}$ | $\rho_{p-i}$ |
|----|------------|-----------|----------|-----------|--------------|-----------|-----------|-----------|--------------|
| 01 | 206 | 14.867 | 0.439 | 0.470 | 6.259 | 44 | 12.582 | 0.146 | 1.324 |
| 02 | 248 | 15.815 | 0.466 | 0.506 | 6.079 | 52 | 13.371 | 0.157 | 1.286 |
| 03 | 330 | 17.395 | 0.513 | 0.566 | 5.812 | 70 | 14.716 | 0.177 | 1.229 |
| 04 | 495 | 19.913 | 0.587 | 0.664 | 5.452 | 105 | 16.846 | 0.209 | 1.153 |
| 05 | 660 | 21.916 | 0.646 | 0.744 | 5.211 | 140 | 18.541 | 0.236 | 1.102 |
| 06 | 825 | 23.609 | 0.696 | 0.812 | 5.032 | 175 | 19.973 | 0.259 | 1.064 |
| 07 | 1238 | 27.029 | 0.797 | 0.952 | 4.722 | 262 | 22.863 | 0.305 | 0.999 |
| 08 | 1651 | 29.752 | 0.877 | 1.067 | 4.513 | 349 | 25.164 | 0.344 | 0.954 |
| 09 | 2476 | 34.055 | 1.004 | 1.251 | 4.236 | 524 | 28.805 | 0.406 | 0.896 |
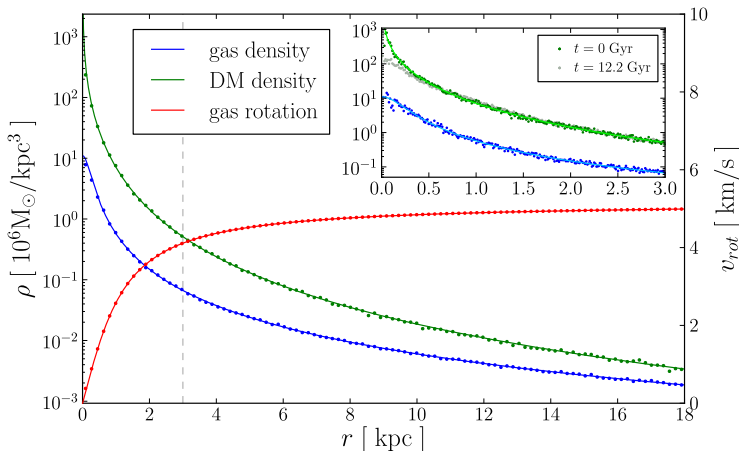


**Figure 2.1:** Initial conditions of our dwarf galaxy '05' model (see Table 2.1). Several radial profiles are shown: the blue and green are the density profiles of, respectively, the gas (pseudo-isothermal) and dark matter (NFW) haloes (left $y$-axis) - red shows the rotational velocity profile of the gas (right $y$-axis). Full lines represent the theoretical curves (found in Paragraphs 2.1.1, 2.1.2, 2.1.4) while dots are the actual radial profiles. Inset in the upper right corner shows a zoom-in on the central part of the density profiles, with a higher number of sampling bins (the same units on the axes as the large plot, central part is indicated with a dashed grey line). The dark and light shades of green respectively are the dark matter density profiles at 0 Gyr and 12.2 Gyr, showing the flattening of the NFW cusp as in Cloet-Osselaer *et al.* (2012).

### 2.1.1   Dark matter halo *

The dark matter (DM) halo in our dwarf galaxy models, which is implemented as a "live" halo, basically serves as the background potential in which the baryonic matter collapses, but with which the baryonic matter can also interact. A static potential without interaction between baryons and dark matter is computationally much cheaper, but could lead to unrealistic behaviour. The density profile can be set to either a "cored" or a "cusped" profile, which in this case corresponds to halos with either a finite central density with zero slope or a density profile that diverges with radius as $r^{-1}$. A cored profile is what is generally observed in real galaxies, while a cusped profile is what is predicted by cosmological dark-matter-only simulations (see the overview in de Blok, 2010).

As a cored profile we employ the analytical and well behaved Kuz'min-Kutuzov profile (Dejonghe & de Zeeuw, 1988)

$$\rho_{KK}(R, z) = \frac{Mc^2}{4\pi} \frac{(a^2 + c^2)R^2 + 2a^2 z^2 + 2a^2 c^2 + a^4 + 3a^2\sqrt{a^2 c^2 + c^2 R^2 + a^2 z^2}}{(a^2 c^2 + c^2 R^2 + a^2 z^2)^{3/2}(R^2 + z^2 + a^2 + c^2 + 2\sqrt{a^2 c^2 + c^2 R^2 + a^2 z^2})},$$
(2.2)

where $a$ and $c$ are parameters for, respectively, the length of the major and minor axis, $R$ is the distance in the equatorial plane, and $z$ the height above or below this plane.

The employed cusped density profile profile is the so-called "NFW" density profile (Navarro-Frenk-White, Navarro *et al.* 1996, 1997):

$$\rho_{dm}(r) = \frac{\rho_s}{\frac{r}{r_s}(1 + \frac{r}{r_s})^2},$$
(2.3)

with radius $r$ and characteristic parameters $\rho_s$ and $r_s$ (see Fig. 2.1). In Cloet-Osselaer *et al.* (2012) the details of the implementation are discussed, with the difference that instead of using the parameter correlations from Wechsler *et al.* (2002) and Gentile *et al.* (2004) we now use those from Strigari *et al.* (2007), since they are derived specifically for low-mass systems. However, even when selecting this cusped density profile for the initial conditions, one ends up with a cored density profile when running the simulation. It is shown convincingly in Cloet-Osselaer *et al.* (2012) how the central dark-matter cusp is naturally and quickly flattened through gravitational interactions between dark and baryonic matter:

1. when collapsing into the DM potential well the central density of the gas gradually increases, thus adiabatically compressing the center of the DM halo

2. when the gas density reaches the threshold for star formation (see Section 2.2.2), stellar feedback causes a fast removal of gas from the central regions of the DM halo, making the DM halo expand non-adiabatically, resulting in a net lowering of the central density.

A cusped density profile will thus naturally evolve into a more cored density profile if a self-consistent star formation cycle is included in the model, as shown in the inset in Fig. 2.1.

This flattening effect is seen in all our models, with its strength related to the value of the density threshold ((ranging from 0.1 to $100\,\mathrm{amu/cm^3}$, see Section 2.2.2). While this cusp flattening effect has also been found by other authors, such as Governato *et al.* (2010), its strength and the sizes of the formed cores may vary between authors. This can be explained by the fact that different authors use different star-formation density thresholds and that some, like Governato *et al.* (2010), select dwarf galaxies from fully cosmological simulations of a larger volume of the universe. The latter type of simulations includes the dwarf galaxies' full formation and merger history. This is much more disruptive than what we employ here. Our simulations start with an idealized, isolated setup where all the baryonic matter is already present and free to collapse into the DM potential.

Although in both cases it results in getting a cored dark matter density profile, we prefer starting our simulations with the cusped NFW density profile. Seeing that this is what dark matter overdensities will naturally evolve towards when left on their own, it is the most appropriate form for our dark matter halos to begin with, since we take the start of our simulations to be at the moment when baryonic matter starts falling into the already present dark matter overdensities (which have evolved independently until that point). Afterwards they will get flattened into a cored density profile naturally, by the baryonic processes involved in forming the (simulated) galaxy.

### 2.1.2   Gas halo †

The gaseous halo in our dwarf galaxy models is set up without any requirements about hydrostatic equilibrium, either as a homogeneous sphere (in other words, with a flat density profile) or on a pseudo-isothermal density profile of the form

$$\rho_g(r) = \frac{\rho_c}{1 + \left(\frac{r}{r_c}\right)^2}, \tag{2.4}$$

with radius $r$ and the two model parameters $\rho_c$ and $r_c$, respectively the characteristic density and scale radius. The characteristic density of the pseudo-isothermal gas density profile is related to the characteristic density of the dark matter density profile (see Paragraph 2.1.1) in the following way:

$$\rho_{g,c} = \frac{\Omega_b}{\Omega_{dm}}\rho_{dm,c}, \tag{2.5}$$

where $\rho_{g,c}$ and $\rho_{dm,c}$ are the relevant characteristic gas and dark matter densities, respectively, and $\Omega_b/\Omega_{dm} = 0.2115$ the fraction of baryonic to dark matter (values for the latter taken from the 3-year WMAP results, Spergel *et al.* 2007). Since the total gas mass and the maximum radius are set (see beginning of Section 2.1) this fixes the scale radius $r_c$. Fig. 2.1 shows the initial setup for one of our models, while Table 2.1 lists the gas halo parameters for all our models.

The gas particles in the halo can also be given random motions (Section 2.1.3) or ordered motions, the latter in the form of a rotation profile (Section 2.1.4).

In most cases there is no significant or qualitative difference in behaviour of the dwarf galaxy models when using either of these initial gas density profiles. Only when employing

a high star formation density threshold (such as $100 \, \mathrm{amu/cm^3}$, Section 2.2.2) in a dwarf galaxy model with high angular momentum (profile value of e.g. 5 km/s, Section 2.1.4) do we specifically need to use the pseudo-isothermal profile. The homogeneous sphere will in this case cause the models to hardly form any stars, and only very late in the evolution (after several gigayears), since the rotation prevents gas particles from falling into the gravitational potential and reaching densities high enough for star formation to occur. To ensure a realistic dwarf galaxy is being formed in the simulation that compares well with observations, we resort to the pseudo-isothermal gas density profile which facilitates the gas reaching this density.

### 2.1.3 Random motions †

Simple random motions can be added to the gas particles, using a standard random number generator in C++. These can be chosen to be tangential, radial, orthogonal, or full 3-dimensional velocities. No specific velocity distribution is assumed here.

### 2.1.4 Angular momentum (ordered motions) †

Rotation is added *to the gas only* in the initial conditions because the DM halo, although implemented as a live halo, simply provides a background gravitational potential with interaction between baryons and DM, and is not given any rotation. Every gas particle is given a tangential velocity in the $xy$-plane around the $z$-axis, according to the desired "rotation profile" which expresses the value of the rotational velocity in function of the distance to the rotation axis (see Figure 2.1). The indicative value $v_{rot}$ for the strength of the rotation given to the model is the maximum value of the rotation curve which is reached at the outer edge of the gas sphere, regardless of the specific rotation profile. The available rotation profiles are:

- a simple constant rotation profile,

- a linearly rising profile ("solid body" rotation),

- an arctangens profile that goes to 0 in the center,

- a combination of those : e.g. a linear or arctangens section rising with radius until a certain point, and then remaining constant on larger radii.

Which rotation profile to choose depends to some extent on the chosen density profile for the gas halo (Section 2.1.2).
Firstly we can generally state that, whatever the specifications of the gas halo, we prefer not to use a full linear solid body profile, since in test simulations a significant fraction of the gas content of the galaxy immediately became unbound and was lost for future star formation, even at low rotation speeds. A combination of a linear part out to a few kiloparsec and a constant part further outward remains however a viable option.
Secondly, in case of a homogeneous gas sphere, it does not appear to matter much which of the profiles is chosen. Since the remaining possibilities only show significant differences

in their inner few kiloparsecs (constant, linearly rising, arctangens rising), and the central regions in the homogeneous sphere do not contain a large amount of gas (relative to the total amount of gas), the specific rotation profile is of no importance (see Figure 2.2). We usually simply take a constant profile here, even though it actually means that the angular rotation velocity shoots up when getting close to the center. Only a small number of gas particles will actually get these high angular velocities, lose them quickly through interactions with other gas particles, and convert them to heat which is radiated away efficiently through the implemented radiative cooling curves (Section 2.2.1).

Lastly, in case of a pseudo-isothermal gas halo, it is necessary to choose a rotation profile that goes to zero in the center, since the previous reasoning is invalid here: now the gas *is* quite centrally concentrated, with an important fraction of the gas residing in the central regions, so employing a constant rotation profile here would deliver a high amount of angular momentum to a significant fraction of the central gas, expelling most of it to large radii and preventing star formation. Usually an arctangens profile is chosen in this case, of the form

$$v_{tan,i}(r) = \frac{2}{\pi} \arctan\left(\frac{r}{r_s}\right) v_{rot}, \qquad (2.6)$$

with radius $r$ and scale radius $r_s$, although a combined linear-constant profile would give similar results.

### 2.1.5   Geometric flattening †

As a parameter to indicate geometric flattening we consistently use the axis ratio $q = c/a$, where $c$ is the shortened diameter of the model and $a$ is the diameter in the plane of the galaxy (assuming axially symmetric models). Although flattening like this will naturally arise when there is a significant amount of angular momentum present in the model, we can also already impose a flattening on the initial setup, both on the DM component (in case of a Kuz'min Kutuzov profile, Section 2.1.1) and the gas component (in case of a
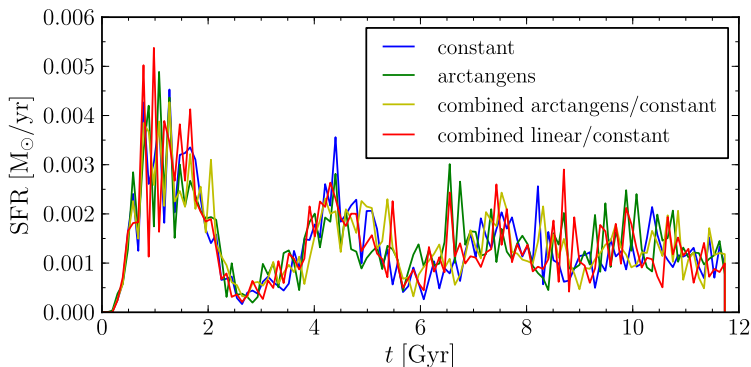


**Figure 2.2:** The star formation rate as a function of time for four different rotation profiles in a homogeneous gas sphere.

homogeneous sphere, Section 2.1.2).

The parameters of the Kuz'min Kutuzov profile naturally allow for introducing a flattening
in the DM halo in the form of an axial ratio (Dejonghe & de Zeeuw, 1988), while flattening
the homogeneous gassphere takes a little bit more care. The diameter of the model in the
direction perpendicular to the flattening direction needs to scale up appropriately while
the diameter in the direction of the flattening scales down, to ensure that the density
of the gas cloud remains the same. Starting from a sphere with radius $r$, if we want to
achieve a flattening $q$ we produce it by calculating the $a$ and $c$ axes as follows:

$$a = rq^{-1/3} \tag{2.7}$$

$$c = rq^{2/3}. \tag{2.8}$$

This will ensure that the volume of the ellipsoid is constant for any value of $q$, and therefore
so is the density.

## 2.2   Recipes

With all the necessary initial ingredients described in Section 2.1 ready in hand, we will
need a collection of recipes and prescriptions to describe what to *do* with these ingredients
in order to cook up a realistic dwarf galaxy.

A solid physical base of gravity with hydrodynamics will be provided by most simulation
codes (Section 2.3.2), so we need to concern ourselves only with adding tasteful astrophys-
ical spicings to the baryonic component, to be able to form and evolve galaxies in our
simulations.

Suggested additions are (in a somewhat logical order):

- radiative cooling (and heating) (Section 2.2.1)

- star formation (Section 2.2.2)

- feedback (Section 2.2.3)

- metal enrichment (Section 2.2.4)

which form what one might call an "astrophysical cycle", where each process influences the
others in a complex self-regulating behaviour, describing how baryonic matter is processed
and recycled in a galactic environment. While the basic physics are explicitly integrated as
"on-grid" physics in the simulation code (as fundamental interactions between simulation
particles), the whole astrophysical cycle is implemented as "sub-grid" physics because
they take place on scales below the resolution of the simulations (inevitably involving
assumptions about internal properties and evolutions of the simulation particles).

### 2.2.1   Radiative processes ↻

Radiative processes (cooling and heating) are an important source and sink of energy for
the gas content of a galaxy. One of the first and most important things baryonic matter

can do in the Universe, is cool - if it could not, the Universe would be quite an rarefied, hot and boring place, where nothing could ever start to collapse to densities high enough to form any structure at all.

Since we are at the level of sub-grid physics, we need some external prescriptions to be able to estimate by how much a gas particle will cool in a certain time interval, based on only a limited amount of global properties of the particle (such as temperature, density, metallicity, etc.). This is usually done with the aid of precomputed tables of the cooling rate for certain different values of the employed parameters, the so-called "cooling curves". These tables are interpolated or extrapolated on during the simulation. Several types of cooling curves are available for use in our models, each with their own assumptions, schemes, strengths and weaknesses. We will give an overview here in chronological order of usage, which coincides with the order of complexity of their modeling.

The first option is to use the cooling curves from Sutherland & Dopita (1993), which are often used in this kind of simulations (see Figure 2.3), and which was used in the first part of this PhD research that is presented in Chapter 3. The radiative cooling rate depends on the density of a gas particle and on its chemical composition. In the calculations the former is taken into account as a quadratical multiplication factor, while the latter is estimated using the metallicity as a parameter, assuming the gas is fully ionized. This requires us to only interpolate in metallicity and temperature to obtain the cooling rate for a gas particle, which is computationally very cheap, but it has some drawbacks. These are mostly due to the oversimplification of the chemical composition model, where several assumptions about the employed abundance ratios make the radiative cooling strength to be quite off in certain situations. When $[\mathrm{Fe/H}] < -1$, supernova type II abundances are assumed, while on the other hand linearly scaled solar abundances are assumed when $[\mathrm{Fe/H}] > -1$. In particular in the case of dwarf galaxies this could lead to significant over- or underestimates of the chemical abundances and the cooling rates (De Rijcke *et al.* 2013). Another drawback is their limited temperature range, going from $10^4$ to $10^9$ K.

Since we want to explore higher density thresholds in our star formation scheme (Section 2.2.2), we will require gas to be able to cool further, below $10^4$ K, in order to reach these high densities and form stars. So we are in need of cooling curves with an extended temperature range, which can be achieved in two ways. The first is what can be dubbed the "quick and dirty" method: finding supplementary cooling curves in the literature for temperatures below $10^4$ K (e.g. the curves from Maio *et al.* 2007), and pasting them together with the Sutherland & Dopita (1993) cooling curves. This is an often used approach in numerical simulations (Sawala *et al.*, 2010; Revaz *et al.*, 2009; Cloet-Osselaer *et al.*, 2012). However, besides the individual drawbacks of both types of cooling curves and the lack of consistency between them, since both were calculated separately with their own assumptions and modeling, this approach also features an unnaturally sharp drop of the cooling rate by about 4 orders of magnitude at $10^4$ K (see Fig. 2.3). This leads to a pile-up of gas particles at precisely this temperature. The second way is to produce fully self-consistent radiative cooling curves, featuring a continuous temperature range from $10$ K to $10^9$ K in one calculation scheme incorporating all relevant processes and elements

(De Rijcke *et al.*, 2013). In the first available version of these novel cooling curves (Figure 2.4) the radiative cooling strength depends on temperature, metallicity (in the form of [Fe/H]) and alpha element abundance (quantified by [Mg/Fe]). Since iron is produced in relatively high amounts in supernovae type Ia (SNIa) and in relatively low amounts in supernovae type II (SNII), and magnesium shows similar but opposite characteristics, they are good tracers of the contribution of the abundances of, respectively, SNIa and SNII to the total composition of the gas. This gives a more sophisticated estimate on the complete composition of the gas, predicting well the chemical abundances of standard stars from just their iron and magnesium abundances (De Rijcke *et al.*, 2013). For this chemical composition the ionization equilibrium and level populations are calculated, while taking into account all the relevant interaction processes. A modified version of the ChiantiPy atomic database (Dere *et al.*, 2009) is then used to predict the total radiative cooling rate for this gas. Using the tables produced in this way in our simulations now requires a 3-dimensional interpolation (in temperature, [Fe/H] and [Mg/Fe]), but eliminates most of the drawbacks of the previous cooling curves: wide range of temperatures ($10\,\mathrm{K}$ to $10^9\,\mathrm{K}$), one consistent calculation scheme over the whole range without a sharp discontinuity, and much more sensible estimates for the chemical composition in a much wider range of situations. For the parameter values were chosen: 8 [Fe/H] values and 6 [Mg/Fe] values - which give (plus a zero metallicity curve) a total of 49 cooling curves, shown in Figure 2.4. These cooling curves were used in the second part of this PhD research, which is presented in Chapter 4.

This is however not yet the end of the story. For a fully realistic treatment of the radiative processes in the baryonic component of our model dwarf galaxies we also need to account for radiative heating, by the cosmic UV background and the interstellar radiation field. This can be done as an extension to the previous calculation scheme, where radiative heating now has to be considered as well when calculating the ionization equilibrium and optimizing the level populations, since it significantly affects the energy balance of the elements. Introducing radiative heating also introduces an extra parameter in the calculations: the redshift, since the strength of the UV background is highly dependent on this (the UV background model as calculated by Faucher-Giguère *et al.* (2009) is adopted). Furthermore, a form of self-shielding should be included, so that the gas is not homogeneously bathed in the UV background, but can be shielded from it by neutral hydrogen that absorbs the radiation. A fully consistent treatment of this would however require running a ray-tracing code on top of the simulations code in real time, increasing the computational cost by orders of magnitude, so we resort to the best approximation where the strength of the shielding is simply linked to the local neutral hydrogen density of the gas. Hydrogen-ionizing UV radiation is hereby exponentially suppressed for gas with neutral hydrogen densities above $0.007\,\mathrm{amu/cm^3}$. Thus introducing another parameter, density, into the calculations, requiring us to *only* do 5-dimensional interpolations on both the cooling and the heating tables during a simulation (see Figures 2.5 and 2.6). For this purpose we coded a general $N$-dimensional interpolator that we use in both the simulation and analysis codes (Section 2.3.4). This is the (current) final form of the treatment of

radiative processes in the interstellar medium that we employ in our simulations and that has been published in De Rijcke *et al.* (2013). Chapter 5 presents the third and most recent part of this PhD research, which features the full capabilities of the radiative processes described here, and which provides a more in-depth analysis and comparison between the different types of cooling/heating curves. All the data tables have been made publicly available on-line[1], and for the parameter values were chosen: 6 [Fe/H] values, 3 [Mg/Fe] values, 8 redshifts and 8 neutral hydrogen densities - which give (plus $8 \times 8$ zero metallicity curves) a grand total of 1216 cooling curves and 1216 heating curves.

Note: since we have calculations at our disposal of the full composition and ionization equilibrium of the gas in our simulations, we can basically derive any quantity of interest from this, to be used on-the-fly in the simulations or in post-processing of the simulation data. In Sections 5.2 and 5.3 we present an analysis of, respectively, the neutral fraction of the gas and emission line fluxes that can be derived in this chemical framework. The former only needs the chemical composition and basically measures how much gas is neutral, while the latter also needs the ionization equilibrium to calculate the volume emissivity of a parcel of gas in a given emission line. These derived features depend on the same parameters as the cooling and heating, and are tabulated in the same format.

### 2.2.2 Star formation ↻

When gas cools and, as a result, collapses to higher densities, logically the next step is that it should form stars if the conditions are right. Star formation is implemented in our simulations in the form of 3 criteria that a gas particle must fulfill in order to be eligible

---

[1]http://users.ugent.be/~sdrijcke/cooling.html
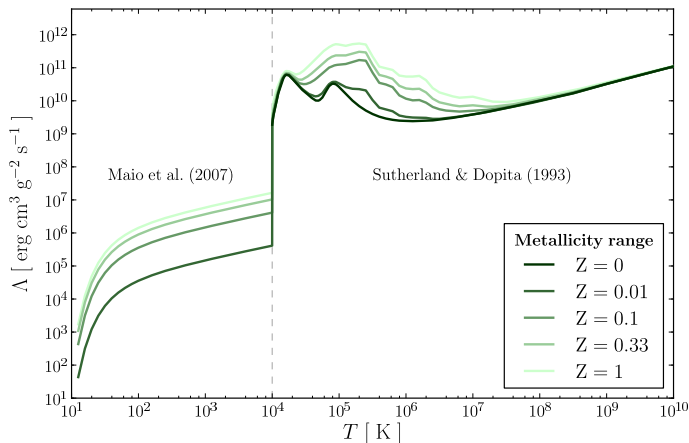


**Figure 2.3:** Plot of the first approach for extending the cooling curves below $10^4$ K. Right of the dashed grey line are the cooling curves as calculated by Sutherland & Dopita (1993), left are the extensions as calculated by Maio *et al.* (2007). In simulations these curves are interpolated in temperature and metallicity.
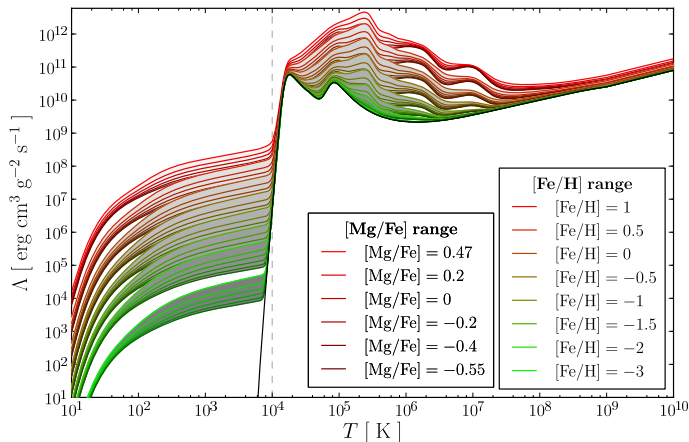
**Figure 2.4:** Similar plot as Fig. 2.3, but now for the "first stage" improved cooling curves. There is no discontinuity anymore around $10^4$ K now, due to the consistency in the calculations across the entire temperature range. In simulations these curves are now interpolated in temperature, [Fe/H] and [Mg/Fe], where the latter two respectively encode the contribution of supernovae type Ia and type II to the composition of the gas. Different [Fe/H] are indicated by a colorscale from green to red, while different [Mg/Fe] are indicated through the intensity of the color (colorscale for the latter only shown for the highest [Fe/H]). The black line represents the zero metallicity curve.

for being converted into a star particle:

$$\vec{\nabla}.\vec{v} \ \leq \ 0 \tag{2.9}$$

$$T \ \leq \ T_{threshold} = 15000\text{K} \tag{2.10}$$

$$\rho_g \ \geq \ \rho_{threshold} \ , \tag{2.11}$$

of which only the density criterion will be of major importance. The first requires the gas to be converging, and the second makes sure the gas is cold enough. In practice, the gas particles which already comply to the density criterion will in the majority of the cases also already comply to the other two, since they would have had to cool down and collapse to reach this density in the first place. These are the only criteria imposed on the gas particles, we do not explicitly implement a Jeans criterion. Gas particles deemed eligible for star formation are turned into star particles according to the Schmidt law (Schmidt, 1959):

$$\frac{\mathrm{d}\rho_s}{\mathrm{d}t} = -\frac{\mathrm{d}\rho_g}{\mathrm{d}t} = c_\star \frac{\rho_g}{t_g}, \tag{2.12}$$

where $\rho_s$, $\rho_g$ and $c_\star$ are, respectively, the density of stars and gas, and a dimensionless star formation efficiency factor. $t_g$ is taken to be the dynamical time for the gas $1/\sqrt{4\pi G\rho_g}$. The only issue that we have to decide on here is the *value* of the density threshold. This will determine how dense and clumpy the gas will become in the simulations, and therefore has
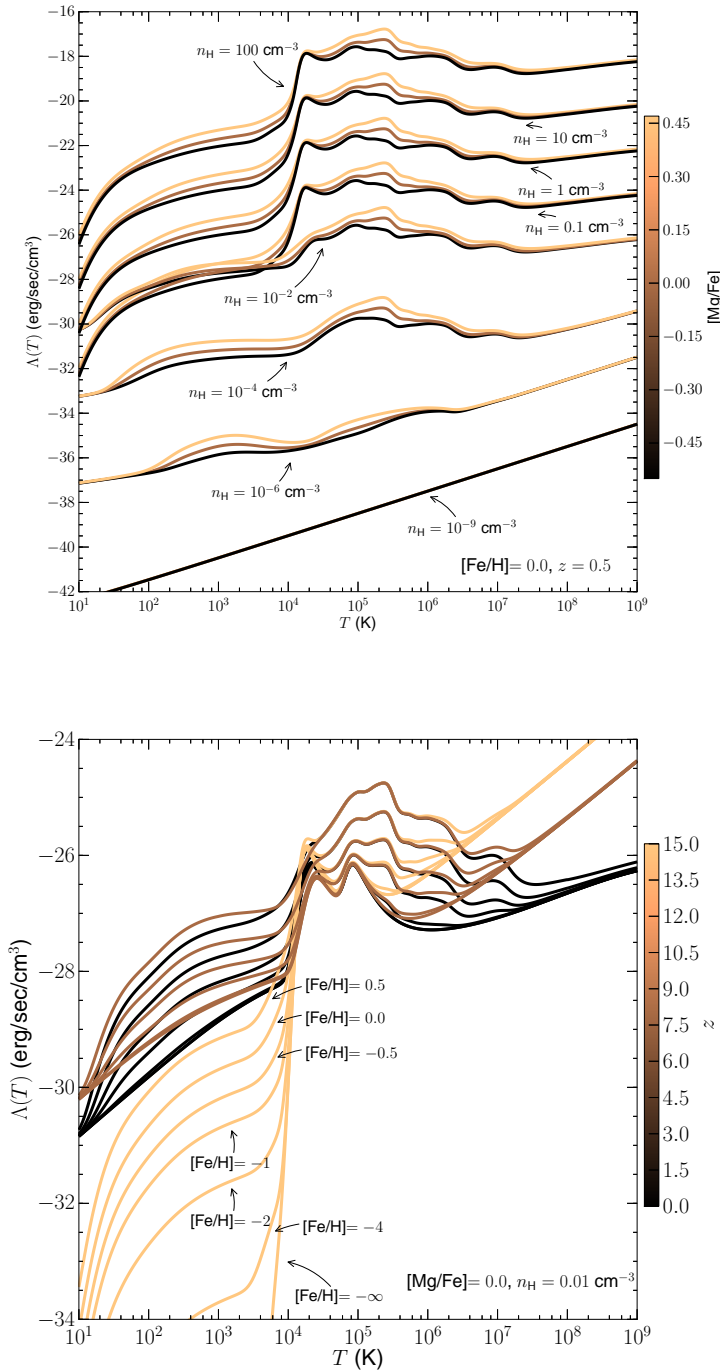
**Figure 2.5:** Similar to Figures 2.3 and 2.4, now for a small selection of the full 5-dimensional cooling curves. The upper panel shows the influence of [Mg/Fe] (color scale), and the influence of the neutral hydrogen density (arrows). The lower panel shows the influence of [Fe/H] (arrows), and the influence of redshift (color scale).
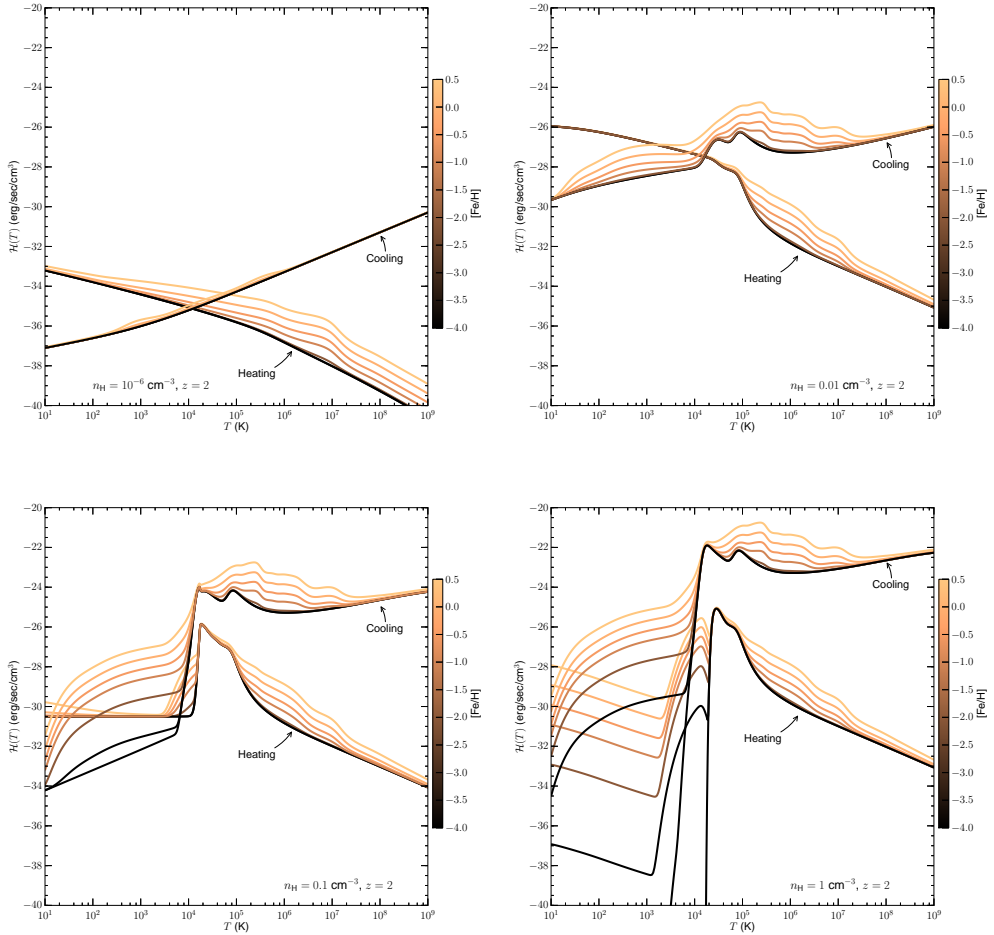
**Figure 2.6:** Small selection of the full 5-dimensional heating curves, shown together with their respective cooling curve "counterparts" for the same parameter values. The point where they intersect is the equilibrium temperature that the gas would evolve towards if given the time to relax. Curves are shown for a range of [Fe/H] values (color bar) and density values (different frames), and for an intermediate redshift of 2.

a fundamental impact on the gas dynamics, the structure formation scale, and the general star formation behavior of the model galaxy. Traditionally, this threshold was set to the "low" value of $0.1\,\mathrm{amu/cm^3}$ (LDT), a value which has been in general use by several authors (e.g. Katz *et al.* 1996; Stinson *et al.* 2006; Valcke *et al.* 2008; Revaz *et al.* 2009; Schroyen *et al.* 2011; and references therein). More recently, with numerical resolution following the steady increase of computing power, it has become possible to follow the formation of cold, high-density clouds in which star formation is supposed to occur. Governato *et al.* (2010), amongst others, therefore advocate using a much higher density threshold of

100 amu/cm$^3$ (HDT), which, together with an extension of the cooling curves below $10^4$ K (Section 2.2.1), is argued to be a much more realistic description of star forming regions. To be really realistic, according to observational constraints, this threshold should be even higher, $10^5$ amu/cm$^3$ or higher are realistic values for the density of molecular clouds. However, practical and computational problems currently don't allow to reach this high in simulations. A value of 100 amu/cm$^3$ is therefore a trade-off, but already allows us to "resolve" the astrophysical process of gas collapse and star formation much further and in more detail. At this high threshold density, the SPH smoothing length, which encompasses about 50-60 gas particles, resolves the Jeans scale down to temperatures of $T_{\min} \sim 100$ K. At these high densities and low temperatures, the gravitational softening is larger than both the SPH smoothing and the Jeans lengths and artificial fragmentation is suppressed (softening is set to 30 pc, while the SPH smoothing is typically 8 pc at these densities). Hence, the cold, dense clumps forming in the interstellar medium - with dimensions larger than the gravitational softening scale - are real and they are the cradles of star formation, which is the main aim of the employed star-formation criteria.

As hinted in some of the previous and next sections, switching from a low to a high density threshold for star formation brings with it several other changes to the initial setup and the astrophysical prescriptions:

- As an integral part of the high density threshold scheme, radiative cooling curves that extend below $10^4$ K are needed, to enable the gas to collapse strongly enough to reach these densities (Section 2.2.1).

- In order to produce dwarf galaxy models which lie on the observed photometric and kinematic scaling relations, an increase of the star-formation density threshold needs to be accompanied by a simultaneous increase in stellar feedback efficiency, in order to counteract the stronger gravitational forces in collapsed areas. This constitutes a fundamental degeneracy in the parameter space of this branch of galaxy modeling (Section 2.2.3).

- When simulating rotating dwarf galaxies, we need to use a pseudo-isothermal profile for the initial gas sphere, because the homogeneous sphere causes stars to hardly form at all, and only very late in the model's evolution. The centrally concentrated profile facilitates the collapse of gas to densities high enough to form stars (Section 2.1.2), so we always use this density profile when simulating with a high density threshold.

- Using these pseudo-isothermal density profiles for the initial gas sphere entails the further requirement that, when rotation is desired, this should be imposed with an arctangens rotation profile (or at least a rotation profile that goes to 0 in the center). Otherwise the centrally concentrated gas will receive too much angular momentum and prevent star formation (Section 2.1.4).

This collection of prescriptions is referred to as the "HDT scheme" for star formation.

Due to the (still) limited resolution of galaxy simulations, produced star particles are actually not to be seen as individual stars, but are represented as "simple stellar populations" (SSP) of a few 100 to a few 1000 solar masses (depending on the mass resolution). We use a Salpeter IMF (Salpeter, 1955) for the stellar particles, where the probability that a star of mass $m$ is born equals:

$$\Phi(m)\mathrm{d}m = Am^{-(1+x)}\mathrm{d}m, \tag{2.13}$$

with $x = 1.35$, $A = 0.06$, and the limits for stellar masses are $m_\mathrm{l} = 0.01$ $M_\odot$ and $m_\mathrm{u} = 60$ $M_\odot$. This might or might not be the most realistic choice of IMF, but since the main goals of this PhD research are to investigate the influence of other model parameters, where the IMF is not expected to play a significant role in the results, it is simply kept fixed. One of the main consequences one could imagine is that the amount of feedback from a star particle changes, but this effect can be countered by tuning other free parameters (such as feedback efficiency, see Section 2.2.3) - in other words, the IMF as a model parameter is degenerate.

### 2.2.3   Stellar feedback *

Once gas has finally managed to collect itself densely enough and stars are formed, they will return processed materials and energy to the environment. Any process through which a star expels or returns something to the environment is collected under the name of "stellar feedback".

Feedback from a star particle (=SSP, Section 2.2.2) is given through the stellar winds (SW) and supernovae (SN, type II and Ia) occurring in its stellar population, and includes the return of both material, enriched with elements, and energy to the ISM (the latter only in the form of thermal feedback). These are transferred to the surrounding gas particles according to the SPH smoothing kernel (Section 2.3.2) that the star particle inherited from its ancestral gas particle. The lower mass limits for a star to end up as a SNIa or SNII, respectively, are $3\,M_\odot$ and $8\,M_\odot$, upper limits are $8\,M_\odot$ and $60\,M_\odot$. The times at which the stellar population will start and stop giving the different types of feedback can be calculated from these upper and lower limits of stellar masses, by inserting them in the following equation for the main sequence lifetime of a star in function of its mass $m$ (David *et al.*, 1990):

$$log\,t(m) = 10 - 3.42\,log(m) + 0.88(log(m))^2. \tag{2.14}$$

SNII feedback is given relatively soon after the moment a star particle is born, since the lifetime of the most massive stars ($\sim 10^7\,yr$) is short compared to the average length of the simulation ($\sim 12 \times 10^9\,yr$), but for SNIa we employ a delay of $1.5\,\mathrm{Gyr}$, since this is the average lifetime of its progenitor before it goes supernova. The total energy output for both types of SN is taken to be $10^{51}$ erg, for SW this is $10^{50}$ erg, and these energies are deposited into the environment at a constant rate during their lifetime. The abundance ratios of the different elements they expel are discussed in Section 2.2.4.

The feedback efficiency parameter, which denotes fraction of the expelled feedback energy that is actually absorbed by the ISM (or in other words how efficiently the thermal feedback couples to the ISM), is basically the dial we have in hands to modify the strength of the feedback in our simulations. However, we cannot just freely adjust it to our liking, since it appears that this parameter is actually coupled to the density threshold for star formation (Section 2.2.2): when dialing up the density threshold, we need to dial up the feedback efficiency as well in order to counteract the stronger gravitational forces in collapsed areas, since otherwise we would have runaway star formation that produces much too centrally concentrated stellar bodies. The increased feedback efficiency is necessary to ensure that we produce dwarf galaxy models which lie on the observed photometric and kinematic scaling relations, only shifted downward along the relations relative to the low density threshold simulations. This behavior constitutes a fundamental degeneracy in the parameter space of this branch of galaxy modeling (Cloet-Osselaer *et al.*, 2012).

The traditional value here, corresponding to the low density threshold of $0.1 \, \text{amu/cm}^3$, is an efficiency factor of 0.1 - while the high density threshold of $100 \, \text{amu/cm}^3$ requires an efficiency of around 0.7.

### 2.2.4 Metal enrichment *

When giving feedback (Section 2.2.3), stars will enrich their environment with new elements that they synthesized during their lifetime, or at the moment of their death (when going supernova).

The returned element yields from SNIa and SNII are taken from, respectively, Travaglio *et al.* (2004) (their b20_3d_768 model) and Tsujimoto *et al.* (1995). From the last authors we also adopt $N_{SNIa}/N_{SNII} = 0.15$ to set the fraction of stars in the relevant mass range that reside in binary systems and that can go SNIa. The yield $M_i$ of element $i$ by e.g. SNII is then calculated as:

$$M_i = M_{SSP} \frac{\int_{m_{\text{SNII,l}}}^{m_{\text{SNII,u}}} M_i(m)\Phi(m)\mathrm{d}m}{\int_{m_{\text{l}}}^{m_{\text{u}}} m\Phi(m)\mathrm{d}m}, \qquad (2.15)$$

where we integrate over stellar mass $m$. The formula for SNIa is similar but simpler, since there is no dependence on progenitor mass ($M_i(m)$ becomes $M_i$).

One can therefore calculate supernova yields on-the-fly and keep track of the abundance of any desired element during the simulation, but to keep the overhead calculations and memory usage to a minimum we choose to keep track of the total amount of gas and the total amount of metals, and only follow the evolution of Iron (Fe) and Magnesium (Mg) in detail with the above formula. However, as discussed in Section 2.2.1, these two elements are enough to have a good grasp on the total composition of the gas, and allow for any relevant quantity concerning the gas to be calculated.

In order not to add more free parameters to the formalism, we opted not to include a prescription for metal diffusion (Shen *et al.*, 2010; Gibson *et al.*, 2013). Judging from figure 9 from Shen *et al.* (2010), the gas enriched by metal diffusion achieves metallicities that are more than an order of magnitude smaller than the "enriching" material. We

therefore expect that the inclusion of diffusion would only have a minor effect on our models and results.

### 2.2.5   The circle closes...

At the end of this logical train of thought, the metal enrichment process described in Section 2.2.4 couples back to the beginning. Enriching the gas with elements will significantly alter its cooling properties, providing it with many more possible radiative transitions or cooling lines so that it can cool faster in the future - which will on its turn influence the star formation - and therefore affect the stellar feedback again ... etc. The whole astrophysical mix of spices added to the physical base of gravity and hydrodynamics is therefore a complex cycle, where all processes influence each other. And most importantly, it is a self-regulating cycle: for instance, a period of intense localized star formation will induce intense supernova feedback, which injects a large amount of energy into the surrounding gas - making the gas expand, halting any further collapse and star formation at this location, while however triggering small amounts of secondary star formation in the compressed edge of the expanding bubble. In a "natural" way an equilibrium is sought between the different processes, without any external intervention.

## 2.3   Cookware

Even with all the required ingredients and a collection of nice recipes, one will not get anywhere without some proper cookware to actually cook up something interesting with. Here we give an overview and description of the different codes used in setting up, simulating, and analysing our N-Body/SPH dwarf galaxy models.
We rely mainly on three categories of codes:

- firstly, we have a collection of home-made codes to generate the initial conditions,

- secondly, and most importantly, we have a simulation code to do the actual calculations with and evolve the initial setup with all required physical processes,

- and lastly, we developed our own in-house analysis tool HYPLOT for analysing and visualizing the output of the simulation code.

### 2.3.1   Initial conditions codes ↺

For generating the initial conditions of our dwarf galaxy models we have a collection of home-made codes, written in Fortran and C++. These are all bundled in one initial conditions tool, GOGOIC, written in Python, with a PyQT graphical user interface to easily set up dwarf galaxy simulations with all the different possible ingredients and properties described in Section 2.1 of this chapter.

### 2.3.1.1   Dark matter halo *

For the dark matter halo we have two Fortran codes at our disposal, KUZKUT and NFW, which are aptly named after the respective density profiles they employ for the dark matter halo. The particles are set up according to the specifications discussed in Sections 2.1 and 2.1.1, and they are given velocities drawn from an isotropic orbital distribution function that is set up for each density profile using the Eddington equation (Van Hese et al., 2009). Both the density and velocity distributions are realized by a standard acceptance/rejectance technique that draws positions and velocities, and stores or discards them according to the probability functions of the distributions (Cloet-Osselaer et al., 2012).

We use an additional numerical procedure where we employ "mirror particles" to greatly improve the cusped NFW halo's stability by protecting it from numerical effects. For this we only generate half of the total amount of particles, and for each of them generate a twin particle mirrored across the center, with position coordinates $(r, -\theta, -\phi)$ and velocity coordinates $(-v_r, -v_\theta, -v_\phi)$. This is a very efficient way to cancel out numerical errors originating from the finite amount of particles used to sample the DM halo, which introduce unbalanced angular momenta in the inner part of the cusp through 2-body interactions. These accumulate quickly, lead to the ejection of particles from the cusp, and trigger a general dynamical response of the DM halo that erases the inner cusp even during a dark-matter-only simulation. The mirrored particle introduces the same erroneous angular momentum as the original particle, but with an opposite sign, so that both particles together effectively cancel out. This often used numerical approach is also called a "quiet start" (Sellwood, 1983).

As input these routines only need the total dark matter mass and the number of particles, and in the case of a Kuz'min-Kutuzov profile also the axis parameters $a$ and $c$ (see Section 2.1.1). In case of an NFW profile, all other parameters are fixed by the parameter correlations from Strigari et al. (2007) that we use (Section 2.1.1).

### 2.3.1.2   Gas halo ↻

To set up the gas halo we use the C++ code GANIC, which loads the output file containing the dark matter halo produced by KUZKUT or NFW, adds gas particles to the setup in the proper way as described in Sections 2.1 with the desired properties from Section 2.1.2, and writes all necessary quantities to an output file which is readable by GADGET (Section 2.3.2).

It is actually capable of generating a whole range of different types of initial conditions, including 2D and 3D grids, idealized setups for astrophysical and hydrodynamical test cases (Valcke et al., 2010), and dwarf galaxy models. For the latter it can create a triaxial gas body of uniform density by generating random positions within an ellipsoid with arbitrary axes, or a gas sphere with a pseudo-isothermal density profile through a standard acceptance/rejectance technique as in Section 2.3.1.1. By default the gas particles do not receive any velocities, but rotation can be given to the gas according to the desired rotation

profile (Section 2.1.4), as can be random motions (Section 2.1.3).

As input the routine needs info on the dark matter halo, total gas mass and number of gas particles, some cosmological parameters and a redshift to determine the densities, geometric flattening, rotation parameters (strength, profile) and random motion parameters.

### 2.3.1.3  The GOGOIC tool †

To be able to easily set up all the above for starting a dwarf galaxy simulation, we developed the GOGOIC GUI tool which connects and communicates with the different initial conditions codes. All the relevant options for the initial conditions which are listed in this chapter can be chosen from the menus and tabs, the generated initial conditions file and GADGET-2 parameter file can be copied to the appropriate directories on a remote machine for starting simulations, and a log is kept of the generated initial conditions.

## 2.3.2  Nbody-SPH code ↺

To do the actual simulation work to evolve the initial conditions in time we use a modified version of the Nbody-SPH code GADGET-2[2] (Springel, 2005). To the freely available basic version, which only incorporates gravity and hydrodynamics, we added the astrophysical extensions described in Section 2.2 that give rise to the self-regulating chemical evolution cycle in galaxies.

Technically, for a Newtonian system of $N$ particles in a simulation, gravity should be calculated between each unique pair of particles (with masses $m_1$ and $m_2$ and distance $r_{12}$) in each timestep of the simulation by

$$F = -G\frac{m_1 m_2}{r_{12}^2},\qquad(2.16)$$

which would make the computational cost scale as $N^2$. A number of clever techniques and approximations however make (computational) life much easier, such as the so-called "tree"-method which divides the simulation volume in levels of nested cells, and calculates the center of mass for each of these cells (Barnes & Hut, 1986). Gravitational forces are thereby calculated between a particle and the center of mass of all cells of the simulation, and the further away from the particle we look, the lower we can take the level of nesting of the cell to be - meaning that we consider bigger cells and average over more particles when we go farther away. This adaptively approximating of the gravitational force depending on the distance makes it possible to go to a computational regime that scales as $Nlog(N)$. In standard GADGET-2, gravity is treated by an N-Body code that uses such a tree algorithm, and that can optionally be combined with an FFT-based particle-mesh scheme for long range forces and can be cosmologically evolved in co-moving coordinates (though we only use the standard tree method in non-cosmological Newtonian mode for our simulations). In standard GADGET-2, hydrodynamics are included with the well-known *Smoothed Particle Hydrodynamics*, or "SPH", method (Gingold & Monaghan, 1977; Lucy, 1977; Monaghan, 1992), which is a Lagrangian approach that integrates well with the gravitational

---

[2]http://www.mpa-garching.mpg.de/gadget/

N-Body particle method (Hernquist & Katz, 1989; Katz *et al.*, 1996; Springel, 2005). Although the gas phase is an approximately continuous medium, we still work with gas "particles" to describe it in this context - which is why it is very compatible with an N-Body particle method - but they are more than simply dimensionless points. The best way to view these gas particles is as anchor points sampling a continuous fluid, which are given a certain spatial extent (smoothing radius $h$) in which they can interact hydrodynamically with other gas particles, and the strength of this interaction in function of the distance $r$ is described by a "smoothing kernel" function (usually a cubic spline, denoted by $W(r, h)$, that falls to 0 at the edge of the smoothing radius). All the particle's properties (mass, energy,...) are spread out or "smoothed" in space by this kernel function, and the value of a hydrodynamical quantity $Q$ at any point $\mathbf{r}$ in the gas phase medium, or at any gas particle, is calculated through the basic SPH weighted discrete summing formula

$$Q(\mathbf{r}) = \sum_j m_j \frac{Q_j}{\rho_j} W(|\mathbf{r} - \mathbf{r}_j|, h), \qquad (2.17)$$

and is therefore inseparably connected to the surrounding gas particles $j$ which feel/exert influence from/on this point in the fluid depending on their distance $|r - r_j|$, mass $m_j$, and density $\rho_j$. Computational advantages here are the so-called compact support, meaning only a limited amount of neighboring particles need to be taken into account in calculations (those within the smoothing radius), and the fact that due to this formula it also becomes computationally easy to calculate spatial derivatives of any quantity, since this simplifies to calculating the spatial derivative of the kernel function (which can be precomputed). The great strength of the SPH method, however, comes from the fact that the smoothing lengths can be set for *each particle individually*. Its value is determined by certain local conditions of the particle, usually aiming to keep the amount of neighboring particles within the radius at a certain amount, meaning that the spatial resolution automatically adapts to the situation (high density regions automatically have higher resolution and vice versa). SPH is therefore inherently able to cope with a virtually unlimited range of scales within a single simulation, with efficient use of computational resources.

The gravitational and hydrodynamical particles are evolved through time by periodically updating their positions, velocities, masses, and all relevant hydrodynamical properties, where the time interval between updates is set for each particle individually according to its current conditions and the forces acting on it. A particle's new position is calculated by determining the gravitational force acting on it by the whole system, through the tree method, and by determining the hydrodynamical force it experiences, which is described by the hydrodynamical equations that use the particle's hydrodynamical quantities, and is therefore determined locally by the neighboring particles. The hydrodynamical quantities themselves are also updated by this same set of hydrodynamical equations in each timestep. The astrophysical extensions described in Section 2.2 are added to this standard Nbody-SPH scheme as an additional layer of calculations. In each timestep the difference in energy/entropy of each gas particle due to radiative cooling (and heating) is calculated and applied by interpolating on the data tables, and all gas particles are checked for the star formation criteria to see which ones are eligible to become a star particle. The ones

flagged as star candidates are allowed to form a star particle when a randomly generated number is lower than the value of the probability function derived from the Schmidt law

$$p = 1 - exp\left(\frac{\delta t}{t_d}\right), \tag{2.18}$$

with $t_d$ being the dynamical time, defined as $1/\sqrt{4\pi G\rho_g}$. Furthermore, for all existing star particles it is checked whether their stellar population will give feedback in the current timestep, and if so, which types feedback and how much of each, and the corresponding amounts of energy and metals are distributed among the neighboring gas particles according to the kernel function.

The simulation code takes the output of GANIC as initial conditions and provides us on regular time intervals during the simulation with snapshots of the model dwarf galaxies - which contain positions, masses and velocities for all particles, and properties specific to stellar and gaseous particles such as ages, metallicities and densities.

### 2.3.3 Analysis codes: the HYPLOT package ☉

Finally, after all our toiling to select proper ingredients, tasteful recipes, and the appropriate cookware, we would of course eagerly want to have a proper taste of the good stuff, to see if everything is ok with the added spicings before serving. For analysing and visualizing the data files that the simulation code gives us, we used our own HYPLOT package (freely available on SourceForge[3]), which is able to calculate any desired physical quantity of the dwarf galaxy model, and also transform them to mimic observational quantities. It is an analysis/visualisation tool especially suited for Nbody-SPH simulations (currently only for GADGET-2 datafiles, but easily extensible to any data format).

Most of the heavy lifting in the HYPLOT package is done with C++ routines (plus a few Fortran routines), which covers basically anything that is directly involved in doing operations or calculations on a set of particles (reading in snapshots, calculating its global quantities, gridding, rendering,...). The Python routines are responsible for any aspect involving user interfacing, plotting and scripting, where PyQT is used for generating the Graphical User Interface and Matplotlib is used for generating the images and plots. Communicating between the two languages is done through the SIP libraries. For scripting, a self-written Python script can either be attached to the GUI or a specific plot within the GUI during run-time, or written as a stand-alone script that imports the hyplot package and its functions.

All analyses, plots and many of the visualizations in this thesis, as well as in all of or published work, have been made using HYPLOT.

#### 2.3.3.1 Snapshot I-O

The program is able to read in (and write out) binary GADGET-2 snapshots, extract the data from all particles, and store them in individual CParticle objects (subclassed

---

[3]http://sourceforge.net/projects/hyplot/

in CDarkParticle, CGasParticle, and CStarParticle) that contain all their own properties
and methods to extract them or calculate others. All CParticles are grouped together in
one CDataBlock, representing the snapshot, that has numerous methods to extract and
calculate properties from the whole - or a selection of - its particle set.

### 2.3.3.2   Analysis mode

If run in command line mode

```
hyplot --nox
```

the user provides several predefined analysis modes, among which the main option is
"analyze all". This routine will produce an array of summary files with global quantities
of one simulation over the full range of its snapshots, which can therefore be used to plot
the evolution of those quantities over time in this simulation. Secondary analysis options
are the "summary of summary files", which collects the summary file data from several
different simulations at the same snapshot time and can therefore be use to plot scaling
relations, and the "single particle" option, that can extract data for a specific (set of)
particles over a range of snapshots and can therefore be used to plot orbits (or other
evolutions) of individual particles.

### 2.3.3.3   Calculation routines

To produce these analyses from the snapshot data, the CDataBlock and CParticle classes
have an extensive set of methods to extract or calculate properties, either globally for the
whole model or for individual particles. Most basic quantities are calculated internally
in these objects, but the more involved calculations are done with separate routines and
objects that are called by the CDataBlock and CParticle classes, or act upon them. Hereby
an attempt at a comprehensive list of the most important of these calculation routines
(most are written in C++, except when indicated otherwise):

- † CEmissionTable: given the properties of a gas particle (temperature, [Fe/H]),
  [Mg/Fe], density) and the redshift of the snapshot, the `getEmission` method of this
  class interpolates on 5D emission tables that are produced from the estimates of the
  composition and ionization equilibrium of gas (Section 2.2.1) to determine the total
  emission of this gas particle. Currently available emission lines are H$\alpha$ and CII.

- CImf: provides all necessary functions related to the initial mass function.

- † CLuminosityTable: given the properties of a star particle (mass, [Fe/H], age), the
  `getLuminosity` method of this class interpolates on 2D stellar luminosity tables from
  vazdekis96 to determine the total luminosity of this star particle in the UBVRIJHK
  band. The additional `maggal` method calculates the magnitudes in these bands for
  an entire galaxy model.

- `make_cmd:`this function produces a color-magnitude diagram of the stars in a simulation, by sampling each stellar particle's SSP. It is possible to convolve this diagram with a Gaussian.

- † CNeutralFracTable: input and methodology similar to the CEmissionTable, but now to determine the fraction of neutral gas in a gas particle.

- † CProfile: class with an array of methods to do anything involving profiles or histograms of any quantity against any quantity - so basically 1-dimensional gridding. It can handle all types of profiling (simple summing per bin, averaged profiles, weighted averaging with mass or luminosity, density profiles) and produce them with static bins or with adaptive bins that resize according to the number of particles in a bin. Different profiles can also be added or subtracted, and multiplied or divided by constants, to average over profiles.

- † CBinner: class that provides the binner for the CProfile class - which basically returns the number of the bin in which a particle needs to be put, according to the requested quantity, range, and number of bins it has been set with. Subclasses are CBinnerLinear and CBinnerLog, providing linearly and logarithmicly spaced bins.

- ⊙ disp: Fortran subroutine that can calculate velocity dispersion profiles and central velocity dispersions of the stellar body.

- * flat: Fortran subroutine that calculates the flattening of a galaxy's body (stars or dark matter).

- halfl: Fortran subroutine that calculates the half-light and half-mass radius of the stellar body.

- SBprofile: Fortran subroutine that calculates surface brightness profiles and fits a Sersic profile to it.

- sfr: function that calculates the total amount of newly formed stars in a certain snapshot, and for a range of metallicity bins.

- sfradvanced: Fortran subroutine that extracts radial star formation density histograms over the evolution of a simulation, so producing a 2D grid of radius versus time where each bin indicates the star formation density at that time and radius in the simulated galaxy.

- several smaller routines for different total metallicity values.

- † extractParticles: function to extract data of specific particles over the entire simulation, giving us these particle's individual evolutions in separate output files.

### 2.3.3.4 Plotting

The plotting machinery in HYPLOT is split into two parts:

- the C++ routines `make_map` and `make_scatter_data` that use the CGridder class to process the particles and provide the requested type of plot-data (simple 2D grid, rendered 2D grid, arrays of particle data for scatter plots).

- the host of Python codes that make up the visual framework: producing images from the different types of raw data provided by the C++ routines, managing their data and layout, showing them to the user and writing them to image files, both from the GUI and from self-made scripts.

To be able to communicate between the two parts, there is a translation layer needed between them, which is done in HYPLOT using the SIP libraries. The main program is run in Python, so all C++ objects, methods and routines which need to be directly accessible/callable from Python are collected in the appropriate SIP files, with extra SIP-code - where needed - to explicitly describe the translating of arguments and returned objects between the languages if no standard method is available.

### 2.3.3.5 Python scripting ("visual mode")

What makes the HYPLOT package the most versatile is the ability to import it into Python scripts, because in this way much more advanced and specific analyses can be done that are able to use all the basic functionalities of HYPLOT (snapshot handling, analysis and calculation routines, plotting), without having to integrate everything in the source code. The most effective way to do this is to invoke HYPLOT with the command

```
hyplot --visual=script.py
```

where `script.py` is the self-written Python script.
Using the functionalities of the Python component of HYPLOT in a script is straightforward, by just importing the required Python files in the standard way, but also the C++ routines that have been made accessible from Python (see Section 2.3.3.4) can be imported with

```
import chyplot
```

This makes it possible to generate CDataBlock instances in a script, and therefore directly read, manage and analyze the snapshots from Python, with all the object's interface functionalities, while all computationally heavy operations are efficiently done in a C++ environment.
In Appendix A a comprehensive reference guide is presented of all the more advanced and useful analysis scripts that have been created and used during this PhD research, and might prove useful to others in the future.

### 2.3.4 N-dimensional interpolator †

To be able to use the new radiative cooling and heating curves described in Section 2.2.1 in the simulation code, and use any of the other estimates that can be derived from the underlying chemical framework (neutral fractions, emissions, ... see Sections 5.2 and 5.3) to analyze the simulation output - which all fundamentally depend on temperature, [Fe/H], [Mg/Fe], redshift and neutral gas density - we need to interpolate in 5 dimensions between precomputed data tables. In order to be somewhat foreseeing and be prepared for possible future changes to the chemical composition schemes, and avoid hard-coding a 5-dimensional interpolator that can only be specifically used in this situation, we set ourselves to coding a general *N-dimensional* interpolator algorithm that can handle any number of dimensions.

The algorithm therefore had to be extremely flexible and be able to accept data arrays of any shape. GADGET-2 being written in plain C code posed some difficulties to achieve this, but in the end resulted in a fairly efficiently written algorithm, which was later ported to C++ for use in the analysis codes.

#### 2.3.4.1 Input

As input the interpolator needs

- the N-dimensional data table in which to interpolate,

- the arrays containing the parameter values for which the data table holds the pre-calculated values of interest,

- the sizes of these parameter arrays - in other words, how many values are tabulated for each parameter,

- the parameter values of the interpolation point,

- the number of dimensions,

- array to store indexes in, or provide indexes to the interpolator that have been calculated before and can be reused,

- array to store the interpolation factors in - values between 0 and 1, indicating the position of the interpolation point between the two surrounding tabulated points - or to provide them, as with the indexes,

- flag to indicate whether to extrapolate or not, when the interpolation point is outside of the data table range in any dimension,

- a variable to store the resulting interpolated value in.

Besides the input arguments, the interpolator also needs to have two auxiliary routines available:

- a "hunting" routine, that gives the index of the element in an array whose value the closest to, but smaller than, a given value,

- a routine that converts an unsigned integer to an array of integers containing its binary representation.

### 2.3.4.2   Mechanism

The N-dimensional data table that the interpolator receives as an N-dimensional array, will be interpreted as one long one-dimensional array where all data rows are stored one after the other, since this is also how the data is actually stored in the memory. Technically, it just receives a pointer to the first element of the array, so then it can just go through the memory array and ignore the array structure in order to be able to deal with arbitrary dimensions. From the number of dimensions and the sizes of the different parameter arrays we know how long the array is, and the algorithm can skip back and forth through it with the correct stepsizes to adress individual elements in the N-dimensional array (which is basically a hand-coded version of what the compiler does when a specific element in a multi-dimensional array is requested).

Firstly, the parameter values of the interpolation point are hunted in the respective parameter arrays to obtain the lower indexes of the point in the data table, and the interpolation factors are calculated. Then the "box" of data points surrounding the interpolation point is extracted from the data table, and temporarily allocated in a separate array. Lastly, this box is "collapsed" dimension per dimension, by multiplying the surrounding data points with the respective interpolation factors and adding all elements onto the first element of the array. The first element of the box-array will finally hold the interpolated value at the requested interpolation point.

# 3

# Angular momentum and metallicity profiles

**J. Schroyen, S. De Rijcke, S. Valcke,**
**A. Cloet-Osselaer & H. Dejonghe :**
**"Simulations of the formation and evolution of isolated dwarf**
**galaxies - II : Angular momentum as a second parameter"**
**MNRAS, 2011, 416:601-617**

In this chapter we investigate the effects of *angular momentum* on the behavior and evolution of our dwarf galaxy models, described in Chapter 2, try to formulate it in one coherent mechanism, and evaluate the importance of angular momentum as a model parameter for dwarf galaxy evolution. In particular we are interested in the effects concerning their radial stellar metallicity profiles - so in how the average metallicity of the stars varies with projected radius from the center of the galaxy - and its potential in explaining the observed dichotomy in radial stellar metallicity profiles of dwarf galaxies: dwarf irregulars (dIrr) and flat, rotating dwarf ellipticals (dE) generally possess flat metallicity profiles, while rounder and non-rotating dEs show strong negative metallicity gradients.

For this part of our research, we made use of the basic dwarf galaxy models in the configuration they were presented in in Valcke *et al.* (2008):

- Kuz'min-Kutuzov cored dark matter halo,

- homogeneous gas sphere,

- cooling tables from Sutherland & Dopita (1993), no heating,

- low star formation density threshold of $0.1\,\mathrm{cm}^{-3}$,

- low feedback efficiency factor of 0.1,

supplemented with

- constant rotation curves,

- initial geometrical flattenings.

These models are here indicated with a capital "C" in front of the model number.


## 3.1    Introduction

Morphologically, dwarfs come in two broad classes. Early-type dwarfs, or dwarf elliptical galaxies (Ferguson & Binggeli, 1994, dE;), are "red and dead" in the sense that their stellar populations are predominantly old and that they are usually not actively forming stars. They almost completely lack the raw material for star formation: gas. In a small fraction of dEs, low level central star formation continues at a rate of less than one solar mass every 1000 years (De Rijcke *et al.*, 2003b; Lisker *et al.*, 2006). dEs with luminosities below $M_V \sim -14$ mag are usually called dwarf spheroidals, or dSphs. As a class, dEs are slowly rotating objects, flattened by velocity anisotropy (Geha *et al.*, 2003). Late-type dwarfs, or dwarf irregular galaxies (dIrr; see e.g. Skillman 2005), are gas-rich and are actively forming stars at a rate of about one solar mass every $100 - 1000$ years. As a class, dIrrs are flattened by rotation (Côté *et al.*, 2000). Noticeably, dSphs/dEs are found predominantly in dense galactic environments while dIrrs are typically found in more sparsely populated environments. This is the so-called morphology-density relation (Binggeli *et al.*, 1987; Côté *et al.*, 2009). In the Perseus cluster, all dwarfs, irrespective of type, appear to avoid the very dense cluster center (Penny *et al.*, 2009). All this suggests that the environment is at least to some extent responsible for many of the differences between dIrrs and dEs.

Despite their quite different properties, the two types of dwarfs also share many properties. They populate roughly the same mass, metallicity, luminosity, flattening (Binggeli & Popescu, 1995) and size regimes and they have, to a good approximation, exponentially declining surface-brightness profiles. Moreover, the "boundaries" between the dwarf classes are not clear-cut and transition-type objects with mixed properties exist (Grebel *et al.*, 2003). This body of data provides us with evidence for evolutionary links between, or at least a "common ancestry" for, the different types of dwarfs. As shown by e.g. Mayer *et al.* (2006), the combined action of ram-pressure stripping and tidal stirring on a star-forming, rotating late-type dwarf entering the halo of a Milky Way-like massive galaxy can remove most of its gas and angular momentum, effectively transforming it into a quiescent, non-rotating early-type dwarf.

Dwarf galaxies entering a dense environment that are affected by ram-pressure stripping but not (or much less so) by tidal stirring, would be expected to keep many of their late-type structural properties and one would expect to find dIrr/dE transition-type dwarfs. Indeed, quiescent dwarfs have been observed that are significantly more flattened and

faster rotating than the average dE (De Rijcke *et al.*, 2003a; van Zee *et al.*, 2004), contain gas and dust (Conselice *et al.*, 2003; Buyle *et al.*, 2005; de Looze *et al.*, 2010), and often host embedded stellar disks and spiral structures (Jerjen *et al.*, 2000; Barazza *et al.*, 2002; De Rijcke *et al.*, 2003a; Graham *et al.*, 2003).

### 3.1.1   Metallicity profiles

In general, dIrrs display chemical homogeneity practically throughout their entire stellar and gaseous bodies (Tolstoy *et al.*, 2009; Kobulnicky & Skillman, 1997). The Small Magellanic Cloud (SMC; Dufour & Harlow, 1977; Pagel *et al.*, 1978), NGC 6822 (Hernández-Martínez *et al.*, 2009), and Sextans A (Kaufer *et al.*, 2004) are examples of dIrrs without a significant chemical or abundance gradient in their gas content; the SMC (Cioni, 2009) and IC 1613 (Bernard *et al.*, 2007) also lack a stellar metallicity gradient. Thus, a flat radial metallicity profile seems to be a rather general characteristic of dIrrs. Koleva *et al.* (2009) present radial stellar metallicity profiles, derived from optical VLT spectra, of a sample of 16 dEs belonging to the Fornax cluster and to nearby groups of galaxies. They find that ten of those, predominantly round and non-rotating, show a strong negative metallicity gradient. The six most flattened and most strongly rotating galaxies in the sample, however, show no significant gradient: like the rotationally flattened dIrrs, they are chemically homogeneous. Previous studies have also predominantly found negative metallicity gradients for dEs in the Local Group (e.g. Harbeck *et al.* 2001; Alard 2001, Saggitarius; - the DART project: Tolstoy *et al.* 2004, Sculptor; Battaglia *et al.* 2006, Fornax; Battaglia *et al.* 2011, Sextans), around M81 (Lianou *et al.*, 2010) and in the Coma cluster (den Brok *et al.*, 2011).

The findings of Koleva *et al.* (2009) suggest that, while total mass is most likely the dominant factor (as is concluded from the simulations of: Valcke *et al.*, 2008; Sawala *et al.*, 2010; Revaz *et al.*, 2009; Stinson *et al.*, 2007), angular momentum is an important second parameter in the chemical evolution of dwarf galaxies: fast rotating dwarf galaxies show a tendency to be chemically much more homogeneous than dwarfs with slow or no rotation.

An often quoted means of erasing metallicity gradients in flattened dwarf galaxies is the so-called "fountain mechanism" (for example : Mac Low & Ferrara, 1999; Ferrara & Tolstoy, 2000; De Young & Gallagher, 1990; De Young & Heckman, 1994; Barazza & Binggeli, 2002, and references therein). The idea behind this mechanism is that the supernova feedback of a centralized star-formation event is capable of ejecting significant amounts of hot, enriched gas through a cavity or "chimney" along the galaxy's minor axis. Subsequently, part of this gas can rain back down on the galaxy's disk, as in a fountain, diluting any metallicity gradient that might be present. In round low-mass galaxies, centrally concentrated supernova feedback is expected to "blow away" *all* the gas rather than to "blow out" only the enriched hot gas. If this fountain mechanism is correct, the absence or presence of a metallicity gradient is determined by two parameters: a dwarf galaxy's mass and its flattening or geometry.

Alternatively, due to the "centrifugal barrier" in a rotating galaxy, gas cannot readily

flow to the center and build up a strong centrally concentrated star formation event. One would therefore expect that rotation will naturally lead to more spatially extended star formation and thus to more spatially homogeneous stellar populations. In a similar vein, angular momentum has been proposed in the literature as the fundamental parameter setting low angular momentum starbursting Blue Compact Dwarfs apart from the more continuously star-forming high angular momentum dIrrs (van Zee *et al.*, 2001).

### 3.1.2   Research plan

In this research, we use a suite of Nbody-SPH simulations to investigate how flattening affects the star-formation histories and chemical evolution of the isolated dwarf galaxy models. Other Nbody-SPH simulations of similar star-forming, gas-rich dwarf galaxy models, though not always isolated, have been performed by e.g. Pelupessy *et al.* (2004); Stinson *et al.* (2006, 2007); Revaz *et al.* (2009); Governato *et al.* (2010); Sawala *et al.* (2010, 2011). We flatten our originally spherically symmetric models in different ways by adapting their initial conditions, with and without adding rotation, and compare the results both with the spherically symmetric originals and with the available observations. Our main goal is to contrast the "fountain mechanism" with the "centrifugal barrier" hypothesis, and to see if it's possible to produce dwarf galaxies with flat metallicity profiles in isolation. A description of the simulations themselves is in section 3.2. We present an analysis of the simulations in section 3.3, discuss the results in section 3.4 and conclude in section 3.5.

## 3.2   Simulations

In this section we will describe the simulations themselves: the models used for the basic initial conditions and the grid of our production runs, together with a preliminary evaluation of those runs to have an idea of the simulated objects we have at our disposal.

### 3.2.1   Initial conditions

We base the initial conditions of our flattened dwarf galaxy simulations on the spherically symmetric dwarf galaxy models of Valcke *et al.* (2008), which consist of a Kuz'min-Kutuzov cored dark matter halo and a homogeneous gas sphere. We introduce flattening into the models by adding initial flattening and/or constant rotation profiles. The precise ways in which these elements are set up are described in Chapter 2 and details can be found in Table 2.1. In the end, we have a set of flattened dwarf galaxies, both rotating and non-rotating. This way, we can distinguish between the effects of the *geometry* (flattening only) and the *kinematics* (i.e. rotation).

### 3.2.2   Production runs

In Table 3.1 we show an overview of the run numbers and specifications of our production runs. We simulate dwarf galaxies with a range of masses, flattenings and rotation speeds

using the dwarf galaxy models described above. Both the gas and the dark matter components were represented by 200000 particles, and the simulations were evolved in time during 11.7 gigayears, corresponding to the time from $z = 4.3$ to the present. The seeds used for sampling the particles from the specified density profiles (see Sections 2.1.1 and 2.1.2) are chosen at random for all production runs.

### 3.2.3 Preliminary evaluation of simulations

Table 3.2 lists many different physical quantities for all of the simulated dwarf galaxies in our set from Table 3.1. These are the final values for these quantities, evaluated at the end of the simulation, except those explicitly indexed with 'i', which are initial values. Broadband colours are calculated (with bilinear interpolation) using the models of Vazdekis *et al.* (1996), who provide mass/luminosity values for SSPs according to metallicity and age. For those simulations that form little or no stars, making an accurate evaluation of the physical parameters impossible, we simply enter a "−" in Table 3.2.

To evaluate our methods for setting up the initial conditions, we discuss the 05 models below (see Table 3.1).

**Table 3.1:** Grid of the production runs, given with runnumbers and specifications of the three used parameters: mass (first column, see Table 2.1), initial flattening ($q$, last column) and initial rotation speed ($v_i$, 3 different rotation speeds) (see above).

| DG model | | | | $q$ |
|---|---|---|---|---|
| | $0\,\mathrm{km/s}$ | $1\,\mathrm{km/s}$ | $5\,\mathrm{km/s}$ | |
| C01 | 201 | 211 | 221 | 1 |
| | 231 | 241 | 251 | 0.5 |
| | 261 | 271 | 281 | 0.1 |
| C03 | 203 | 213 | 223 | 1 |
| | 233 | 243 | 253 | 0.5 |
| | 263 | 273 | 283 | 0.1 |
| C05 | 205 | 215 | 225 | 1 |
| | 235 | 245 | 255 | 0.5 |
| | 265 | 275 | 285 | 0.1 |
| C07 | 207 | 217 | 227 | 1 |
| | 237 | 247 | 257 | 0.5 |
| | 267 | 277 | 287 | 0.1 |
| C09 | 209 | 219 | 229 | 1 |
| | 239 | 249 | 259 | 0.5 |
| | 269 | 279 | 289 | 0.1 |

**Table 3.2:** Details of simulations. All physical quantities are evaluated at the end of the simulation (11.7 Gyr), except those indexed with 'i', which are evaluated at the beginning. Columns: (1) model number (see Table 2.1), (2) simulation number, (3) initial flattening (gas/DM), (4) initial rotation speed of gas [km/s], (5) spin parameter of gas in IC, (6) final gas mass [$10^6 M_\odot$], (7) stellar mass [$10^6 M_\odot$], (8) half-light radius [kpc], (9)(10) B-band and V-band magnitude, (11)(12) fitted Sérsic parameters of surface brightness profile, (13) central stellar velocity dispersion along line of sight (edge-on) [km/s], (14)(15) luminosity-weighted metallicity (B-band), (16) final flattening of the stellar component (averaged over last 3 Gyr), (17) final stellar peak rotation speed [km/s]. Omitted values were irrelevant due to low stellar mass.

| nr | run | $q_i$ | $v_i$ | $\lambda$ | $M_{g,f}$ | $M_\star$ | $R_e$ | $M_B$ | $M_V$ | $I_0$ | $n$ | $\sigma_c$ | $Z(Z_\odot)$ | $[Fe/H]$ | $q_f$ | $v_f$ |
|---|---|---|---|---|---|---|---|---|---|---|---|---|---|---|---|---|
| 01 | 201 | 1 | 0 | 0.0 | 43.5 | 0.485 | 0.18 | -7.84 | -8.44 | 26.3 | 0.81 | 8.9 | 0.00036 | -1.907 | 0.99 | 0.7 |
| | 211 | 1 | 1 | 0.007 | 43.5 | 0.519 | 0.15 | -8.23 | -8.76 | 26.5 | 0.62 | 8.2 | 0.00169 | -1.088 | 1.0 | 3.0 |
| | 221 | 1 | 5 | 0.036 | 43.8 | 0.235 | 0.13 | -7.89 | -8.39 | 27.0 | 0.35 | 6.5 | 0.00247 | -1.005 | 0.96 | 2.9 |
| | 231 | 0.5 | 0 | 0.0 | 43.6 | 0.373 | 0.17 | -7.83 | -8.37 | 26.4 | 0.8 | 7.7 | 0.00113 | -1.241 | 0.74 | 1.0 |
| | 241 | 0.5 | 1 | 0.009 | 43.6 | 0.419 | 0.17 | -7.91 | -8.51 | 26.3 | 0.78 | 7.3 | 0.0016 | -1.109 | 0.72 | 5.8 |
| | 251 | 0.5 | 5 | 0.046 | 43.9 | 0.138 | 0.13 | -7.65 | -8.08 | 26.5 | 0.57 | 5.8 | 0.00188 | -1.106 | 0.69 | 1.9 |
| | 261 | 0.1 | 0 | 0.0 | 44.0 | 0.008 | 0.11 | -3.57 | -4.19 | – | – | 5.6 | 0.00073 | -1.561 | – | -0.1 |
| | 271 | 0.1 | 1 | 0.014 | 44.0 | 0.004 | 0.11 | -2.65 | -3.25 | – | – | 4.6 | 0.00021 | -2.03 | – | – |
| | 281 | 0.1 | 5 | 0.071 | 44.0 | 0.0 | – | – | – | – | – | – | – | – | – | – |
| | | | | | | | | | | | | | | | | |
| 03 | 203 | 1 | 0 | 0.0 | 67.6 | 2.316 | 0.22 | -9.8 | -10.34 | 25.2 | 0.68 | 12.1 | 0.00187 | -1.103 | 1.02 | 1.4 |
| | 213 | 1 | 1 | 0.008 | 67.9 | 2.101 | 0.22 | -9.77 | -10.3 | 25.3 | 0.68 | 12.0 | 0.00219 | -1.058 | 0.93 | 4.9 |
| | 223 | 1 | 5 | 0.039 | 68.3 | 1.671 | 0.25 | -9.84 | -10.36 | 25.2 | 0.59 | 10.7 | 0.00368 | -0.825 | 0.76 | 13.7 |
| | 233 | 0.5 | 0 | 0.0 | 67.7 | 2.283 | 0.25 | -9.65 | -10.25 | 25.9 | 0.55 | 11.3 | 0.00163 | -1.095 | 0.75 | 1.0 |
| | 243 | 0.5 | 1 | 0.01 | 67.6 | 2.354 | 0.28 | -9.94 | -10.49 | 24.8 | 0.72 | 11.2 | 0.00371 | -0.795 | 0.7 | 8.2 |
| | 253 | 0.5 | 5 | 0.05 | 68.6 | 1.377 | 0.26 | -9.69 | -10.21 | 25.4 | 0.56 | 10.0 | 0.00373 | -0.826 | 0.61 | 12.9 |
| | 263 | 0.1 | 0 | 0.0 | 69.3 | 0.691 | 0.19 | -8.88 | -9.39 | 24.5 | 0.92 | 9.2 | 0.00256 | -0.964 | 0.64 | 0.7 |
| | 273 | 0.1 | 1 | 0.015 | 69.3 | 0.68 | 0.19 | -8.75 | -9.3 | 24.7 | 0.98 | 9.5 | 0.00262 | -0.97 | 0.6 | 4.1 |
| | 283 | 0.1 | 5 | 0.076 | 69.7 | 0.293 | 0.15 | -8.32 | -8.78 | 24.8 | 0.85 | 8.3 | 0.00284 | -0.958 | 0.57 | 3.0 |
| | | | | | | | | | | | | | | | | |
| 05 | 205 | 1 | 0 | 0.0 | 122.2 | 17.538 | 0.39 | -11.84 | -12.48 | 24.2 | 0.62 | 19.5 | 0.00445 | -0.699 | 1.0 | 0.4 |
| | 215 | 1 | 1 | 0.009 | 114.1 | 25.561 | 0.45 | -12.1 | -12.79 | 24.4 | 0.59 | 24.0 | 0.00513 | -0.674 | 0.94 | 9.3 |
| | 225 | 1 | 5 | 0.043 | 123.3 | 16.562 | 0.63 | -12.37 | -12.86 | 24.5 | 0.5 | 14.4 | 0.00623 | -0.61 | 0.53 | 24.2 |
| | 235 | 0.5 | 0 | 0.0 | 128.3 | 11.496 | 0.35 | -11.54 | -12.12 | 24.1 | 0.66 | 16.1 | 0.00291 | -0.886 | 1.03 | 1.2 |
| | 245 | 0.5 | 1 | 0.011 | 111.2 | 28.514 | 0.59 | -12.76 | -13.3 | 24.5 | 0.36 | 20.4 | 0.00822 | -0.484 | 0.72 | 14.4 |
| | 255 | 0.5 | 5 | 0.056 | 126.4 | 13.42 | 0.65 | -12.14 | -12.65 | 25.2 | 0.38 | 12.6 | 0.0063 | -0.609 | 0.45 | 24.2 |
| | 265 | 0.1 | 0 | 0.0 | 133.4 | 6.491 | 0.38 | -11.18 | -11.71 | 24.9 | 0.47 | 16.4 | 0.00305 | -0.871 | 0.67 | -0.3 |
| | 275 | 0.1 | 1 | 0.017 | 129.5 | 10.351 | 0.47 | -11.87 | -12.38 | 24.8 | 0.43 | 16.5 | 0.0052 | -0.69 | 0.63 | 8.7 |
| | 285 | 0.1 | 5 | 0.086 | 136.3 | 3.633 | 0.42 | -10.96 | -11.43 | 25.3 | 0.45 | 15.2 | 0.00436 | -0.771 | 0.49 | 11.7 |
| | | | | | | | | | | | | | | | | |
| 07 | 207 | 1 | 0 | 0.0 | 84.9 | 175.6 | 0.55 | -14.21 | -14.92 | 22.8 | 0.67 | 32.8 | 0.01396 | -0.241 | 1.0 | 4.4 |
| | 217 | 1 | 1 | 0.01 | 88.1 | 172.35 | 0.57 | -14.16 | -14.86 | 22.6 | 0.71 | 31.0 | 0.01525 | -0.191 | 0.88 | 18.6 |
| | 227 | 1 | 5 | 0.048 | 173.6 | 87.62 | 1.09 | -14.0 | -14.53 | 24.6 | 0.39 | 18.5 | 0.00836 | -0.478 | 0.45 | 33.6 |
| | 237 | 0.5 | 0 | 0.0 | 144.9 | 115.46 | 0.7 | -14.09 | -14.7 | 23.5 | 0.48 | 32.1 | 0.01103 | -0.355 | 0.89 | 2.4 |
| | 247 | 0.5 | 1 | 0.012 | 110.1 | 150.53 | 0.69 | -14.27 | -14.9 | 23.2 | 0.58 | 29.0 | 0.01346 | -0.257 | 0.73 | 18.5 |
| | 257 | 0.5 | 5 | 0.062 | 197.8 | 63.68 | 1.17 | -13.51 | -14.09 | 25.2 | 0.38 | 16.5 | 0.00631 | -0.609 | 0.38 | 34.4 |
| | 267 | 0.1 | 0 | 0.0 | 195.6 | 65.82 | 0.81 | -13.95 | -14.45 | 24.1 | 0.41 | 26.6 | 0.00853 | -0.482 | 0.76 | 1.6 |
| | 277 | 0.1 | 1 | 0.019 | 194.0 | 67.354 | 0.82 | -13.98 | -14.46 | 24.2 | 0.36 | 28.1 | 0.00892 | -0.455 | 0.68 | 8.5 |
| | 287 | 0.1 | 5 | 0.095 | 240.6 | 21.168 | 0.84 | -12.91 | -13.37 | 25.0 | 0.38 | 18.2 | 0.00595 | -0.642 | 0.39 | 25.3 |
| | | | | | | | | | | | | | | | | |
| 09 | 209 | 1 | 0 | 0.0 | 44.0 | 475.84 | 0.33 | -14.79 | -15.56 | 20.4 | 1.29 | 43.0 | 0.01594 | -0.109 | 1.02 | 2.7 |
| | 219 | 1 | 1 | 0.011 | 46.7 | 473.57 | 0.48 | -14.8 | -15.58 | 21.0 | 1.11 | 40.3 | 0.01591 | -0.135 | 0.83 | 28.4 |
| | 229 | 1 | 5 | 0.054 | 177.0 | 344.39 | 1.34 | -15.12 | -15.71 | 23.8 | 0.51 | 24.1 | 0.01363 | -0.238 | 0.4 | 45.3 |
| | 239 | 0.5 | 0 | 0.0 | 61.5 | 458.48 | 0.43 | -14.84 | -15.6 | 20.9 | 1.12 | 42.7 | 0.0167 | -0.104 | 0.83 | 2.0 |
| | 249 | 0.5 | 1 | 0.014 | 67.8 | 452.32 | 0.58 | -14.86 | -15.63 | 21.8 | 0.89 | 37.3 | 0.01634 | -0.129 | 0.69 | 29.6 |
| | 259 | 0.5 | 5 | 0.07 | 238.4 | 283.58 | 1.52 | -14.9 | -15.5 | 24.1 | 0.61 | 21.2 | 0.01078 | -0.348 | 0.36 | 44.5 |
| | 269 | 0.1 | 0 | 0.0 | 211.0 | 310.25 | 0.61 | -15.28 | -15.82 | 21.6 | 0.75 | 36.0 | 0.01835 | -0.086 | 0.79 | 0.4 |
| | 279 | 0.1 | 1 | 0.021 | 225.5 | 295.97 | 0.74 | -15.18 | -15.74 | 22.5 | 0.58 | 35.6 | 0.01663 | -0.137 | 0.72 | 14.2 |
| | 289 | 0.1 | 5 | 0.107 | 410.0 | 113.12 | 1.19 | -14.36 | -14.89 | 23.7 | 0.9 | 27.2 | 0.00812 | -0.491 | 0.39 | 29.7 |

#### 3.2.3.1 Variance

We first make note of the inherent variance in our models. To this end we have produced a set of 25 simulations of the basic spherical C05 model, with different samplings of the dark matter halo and the gas sphere. For each simulation, different random seeds are used

to construct the initial condition. As shown by the 15.9th/84.1th percentile area and the total range of the SFHs of this set of simulations in Fig. 3.1, the variance is significant, allowing for a variety of SFHs. This is however not unexpected. Systems of this kind, with stochastic star formation and feedback, are inherently chaotic. Small differences are continuously amplified and can, over time, lead to large deviations. But on the other hand, more importantly, the green band depicting the 15.9th/84.1th percentile area (which would correspond to the $1\sigma$ interval if the underlying distribution was Gaussian) shows quite clearly the generic behaviour of the models. So we keep in mind that our models can show a spread in their properties, but that they also exhibit a clear general behaviour.

### 3.2.3.2   Rotating models

As described above, to obtain a rotating galaxy we add initial angular momentum to the *gas*. We need to check if this actually results in a rotating *stellar* component of the galaxy. In the upper panel of Fig. 3.2, we present the rotation curve of the gas particles at different times. In the lower panel, we show the final stellar rotation curve (at $11.7\,Gyr$). These are binned profiles of tangential velocity versus distance to the $z$ axis, where the profile value in every bin is the average rotation velocity per particle in that bin.
The rotation profile of the gas rises due to the gas falling into the potential well, and quickly evolves to a rather stable form, only perturbed temporarily by the turbulence caused by strong star formation events. This "steady state" is a consequence of the balance between cooling, which makes the rotating gas sink inwards, and supernova feedback, which heats and disperses gas. The stars that form from the gas finally follow a rotation profile that rises out to one half-light radius and flattens off beyond that radius. This confirms that using a constant rotation profile for the initial conditions for the gas is adequate to achieve stable, rotating dwarf galaxies. The final rotation speed of the stars which is included in Table 3.2 is the peak value of this rotation curve. In Fig. 3.3 the evolution of the stellar rotation profile is shown for our fastest rotating models, from 221 to 229. It can be seen that in the most massive models the rotation curve quickly attains its final shape, while in the least massive models, which basically form in one major initial burst, the rotation curve slowly decreases due to the relatively strong turbulence in the lower mass regime.

### 3.2.3.3   Flattened models

In Fig. 3.4 we show three of our model galaxies (a non-rotating spherically symmetric model on the left, a rotating model and a flattened model) to see the resulting flattenings at the end of the simulations. The latter two both show a considerable and stable flattening (see the C05 model in Fig. 3.5). Some trends become apparent when looking at the total mass range in Table 3.2 and Fig. 3.5. It appears that the stability of $q$ for the stellar component significantly increases with rising mass in the rotating models. Only in the least massive models does $q$ rise significantly with time. The more massive models all exhibit a stable flattening around $q \sim 0.4 - 0.5$, so our model dwarf galaxies are relatively "thick". In non-rotating models with an initially strongly flattened halo, the halo thickens and it turns out to be impossible to make stellar bodies more flattened than $q \sim 0.6 - 0.8$. As can
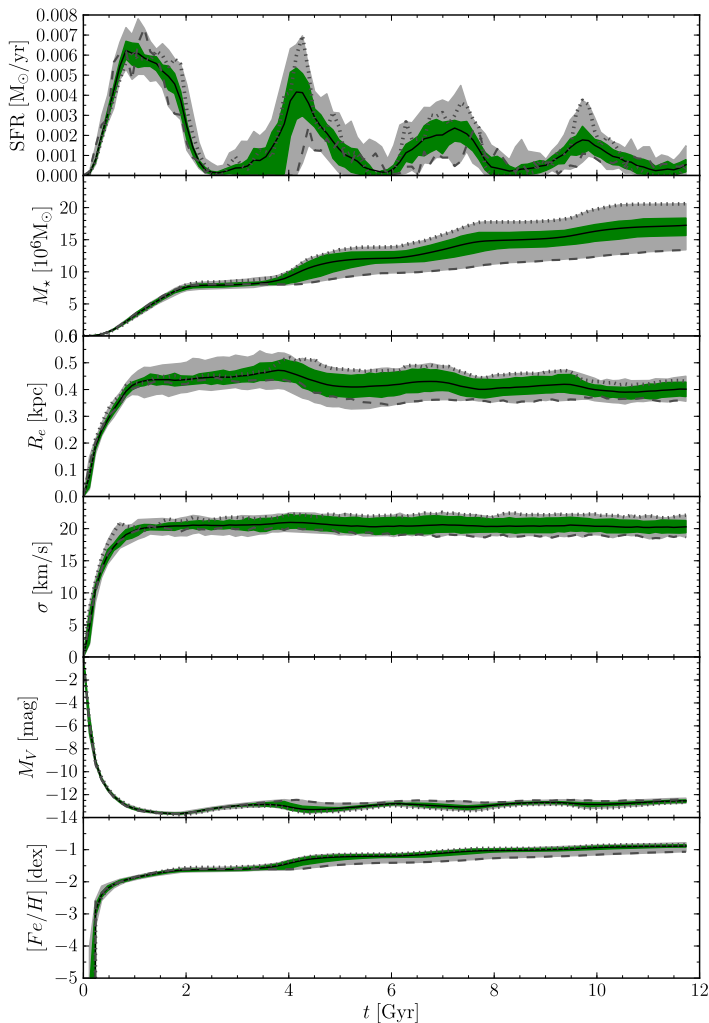
**Figure 3.1:** Depiction of the variance inherent to our models, using a set of 25 differently sampled
initial conditions. The different panels show different quantities of the simulations.
The black line is the mean curve for our set. The green band shows the area
between the 15.9th and 84.1st percentile (which are linearly interpolated between the
closest ranks, and would correspond to the $1\sigma$ interval if the underlying distribution
was Gaussian), and the light grey band shows the area between the minimum and
maximum value of our set. These percentiles and extrema are calculated in each
time-bin (of which there are 100). The two dark grey lines show the evolution of two
individual runs: the dashed and dotted line represent the runs which, respectively,
produced the lowest and the highest total stellar mass at the end of the simulation.

be read from Table 3.2, combining initial rotation and initial flattening helps somewhat
to achieve stronger flattenings in the least massive models.

We thus note from Table 3.2 and Fig. 3.5 that we are not able to make extremely flat
galaxies. In the work of Roychowdhury *et al.* (2010) a collection of dIrrs from the FIGGS

**Figure 3.2:** Rotation curves of our showcase model (225), *upper panel* displays the gas at different times during the simulation, *lower panel* displays the stars at 11.7 Gyr (with adaptive binning).
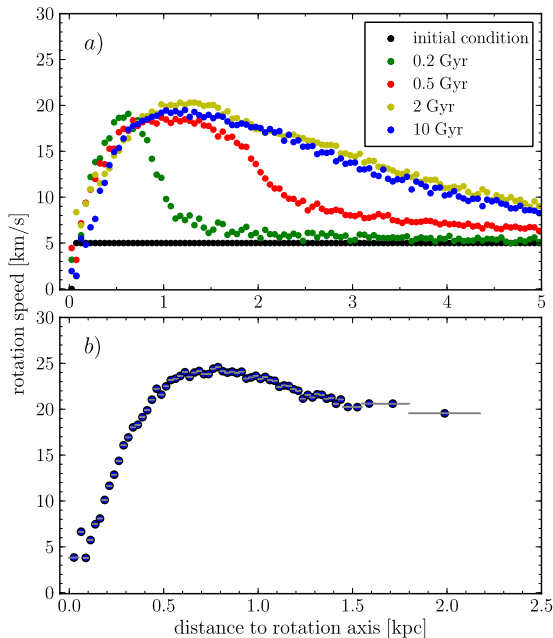
survey is investigated, and they find from the flattening distribution a mean axial ratio $\langle q \rangle \approx 0.6$ for the *HI disks*. Similar values are obtained by Binggeli & Popescu (1995), Staveley-Smith *et al.* (1992), Hunter & Elmegreen (2006), Sung *et al.* (1998) and Sánchez-Janssen *et al.* (2010) for the *stellar* content of dwarf galaxies. Also other simulations suggest that low mass galaxies are not born as thin discs, but as thick, puffy systems (e.g. Kaufmann *et al.* 2007; and to a lesser extent the (more massive) models of Governato *et al.* 2010, which are still not extremely flat). The reason for this is sought in the increasing importance of turbulent motions, plausibly caused by star formation and feedback, with respect to rotational motion in low mass systems (Kaufmann *et al.*, 2007; Roychowdhury *et al.*, 2010; Sánchez-Janssen *et al.*, 2010). Besides the moderate value of the flattening itself, we also qualitatively reproduce the trend with galaxy mass from Sánchez-Janssen *et al.* (2010). All our simulations are below their 'limiting mass' of $M_* \approx 2 \times 10^9 \ M_\odot$, and indeed for simulations with identical initial setup, the final stellar bodies thicken with decreasing mass. This can be seen in Fig. 3.6, where we mimic their Fig. 1 (the leftmost and rightmost panels). Our most massive, flat models ($M_* \approx 3.4 \times 10^8 \ M_\odot$, $q \approx 0.4$) connect nicely to models DG1 and DG2 of Governato *et al.* (2010), who are slightly more massive and slightly flatter ($M_* \approx 4.8 \times 10^8 \ M_\odot$, $q \approx 0.35$).
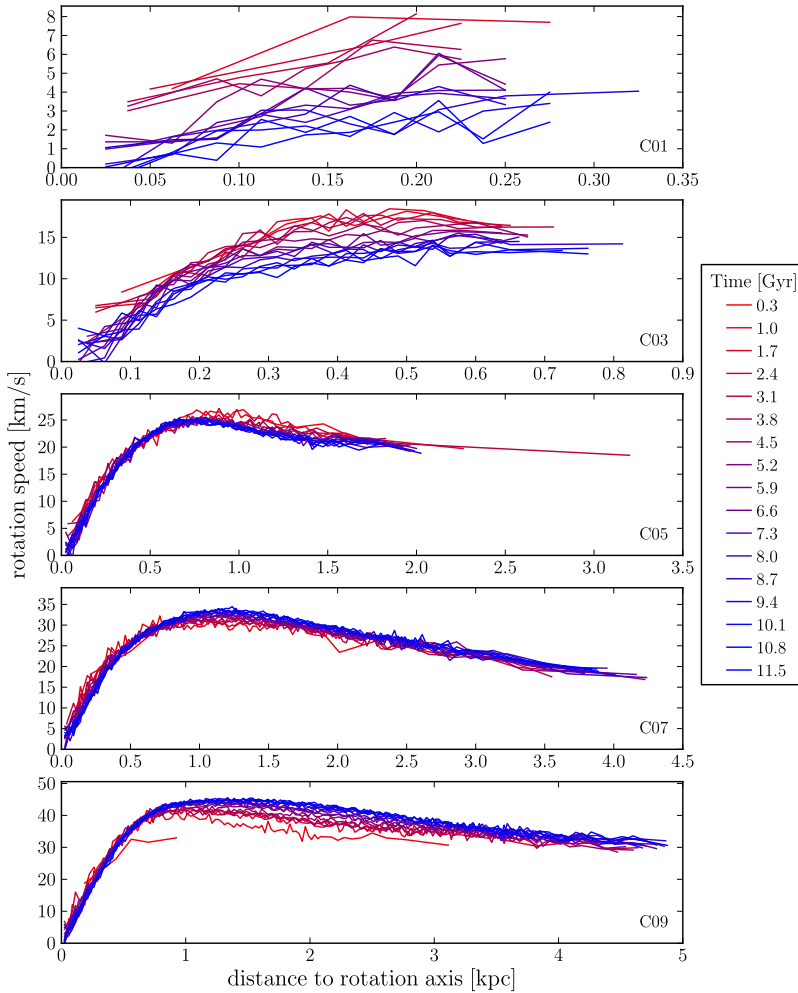
**Figure 3.3:** Evolution of the rotation curves in the fastest rotating models (22x), which will also be used further on for the rest of the analysis in this chapter. Time is indicated with color from red to blue, see legend.

### 3.2.3.4   Galaxy mass and concentration

For a rotating model the half-light radius ($R_{eL}$), defined as the radius of the sphere containing half of the light) is considerably larger than that of a sperical model, as can be seen in Table 3.2 and Fig. 3.4. The total stellar mass usually decreases when adding significant rotation. Non-rotating flattened models on the other hand are generally not much larger than the spherical models, sometimes even smaller. The half-light radius decreases slightly in flattened galaxies at lower masses, and increases slightly at higher masses (with respect to the spherical model). The total stellar mass decreases with increasing flattening.

The rotating models are thus spatially more extended than their spherical progenitor and at the same time they generally are also less massive (in stellar mass) so they are
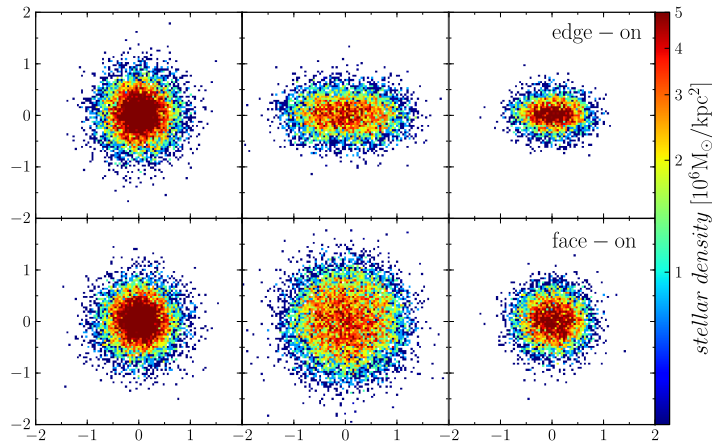
**Figure 3.4:** Edge-on and face-on views of the stellar distributions of a non-rotating spherical model (left, 205), a rotating model (middle, 225) and a flattened, non-rotating model (right, 265). All are slices of thickness 0.4 kpc, axes are in kpc, and color denotes projected stellar density.
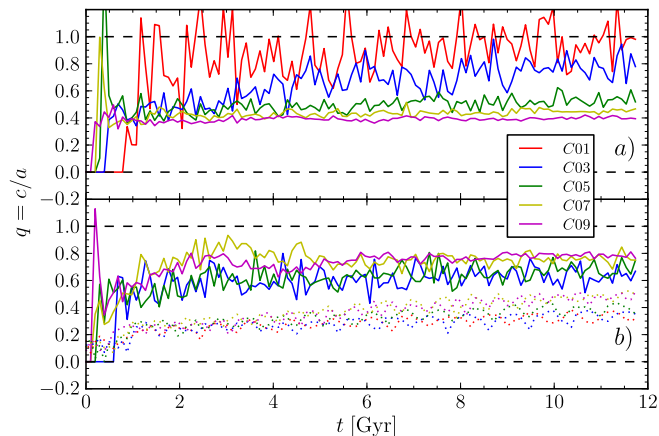


**Figure 3.5:** Evolution of the flattening parameter $q = c/a$ of the stellar component during the simulations for different galaxy masses. *Upper panel*: rotating models (all with $v_i = 5\,km/s$), *lower panel*: flattened models (all with $q_i = 0.1$). Per panel all properties are identical, except for the mass. Only galaxies with an appreciable stellar mass are shown (see Table 3.2). Dotted lines show the $q$ of the DM component, only shown in the bottom panel because the DM consistently has $q = 1$ in the top panel.

considerably less centrally concentrated. The flattenend, non-rotating models are usually less spatially extended than the spherical models and also less massive, so they have similar central concentrations (see also Fig. 3.4).
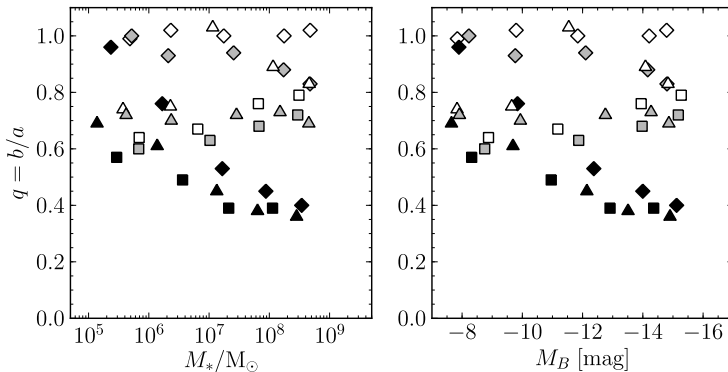
**Figure 3.6:** Axis ratios of all our models. *Left panel*: versus stellar mass (in $M_\odot$), *right panel*: versus B-band luminosity. The different initial rotation speeds are indicated with color (white: 0 km/s, grey: 1 km/s, black: 5 km/s), the initial flattenings are indicated with symbol shapes (lozenge: 1, triangle: 0.5, square: 0.1).

## 3.3 Analysis

In this section we present a more extensive analysis of our production runs.

### 3.3.1 Metallicity profiles

Looking at Fig. 3.7 we see some interesting results concerning the metallicity profiles of the rotating galaxies. For a range of galaxy masses we compare the metallicity profiles of the spherical models with those of the fastest rotating models from Table 3.1 (with $v_i = 5\,km/s$) in Fig. 3.7. The metallicity profiles of the spherical models almost always show a clear, negative gradient, while the profiles of the rotating models are always significantly flatter. For a proper comparison between different models of different sizes, the half-light radius of each simulation is also indicated on the plots with a dashed vertical line. We note that the rotating models can be considered to have flat profiles out to 1.5 times $R_{eL}$, while the spherical models usually show a fall-off well before that. Noticeably, the mean [Fe/H] of the lower mass models appears to be significantly higher when rotating, while the opposite is true for the higher mass models. This will be discussed further on in section 3.3.4.4.

Fig. 3.8 shows the same quantities for some of the flattened models. Surprisingly, there appears to be no obvious trend between the flattening and the shape of the metallicity profile, with most galaxies showing strong negative metallicity gradients. We show all models from Table 3.1 which received an initial flattening but no initial rotation, so for each mass we have 2 different degrees of initial flattening ($q = 0.5$ and $q = 0.1$). It is clear that the flattening generally has no significant effect on the metallicity gradient, almost all simulations have a negative slope. Only in the most massive ones, or where the spherical model does not have a strong gradient to begin with, does the initial flattening appear to
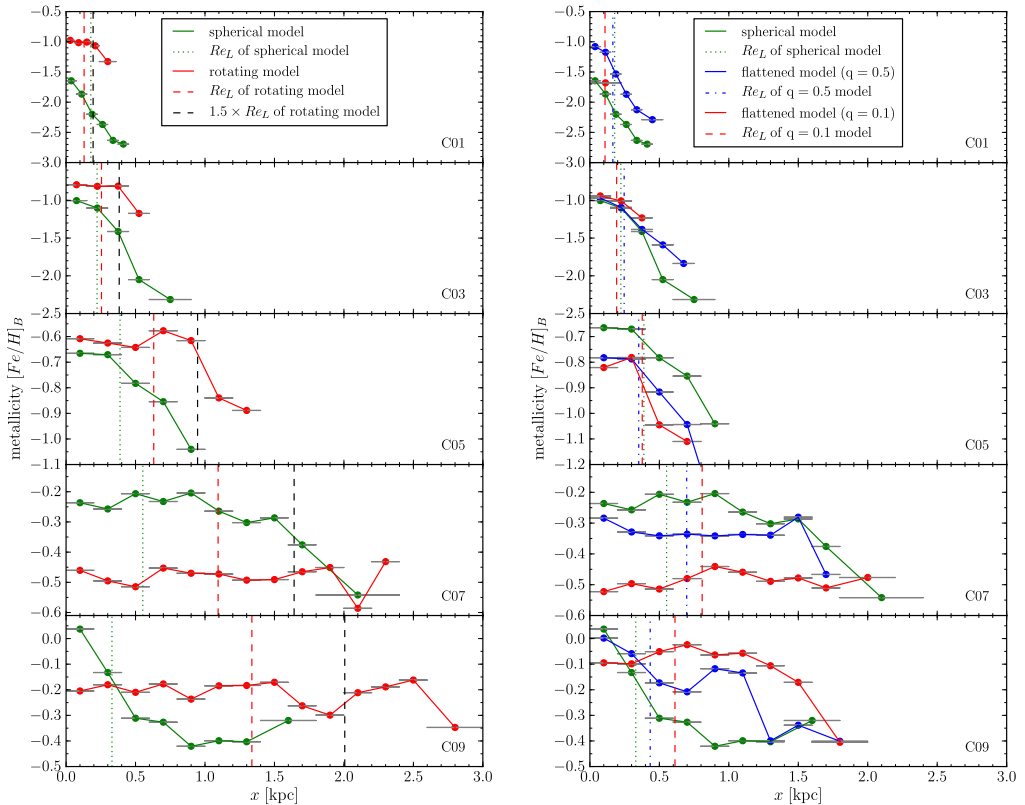
**Figure 3.7:** [*LEFT*] Metallicity profiles of our productions runs, see Table 3.1. Each frame compares, for a certain galaxy mass, the spherical model ($20x$) with the fastest rotating model ($22x$). The $R_{eL}$ of each model is also indicated with a dashed line, and for the rotating model we also show $1.5 \times R_{eL}$ for indicative purposes. Adaptive binning was used to produce these profiles, the width of each bin being indicated by a horizontal grey bar.

**Figure 3.8:** [*RIGHT*] Metallicity profiles of our productions runs, see Table 3.1. Each frame compares, for a certain galaxy mass, the spherical model ($20x$) with the 2 non-rotating flattened models ($23x$ and $26x$). Further details of the plot are similar to those of Fig. 3.7.

have some ability to somewhat flatten the metallicity profile.

### 3.3.2   Star formation histories

Next we turn our attention to the star formation, and for this we look at Fig. 3.9, where star formation histories (SFH) of different simulations are shown. Rotation also seems to have a significant influence here. We again compare the spherical models with the fastest rotating models from Table 3.1 for a range of galaxy masses in Fig. 3.9, where we show
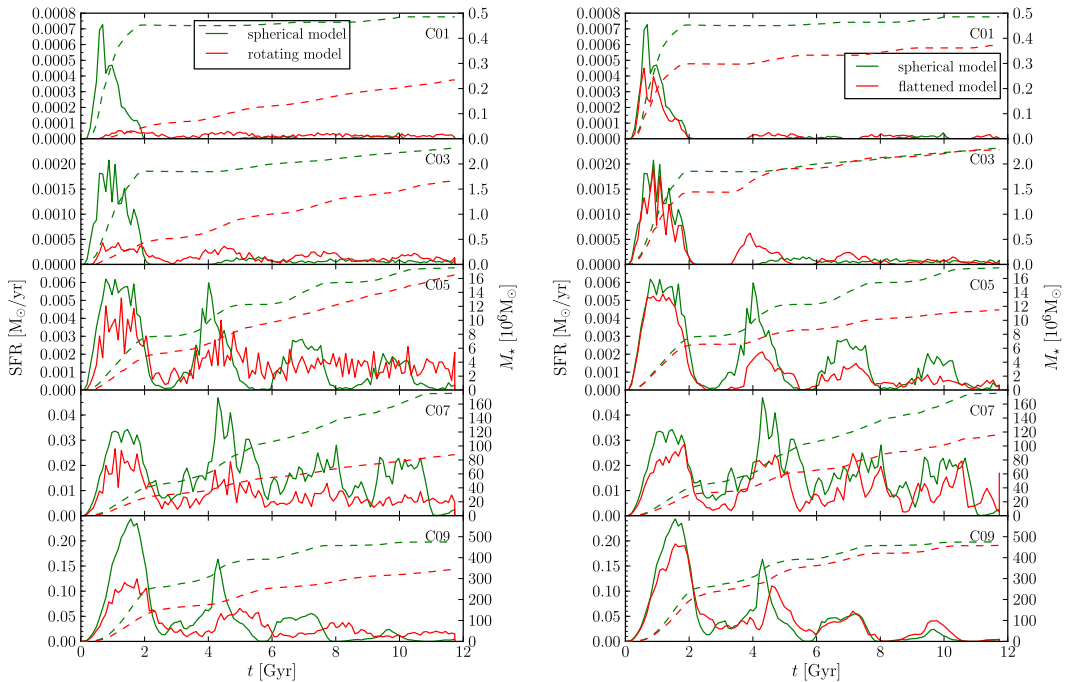
**Figure 3.9:** [*LEFT*] SFHs of our productions runs, see Table 3.1. The same runs as in Fig. 3.7 are plotted here, comparing spherical and rotating models for different masses. Both their SFH (solid lines) and evolution of their stellar mass (dashed lines) are shown.

**Figure 3.10:** [*RIGHT*] SFHs of our productions runs, see Table 3.1. The runs with $q = 0.5$ from Fig. 3.8 are plotted here, comparing spherical and flattened models for different masses. Similar to Fig. 3.9.

the evolution of the produced stellar mass expressed in solar mass per year ($M_\odot$/yr). The total stellar mass of the galaxy is plotted in dashed lines alongside the SFHs.

Non-rotating spherical models typically have "breathing" or "bursty" SFHs, with strong SF peaks a few Gyr long, separated by quiescent periods where the star formation rate (SFR) essentially goes to zero (Valcke *et al.*, 2008; Stinson *et al.*, 2007; Revaz *et al.*, 2009). The strength and duration of these peaks, as well as the intermittent pauses, depend mainly on galaxy mass.

The models with rotation, however, are able to reduce this burstiness and make the SFH much more continuous. Periods of increased star formation still exist, alternated with lulls, but the SFR never drops down to zero. The effectiveness of reducing the SF peaks varies in our simulations, and depends primarily on the galaxy mass. In the least massive models, which in the non-rotating spherical case show the most extreme bursty behaviour (one big initial burst almost completely shutting down further SF activity), the effect of adding rotation is most noticeable. The SFR now becomes virtually flat. The more

massive models still show some SF fluctuations but not nearly as pronounced as in their
spherically symmetric analogs.

Flattening on the other hand does not have a large effect on the star formation history
of the galaxies. When looking at Fig. 3.10 we can see that flattening, unlike rotation,
generally does not induce major qualitative differences in the SFH. The SFHs are generally
very much like the SFHs of the spherical models, still having large peaks separated by
periods with zero star formation.

### 3.3.3 Gas structure

The structure of the gas of dwarf galaxies is another typical characteristic that we will
consider. The best observations available in this respect come from the Magellanic Clouds;
for instance Kim *et al.* (2005) present HI data for the LMC. Another very useful source
of observational data about the HI gas content and structure of dwarf galaxies is the
THINGS survey (The HI Nearby Galaxy Survey; Walter *et al.*, 2008; Weisz *et al.*, 2009).
These studies show that the neutral hydrogen gas of dIrrs generally shows an obvious
"bubble structure", consisting of myriad spherical low density regions or "holes" in the
gas with a large range of sizes.

The origin of these holes has long been attributed to stellar feedback by single-age new-
born stellar clusters (Weaver *et al.*, 1977; McCray & Kafatos, 1987, and references therein).
However, for the LMC it has proven to be not at all evident to correlate HI holes or shells
with H$\alpha$ emission (Kim *et al.*, 1999; Book *et al.*, 2008). Holmberg II has similar issues,
with H$\alpha$ not tracing the holes, and the stellar ages found therein not corresponding well
with the kinematical age of the holes (Stewart *et al.*, 2000; Rhode *et al.*, 1999; Weisz *et al.*,
2009). Studying this last galaxy in detail, Weisz *et al.* (2009) propose a multi-age model,
where HI holes are created by stellar feedback from multiple generations of star formation
spread out over tens to hundreds of Myr. This model is supported by the fact that H$\alpha$
and 24 micron emission, which trace the most recent SF, do not correlate well with HI
holes, while UV emission, which traces SF over roughly the last 100 Myr, correlates much
better. The concept of a single age for a hole is rendered ambiguous.

In Fig. 3.11 we show the structure of 3 of our simulated dwarf galaxies, in a sequence of
snapshots taken throughout their entire evolution (all shown face on). The projected gas
density is rendered as the background color (see colorbar), and two different age selections
of the stellar population are plotted. In accordance with Weisz *et al.* (2009) we choose
these to represent the *newest* stars (yellow dots, stellar age < 20Myr) which would be
detected in H$\alpha$, and the *recent* stars (red dots, 40Myr < stellar age < 100Myr) which
would show up in UV. The gap between the two populations serves to provide a clearer
distinction between them on the plots. For a comparison, we turn to HST observations of
the Sextans A dwarf irregular galaxy. Dohm-Palmer *et al.* (2002) have shown the presence
of a region where star formation has been ongoing for $\sim$ 400 Myr and has depleted the gas
reservoir to the point where star formation is about to be extinguished. A more gas-dense
region appears to have supported star formation for the last $\sim$ 200 Myr but star formation
seems to have migrated within this region. The youngest star-formation region, less than
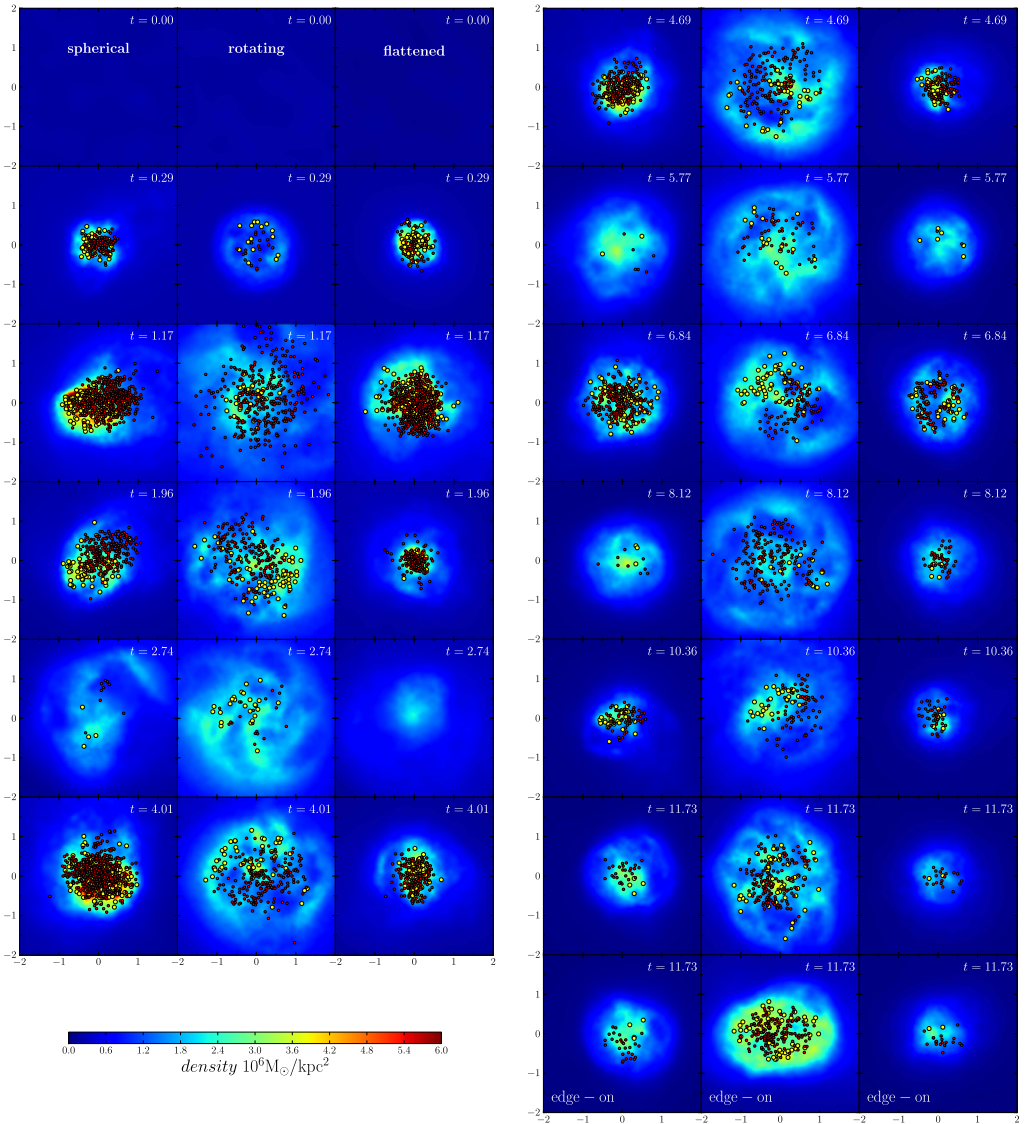
**Figure 3.11:** A series of snapshots from the evolution of 3 simulated dwarf galaxies based on the C05 DG model. *Left column*: basic spherical model (205), *middle column*: rotating model (225), *right column*: flattened, non-rotating model (265). The bottom of the left 3 columns continues on the top of the right 3 colums. Snapshots show rendered gas density (colorbar), *new* star particles (yellow dots, stellar age < 20Myr) and *recent* star particles (red dots, 40Myr < stellar age < 100Myr). The label in the top right corner indicates the time in the simulation (Gyr), and all galaxies are shown face-on in the $x - y$ plane, except the last 3 snapshots which are edge-on in the $x - z$ plane (axes are in kpc). A full, high quality animation can be found online, see text.

20 Myr old, is associated with a very high gas density region that had not undergone star formation at any point within the last 700 Myr. This suggested to these authors a scenario of what they call an oderly stochastic process with "star formation burning through the gas clouds like a lit fuse". In our simulations, we indeed see regions (e.g. near the center) where long-term star formation seems to be ongoing but never at exactly the same place. In other places, feedback is able to heat and disperse the gas, locally switching off star formation for the near future, while at places where the swept-up gas reaches sufficiently high densities, induced star formation occurs. Given the time it takes for feedback to evacuate a region several 100 pc wide, these empty regions are associated with stellar populations with ages over $\sim 100$ Myr.

These 3 simulations compare a spherical model (205, left column), a flattened non-rotating model (265, right column) and a rotating model (225, center column), all based on the C05 model (see Tables 2.1 and 3.1). The specific snapshot times have been selected to represent "interesting" moments in the galaxies' SFHs, coinciding with SF peaks or lulls, see Figs. 3.9, 3.10. A high quality animation, corresponding to Fig. 3.11, can be found online[1].

Note: more quantitative and sophisticated analyses of the gas structure in the most up-to-date simulations performed in this PhD research are given in Chapter 5, along with consistent comparisons with observations of dwarf galaxies.

### 3.3.3.1 Spherical simulations

In the spherical models gas collapses to the center and forms stars that collectively blow out the gas through feedback, preferably to one side in a so-called chimney (see snapshots at $t = 1.17$). Over time, the gas cools and re-collapses after which star formation can resume again (snapshots at $t = 2.74$, $t = 5.77$ and $t = 8.12$). This cycle continues throughout the entire evolution. There is no significant difference in the correlation with the local gas density between the two stellar populations shown in Fig. 3.11. Both populations are centrally concentrated, and so is the gas density.

Overall there is little small-scale structure: the behaviour of the gas takes place on a large, collective scale. This becomes particularly apparent when comparing to the rotating model, discussed further on in 3.3.3.3. An occasional small bubble can be spotted in the gas when the galaxy is forming stars (e.g. snapshot at $t = 4.69$, on the upper side of the galaxy). This large-scale behaviour translates into the characteristics of the SFHs of the spherical models discussed before: large SF peaks separated by quiescent periods.

### 3.3.3.2 Flattened simulations

The structure of the gas in the flattened dwarf galaxies is quite similar to the spherical ones. Large-scale behaviour with a centralized structure is still very much the case, which again can be connected to the discussion and conclusions about the SFHs of the flattened

---

[1]HD video: `http://www.youtube.com/watch?v=L2OWqfM1azo`; YouTube channel of Astronomy department at Ghent University: `http://www.youtube.com/user/AstroUGent`; YouTube playlist with all additional material for this paper: `http://www.youtube.com/playlist?list=PLEFAA5AAE5C5E474D`

galaxies. Small-scale structure is not significantly more present than in the spherical models, and the previous discussion of the evolution of the spherical models is equally valid for the initially flattened, non-rotating models.

#### 3.3.3.3   Rotating simulations

The structure of the gas content of the simulated dwarf galaxies is noticeably different when adding rotation. There is now much more small-scale structure in the gas. A "bubble structure" emerges in the gas, caused by the stellar feedback of individual star particles (snapshot at $t = 0.29$) or small pockets of star particles (very clear at e.g. $t = 6.84$). Apparently, the influence of stellar feedback has become more *local*, and the gas does not exhibit the same *global*, large scale behaviour seen in the rotationless models.

There is now a very strong difference in the correlation between the local gas density and the separate stellar populations. The newest stars are always found in the densest regions of the gas, which is not unlogical considering the star formation criteria (Valcke *et al.*, 2008). The slightly older stars are much more likely to be found in the bubbles or holes because individual groups of star particles have had sufficient time to accumulate enough collective feedback. This all speaks in favor of the multi-age model of Weisz *et al.* (2009) for creating HI holes, and the findings of Stewart *et al.* (2000) that young stars (H$\alpha$) prefer high density HI regions while older stars (FUV) are more likely found in low density regions. The idea that UV should be a better tracer for HI holes than H$\alpha$ therefore seems very plausible. We can also spot cases of triggered secondary star formation, the clearest example being at $t = 4.69$ where a large bubble at the lower left side expands outwards and compresses the gas along a rim on the outside of the bubble, spawning new star formation in this rim. Observational evidence for similar events can be found where secondary SF is detected in H$\alpha$ along rims around HI holes (Stewart *et al.*, 2000; Book *et al.*, 2008).

All this again translates into the SFH characteristics we discussed before for rotating dwarf galaxies, where the periodicity, or in other words the large scale oscillation, of the SFHs from the spherical models is significantly reduced. At times when in the spherical and flattened models star formation has almost completely ceased, the rotating model still shows a significant activity. It continuously forms stars throughout the entire simulation. As a last point, the SF is also noticeably more spatially extended than in the spherical and flattened cases. Moreover, the spatial extent is quite constant during the entire simulation. Stars are always formed throughout practically the entire body of the galaxy, while in the spherical/flattened cases the subsequent SF bursts become increasingly centrally concentrated.

### 3.3.4   Scaling relations

Aside from the specific characteristics of individual models we discussed above, we also consider the global photometric and kinematical scaling relations traced by the stars in the simulated galaxies. Our main aim is to see how well the general characteristics of our

simulated dwarf galaxies agree with observational data of dwarf galaxies as a class.
Scaling relations for gas properties are, however, not considered here. At this point in the
research we do not yet have all the proper tools to make meaningful comparisons between
the simulated gas and observations of dwarf galaxies, which are usually of gas in a specific
astrophysical state (such as HI, neutral atomic gas). This is something that has only
become possible in our most recent simulations presented in Chapter 5, where we are able
to use the necessary gas physics to separate the simulated gas into different astrophysical
states.

In the following, two series of simulations are plotted. Firstly, all non-rotating galaxy
models, both with spherically symmetric and with flattened halos, represented with white
symbols in Figs. 3.12 to 3.19. Secondly, all galaxy models initially rotating at $v_{rot} = 5$
km/s, both with spherically symmetric and with flattened halos, are represented with
grey symbols in these figures. The symbol shapes distinguish the initial halo flattenings:
simulations with $q = 1$ are shown with lozenges, $q = 0.5$ with triangles, $q = 0.1$ with
squares. See Tables 3.1 and 3.2.

### 3.3.4.1   Half-light radius $R_e$

The effects of flattening and rotation on the half-light radius are clear in Fig. 3.12, where
$R_e$ versus $M_V$ is shown. Overall, at a fixed luminosity, rotation causes $R_e$ to increase. The
initial flattening of the halo does not seem to make a significant difference since both model
sequences are quite narrow. Only at the high mass end of the non-rotating series does $R_e$
increase with flattening, the rotating series are unaffected. Overall, there does not seem
to be a second parameter effect. Both series together nicely encompass the observational
width of the scaling relation. The third series of simulations (with a low initial rotation
speed of $v_{rot} = 1$ km/s) were omitted for clarity of the plot. They simply lie between the
two plotted series, providing us with rotation as a possible explanation for the width of
the scaling relation. The inherent variance of the models, as discussed in Section 3.2.3.1
and shown in Fig. 3.1, is too small to be responsible for this spread.

### 3.3.4.2   Velocity dispersion $\sigma$

Fig. 3.13 shows the stellar central velocity dispersion $\sigma$ versus $M_V$, projected along the
line of sight. We take this to be the $x$-axis, viewing the models edge-on. As in Valcke
*et al.* (2008), the central velocity dispersion is in general somewhat too high. However,
the rotating models, having lower velocity dispersions, compare favorably to spherically
symmetric or flattened ones. This decrease of the velocity dispersion in the more massive
models is tied to the increase of the half-light radius in the more massive models. In the
rotating series the initial flattening also appears to have somewhat of an effect, leading
to slightly higher velocity dispersions in the most flattened cases (squares). This is pos-
sibly due to the high M/L ratio of these systems, since they have a considerably higher
dynamical mass (for a given stellar mass) than their initially less flattened counterparts
(see Table 3.2).
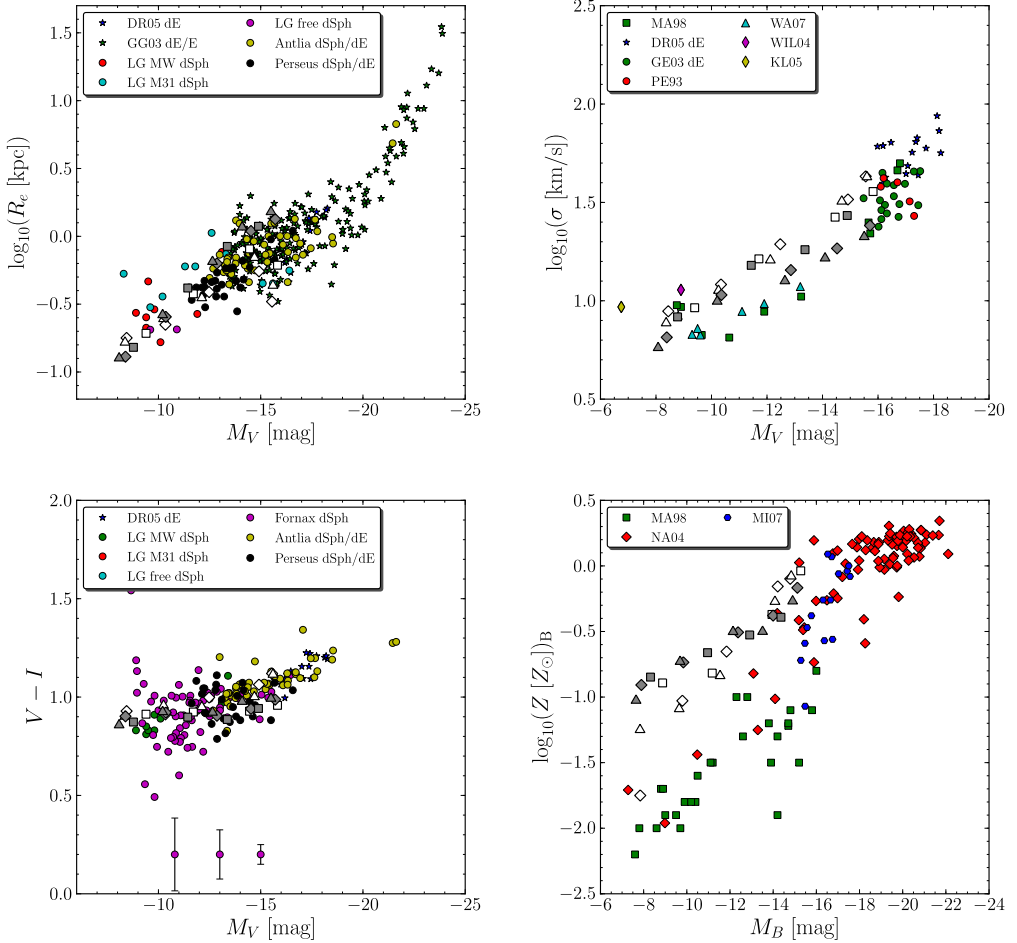
**Figure 3.12:** [top left] Half-light radius versus V-magnitude. White symbols are our non-rotating galaxies; the grey ones are the fastest rotating galaxies (see text). All other points on the plot are observational data found in de Rijcke *et al.* (2009). The symbol shapes distinguish the initial halo flattenings: simulations with $q = 1$ are shown with lozenges, $q = 0.5$ with triangles, $q = 0.1$ with squares.

**Figure 3.13:** [top right] Stellar velocity dispersion versus V-magnitude. Observations: Mateo 1998 (MA98), de Rijcke *et al.* 2005 (DR05), Geha *et al.* 2003 (GE03), Peterson & Caldwell 1993 (PE93), 7 MW dSphs from Walker *et al.* 2007 (WA07), Ursa Minor from Wilkinson *et al.* 2004 (WIL04), Ursa Major from Kleyna *et al.* 2005 (KL05).

**Figure 3.14:** [bottom left] $V - I$ color versus V-magnitude. Symbols and data as in Fig.3.12, and the typical error bars for the Fornax Cluster dSph data are shown.

**Figure 3.15:** [bottom right] Metallicity in $\log_{10}(Z \ [Z_\odot])_{\rm B}$ (weighed with B-band luminosity, with $Z_\odot = 0.02$) versus B-magnitude. Data : Mateo 1998 (MA98), Nagashima & Yoshii 2004 (NA04), Michielsen *et al.* 2007 (MI07).

### 3.3.4.3 Color $V - I$

The global $V - I$ colors of the models are shown in Fig. 3.14. The rotating galaxies lie a little lower than the non-rotating on this plot, meaning these galaxies are slightly bluer. This can be understood from their star formation histories (Fig. 3.9). The strength of the first SF peak is reduced, while at later times SF is enhanced with respect to the non-rotating case, producing more younger, bluer stars. Otherwise, all simulations fall well within the observational range. This is, however, not a very stringent test of the models, given the fact that the $V - I$ color of an intermediate-age stellar population is relatively insensitive to metallicity (see next paragraph).

### 3.3.4.4 Metallicity

The metallicity of all dwarf models is too high, especially in the low-mass regime. This problem was already encountered by Valcke *et al.* (2008) for the spherically symmetric models. Below $M_B \approx -12$ mag, the rotating models are more metalrich than non-rotating ones whereas above this magnitude they are less metalrich. An explanation for the low mass models can again be found in the respective SFHs (Fig. 3.9). In the least massive non-rotating models, the large first peak in the SFH strongly inhibits further star formation because the combined force of the feedback is strong enough to severely lower the gas density. Adding rotation reduces this first peak and thus also its truncating power, allowing SF to proceed continuously and enrich the gas further with subsequent stellar generations. When going to higher masses however, the effect and importance of the first peak decreases. From the C07 model on, the trend reverses. This is most likely due to the strong decrease in central concentration of SF and feedback because of rotation (see Figs. 3.11 and 3.20 at the end of this chapter), together with the simple fact that less stellar mass is produced. SF, metal production and gas enrichment are much more diffuse, providing (on average) less-metalrich gas for subsequent stellar generations.

### 3.3.4.5 Surface brightness profiles

The surface brightness profiles are fitted with a Sérsic law

$$I(R) = I_0 e^{-\left(\frac{R}{R_0}\right)^{1/n}}, \tag{3.1}$$

from which the parameters $\mu_0$ and $n$ are plotted and compared with observational data in Fig. 3.16. The Sérsic index $n$ does not differ significantly between rotating and non-rotating models. The central surface brightness $\mu_0$, on the other hand, is consistently lower in the rotating models. This is to be expected: with rotation the SF becomes less centrally concentrated and more widespread, lowering the central surface brightness.

#### 3.3.4.6   Fundamental plane

The fundamental plane (Bender *et al.*, 1992; Burstein *et al.*, 1997) is shown in physical coordinates (Fig. 3.18) and in $\kappa$ space (Fig. 3.17). The "vertical" deviation from the fundamental plane is shown in Fig. 3.19. Except for the most massive non-rotating galaxy models (white lozenges), which are very compact, most dwarf galaxy models lie significantly above the fundamental plane. These compact non-rotating dwarfs have small $R_e$ and consequently high mean surface brightness within $R_e$ (denoted by $I_e$), making them stick out in the side-view of the fundamental plane (Fig. 3.18) and in its $\kappa_1 - \kappa_2$ projection (Fig. 3.17).

Overall, the simulations agree very well with the observational trends and luminosity dependent deviations from the fundamental plane (observational data taken from Burstein *et al.* 1997). Even the compact non-rotating models fall within the observational spread of the relation.

## 3.4   Results / Discussion

### 3.4.1   Evaluation of analysis

From the previous paragraph, it is clear that rotation has a more pronounced influence on the observational properties of the simulated dwarf galaxies, quantified by photometric and kinematical scaling relations, than the flattening of the initial conditions. The differences *between* the sequences of rotating and non-rotating models are significantly larger than those between flattened and non-flattened galaxies *within* each sequence. Still, all models fall within the range allowed by the data, apart from the problems we noted with metallicities being to high. Moreover, despite their simplicity, this suite of simulations suggests a possible explanation for the widths of the observed scaling relations. While mass is the dominant parameter that determines the shape and slope of each scaling relation, angular momentum could be an important second parameter that determines the width of the relations. This will however not be the only factor, since external influences such as environment and merger history are likely to also have a significant influence here. And we should also note the inherent variance that is present in our models, as discussed in section 3.2.3.1 and shown in Fig. 3.1.

While the effects of flattening and rotation on the observed scaling relations are modest, the addition of rotation has a strong effect on the details of the evolution of dwarf galaxies. This is most clearly seen in the properties of the stellar populations, e.g. in the metallicity profiles (Figs. 3.7 and 3.8), SFHs (Figs. 3.9 and 3.10), and overall appearances (Fig. 3.11). In this respect, rotating models are qualitatively quite distinct from non-rotating ones, independent of initial flattening: rotating models have continuous SFHs with widespread SF while non-rotating models have "breathing" SFHs with centrally concentrated SF. Observationally, this leads to rotating models having flat metallicity profiles while non-rotating models show pronounced negative metallicity gradients.
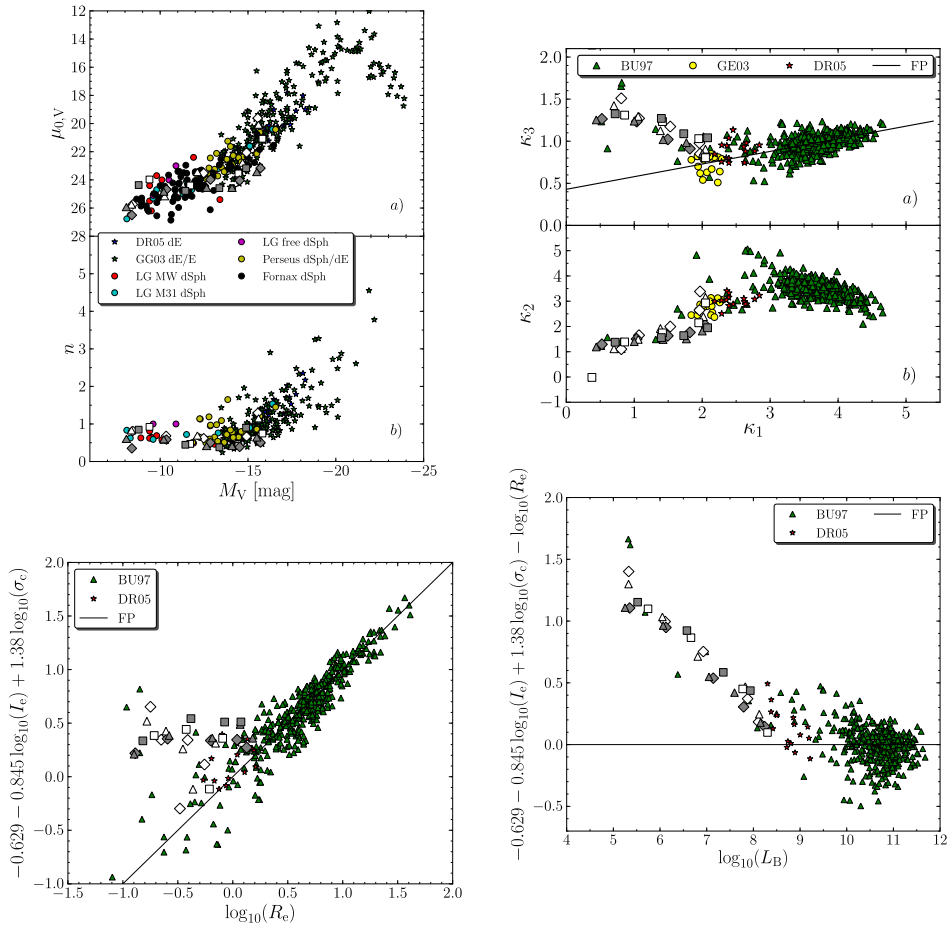
**Figure 3.16:** [top left] Sérsic parameters versus V-magnitude. *Upper panel*: central surface brightness $\mu_0$ in the V-band, *lower panel*: Sérsic index $n$. Observational data as in Fig. 3.12.

**Figure 3.17:** [top right] The fundamental plane in $\kappa$-space. *Upper panel*: side view of fundamental plane ($\kappa_3$, $\kappa_1$), *lower panel*: face-on view ($\kappa_2$, $\kappa_1$). Observational data from Geha *et al.* 2003 (GE03), other symbols as in Fig. 3.18.

**Figure 3.18:** [bottom left] Side-view of the fundamental plane in physical coordinates. White symbols are our non-rotating galaxies; the grey ones are the fastest rotating galaxies, shapes denote initial flattening as in Fig. 3.12. All other points on the plot are observational data, taken from Burstein *et al.* 1997 (BU97) and de Rijcke *et al.* 2005 (DR05).

**Figure 3.19:** [bottom right] Deviation from the fundamental plane. Symbols as in Fig. 3.18.

### 3.4.2   Mechanism

Within the sequence of non-rotating models, flatttening of the initial conditions appears to have very little effect on the models' properties, which is of importance especially when considering the metallicity profiles. It therefore seems doubtful that the fountain mechanism is very important for dwarfs. Still, if there are large feedback driven outbursts of gas, they tend to be aligned preferentially along the minor axis. But the expelled enriched gas does not fall back onto the galaxy. This is most likely because of the shallow potential wells of dwarf galaxies, and because the remaining cold gas is simply "in the way". Another important argument against the fountain mechanism is the actual flattening of dwarf galaxies, both in observations and in our simulations, as we discussed in section 3.2.3.3. Dwarf galaxies simply are not likely to occur with very flat shapes (Sánchez-Janssen *et al.*, 2010). Their flattenings are not comparable to those of massive spiral galaxies ($q \approx 0.2$), they are on average much thicker ($\langle q \rangle \approx 0.6$). This often makes it difficult to even speak of a "disk" in the context of dwarf galaxies. Therefore, while the fountain mechanism might be very relevant in the domain of large spiral galaxies, with much deeper potential wells and much flatter shapes, it does not appear an important mechanism in dwarf galaxies.

Rotation, on the other hand, leads to important qualitative and quantitative changes in the SFHs of dwarfs. The consequences of the addition of angular momentum are the following:

1. Gas will spiral inward, instead of falling straight to the center. There is a "*centrifugal barrier*" preventing the gas from collapsing to a dense central region.

2. Since the gas density is much more smeared out, so is the star formation. The density criterion (see section 2.2.2) for star formation is now reached in a much larger region of the gas, so that star formation will occur throughout practically the entire body of the galaxy. This is evident in Figs. 3.11 and 3.20: star formation is consistently more spatially extended in comparison with non-rotating models.

3. This naturally produces more spatially homogeneous stellar populations. Therefore the gas is enriched much more homogeneously across the entire galaxy, explaining the flat metallicity profiles in Fig. 3.7.

4. Where there is star formation, unavoidingly there will also be stellar feedback. Since the former is smeared out across almost the entire galaxy, so is the latter. The supernova feedback now being less centrally concentrated, this leads to much less pronounced large-scale collective behaviour of the gas. The effects of feedback are now more *local*. This has two distinct but related effects:

   - The supernovae combine their energy locally on a smaller scale, and produce *low-density holes* in the gas, instead of collectively blowing out the gas and lowering the global gas density after a large centralized star formation event. This hole or bubble structure is clearly visible in Fig. 3.11 and is discussed in section 3.3.3.
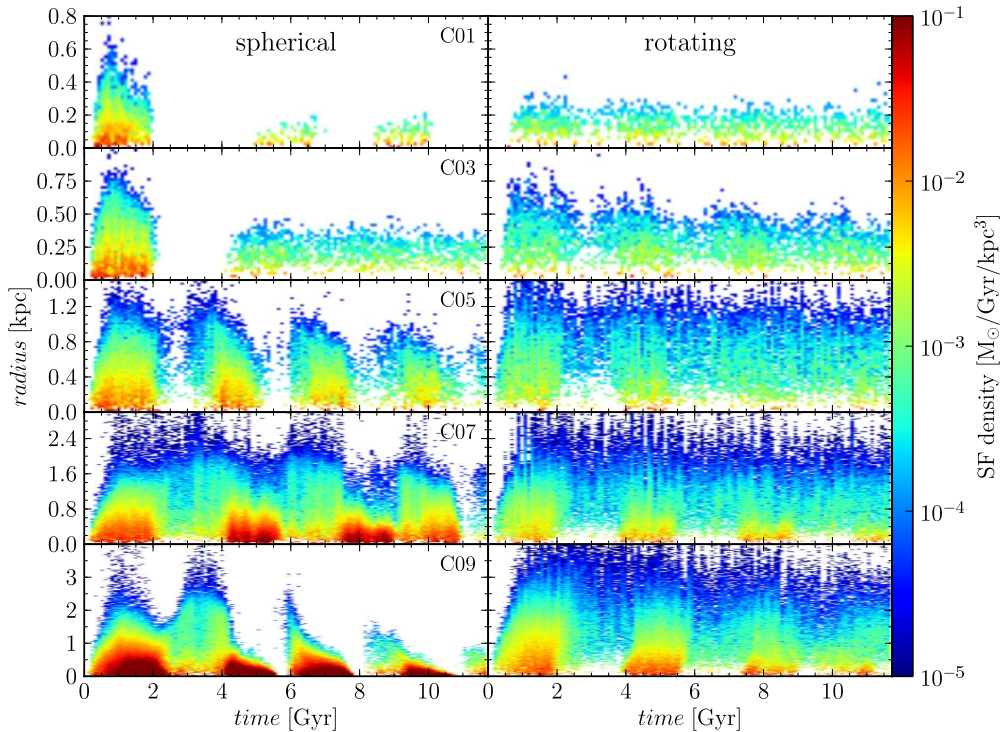
**Figure 3.20:** Star formation density in $M_\odot/Gyr/kpc^3$ for spherical, non-rotating (*left column*) and rotating models (*right column*), binned in time (*x*-axis) and radius from the center (*y*-axis). The total mass of the models increases from the top down as indicated in the figure. SF density is plotted in color-code according to the color bar on the right.

- This can also be linked to our findings concerning the SFHs in section 3.3.2 and Fig. 3.9. Since the gas does not collectively blow out due to feedback, star formation will not shut down completely across the entire galaxy, because only locally the density criterion for star formation is not satisfied (in the feedback holes, Fig. 3.11). This is also seen in Fig. 3.20. Collective behaviour - i.e. large-scale oscillations in the SFR - is diminished, leading to more continuous, less variable SFH. The "breathing" SF, typical of non-rotating models, is largely absent.

The density criterion mentioned in section 2.2.2 and here in point (2) is an important element of our models. We should note that we employ a treshold of 0.1 cm$^{-3}$, while Governato *et al.* (2010) suggest the usage of a treshold of 100 cm$^{-3}$, reflecting more realistically the conditions of real star-forming gas clumps. We do not expect this to qualitatively change the proposed mechanism however: the higher treshold will take the gas longer to reach it when collapsing, but the extension of the cooling curves below $10^4$K (Maio *et al.*, 2007) will cause the gas to collapse easier and on smaller scales. These effects

might not cancel each other out, but the relative influence of added rotation, as discussed above, will remain qualitatively similar. Perhaps on small scales the chemical homogeneity will be less, but on large scales rotating galaxies will still be chemically homogeneous. The inclusion of the high-density treshold and the extra cooling are the subject of our further research (Chapter 4).

### 3.4.3   Galaxy types

As already mentioned in paragraph 3.3.4, our dwarf galaxy models agree quite well with the observed the scaling relations of early-type galaxies. However, since the model galaxies still contain gas and have ongoing star formation at the end of the simulation, they should be classified as late-type dwarfs.

#### 3.4.3.1   dIrrs?

The non-rotating and slowly rotating models, both flattened and non-flattened, are characterized by

- centrally concentrated gas distribution; high central density

- low specific angular momentum

- strong stellar population gradients

- bursty or episodic SF

- centrally concentrated SF

- large-scale feedback driven outflows and a largely featureless ISM.

The fast rotating models, both flattened and non-flattened, are characterized by

- spatially extended gas distribution; low central density

- high specific angular momentum

- small stellar population gradients, if any

- continuous SF

- small star forming regions, scattered across the galaxy

- turbulent ISM with distinct feedback driven holes.

dIrrs are known to have a more extensive and less centrally concentrated gas distribution that other gas-rich dwarf galaxy types (e.g BCDs), and also a relatively high specific angular momentum. Chemical homogeneity is a general trait of dIrrs, both in their gas and their stellar content (Tolstoy *et al.*, 2009; Kobulnicky & Skillman, 1997). From the review of dwarf galaxy properties in Tolstoy *et al.* (2009) and the extensive work of Dolphin *et al.* (2005), using CMD analysis to reconstruct dwarf galaxy SFHs (Aparicio *et al.* 1996;

Dolphin 1997, 2002; Tolstoy & Saha 1996; Tosi *et al.* 1991), it is clear that dIrrs generally have a "continuous" SFH without quiescent periods without SF. The characteristic gas structures of dIrrs have already been discussed in section 3.3.3.

From this short overview of the observed properties of late-type dwarfs, it is clear that our fast rotating models resemble dIrrs, at least qualitatively. But our non-rotating and slowly rotating models do not, although they do also still contain gas and show ongoing (periodic) star formation. Angular momentum, it seems, invokes different star formation modes in dwarf galaxies. It differentiates between centralized/bursty and extended/continuous star formation, and all dwarf galaxy properties connected with this which are mentioned above. Although quantitatively not comparable to our models, it is worth mentioning BCDs and their differences with dIrrs. They too are gas-rich late-type dwarf galaxies, but have a lower specific angular momentum and much more concentrated gas distribution (van Zee *et al.*, 2001; van Zee, 2002). BCDs also show substantial color gradients (van Zee, 2002), indicating chemical inhomogeneity, and by definition have bursting SFHs.

### 3.4.3.2   Conversion of late-type dwarfs to early types

Since internal processes such as supernova feedback are not capable of removing the gas from a dwarf galaxy, we turn to external or environmental processes, e.g. tidal stripping and ram pressure stripping (Mayer *et al.*, 2006). Ram-pressure stripping is able to remove a large fraction of the gas and leaves the structure and kinematics of the stars relatively undisturbed, thus preserving any pre-existing stellar population gradients and rotation (Grebel *et al.*, 2003; Marcolini *et al.*, 2003). Tidal interactions can cause violent reactions in dynamically cold thin-disk dwarf galaxies and can significantly disturb them (Mayer *et al.*, 2001a,b). However, the majority of the dwarf late-type population is quite round, with mean axis ratio $\langle q \rangle \approx 0.6$. In such galaxies, tidal interactions wreak much less havoc (Valcke, 2010).

We therefore argue that it is possible to convert late-type dwarfs into early-type ones inside a cluster environment by removing their gas and halting SF without significantly altering their structural and kinematical properties. So the rotation which is present in dIrrs can be preserved in their dE descendants along with the stellar characteristics connected with rotation (metallicity profiles).

## 3.5   Conclusion

The centrifugal barrier mechanism formulated in section 3.4, is able to combine all our findings we discussed in the analysis into one coherent picture, emphasizing the importance of rotation in dwarf galaxy behaviour.

### 3.5.1   Metallicity profiles

Our interest in this subject was triggered initially by the finds of Koleva *et al.* (2009), who found that dwarf early-type galaxies without stellar population gradients were also

the fastest rotating ones. We conclude from our simulations that (in isolation) rotation, or the absence thereof, is indeed a key factor in creating stellar population gradients. The "fountain mechanism" does not seem relevant on the scale of dwarf galaxies, and our simulations clearly indicate that the *geometry* or *flattening* of a dwarf galaxy does not have any significant influence: pressure-supported, non-rotating systems behave very much alike, independent of flattening.

We therefore propose the alternative "centrifugal barrier mechanism" in section 3.4.2, which explains the existence of flat metallicity profiles as a natural consequence of its rotation.

### 3.5.2   Angular momentum as second parameter

We suggest angular momentum as being a crucial *second parameter* in determining the appearance and evolution of dwarf galaxies, with the total galaxy mass being the prominent first parameter. While our simulations are admittedly very idealized and cannot purport to paint a cosmologically up-to-date picture of dwarf galaxy formation, they have the enormous benefit of allowing us to unambiguously identify the influence of individual parameters, such as angular momentum.

We have shown that rotation has a significant impact on the stellar populations of dwarf galaxies. And in the same vein we can say the opposite for dwarf galaxy flattening, which shows no significant influence in our simulations, and thus is less likely to be a major player in dwarf galaxy evolution.

### 3.5.3   Making dIrrs

We find that without rotation, it does not seem possible to qualitatively produce the type of behaviour of "typical" dIrrs with spatially extended SF, continuous SFHs, a turbulent ISM with low-density holes, and most importantly with chemical homogeneity throughout its body of gas and stars. Non-rotating models do not display any of these characteristics (having centralized SF, bursty SFHs, featureless ISMs and metallicity gradients). Angular momentum appears to differentiate between bursty and continuous star formation modes.

# 4

# Stellar orbits and survival of metallicity gradients

**J. Schroyen, S. De Rijcke, M. Koleva, A. Cloet-Osselaer,**
**B. Vandenbroucke :**

In this chapter we focus on the *metallicity profiles* themselves in rotating and non-rotating spherical models, but mostly on the metallicity *gradients* in non-rotating ones: how they are formed and whether they are significant, their evolution and stability, and how they compare qualitatively and quantitatively with observed metallicity gradients of dwarf spheroidals in the Local Group. To have a good quantitative grip on the stability of the formed metallicity gradients, we also look further to the underlying stellar orbits. We quantify their statistical changes over time, and assess which orbit-changing processes could play a role here and why.

In this second part of our research, we made use of both the "old" (as in the previous part of our research in Chapter 3) and the "new and improved" configuration of our dwarf galaxy models described in Chapter 2, which now employs our so-called HDT-scheme for the astrophysical implementations:

- NFW cusped dark matter halo,

- pseudo-isothermal gas sphere,

- the "intermediate" form of the novel cooling curves (with 3 parameters) that extend below $10^4$ K, no heating,

- high star formation density threshold of $100\,\mathrm{cm}^{-3}$,

- high feedback efficiency factor of 0.7,

- arctangens-shaped initial rotation curves

- strictly spherical setups, no initial flattenings.

## 4.1   Introduction

Comparing observations to simulations is a powerful approach to studying the physical processes involved in the formation and evolution of galaxies. Dwarf galaxies, in particular, are ideal probes for this. Their low masses and small sizes allow hydrodynamical simulations to reach high spatial resolutions. For the same reasons, they are also very sensitive to the effects of star formation (e.g. supernova explosions), contrary to massive galaxies. And at least the dwarfs within the Local Group can be studied in great depth, thus providing sufficiently detailed data to compare the high resolution simulations to. The results derived from studying dwarf galaxies are of direct relevance to galaxy evolution in general.

Stellar population gradients, i.e. the radial variation of metallicity and age projected along the line of sight, offer direct insights into the past star-formation and metal enrichment histories of galaxies. Observationally, there is an ever growing collection of dwarf galaxies with gradients, found both in the Local Group (Alard 2001; Harbeck *et al.* 2001; Tolstoy *et al.* 2004; Battaglia *et al.* 2006, 2011, 2012; Bernard *et al.* 2008; Kirby *et al.* 2011, 2012; Monelli *et al.* 2012) and in nearby galaxy clusters and groups (Koleva *et al.* 2009, 2011; Chilingarian 2009; Crnojević *et al.* 2010; Lianou *et al.* 2010; den Brok *et al.* 2011). These encompass objects of different masses and star formation modes (spheroidals, ellipticals, star-forming, quiescent, transitional type, ...), in different environments (from isolated to densely populated), with different gradient formation histories (slowly built-up gradients, Battaglia *et al.* 2006, 2012; or already present in the oldest populations, Tolstoy *et al.* 2004; Bernard *et al.* 2008; Koleva *et al.* 2009), which are investigated with different techniques. Likewise, on the theoretical/numerical side, there is a physical foundation for the existence of metallicity gradients in both massive galaxies (Bekki & Shioya, 1999; Hopkins *et al.*, 2009; Pipino *et al.*, 2010, and references therein) and for dwarf galaxies (Valcke *et al.*, 2008; Stinson *et al.*, 2009; Schroyen *et al.*, 2011; Lokas *et al.*, 2012), but see Revaz & Jablonka (2012).

This prompts the question of how and when these gradients are formed and how, once formed, they can be maintained. These are the topics we want to investigate in the current chapter. More specifically, we want to address whether radial displacements of stars through orbit-changing processes (such as dynamical heating by scattering of stars

or radial stellar migration through interactions with spiral-like structures) play a role in potentially erasing or weakening any pre-existing population gradients in dwarf galaxies. This part of the research is structured as follows. We present the simulations in Section 4.2. General influences of the model parameters are summarized in Section 4.3 before going on to the more specific results. In Section 4.4 we analyse the evolution of the metallicity profiles in our model dwarf galaxies, and compare them to observed metallicity gradients in the Local Group. Section 4.5 looks into the underlying orbits and kinematics in the stellar body of our simulated dwarf galaxies, and tries to connect these to the findings on metallicity gradients. We summarize and conclude in Section 4.6.

## 4.2 Simulations

Here we describe the details of the simulation runs that have been performed and used for this research. The methods and theory behind the models are discussed in Chapter 2, and have been previously presented in Valcke *et al.* (2008), Schroyen *et al.* (2011) and Cloet-Osselaer *et al.* (2012).

We investigate two types of models in this chapter. On the one hand, we run simulations according to the prescriptions from our previous research (Schroyen *et al.*, 2011, Chapter 3) which employ the, until recently quite standard, low density threshold for star formation and corresponding low feedback efficiency. On the other hand, we also run simulations which feature the specifications discussed in Chapter 2 as the "HDT-scheme", with a high density threshold and a high feedback efficiency. Henceforth, we will refer to them as the low density threshold (LDT) and high density threshold (HDT) models/simulations/runs, respectively.

Several properties of the simulations, however, are shared among the LDT and HDT runs:

- all simulations start with an initial set of 200,000 gas particles and 200,000 dark matter particles.

- initial metallicity is set to $10^{-4}$ solar metallicities.

- initial gas temperature is $10^4$ K.

- runtime is approximately 12 Gyr, starts at redshift 4.3.

- snapshots are made every 5 Myr, resolving the dynamical timescale.

- the models are isolated.

- the gravitational softening length is 30 pc.

### 4.2.1 Low density threshold (LDT) runs

Here, we investigate simulations with initial dark-matter masses of $660 \times 10^6$ M$_\odot$ (these runs have labels that end with "05") and $2476 \times 10^6$ M$_\odot$ (these runs have labels that end with "09"). The density threshold is set to 0.1 cm$^{-3}$, with a feedback efficiency of 0.1 (i.e.

10 % of the supernova energy is absorbed by the interstellar medium), and cooling curves that do not go below $10^4$ K. Simulations with and without rotation have been performed. Rotation was induced by adding a constant rotational velocity of $v_{\text{rot}} = 5$ km s$^{-1}$ to the gas particles. These simulations are basically high time resolution reruns of some of our older models from Chapter 3 and will serve as a "reference sample" to compare with the new models. The details of these 4 simulations can be found in Table 4.1.

### 4.2.2   High density threshold (HDT) runs

Simulations have also been performed that employ the HDT-scheme models as described in Chapter 2. Again we use a lower mass and a higher mass model, with the same initial masses as the LDT runs in 4.2.2, again one rotating and one non-rotating. The density threshold for star formation is now set to 100 cm$^{-3}$ and employs the first stage novel cooling curves as described in Section 2.2.1, which span a temperature range from 10 K to $10^9$ K (and are extended to $10^{10}$ K with a Bremsstrahlung approximation). The feedback efficiency has been increased to 0.7, following the results of Cloet-Osselaer *et al.* (2012) (see Section 2.2.2). On top of the NFW dark matter halo is placed a pseudo-isothermal gas sphere, which in the rotating models is given an arctangens radial rotation profile, as in 2.1.4, with a $v_{\text{rot}}$ of 5km/s and $r_s = 1$ kpc. Further details are found in Table 4.2.

### 4.2.3   Truncated simulations

For each of the abovementioned non-rotating simulations we also run a "truncated" version, where the star formation is shut off at a specific time during the evolution. This allows us to assess most clearly whether any population gradients present at the moment

**Table 4.1:** Details of the LDT runs, re-run from Schroyen *et al.* (2011) (Chapter 3, corresponding simulation number in this previous work shown in brackets, further details on the models can also be found there). All quantities are evaluated at the end of the simulation, except for the initial values indicated with index 'i'. Rows: (1) initial gas mass [$10^6$M$_\odot$], (2) dark matter mass [$10^6$M$_\odot$], (3) stellar mass [$10^6$M$_\odot$], (4) half-light radius [kpc], (5) luminosity-weighted metallicity (B-band), (6)(7) B-band and V-band magnitude, (8) initial rotation speed of gas [km/s].

|            | LDT05 (205) | LDT09 (209) | LDTrot05 (225) | LDTrot09 (229) |
|------------|-------------|-------------|----------------|----------------|
| $M_{g,i}$  | 140         | 524         | 140            | 524            |
| $M_{dm}$   | 660         | 2476        | 660            | 2476           |
| $M_{st}$   | 18.93       | 468.57      | 14.35          | 325.33         |
| $R_e$      | 0.43        | 0.39        | 0.63           | 1.36           |
| $[Fe/H]$   | -0.717      | -0.053      | -0.672         | -0.281         |
| $M_B$      | -11.87      | -14.87      | -12.2          | -15.02         |
| $M_V$      | -12.51      | -15.62      | -12.7          | -15.62         |
| $v_i$      | 0           |             | 5              |                |

**Table 4.2:** Details of the new HDT runs. All values in the first block refer to the initial conditions, the other values (besides those indexed with 'i') are final values. Rows: (1) initial gas mass $[10^6 M_\odot]$, (2)(3)(4) characteristics of pseudo-isothermal sphere: density $[10^7 M_\odot/kpc^3]$ - scale radius [kpc] - cutoff radius [kpc], (5) dark matter mass $[10^6 M_\odot]$, (6)(7)(8) characteristics of NFW halo: density $[10^7 M_\odot/kpc^3]$ - scale radius [kpc] - cutoff radius [kpc], (9) stellar mass $[10^6 M_\odot]$, (10) half-light radius [kpc], (11) luminosity-weighted metallicity (B-band), (12)(13) B-band and V-band magnitude, (14) initial rotation speed of gas [km/s].

|  | HDT05 | HDT09 | HDTrot05 | HDTrot09 |
|---|---|---|---|---|
| $M_{g,i}$ | 140 | 524 | 140 | 524 |
| $\rho_{pseudo-iso}$ | 1.102 | 0.896 | 1.102 | 0.896 |
| $r_{pseudo-iso}$ | 0.234 | 0.403 | 0.234 | 0.403 |
| $r_{g,max}$ | 18.894 | 29.353 | 18.894 | 29.353 |
| $M_{dm}$ | 660 | 2476 | 660 | 2476 |
| $\rho_{nfw}$ | 5.211 | 4.236 | 5.211 | 4.236 |
| $r_{nfw}$ | 0.744 | 1.251 | 0.744 | 1.251 |
| $r_{dm,max}$ | 21.742 | 33.634 | 21.742 | 33.634 |
| $M_{st}$ | 2.37 | 32.19 | 1.58 | 52.813 |
| $R_e$ | 0.23 | 0.58 | 0.22 | 1.06 |
| $[Fe/H]$ | -0.98 | -0.834 | -0.922 | -0.736 |
| $M_B$ | -9.69 | -12.79 | -9.69 | -13.44 |
| $M_V$ | -10.3 | -13.34 | -10.24 | -13.98 |
| $v_i$ | 0 | | 5 | |

of truncation can persist for an extended period.

The truncation can be done in two ways:

1. The star formation routines are shut off at a certain time, which for the HDT simulations also requires shutting off cooling below $10^4$ K because otherwise the gas quickly becomes extremely dense, causing the code to crash. The gas remains present, but becomes inert, the "gastrophysics" are switched off.

2. All gas particles are removed from the simulation, without changing the physics. This is basically a poor man's version of ram-pressure-stripping, mimicking a dwarf galaxy that is stripped of its gas on short timescales by the intergalactic medium.

We opted for the second option, since it stops star formation in a more "natural" way, without tinkering with the physics and switching certain processes off. In practice we take a certain snapshot of the existing simulations, remove the gas particles from it, and use it as the initial condition for a simulation that restarts at the moment of truncation. We have chosen the simulations to be truncated at 8 Gyr, allowing us to study the stability of any existing population gradients over periods of time of the order of 4 billion years.

## 4.3   LDT vs. HDT

Several differences in the physical features of the LDT and HDT simulations are worth highlighting here, before going on to the specific research results in the next sections.

The principal feature of the HDT models is obviously the formation of dense and cold clumps in the gas in which star particles form (Governato *et al.*, 2010). In Fig. 4.1, the difference in gas structure between the LDT and the HDT simulation is apparent. Whereas in the LDT case the gas is quite "fuzzy", and collectively above the density threshold in a large area, in the HDT case it is much more structured and fragmented in dense clumps, with only localized individual density peaks reaching above the density threshold. A full animation of Fig. 4.1 can be found online[1]

This distinction has immediate consequences for the star formation mode, as can be seen in Fig. 4.2. The non-rotating LDT models show clear star formation episodes of about 2 Gyr long with intermittent lulls of a Gyr or so, with an inwards shrinking of the SF area between episodes and within each episode. The HDT models show much shorter star formation bursts in faster sequence with no shrinking within an episode, but still with a shrinking of the SF area over time between episodes. We can see this change in star formation timescale clearly in the Fourier transform of the star formation rate over time in Fig. 4.3. The LDT model shows a peak at a period of 3 Gyr, which agrees well with the very noticeable 4 star formation episodes in 12 Gyr seen in Fig. 4.2, while the HDT model shows a clear shift to shorter periods, with 2 peak values at periods of 0.2 and 0.5 Gyr. These match, respectively, with the sequence of star formation events seen in Fig. 4.2 in the first 2-3 Gyr and the last 6-7 Gyr. The apparent delay of SF in HDTrot5 is due to the rotation, that makes it difficult for the gas in this relatively lightweight model to attain the density threshold for star formation.

In Fig. 4.4, we show the evolution of a HDT model during a single short-duration star-formation event. The event starts when several high-density peaks inside the already dense inner 1 kpc of the galaxy start forming stars. Supernova feedback quickly disrupts the individual star-forming clouds while triggering secondary star formation throughout this dense inner region of the galaxy. Subsequently accumulating feedback evacuates the dense central region about 30-40 Myr after the start of the event, limiting star formation to condensations on the edges of the expanding supernova-blown bubbles until it finally peters out after about 150 Myr. The insets present a zoom on the star-formation event in Fig. 4.2, which shows this rapidly outward evolution by a slight tilt to the right of the corresponding "plume" of the burst. This chain of events is reminiscent of the "flickering star formation" observed in real dwarf galaxies with bursty star-formation histories (McQuinn *et al.*, 2010). A full animation of the simulated star burst event depicted in Fig. 4.4 can be found online[2]. As already concluded by Schroyen *et al.* (2011) (Chapter 3), angular momentum smears out star formation in time and space, making the major star-formation events less conspicuous

---

[1]Video: `http://www.youtube.com/watch?v=lHDcFD6ok7c`; YouTube channel of Astronomy department at Ghent University: `http://www.youtube.com/user/AstroUGent`; Youtube playlist with all additional material for this paper: `http://www.youtube.com/playlist?list=PL-DZsb1G8F_lDNn3G-9ACGgrinen8aSQs`

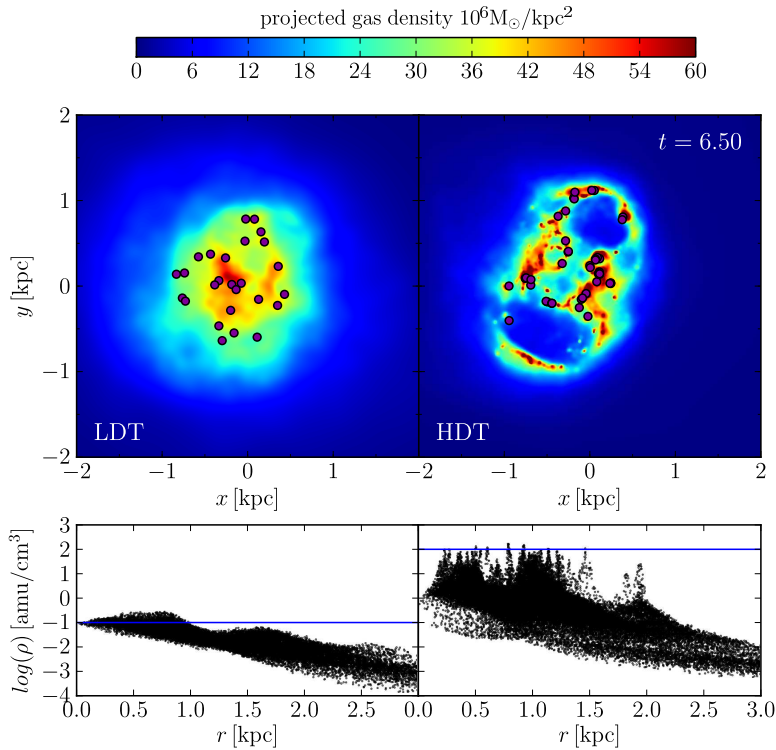[2]Video: `http://www.youtube.com/watch?v=0TB9LQaiKEs`

**Figure 4.1:** The top row shows rendered images of a LDT (left) and HDT (right) model. Superimposed on the color coded (projected) gas density as purple dots are the newly formed stars, of ages 10 Myr and below. The bottom row shows density-radius scatter plots of the gas particles, with a horizontal blue line indicating the density threshold for star formation in the respective star formation schemes. Note: the left rendered LDT image has actually been generated according to a color scale with values scaled down with a factor 1/10, since otherwise none of the gas would get out of the dark blue range. A full animation of this figure can be found online.

(Fig. 4.2).

Moreover, the HDT models produce significantly less stellar mass for the same initial gas mass. However, since all other properties also scale accordingly, the models remain in good agreement with the fundamental observational characteristics: they simply shift along the observed photometric and kinematical scaling relations (Cloet-Osselaer *et al.*, 2012).

In Fig. 4.5 the evolution is shown of the rotation curves of the stars in the rotating models. The LDT models show little or no evolution, after a quick buildup in the first star formation episode the rotation curves stay roughly the same throughout the evolution. The rotation curves of the HDT models, on the other hand, do noticeably change over time. They gradually become less steep, most likely due to the increased turbulence which is expected in these models, while the maximal rotational velocity also decreases noticeably (but not always that strongly). Notice they tend much more towards a solid body rotation profile in their inner regions than the LDT models.
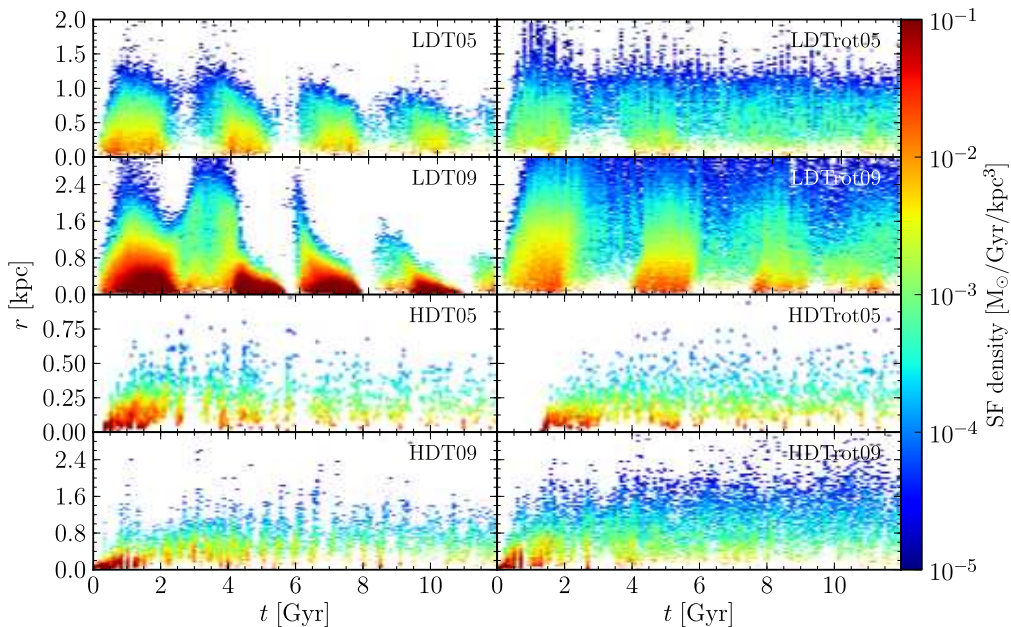
**Figure 4.2:** The star formation density (in $M_\odot/\text{Gyr}/\text{kpc}^3$, color coded according to the color scale) plotted in function of time ($x$-axis) and spatial extent (radius, $y$-axis). The non-rotating models are in the left column, the rotating ones in the right column. The four upper plots show the LDT models, the four bottom models show the HDT models.

## 4.4    Metallicity profiles

In this section we present and discuss the evolution of the radial stellar metallicity profiles throughout the simulations, and compare them qualitatively and quantitatively to observed metallicity gradients of dwarf galaxies in the Local Group. As discussed in Section 4.2 we discern between the LDT/HDT scheme, low/high total mass, and rotating/non-rotating models. Furthermore, for all of the non-rotating models we also present the results from so-called "truncated simulations", where the star formation is shut off at a specific time during the run. In all cases we consider both the luminosity-weighted and mass-weighted metallicity - the former being the quantity which mimics what is generally measured from observations, while the latter reflects the actual physical distribution of metals.

The way of constructing the profiles from the star particles in our simulations tries to mimic an observational configuration. We choose our "line of sight" along the $y$-axis and make bins along the $x$-axis, mimicking a long-slit spectroscopic observation with the slit aligned along the galaxy's major axis. In the $z$ direction we restrict the particles to the range $-0.2$ kpc $\leq z \leq 0.2$ kpc. To reduce numerical scatter and give a clearer picture, we "stack" the profiles in space and time. We use the same procedure as before, now projecting along $x$ and binning $y$, and fold all 4 profiles ($x$ and $y$ axes, both in positive
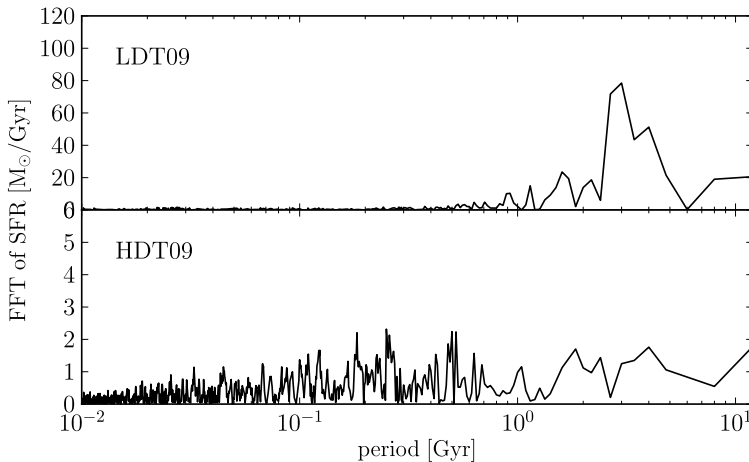
**Figure 4.3:** Fourier transform of the star formation rate in function of time, shown as a function of the period of the mode on the *x*-axis.

and negative direction) onto one profile of metallicity in function of projected distance to the center. Furthermore, we stack subsequent profiles in time, covering an interval of the order of the dynamical timescale ($\sim 50$Myr). Adaptive binning is used at the end of the procedure, to avoid erratic values at the edges of the profiles.

Luminosity weighting is done by multiplying the iron (Fe) and magnesium (Mg) masses of a stellar particle with its B-band luminosity value, which is obtained by interpolating in age and metallicity on the MILES population synthesis data (Vazdekis *et al.*, 1996). When summing over the particles in a bin, the total metal masses of the bin are then divided by the total B-band luminosity of the bin.

### 4.4.1   LDT simulations

Figures 4.6 and 4.7 show the evolution of, respectively, the luminosity-weighted and mass-weighted metallicity profiles in the LDT simulations (Table 4.1).

In the non-rotating cases on the one hand, on the top row of the figures, negative metallicity gradients can be seen to gradually build up inside a radius of $\sim 2$ half-light radii during the model's evolution. This is due to the centrally concentrated, episodic star formation, which is confined to progressively smaller areas over time (see Section 4.3 and Schroyen *et al.* 2011), adding to the overall gradient. The more massive model on the top right plot, however, shows a temporary positive metallicity gradient in its outskirts between 3 and 4 Gyr, which is caused by a star formation episode that starts at larger radii and moves inward (see Fig. 4.2). A central negative gradient is quickly restored once the star formation reaches the center, and remains stable - except for aging/reddening of the stars which affects the luminosity weighted values (compare Fig. 4.6 to 4.7).

The rotating models on the other hand, on the bottom row of the figures, show metallicity profiles which are flat throughout practically the whole evolution, out to well past their
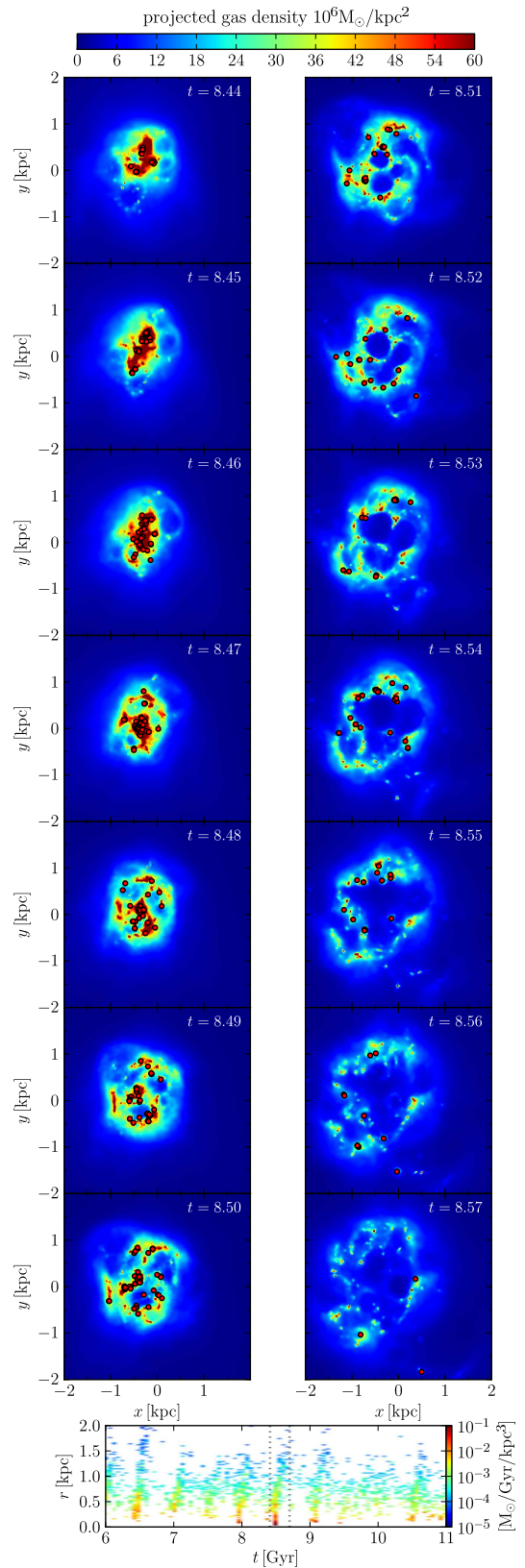
**Figure 4.4:** A high time resolution sequence of snapshots capturing a single star-formation event in a HDT model. Red dots indicate newly born star particles. Below is a zoom of the SF density (Fig. 4.2), with the dotted lines indicating the time range shown. A full animation of the simulated star burst event can be found online.
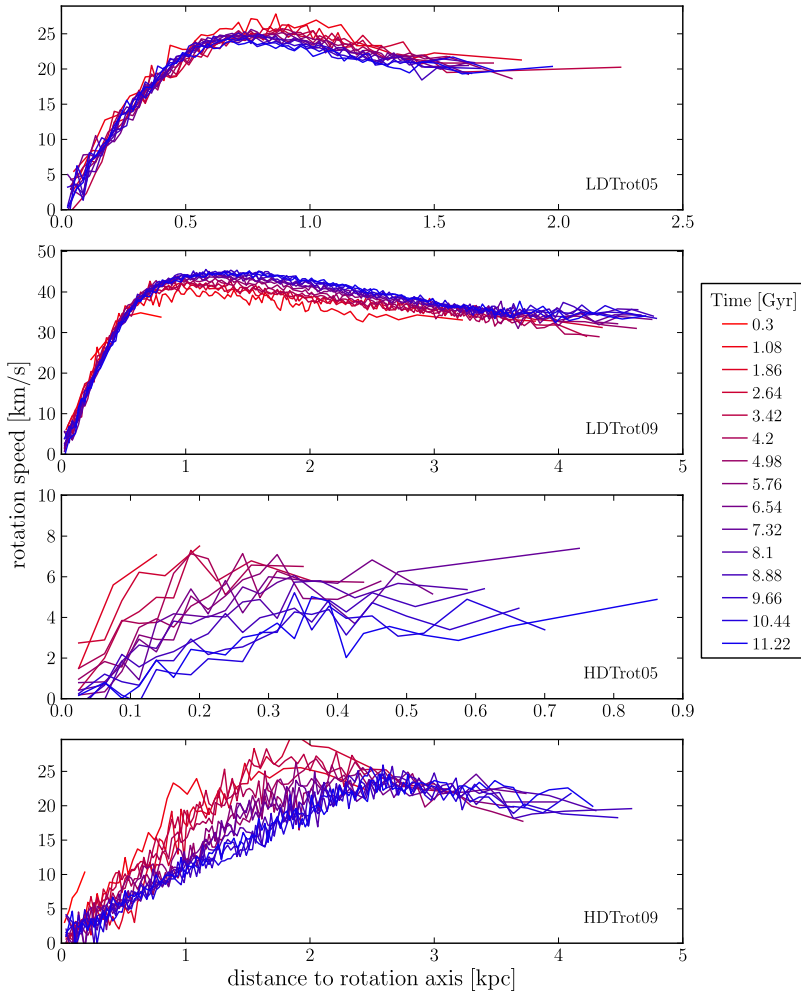
**Figure 4.5:** Evolution of the rotation curves in the rotating models, with the LDT models on top and the HDT models on the bottom. Time is indicated with color from red to blue, see legend.

half-light radius. As shown in Schroyen *et al.* (2011) (Chapter 3), the presence of angular momentum smears out SF in space and time, leading to a chemically more homogeneous galactic body.

#### 4.4.1.1   Truncated LDT simulations

We truncated the star formation around 8 Gyr into the simulation. By then, clear metallicity gradients have built up in all non-rotating simulations. Furthermore, since the model galaxies have already used up or dispersed a substantial amount of their gas when forming stars, the effect of sudden removal of all gas on their structure should be limited.

Figure 4.8 shows the evolution of the luminosity- and mass-weighted metallicity profiles in
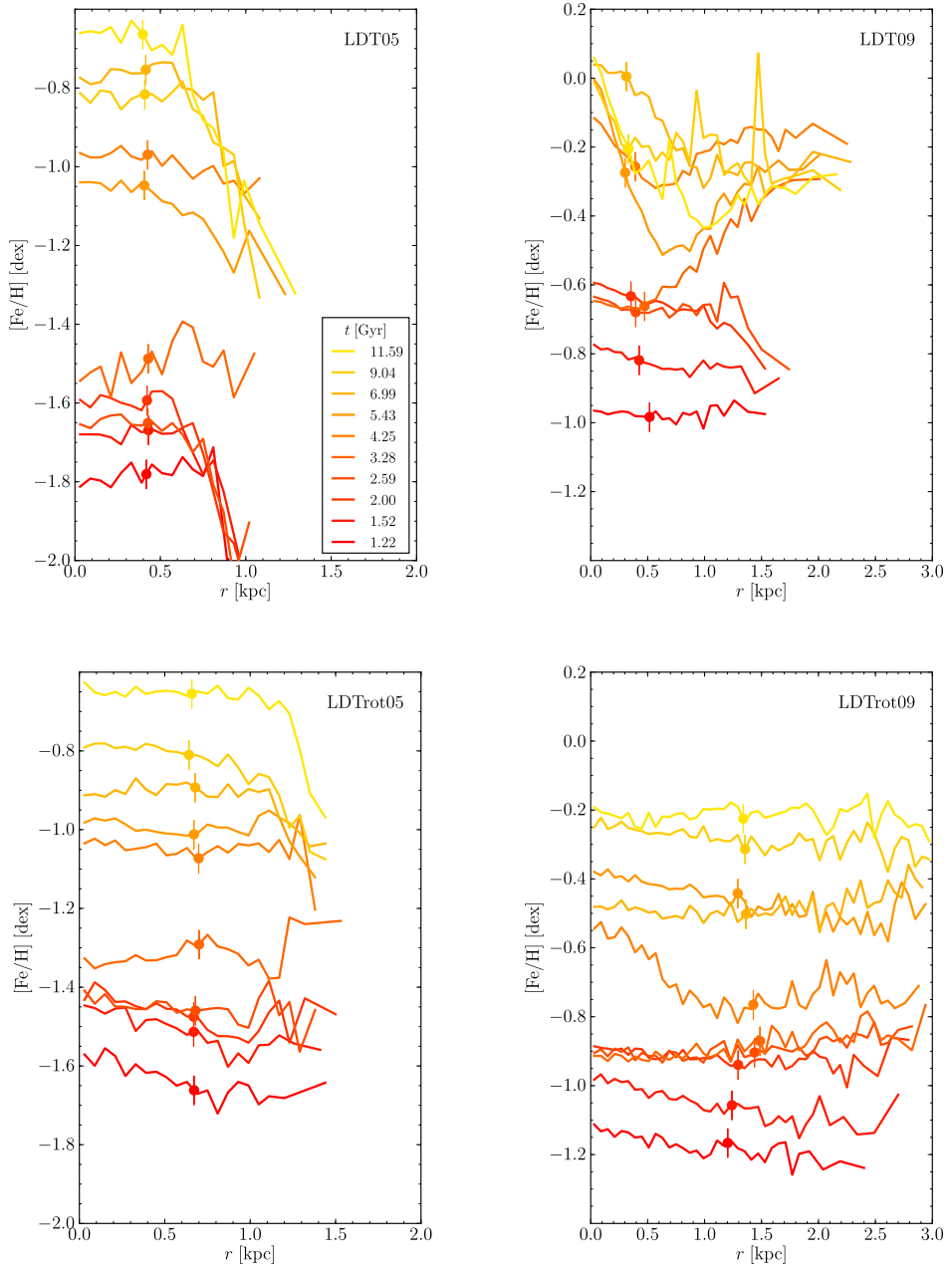
**Figure 4.6:** Luminosity-weighted (B-band) metallicity profiles of the LDT models. Evolution throughout the simulation is shown at logarithmic intervals of time, with 0.11 dex separation - the legend in the top left plot shows the times. The left column shows the low-mass (05) models, the right column shows the high-mass (09) models (see Table 4.1). Non-rotating models are on the top row, rotating models on the bottom row. The metal contribution of each star particle is weighted by its luminosity in the B-band, to mimick the actual observed quantities. The vertical line symbol on each profile indicates the half-light radius of the dwarf galaxy model at that time.

**Figure 4.7:** Mass-weighted metallicity profiles of the LDT models. Plot configuration as in Fig. 4.6. Here, the metal contribution of each star particle is weighted by its mass instead of its luminosity, and therefore the young population does not have the potential to dominate the measureme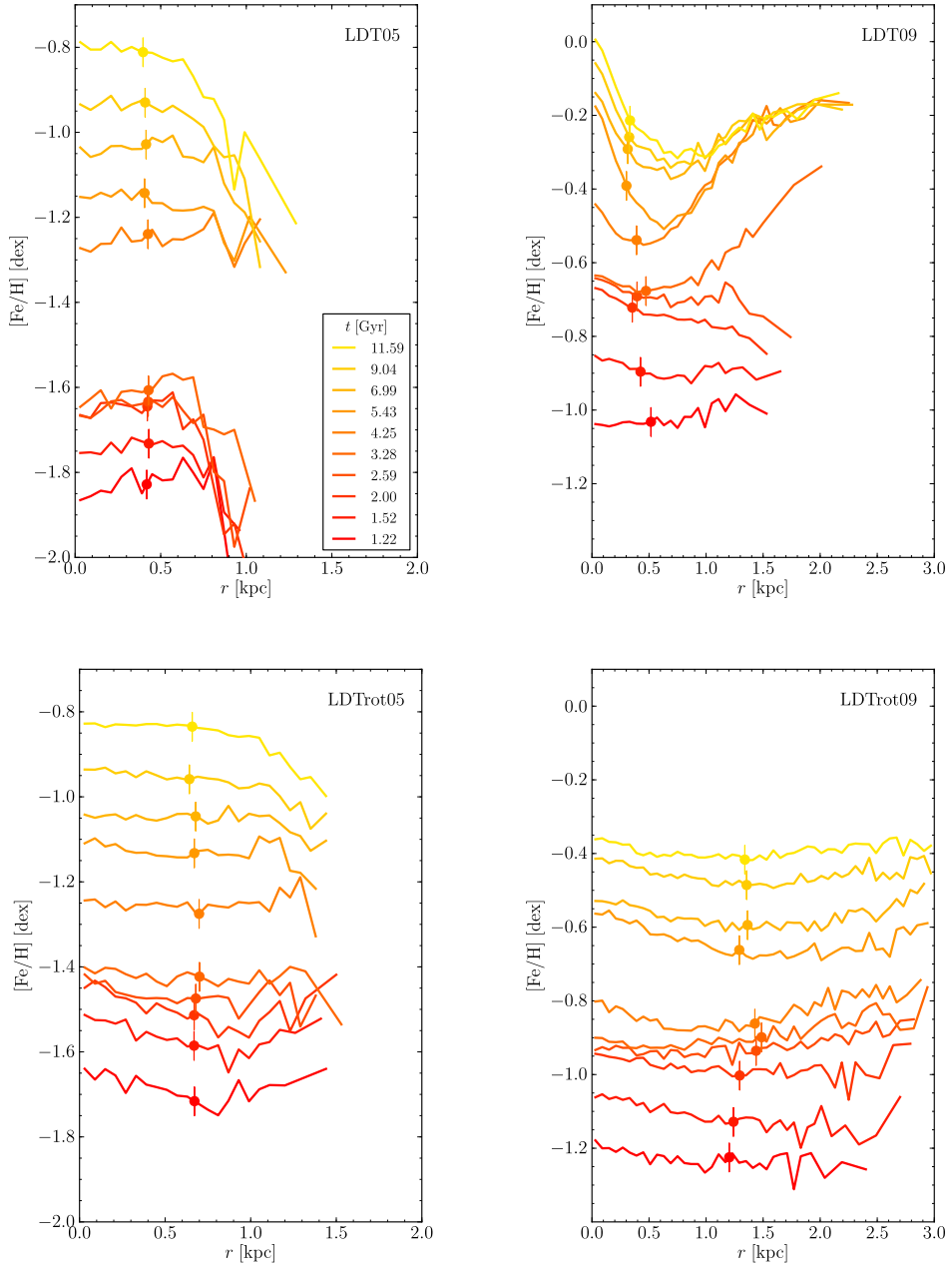nts. This quantity is not what is actually observed, but it gives a better view of the true physical distribution of metals.

the truncated LDT simulations. The luminosity-weighted gradients noticeably diminish over time - or rather, it is mostly the central metallicity that is dropping - but when looking at the mass-weighted profiles it appears that there is hardly any evolution in the physical distribution of metals. The latter can be said to get just slightly shallower over a time span of 4 Gyr, and even the gas removal seems to barely have an effect (the $R_e$ only slightly increases in the first few timesteps).

### 4.4.2   HDT simulations

Figures 4.9 and 4.10 show the evolution of, respectively, the luminosity-weighted and mass-weighted metallicity profiles in the HDT simulations (Table 4.2).

Though the SF timescale is now much shorter (Section 4.3), there still is a general shrinking of the SF area over time, and an overall centrally concentrated star formation - leading to the gradual buildup of negative metallicity gradients in the non-rotating HDT models. The high-mass model features a gradient in its stellar body throughout its entire evolution, while in the low-mass model it is in place from around 5 Gyr onwards. The apparent positive (mass-weighted) gradients during the first few Gyr of the latter, are partly caused by mass recentering difficulties on an initially low number of (stochastically generated) stellar particles, and the stochastic nature of our models in general.

The rotating models show flat(ter) metallicity profiles throughout their evolution, again explained by the spatially and temporally smeared out star formation seen in Fig. 4.2. For the low-mass model, however, the flattening is not as strong as in the LDT case, but the general difference in behaviour with the non-rotating model is still noticeable. This less pronounced effect is due to the different initial rotation curves (which go to zero in the center, Section 2.1.4, instead of being constant), and the fact that the HDT scheme produces smaller galaxies (Section 4.3), causing the models to receive less initial angular momentum overall.
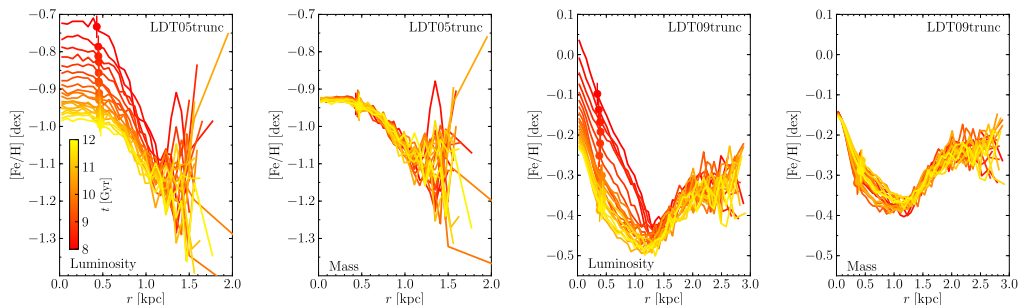


**Figure 4.8:** Metallicity profiles of the truncated LDT simulations. The respective model and weighting method is indicated on the plot. The time is color coded according to the color bar in the leftmost plot.
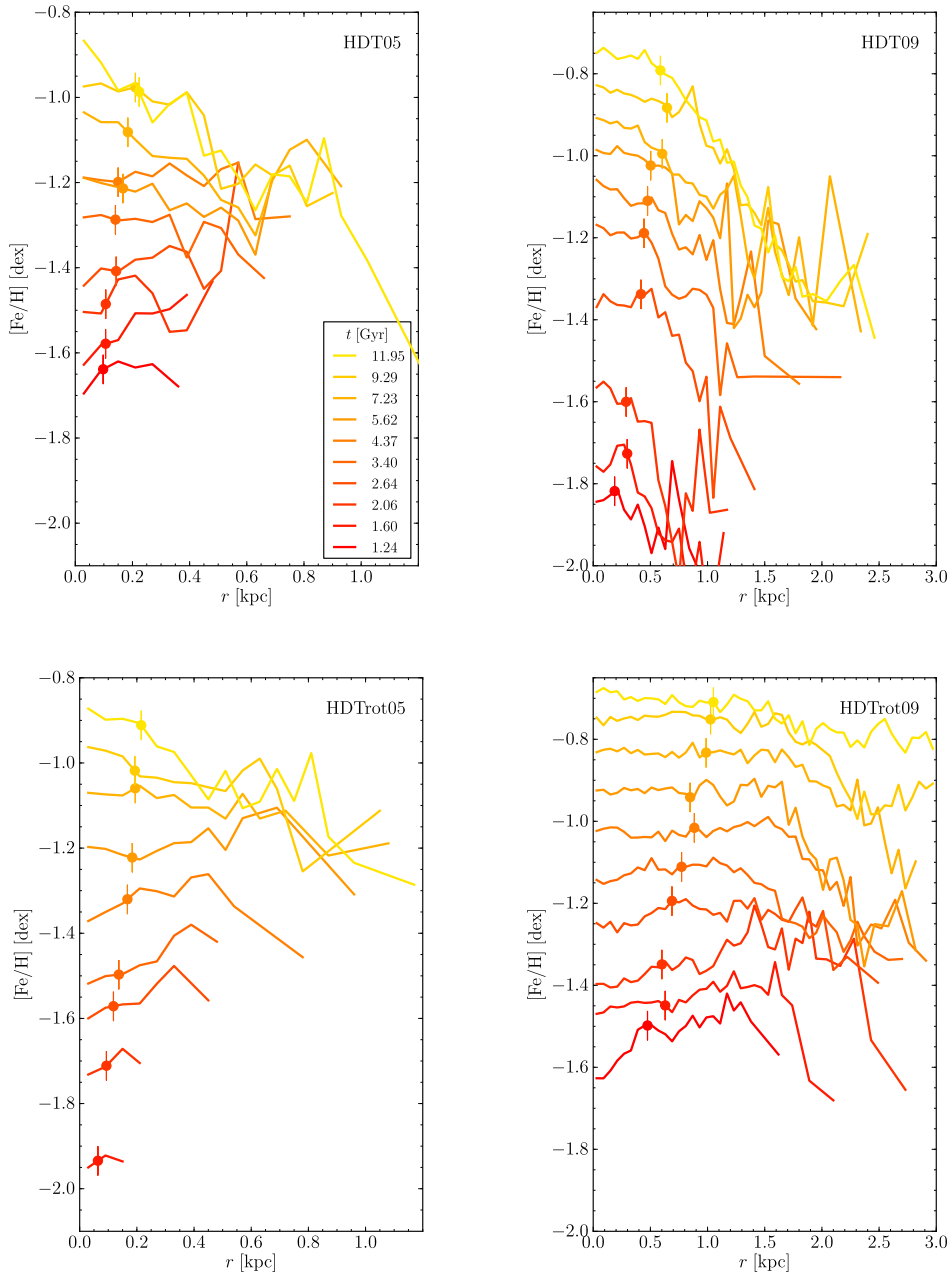
**Figure 4.9:** Luminosity-weighted (B-band) metallicity profiles of the HDT models. Plot setup similar to Fig. 4.6, the simulations can be found in Table 4.2.

#### 4.4.2.1 Truncated HDT simulations

As in the LDT simulations, the truncation time has been chosen to be around 8 Gyr. And similarly, in Fig. 4.11 the luminosity-weighted profiles can be seen to diminish noticeably
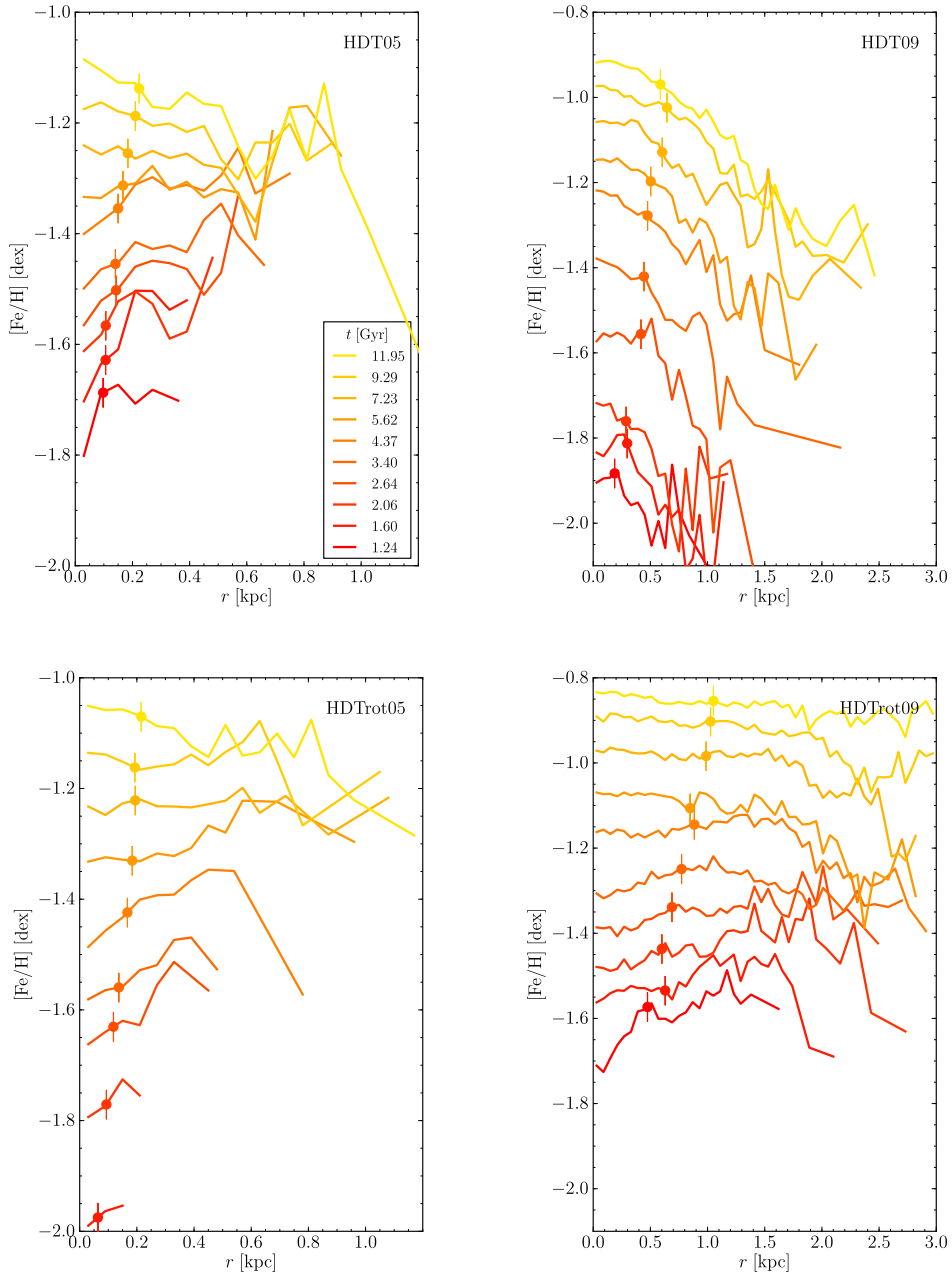
**Figure 4.10:** Mass-weighted metallicity profiles of the HDT models. Plot setup similar to Fig. 4.7.

(but survive), while the mass-weighted profiles are much more stable. It should be noted that the latter vary more significantly than in the LDT models, meaning the physical distribution of metals changes more, but in absolute terms this is still very limited. The evolution of the half-light radius in the first few timesteps also shows that the gas removal

has a bigger effect here, because of the larger amount of gas present in the central regions (due to higher densities and less gas used) which is suddenly removed.

The HDT05trunc profiles are particularly noisy, due to the relatively low number of particles that is actually used for generating the profile. The stellar mass is very low to begin with (see Table 4.2, which shows the value at 12 Gyr), and additionally, the method used to generate the profiles excludes a large part of these stellar particles (see beginning of this section).
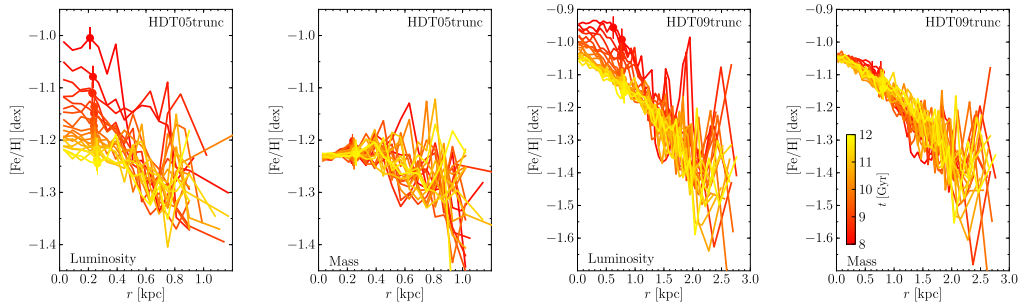


**Figure 4.11:** Metallicity profiles of the truncated HDT simulations. Similar to Fig. 4.8. Color bar is in the rightmost plot.

### 4.4.3    General conclusions on metallicity gradients

The basic findings on metallicity gradients and the mechanism behind their evolution from Schroyen *et al.* (2011) (Chapter 3) hold true in the LDT and HDT schemes.

The general conclusions about the evolution of metallicity gradients in our non-rotating dwarf galaxy models are that

- metallicity gradients are gradually built up during the evolution of the dwarf galaxy, by centrally concentrated star formation which additionally gets limited to smaller areas over time, progressively adding to the overall metallicity gradient.

- formed metallicity gradients seem to be robust, and able to survive over several Gyr, without significantly changing the physical distribution of metals.

All this strongly speaks against the possibility of erasing metallicity gradients in dwarf galaxies without an external disturbance, since even our most realistic (HDT) models do not show any significant decline in the gradients.

#### 4.4.3.1    Comparison to observed metallicity gradients

We can compare the stellar metallicity gradients in our model dwarf galaxies with observed stellar metallicity gradients from dwarf galaxies in the Local Group, with the aid of Fig. 4.12 and Table 4.3. We selected 7 dwarf galaxies from the Local Group, for which the literature provides data on their metallicity gradients that extend far enough outward (several times their half-light radius). These galaxies (and corresponding references) are:

Sculptor (Tolstoy *et al.*, 2004); Fornax (Battaglia *et al.*, 2006); Sextans (Battaglia *et al.*, 2011); LeoI, LeoII, Draco (Kirby *et al.*, 2011); VV124 (Kirby *et al.*, 2012). Structural parameters for these object were taken from the table that Łokas *et al.* (2011) compiled from the literature, which were (for the objects of interest here) mostly obtained from Mateo (1998) and Walker *et al.* (2010).

Figure 4.12 shows the metallicity gradients from the observed dwarf galaxies, where the radial distance is expressed in, respectively, kiloparsec and $R_e$. A line is fit to the data points within $3\,R_e$, the slope of which is in brackets in the legend of the figure and in Table 4.3. This collection of objects displays a wide variety in absolute metallicities, slopes, and profile shapes, as do the models:

- Steep, sharply peaked metallicity profiles with a possible increase or "bump" at larger radii (VV124, Sculptor), which is comparable to the metallicity profile of the LDT09 model (Fig. 4.6, top right, yellow curve). As in the simulations, this bump could indicate a significant star formation episode in the past that mainly took place in the outer regions of the dwarf galaxy, and temporarily enriched these regions more than the inner regions. The central metallicity peak is likely connected to these dwarf galaxies/models being more centrally concentrated.

- Metallicity profiles that show much less or almost no gradient within their $R_e$, but get steeper at larger radii (LeoII, Draco), as is the case in the LDT05 and HDT09 model (respectively top left of Fig. 4.6 and top right of Fig. 4.9, yellow curves).

- Steadily decreasing, almost linear metallicity profiles over their entire range (Fornax, Sextans, LeoI), similar to the HDT05 model (Fig. 4.9, top left, yellow curve).

Table 4.3 lists the slopes of the metallicity profiles in both the observations and the simulations, which have all been calculated in the same way. The simulated dwarf galaxies, which are set up from only two different mass models, show slopes between -0.3 and -0.6 dex per kpc (-0.13 and -0.23 dex per $R_e$). The observed dwarf galaxies, that boast a wider range of masses, show slopes between -0.25 and -1.1 dex per kpc (-0.05 and -0.25 dex per $R_e$).

Both in shapes and slopes the metallicity profiles of our dwarf galaxy models fall well within the observed range of metallicity profiles. In terms of absolute metallicity values the models are located on the high end of the observed range, which is due to the models generally being more massive than the observed galaxies. The values for the HDT models lie around those of Fornax and VV124, while the values for the LDT models however lie significantly higher, which is in agreement with what a comparison of the dynamical masses of the observed and simulated galaxies would imply (as discussed in Section 4.3, the LDT scheme shifts the galaxy models along the scaling relations towards higher stellar masses compared to the HDT scheme).
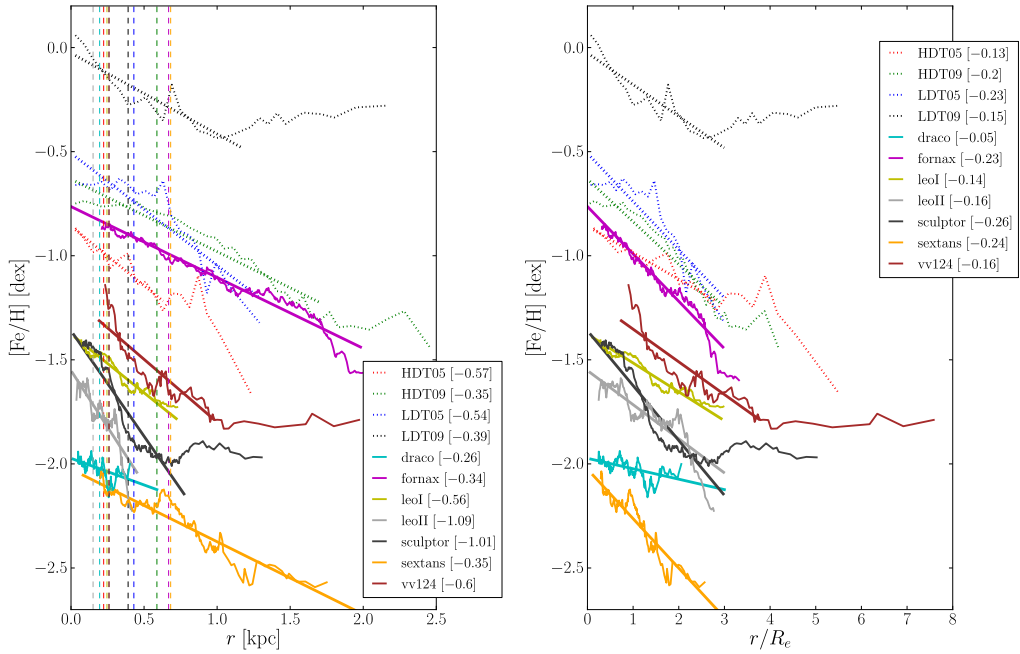
**Figure 4.12:** Observed radial stellar metallicity profiles of 7 Local Group dwarf galaxies (sold lines) and the four non-rotating simulated dwarf galaxy models (dotted lines), in function of radius in kpc (left plot) and in fractions of the half-light radius (right plot). The slopes of the linear fits to these gradients are indicated in brackets in the legend of the figure, and are expressed in dex/kpc (left) or dex/$R_e$ (right). The values of these slopes are also featured in Table 4.3. Dashed vertical lines indicate the half-light radii of the galaxies in the left plot.

## 4.5 Stellar orbits and kinematics

This section is devoted to a more detailed analysis of the stellar particles and their orbits and kinematics in our models. We want to have a measure of how strongly the stellar particles actually move away from their original orbits, to have an idea what is actually happening with them throughout the evolution of the models, and see if this could justify stable stellar metallicity gradients. We do this by looking at the stellar velocity dispersions of different populations in Fig. 4.17 and at the orbital displacements of the stellar particles with respect to the mean radius of their orbits at their time of birth in Fig. 4.13, 4.14, 4.15, and 4.16.

As mentioned in Section 4.2, snapshots are made every 5 Myr, which is sufficient to resolve each particle's orbit in detail. The evolution of a stellar particle's radius during the course of the whole simulation is then re-binned in the time dimension to bins of 1 Gyr wide, so that effectively each bin gives the average value of the stellar particle's radius over several of its orbits. Next, for both radius and time the averaged "birth" values are subtracted, and for each time bin the average (along with several percentiles) is taken over all available

**Table 4.3:** Columns: (1) dynamical mass calculated as $167\beta R_e \sigma_c^2$, with $\beta = 8$ and $\sigma_c$ the central velocity dispersion $[10^6 M_\odot]$, (2) V-band magnitude, (3) half-light radius [kpc], (4) central velocity dispersion [km/s], (5) ratio of final maximal rotation speed over velocity dispersion for the stars, (6) metallicity [dex], (7)(8) slope of metallicity profile. Sources: (1) and (6) use data from Mateo (1998), (2), (3) and (5) use data from Łokas *et al.* (2011), (4) uses data from Walker *et al.* (2010). All data for VV124 comes from Kirby *et al.* (2012) except $M_V$ and $V/\sigma$ from Łokas *et al.* (2011).

| name | mass $[10^6 M_\odot]$ | $M_V$ [mag] | $R_e$ [kpc] | $\sigma_c$ [km/s] | $V/\sigma$ | [Fe/H] [dex] | $\Delta$[Fe/H] [dex/kpc] | $\Delta$[Fe/H] [dex/$R_e$] |
|---|---|---|---|---|---|---|---|---|
| Sculptor | 15.1 | -10.53 | 0.260 | 9.2 | 0.3 | -1.8 | -1.01 | -0.26 |
| Fornax | 98.7 | -13.03 | 0.668 | 11.7 | 0.18 | -1.3 | -0.34 | -0.23 |
| Sextans | 38.7 | -9.20 | 0.682 | 7.9 | 0.48 | -1.7 | -0.35 | -0.24 |
| LeoI | 25.2 | -11.49 | 0.246 | 9.2 | 0.33 | -1.5 | -0.56 | -0.14 |
| LeoII | 9.2 | -9.60 | 0.151 | 6.6 | 0.28 | -1.9 | -1.09 | -0.16 |
| Draco | 24.0 | -8.74 | 0.196 | 9.1 | 0.21 | -2.0 | -0.26 | -0.05 |
| VV124 | 19.5 | -12.40 | 0.260 | 9.4 | 0.45 | -1.14 | -0.60 | -0.16 |
| LDT05 | 260 | -12.51 | 0.430 | 21.3 | 0.18 | -0.717 | -0.54 | -0.23 |
| LDT09 | 1090 | -15.62 | 0.391 | 45.7 | 0.03 | -0.053 | -0.39 | -0.15 |
| HDT05 | 18.2 | -10.30 | 0.224 | 7.8 | 0.08 | -0.98 | -0.57 | -0.13 |
| HDT09 | 147 | -13.34 | 0.588 | 13.7 | 0.57 | -0.834 | -0.35 | -0.20 |
| LDTrot05 | 200 | -12.7 | 0.630 | 15.4 | 1.45 | -0.672 | -0.02 | -0.01 |
| LDTrot09 | 1013 | -15.62 | 1.361 | 23.6 | 1.86 | -0.281 | 0.01 | 0.02 |
| HDTrot05 | 16.7 | -10.24 | 0.217 | 7.6 | 0.95 | -0.922 | -0.31 | -0.07 |
| HDTrot09 | 278 | -13.98 | 1.062 | 14.0 | 1.64 | -0.736 | -0.03 | -0.03 |

stellar particles. This gives us a visualization of the statistical deviation from the original mean orbital radius of the star particles in our models, in function of time since their birth. In our simulations we looked at this statistical deviation of both the absolute difference in mean orbital radius (Fig. 4.13 and 4.14), and the actual, signed, difference in mean orbital radius (Fig. 4.15 and 4.16). The former will give a clearer picture of how strongly the stellar particles move away from their original mean orbital radius, the latter will indicate the preferred direction (inward or outward). For all simulations, only the orbits of a randomly chosen 15 to 25 percent of the stellar particles are extracted from the data snapshots, to keep the amount of files manageable. Particles outside of a radius of $5 \times R_e$ are not considered, since they are in number not important for the metallicity gradients, but could have a disproportionately large influence on the average values of deviation, because they can move about easier at the edge of the potential well. Finally, if a time bin has less than half of the average amount of orbits of the previous time bins, the time bin is removed (and subsequently all that come after that as well), to ensure the amount of stellar particles on which the statistics are done does not become too low.

### 4.5.1 LDT simulations

Figure 4.13 and 4.15 show, respectively, the "absolute" and "signed" radial orbital displacements in our LDT models.

From Fig. 4.13 it is immediately apparent that the orbital displacement in these models is very limited, to just fractions of about 0.1 to 0.3 of the $R_e$, on average, over the lifetime of the simulated dwarf galaxy. Several trends are also noticeable here, :

- More massive models feature *more* displacement, caused by more turbulence and a higher velocity dispersion (properties which are set by the mass of the galaxy as the main parameter - see Table 4.3 and Stinson *et al.* 2007; Valcke *et al.* 2008; Schroyen *et al.* 2011; Section 3.3.4 ).

- Rotating models feature *less* displacement compared to non-rotating models with the same mass. The presence of angular momentum - and so, ordered motions in the stellar body gaining importance over the random motions/turbulence - causes a lower velocity dispersion, as can be seen in Table 4.3 and Fig. 3.13 in Chapter 3.

- The lowering effect of angular momentum gets stronger with increasing mass, as evidenced by the fact that the more massive LDTrot09 model shows a slightly lower stellar migration than the LDTrot05 model. This is because, in higher mass galaxies, ordered motions (if they are present) are *inherently* more important than the random motions, compared to lower mass galaxies. Or in the other direction: the lower the galaxy mass, the more dominant random motions/turbulence become over ordered motions (Kaufmann *et al.*, 2007; Roychowdhury *et al.*, 2010; Sánchez-Janssen *et al.*, 2010; Schroyen *et al.*, 2011); Section 3.2.3.3.

In Fig. 4.17, top panel, no clear trends can be seen in the velocity dispersion over different populations of stars. The only noticeable property is a possible slight increasing of the dispersion in all models for the youngest stellar populations, which can be interpreted as the effect that the (relatively strong) star formation of the model starts having on its own potential.

### 4.5.2 HDT simulations

Figures 4.14 and 4.16 show, respectively, the "absolute" and "signed" orbital displacements in the HDT models.

From Fig. 4.14 we can see that in the HDT models the radial orbital displacement is substantially larger than in the LDT models - roughly 3 times larger. But still this means only fractions of the $R_e$, on average, over timespans of several Gyr (e.g. 0.2 to 0.5 $R_e$ over 5 Gyr), and in the most massive model reaching values of the order of the $R_e$ only over the entire lifespan of the simulated dwarf galaxy. Most of the trends identified in the LDT models in 4.5.1 appear valid here as well: adding mass increases the radial diffusion, while adding angular momentum lowers it - although the latter to a slightly lesser extent than in the LDT models, due to the different rotation curves (Section 2.1.4) that deliver less
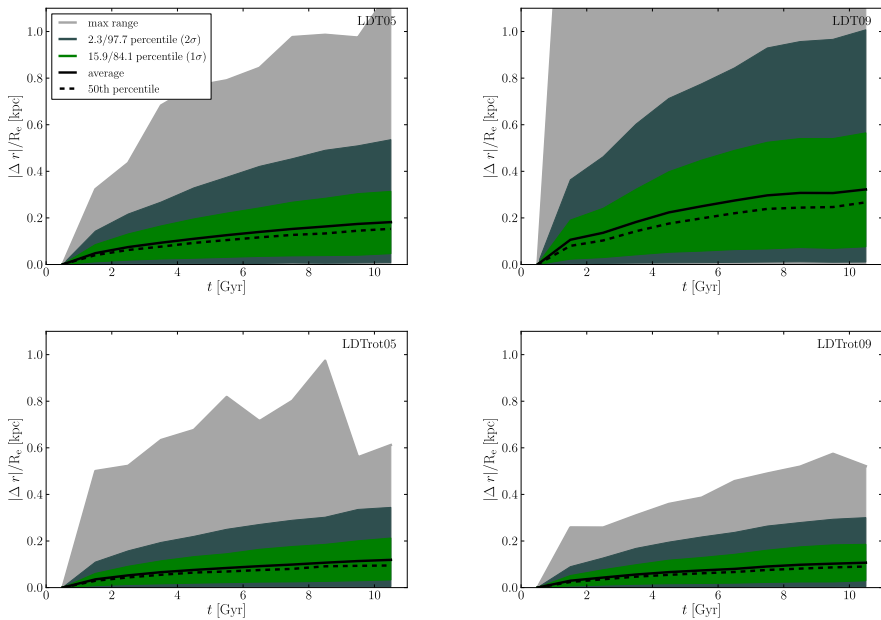
**Figure 4.13:** Radial stellar orbital displacements in the LDT models, visualised by the "absolute" statistical deviation from the birth radius, in function of time since birth (as explained in Section 4.5). Radius is expressed in function of $R_e$. The grey zone marks the maximum range, while the light and darker green respectively represent the 15.9/84.1 and 2.3/97.7 percentile regions (corresponding to $1\sigma$ and $2\sigma$ if the underlying distribution were Gaussian). The dotted and full line show the 50th percentile and the average.



**Figure 4.14:** Radial stellar orbital displacement in the HDT models. Figure identical to Fig. 4.13.

angular momentum to the central gas. This can be seen in the behaviour of the velocity dispersion in Table 4.3 and Fig. 4.17, bottom frame: there is a clear difference between the dispersions of models with different mass, but virtually no difference between models with the same mass but different angular momenta - contrary to the situation in the top frame for the LDT models.

Figure 4.16 shows that in the gradient-producing non-rotating HDT models, stellar particles tend to move significantly outward against the gradient. This is contrary to what is observed in their LDT counterparts, which show both inward and outward stellar diffusion (see Fig. 4.15). There is also an "equalizing" effect seen here, where rotation decreases this outward tendency, though the less massive HDTrot05 model is the only one which comes anywhere close to showing symmetric (equal inward and outward) radial orbital displacements.

In Fig. 4.17, bottom panel, there is now a trend to be seen in the velocity dispersion of the HDT models over different stellar populations: older populations clearly have larger velocity dispersions than younger populations.

### 4.5.3 General conclusions on stellar orbits

The general conclusion here is that radial orbital displacements of stellar particles are limited in our dwarf galaxy models, being generally measured in fractions of the half light radius over time spans of 5 to 10 Gyr. This qualitative statement is true, independent of the employed star-formation scheme. This gives us a more solid foundation for the results concerning the stability of metallicity gradients.

Since this is the case for dwarf galaxy models with either low or high angular momenta, this strongly indicates that there are no radically orbit-changing processes at work in dwarf galaxies like there are in bigger galaxies. In massive spiral galaxies there is the so-called "radial stellar migration", which is caused by gravitational interactions between individual stars and the large-scale spiral structures rotating in the stellar and gaseous discs that drive stars away from the corotation radius (Sellwood & Binney, 2002; Roškar et al., 2008, 2012). This is able to move stars about over large radial distances while maintaining quasi-circular orbits, and it seems the evidence, both theoretical and observational, is building up for this being an effect of broad importance in disc galaxy evolution : it plays a fundamental role in the forming of thick discs, (Schönrich & Binney, 2009; Loebman et al., 2011), the distribution of stellar populations, (Roškar et al., 2008), and has evidently strong implications for the forming/survival of metallicity gradients (Lépine et al., 2003). None of our models show an appreciable disk or spiral structures in their stellar body, because it is generally too thick, dynamically too warm, and influenced by the random motions of the gas in the low mass regime that we are investigating here (Kaufmann et al., 2007; Roychowdhury et al., 2010; Sánchez-Janssen et al., 2010). Only the rotating dwarfs feature a somewhat flattened stellar body and fast-transient spiral structures in their gas distribution, but these structures are produced by outwardly expanding supernova-blown bubbles being deformed by shear, which are too short-lived and fade away too quickly to have any impact on the stellar dynamics of the models. What - if anything - is happening

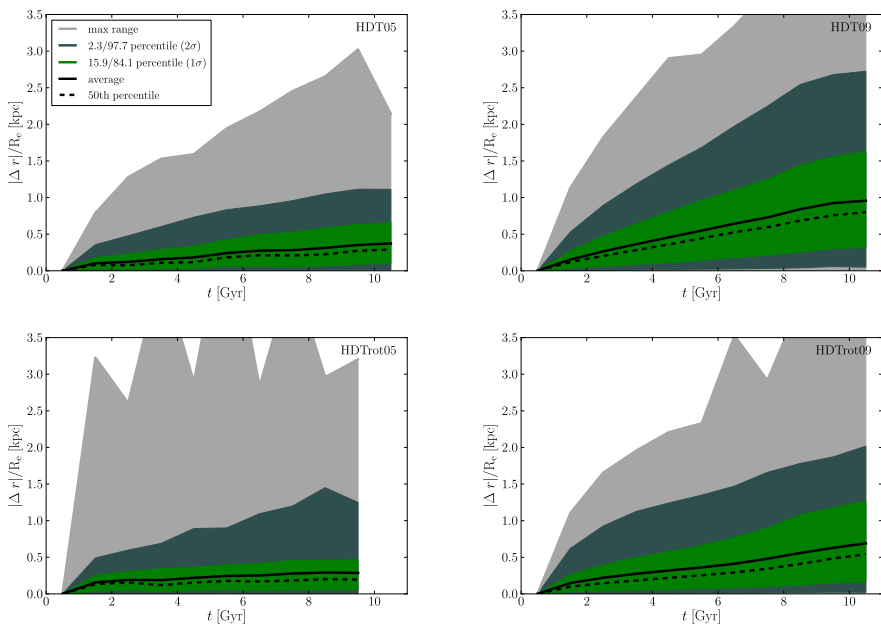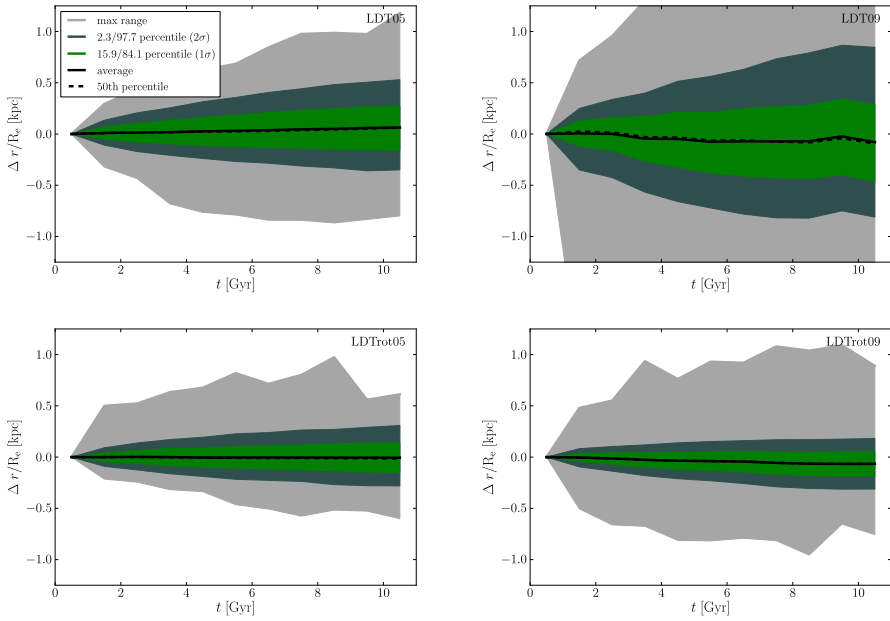**Figure 4.15:** Radial stellar orbital displacement in the LDT models, here in positive or negative distance from the birth radius of the star. Other properties of the plots identical to Fig. 4.13.
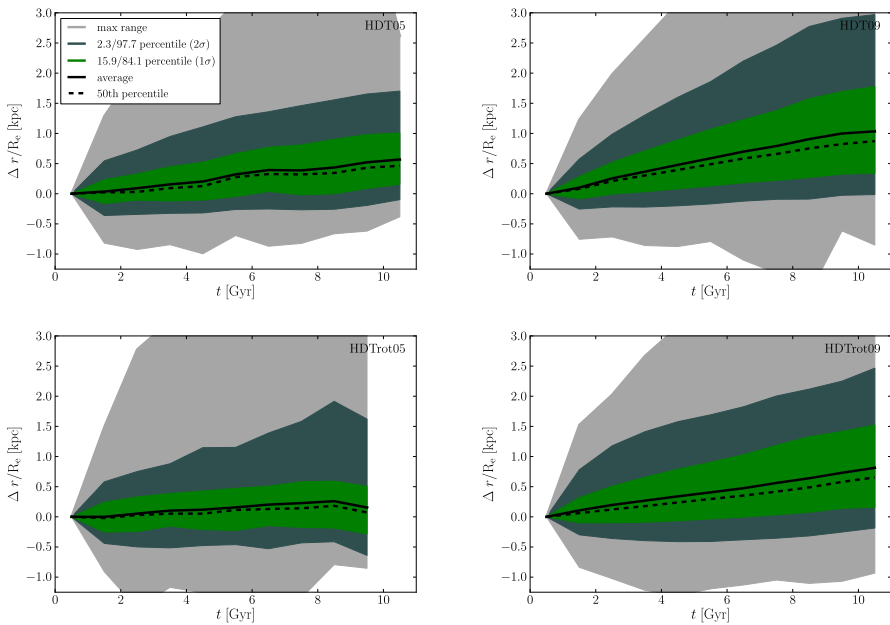


**Figure 4.16:** Radial stellar orbital displacement in the HDT models. Figure identical to Fig. 4.15.

with the orbits in these dwarf galaxy models is most likely linked to the much more gentle effect of "dynamical heating", that changes stellar orbits in a more gradual manner. It was already suggested by Spitzer & Schwarzschild (1953) that, for instance, massive gas clouds could have a noticeable influence on the random velocities of stellar orbits.

Quantitatively, the star formation criteria do play a role, however. The HDT models show noticeably more stellar diffusion than the LDT models, who barely undergo any orbital displacement at all over their entire simulation time. This increased diffusion is also more strongly aimed outward - agains the gradient - though it is still limited in absolute terms. Two likely causes are the more turbulent character of the gas in general (which is adopted by the stellar body), and the increased scattering of stellar particles off dense gas clumps. Both effects are expected to become more important when the density threshold for star formation increases, and will therefore increase the strength of dynamical heating of the stellar body in the HDT models. This is all visualized in Fig. 4.17, where the velocity disperions of different stellar populations in the last snapshot of each simulation are shown. Gradual dynamical heating of the stellar body would be expected to leave a footprint here, by causing the older populations (that have been dynamically heated longer) to have larger velocity dispersions than the younger populations. The LDT models, having extremely small orbital displacements, do not show any trend like this in the upper panel of Fig. 4.17. Besides the scatter on the plots, which is probably due to the model's star formation peaks that influence its own potential, the velocity dispersion is roughly similar for populations of all ages. The HDT models, on the other hand, all clearly show this dynamical heating footprint on their velocity dispersions in the lower panel of Fig. 4.17.

## 4.6    Conclusion

In this chapter we investigated how, in simulated dwarf galaxies in isolation, metallicity gradients are formed, how they evolve and how, once formed, they can be maintained. Furthermore, we adressed the importance of dynamical orbit-changing processes in the dwarf galaxy regime, and their potential in erasing or weakening existing population gradients. We hereby also investigated the role of the density threshold for star formation.

Firstly, in Section 4.4, we found that metallicity gradients are gradually built up during the evolution of non-rotating dwarf galaxy models by ever more centrally concentrated star formation adding to the overall gradient. On themselves, the formed gradients easily survive and their strength hardly declines over several Gyr, indicating that only external disturbances would be able to significantly weaken or erase population gradients in dwarf galaxies. The metallicity gradients produced by our dwarf galaxy models are found to agree well with observed metallicity gradients of dwarf galaxies in the Local Group, both in shapes and slopes.

Secondly, from Section 4.5 we conclude that the orbital displacements of the stars are quite limited in our models, of the order of only fractions of the half light radius over time-spans of 5 to 10 Gyr in both our rotating and non-rotating models. This is contrary to what is found in massive disc galaxies, where scattering of stars off the corotation resonance of
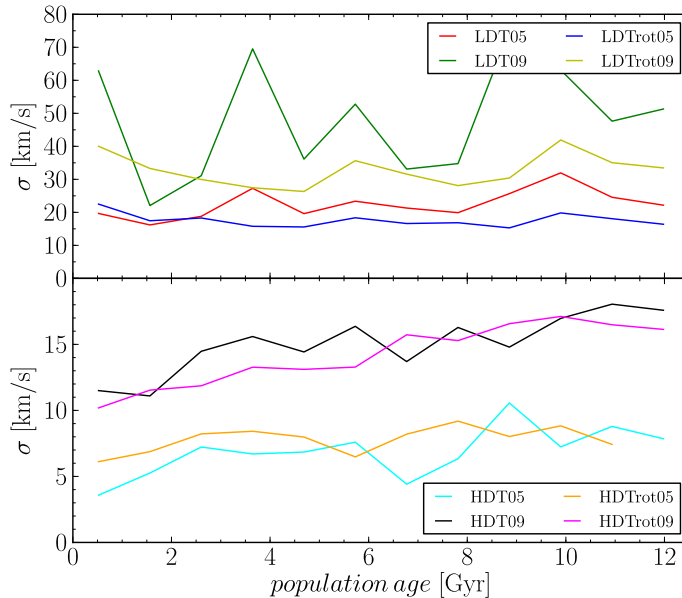
**Figure 4.17:** Velocity dispersions of stellar populations of different ages in the dwarf galaxy models, the upper and lower panel respectively show the LDT models and the HDT models. For all models the last snapshots were taken, their stellar populations divided into 12 equal age bins, and for each age bin the velocity dispersion was calculated in a box with width $R_e$ around the center of the galaxy.

large-scale spiral structure can cause significant radial migration. The absence of long-lived, major spiral structures in the simulated dwarf galaxies leaves only turbulent gas motions and scattering off dense gas clouds as scattering agents of stars, leading to an only mild dynamical heating of the stellar body that allows for the long-term survival of population gradients.

Finally, increasing the density threshold for star formation from 0.1 to 100 amu/cm$^{-3}$, which - together with increased feedback efficiency and novel cooling curves below $10^4$ K - represents a much more realistic description of star forming regions, has profound influences on the mode of star formation in our models. It produces high density, cold, star forming clumps, shorter star formation timescales, and lower stellar masses. On the matter of population gradient evolution and orbital displacements it also has a clear influence, producing stronger dynamical heating of the stellar particles which is seen through larger orbital displacements and clear trends in the velocity dispersion over different stellar populations. In absolute terms, however, the effect of this dynamical heating remains very limited.

# 5

# Latest results

In this chapter we present all our latest results and analyses of our dwarf galaxy models. These simulations are now, unlike the previous chapters on our published results, able to use the *full* capabilities of our models as described in Chapter 2. These all mainly revolve around the different usages of the new chemical framework developed in De Rijcke *et al.* (2013) as explained in Section 2.2.1 - both during runtime to implement physical processes, as in post-processing of the simulation output afterwards:

- most importantly, the on-the-fly calculation of the radiative cooling and heating of gas particles in our simulations,

- estimating their neutral/ionized fraction,

- estimating their emission fluxes in different lines (any emission line is theoretically possible to be calculated - currently available lines are H$\alpha$ and CII),

where the latter two are used to analyze the output of the simulations, and hence provide additional ways to compare our models with different observations and check the implemented astrophysical mechanisms.

## 5.1   Full radiative cooling/heating scheme

In the latest simulations of the dwarf galaxy models, the full radiative processes of the interstellar gas (cooling and heating) as presented at the end of Section 2.2.1 can be accounted for during runtime. To investigate all the effects of the new sub-grid scheme on

the physical behaviour of the gas, and the consequences this has for the formation of stars and of the dwarf galaxy itself, we have run a set of simulations where the new physical modules are switched on, one by one.

### 5.1.1   Simulations

In Table 5.1, the set of new simulations that we will use in this chapter to investigate and present all the functions and features of the new chemical framework is listed. They all employ the same basic setup as the simulations used in Chapter 4:

- NFW dark matter halo and a pseudo-isothermal gas sphere ("09" model), both sampled with 200000 particles,

- rotating models are given an arctangens rotation profile (5 km/s),

- high density threshold scheme for star formation ($100 \, \mathrm{amu/cm^3}$).

They all have *identical* initial setups, for a fixed starting redshift $z_i$, and only differ in their implementations of the *radiative processes.*

Two different starting redshifts are chosen, in order to probe the two different regimes of the UV background: before and after re-ionization (which happened at a redshift $\gtrsim 6$). For both regimes a reference simulation is run, that employs the "old" 3-dimensional cooling curves as used in Chapter 4, then a simulation that only uses the new 5-dimensional cooling curves, and finally a simulation with the full new cooling and heating scheme. Furthermore, for all configurations we have run both a rotating and a non-rotating model. There is, however, one other difference, concerning the HDT star formation scheme in these simulations. Keeping the same high feedback efficiency of 0.7 when switching on the new radiative processes appeared to lead to somewhat unrealistic dwarf galaxies in our simulations, in the sense that they become too extended - as can be seen in the scaling relation in Figure 5.1. Previously our rotating and non-rotating series of models nicely encompassed this observed relation (see Figure 3.12), indicating angular momentum could explain its width or spread, but here the non-rotating simulations are already on the upper edge of the relation, and the rotating simulations clearly lie above the observed trend. This is due to the extra energy input from the UV background and the interstellar radiation field, that makes the gas more extended and less dense. To produce realistic dwarf galaxies in these simulations, we dial down the high feedback efficiency to a value of 0.35, which has the desired effect and brings the angular momentum spread back to covering the observed width of the relation (Figure 5.1). Since 0.7 is a fairly high and possibly unrealistic value, the need to lower it here is a positive thing.

For the simulations using the full new radiative cooling and heating we have run simulations with both feedback efficiency values (0.7 and 0.35), but the new cooling-only simulations have only been run with the 0.7 value, for reasons which are explained in Section 5.1.2.

**Table 5.1:** Table listing the simulations used to investigate the new chemical framework. The columns give: (1) name of the run, (2) redshift at which the simulation starts, (3) initial rotation speed given to the gas (through an arctangens curve), (4) employed radiative physics.

| name | $z_i$ | $v_{rot,i}$ | radiative physics |
|------|-------|-------------|-------------------|
| Z4ref | 4.3 | 0 | reference simulation with old 3D cooling |
| Z4refrot | 4.3 | 5 | reference simulation with old 3D cooling |
| Z4cool | 4.3 | 0 | new cooling-only |
| Z4coolrot | 4.3 | 5 | new cooling-only |
| Z4full | 4.3 | 0 | full new cooling and heating |
| Z4fullrot | 4.3 | 5 | full new cooling and heating |
| Z12ref | 12 | 0 | reference simulation with old 3D cooling |
| Z12refrot | 12 | 5 | reference simulation with old 3D cooling |
| Z12cool | 12 | 0 | new cooling-only |
| Z12coolrot | 12 | 5 | new cooling-only |
| Z12full | 12 | 0 | full new cooling and heating |
| Z12fullrot | 12 | 5 | full new cooling and heating |
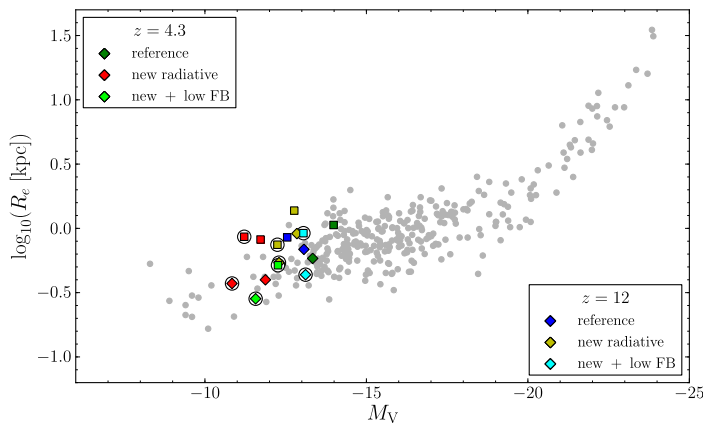


**Figure 5.1:** Scaling relation of the half-light radius versus the V-band magnitude, for the simulations listed in Table 5.1. Reference simulations with 3D-cooling and starting redshifts 4.3 and 12, respectively, are in green and blue, while the according simulations running the new radiative routines are in red and yellow, and the versions of the latter with reduced feedback are in light green and light blue. Non-rotating models are indicated with diamonds, rotating models with squares. For the "new" simulations, the cooling-only simulations are shown with simple markers, while the ones with the full new cooling and heating routines are shown with an extra circle around the marker. Observational data as in Figure 3.12.
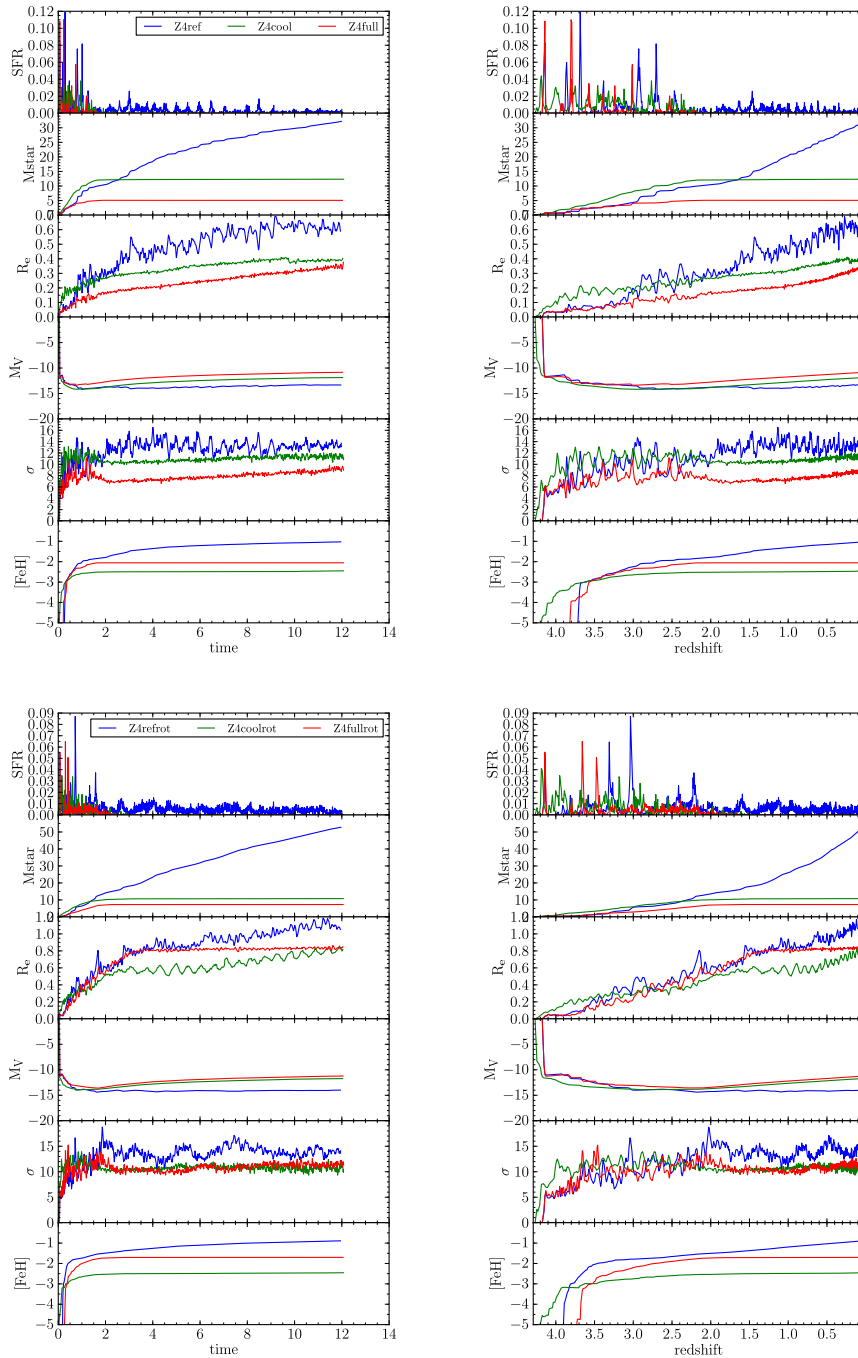
**Figure 5.2:** Evolution of several quantities throughout the simulations from Table 5.1 that start from redshift 4.3, using the (high) feedback efficiency value of 0.7. Left columns show the evolution in function of time, the right columns show the same evolution in function of redshift. Top plots show the non-rotating models, bottom plots show the rotating ones.
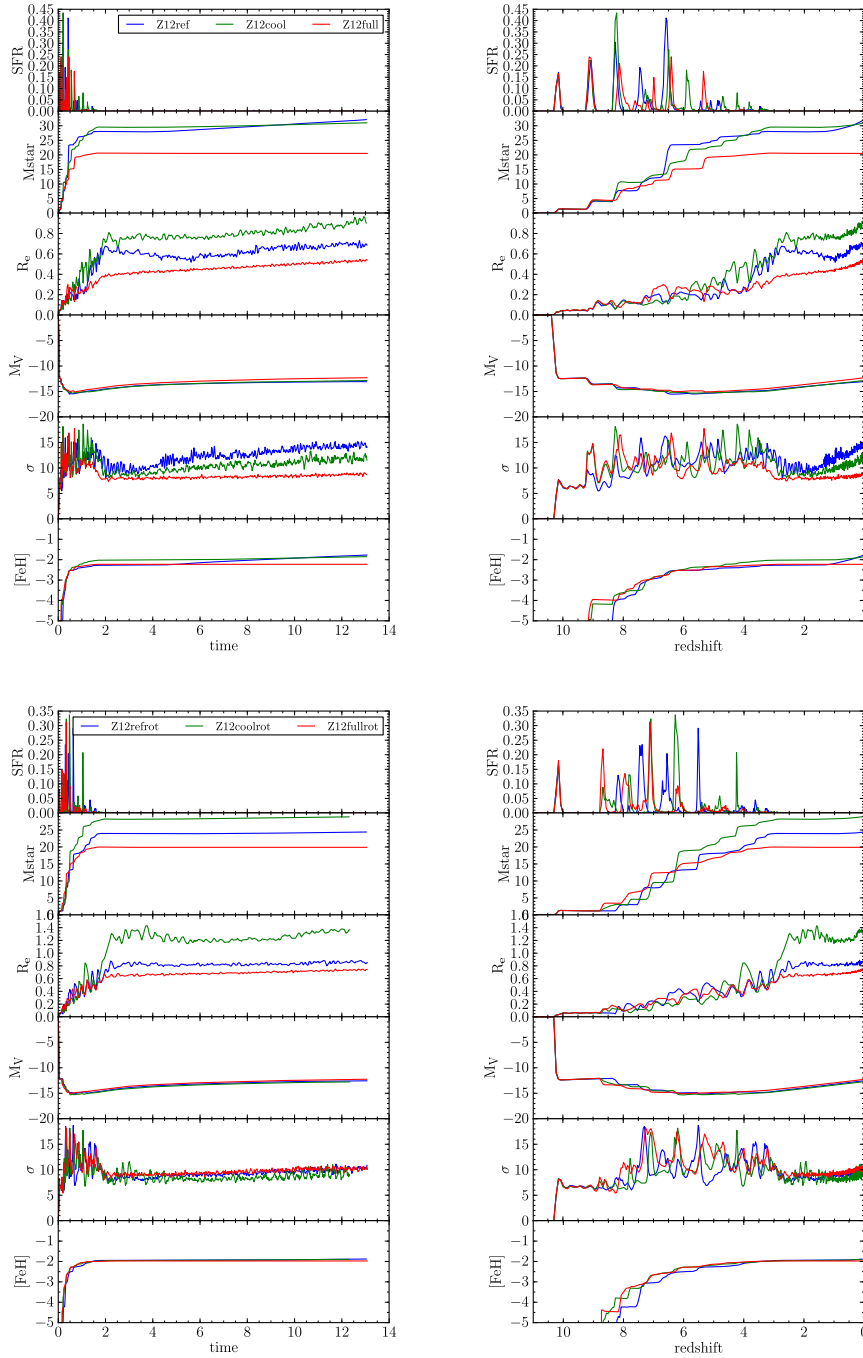
**Figure 5.3:** Evolution of several quantities throughout the simulations from Table 5.1 that start from redshift 12, using the (high) feedback efficiency value of 0.7. Left columns show the evolution in function of time, the right columns show the same evolution in function of redshift. Top plots show the non-rotating models, bottom plots show the rotating ones.

### 5.1.2 Cooling-only

Before discussing the new cooling-only simulations and their effects, we should state that this might not be the wisest option to choose. Employing only the new radiative cooling tables while *not* using the new radiative heating tables, will still include the effects of the background radiation to some degree, since the ionization equilibrium is self-consistently calculated while taking the full array of physical processes and energy sources and sinks into account (Section 2.2.1). The derived cooling and heating tables are therefore inevitably intertwined with each other, and should not be used independently. The only reason not to already add the two and instead to separate them into different tables, is because we wanted to interpolate on them in logarithmic space, but the total radiative curve could cross zero. Since these simulations are not completely physically consistent in any case, we did not re-run them with the lower 0.35 feedback efficiency value when it appeared that the 0.7 value was too high. We make our discussion here only on the basis of the first runs, which yield qualitatively similar results in this context.

Figures 5.2 and 5.3 show the evolution of all the simulations from Table 5.1, that have been run with the high feedback efficiency value of 0.7.

In the case where the simulations start from the "standard" redshift of 4.3, which is after the epoch of reionization, where a strong UV background is present, there is a significant decrease in star formation when using the new cooling tables (as could already be seen from Figure 5.1, the green and red points are relatively far apart on the $x$-axis). The total stellar mass is reduced to only a fraction of the stellar mass of the reference simulation (30% or less), and is mostly produced in the first 2 Gyr. Initially the star formation is actually stronger with the new cooling tables, indicating that the gas momentarily cools faster, but the ensuing feedback is so strong in combination with the (indirect) heating effects included in the cooling tables, that star formation stops completely. The gas is blown out and dispersed to very low densities that would not be able to shield it from the background radiation, and the indirect radiative heating effects in the cooling tables are sufficient to prevent the gas from cooling enough to ever form stars again. However, the half-light radii of the simulated dwarf galaxies produced with the new cooling tables do not scale down proportionally to the difference in mass, when comparing to the reference simulations. This is the problem that was already indicated in the beginning of Section 5.1.1 and shown in Figure 5.1.

On the other hand, when the simulations start from a redshift of 12, which is before the epoch of reionization so that there is not a strong UV background at the beginning, there is hardly any difference in the simulations with the old or new cooling (as we could also already see in Figure 5.1, the blue and yellow points lie fairly close to each other). The differences in stellar mass that are visible in Figure 5.3, largely fall within the inherent variance that is present in our simulations (see Figure 3.1). When looking at the right side panels, we can see that in all simulations, also the reference simulations with the old cooling tables, most of the stars have formed by redshift 6. Around this redshift the UV background plays a major role in the radiative heating (and indirect in the radiative cooling), but it seems to have little effect on the star formation, it continues at roughly

the same rate until redshift 4, as in the reference simulation. This is caused by the fact that at this time (about 1.5-2 Gyr into the evolution) the supernova Type Ia start going off, which give the already heated and loosely bound gas reservoir the final kick to get terminally dispersed. A remedy for this, to make the star formation more extended in time, might be to start the simulations with higher masses, less dense/concentrated initial gas conditions, and/or a more gradual formation through a merger history. As in the previous simulations, when using the new cooling tables the half-light radius is too large in comparison with the stellar mass.

### 5.1.3   Full cooling and heating

Due to the problems with the feedback efficiency being too high and making the models too extended that were mentioned in Section 5.1.1, we will first discuss the simulations with the high feedback efficiency value of 0.7 to see what effects there are with respect to the cooling-only simulations in the previous section. Subsequently we will look at the simulations with the lower feedback efficiency value of 0.35, and discuss its effects.

#### 5.1.3.1   High feedback efficiency

Since the radiative cooling curves on themselves already indirectly carry effects from the radiative heating, adding the actual correct amount of energy from radiative heating to the gas particles in the simulations does not really cause any qualitatively different effects on the results. It mainly amplifies the effects already described in Section 5.1.2, and produces even less stars. This can be seen in Figure 5.1 by the fact that the red points (z=4.3 models) lie relatively close to each other in terms of stellar mass, as do the yellow points (z=12 models) amongst each other. In the simulations that start at redshift 12, unlike the cooling-only simulations the models now produce a significantly lower stellar mass compared to the reference simulation, in the sense that the difference in stellar mass is larger than the inherent variance in our models. The effect itself is however much less drastic than the radiative heating effect that is seen in the simulations that start at redshift 4.3.

One thing to note, however, is that including the radiative heating causes the models that start at redshift 4.3 to have a higher metallicity than the cooling-only simulations. This is probably due to the fact that its lower star formation, that also generates less feedback, causes the enriched material not to be blown away as efficiently - meaning it is available for subsequent star formation and enrichment. The effect is not seen in the simulations that start at redshift 12, most likely because the timescales over which most of the star formation takes place are too short for this effect to play a role.

A second thing to mention is the fact that in the simulations that start at redshift 12, the presence of angular momentum seems to generally have less influence on the spatial extent (half-light radius) of the model dwarf galaxies, compared to the simulations that start at redshift 4.3 (as seen in Figure 5.1). This is most likely due to the fact that the initial conditions of the simulations starting at redshift 12 are denser to start with, while
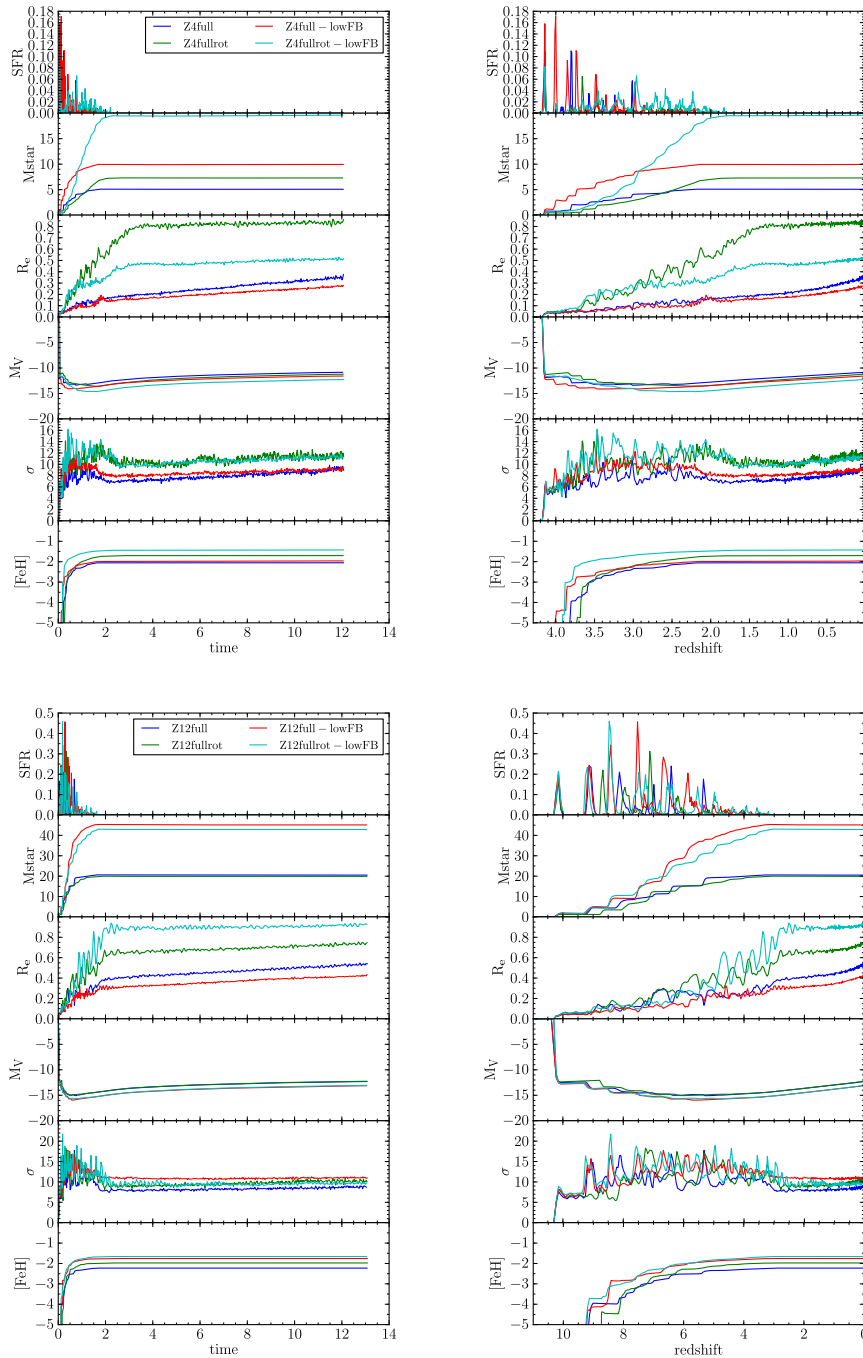
**Figure 5.4:** Evolution of several quantities throughout the simulations from Table 5.1 with the full radiative cooling and heating switched on, comparing the lower feedback efficiency value of 0.35 to the high 0.7 value. Left columns show the evolution in function of time, the right columns show the same evolution in function of redshift. Top plots show the simulations starting at redshift 4.3, bottom plots show the ones starting at redshift 12.

the initial rotation curve stays the same, so there is somewhat less angular momentum delivered to the gas than in the less dense initial conditions at redshift 4.3.

#### 5.1.3.2 Low feedback efficiency

As discussed in Section 5.1.1 and shown in Figure 5.4, lowering the feedback value from 0.7 to 0.35 does what it was expected to do: increase the produced stellar mass, and make the models more concentrated for a given total stellar mass. This pushes the models down and to the right on the scaling relation in Figure 5.1, making their spread overlap with the width of the observed relation.

The only other qualitative effect from this lowering of the feedback efficiency is that the metallicities are systematically higher than before, which is also an expected effect since the synthesized elements are now not expelled as efficiently, and are more easily reused for subsequent star formation. The timespan over which most of the stars are formed seems unaffected.

### 5.1.4 Reionization effect

The reionization epoch itself does not seem to have a significant effect, but whether the simulations start before or after reionization does. The simulations that start before would anyway have formed a significant fraction of their stellar mass before the UV background kicks in, even in the reference simulations where this radiation is not included, partly because the gas in the initial conditions is denser at higher redshifts. They also have had time to collapse a lot of gas densely enough to be shielded from the UV background, making it available for future star formation. There is no clear truncation of the star formation to be seen.

When the simulations start after, they are immediately bathed in the strong UV background, already excluding a lot of gas in the initial setup from cooling and forming stars. For the central, already somewhat dense, portion of the gas that does manage to collapse and form stars: whenever it gets too low in density (e.g. due to supernova feedback), it cannot shield itself from the radiation and receives significant heating from the UV background, making it unavailable for future star formation.

## 5.2 Neutral/ionized fraction

The first derived feature of the calculation scheme for the chemical composition and ionization balance of the interstellar gas, is to calculate the neutral fraction of a gas particle. Several 5-parameter neutral fraction tables (the same parameters as the cooling and heating tables, Section 5.1), together with the N-dimensional interpolator routine (Section 2.3.4), have been built into our analysis software package (Section 2.3.3) to serve as a post-processing analysis and imaging tool. The neutral fraction of a gas particle can be used as a proxy for the amount of neutral HI that it contains, making it suitable to compare simulated images of the neutral gas directly to observed images of the HI emission of

gaseous dwarf galaxies. It should be noted that this is only an approximation, non-ionized gas can of course also exist in the form of molecular gas, which often has a different spatial distribution than the neutral atomic gas. In dwarf galaxies, however, molecular gas is not very abundant, and the majority of the neutral gas will be in atomic form. Krumholz (2012) shows that in low-metallicity systems, the timescale for converting atomic gas to molecular is much longer than that for the gas to reach thermal equilibrium and proceed to form stars.

### 5.2.1 Simulations

For the post-processing analysis of our models in this section and the following sections, we wanted to test it both on a "regular" simulation as we had been running until now, and on a "new" simulation that was run with all the new cooling and heating physics, to have a fully self-consistent situation in the latter case (since all the post-processing features are derived from the basis of the cooling and heating calculations). For this we use the "reference" run starting at redshift 4.3, and the "full cooling and heating" run starting at redshift 12 from the previous section, in Table 5.1. Instead of using the standard mass resolution, these runs have been resimulated with $10^6$ gas particles and 200000 dark matter particles for the imaging analysis (in other words, to make images at higher resolutions). Since we will naturally be comparing the following analyses of our simulations with observations of gas rich dwarf galaxies in the local Universe, most of which are dwarf irregulars that rotate (see Section 5.2.2), we chose to use the rotating version of our models for these high-resolution resimulations, shown in Table 5.2.

In Figure 5.5 the two simulations are shown, with rendered gas density images overplotted with the newborn star particles. For Z4refrot_HR the sequence of snapshots covers its entire evolution, but because the star formation terminally shuts down after about 2 Gyr in Z12fullrot_HR, we restrict ourselves there to the period that it forms stars, since there is no point in imaging the models when they are devoid of gas and star formation (at least in the analyses we do here). Throughout the next chapters, the high-resolution models will always be shown in the same sequence as in Figure 5.5.

### 5.2.2 Observations

The HI observations that we use have been taken from the publicly available data of the LITTLE THINGS survey[1] (Hunter *et al.*, 2012). From their sample of 41 nearby gas rich dwarf galaxies we selected the objects that have a V-band magnitude close to those of the high resolution model starting at redshift 4.3 (Section 5.2.1). The relevant properties of the observations and simulations are presented in Table 5.2 and Figure 5.7.

### 5.2.3 Imaging

The most straightforward method to exploit this tool in comparing our models with observations, is to use it in imaging. From a simulation snapshot we select the gas particles

---

[1]science.nrao.edu/science/surveys/littlethings/the-little-things-survey
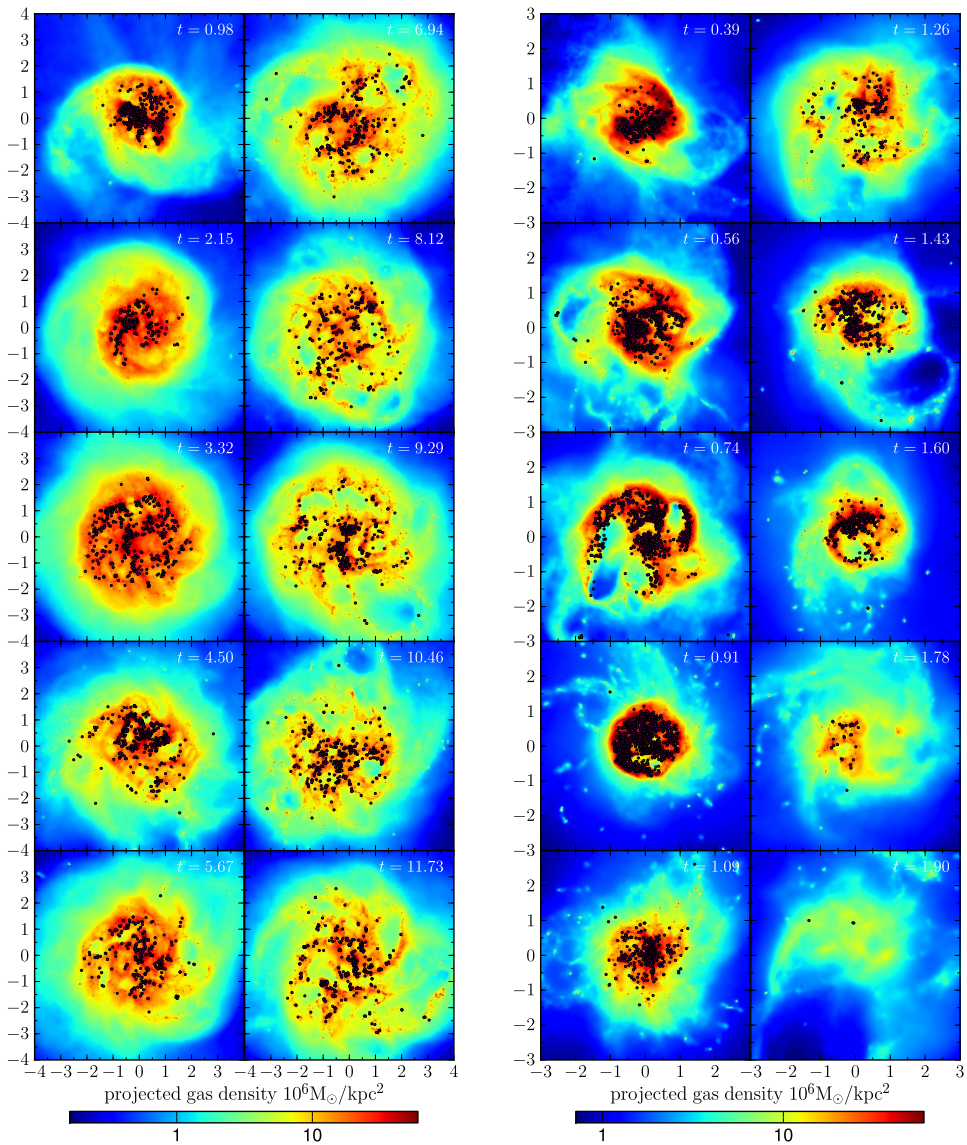
**Figure 5.5:** Density maps of the gas in the high-resolution resimulations mentioned in Table 5.2, overplotted with the newly born star particles (with ages <20 Myr). Left is the reference simulation starting at redshift 4.3 (Z4refrot_HR), right is the full radiative physics simulation starting at redshift 12 (Z12fullrot_HR). Gas density is color coded according to the color bar on the respective figures, which have different ranges. Simulation Z4refrot_HR is shown with snapshots throughout its entire evolution, while simulation Z12fullrot_HR is only shown during the period that it forms stars, which is roughly the first 2 gigayears (see Figure 5.4).

**Table 5.2:** Table showing the observations and simulations used for comparing post-processing predictions of our simulated dwarf galaxy models with observed dwarf galaxies. Columns give: (1) name of the object/model, (2) distance of the observed object [Mpc], (3) V-band magnitude, (4) total HI mass [$10^6$ M$_\odot$], (5) H$\alpha$ luminosity [$10^{38}$ erg/sec]. HI data are taken from the LITTLE THINGS survey (Hunter *et al.*, 2012), H$\alpha$ data are taken from Hunter & Elmegreen (2004). The two simulations are taken from Table 5.1, and have been resimulated with $10^6$ gas particles. The values in columns (4) and (5) for the simulations are average values over their evolution.

| name | distance | $M_V$ | $HI_{tot}$ | $L_{H\alpha}$ |
|---|---|---|---|---|
| DDO 43 | 7.8 | -15.1 | 169.8 | 6.31 |
| DDO 47 | 5.2 | -14.7 | 389.0 | 17.78 |
| DDO 52 | 10.3 | -15.4 | 269.2 | 1.66 |
| DDO 63 | 3.6 | -14.8 | 154.9 | 9.33 |
| DDO 87 | 7.7 | -15.0 | 245.5 | 5.62 |
| DDO 101 | 6.4 | -15.0 | 22.9 | 9.55 |
| DDO 126 | 4.9 | -14.9 | 144.5 | 14.45 |
| DDO 133 | 3.5 | -14.8 | 104.7 | 28.18 |
| Z4refrot_HR | - | -15.13 | 111.0 | 214.38 |
| Z12fullrot_HR | - | -13.05 | 76.9 | 28.89 |

whose neutral fraction is in a certain range of interest, and generate a "standard" SPH-rendered gas density image of only those particles, which can then be compared with the appropriate observational images. We are hence able to look selectively at both the neutral and ionized part of the gas in our simulations, and when combining this with a further selection on density values (high or low densities) we can nicely distinguish and image the different phases of the interstellar gas.

### 5.2.3.1   Neutral gas

When imaging the neutral fraction, we select the gas particles from a simulation snapshot that have a neutral fraction of 0.9 or above. Below that, the amount of ionized gas is already high enough to play a significant role in the radiative processes of the interstellar gas, and therefore too high to be able to designate the gas particle as "neutral". These images can be directly compared with maps of neutral hydrogen from observations, both qualitatively and quantitatively (see Section 5.2.4 for the latter).

In Figure 5.6, maps of the neutral gas density in the high-resolution resimulated dwarf galaxy models are shown (Table 5.2). For Z4refrot_HR, the reference simulation that starts at redshift 4.3, we can show snapshots of the neutral gas content throughout the entire simulation since it continuously contains gas and forms stars. For Z12fullrot_HR however, the full radiative cooling and heating simulation that starts at redshift 12, we have seen in Section 5.1.3 and Figure 5.4 that star formation permanently shuts down after 2 Gyr, and therefore we only image the model during its star forming phase. The neutral gas structures that can be seen in Figure 5.6 are essentially tracing the dense gas regions,

with:

- small bright spots indicating the densest gas clumps that are reaching the star formation density threshold and are about to form stars,

- dark bubbles of a range of different spatial scales completely devoid of neutral gas, which are blown by supernova feedback,

- extended and interconnected gas structures or filaments of intermediate density in which the high-density clumps form, which are sometimes distorted and compressed into short-lived gaseous spiral arms by large outwards-expanding supernovae bubbles that experience shear.

These simulated images visually compare well to observations of the neutral HI gas in nearby dwarf galaxies from the Little Things survey (Hunter *et al.*, 2012) (Figure 5.7), showing similar structures in the neutral gas. In Figure 5.7 also snapshots of both of the simulations are added, which are made to look like mock observations, by processing them with a Gaussian filter and some added random noises. This makes them visually comparable to the observations, with similar details, shapes and structures. A more quantitative comparison of the spatial structures is presented further on in Section 5.2.4. The total HI mass in the models, which is directly derived from the simulated images, is indicated on each frame in Figure 5.6, and the average is given in Table 5.2. The value is of the same order as those derived from the observations, providing a first quantitative check on the post-processing methods, and in general drops off during the evolution of the models.

### 5.2.3.2   Ionized gas

For imaging the ionized fractions of the interstellar gas in our simulations, we can select any range of neutral fraction values below 0.9. In Figure 5.8 we show a series of images with different neutral fraction ranges from the same snapshot of our high-resolution simulations, with cuts that progress from just above neutral to highly ionized gas. In the first frame of the series, so the one showing the least-ionized gas, the gas structure is still somewhat reminiscent of that of the high-density neutral gas in Figure 5.6. In the subsequent frames showing higher and higher ionized gas, these structures gradually disappear and make the gas content relatively featureless in the intermediately ionized range. When reaching the higher ionization ranges, stronger features start appearing again in the ionized gas, while the region that is probed by the gas expands. First in the outer regions we can see bright "barriers" of ionized gas light up, which is compressed on the outer edges of large (and older) expanding supernova bubbles, and subsequently strong features in the more central regions light up very brightly in the highest ionization ranges. The latter are connected to more recent supernova-blown bubbles by young stars.

From here on we will focus on imaging only the highly ionized gas, since it seems to be the most interesting region to investigate due to these strong features. For this we use the gas particles from a simulation snapshot that have a neutral fraction of 0.1 or lower.
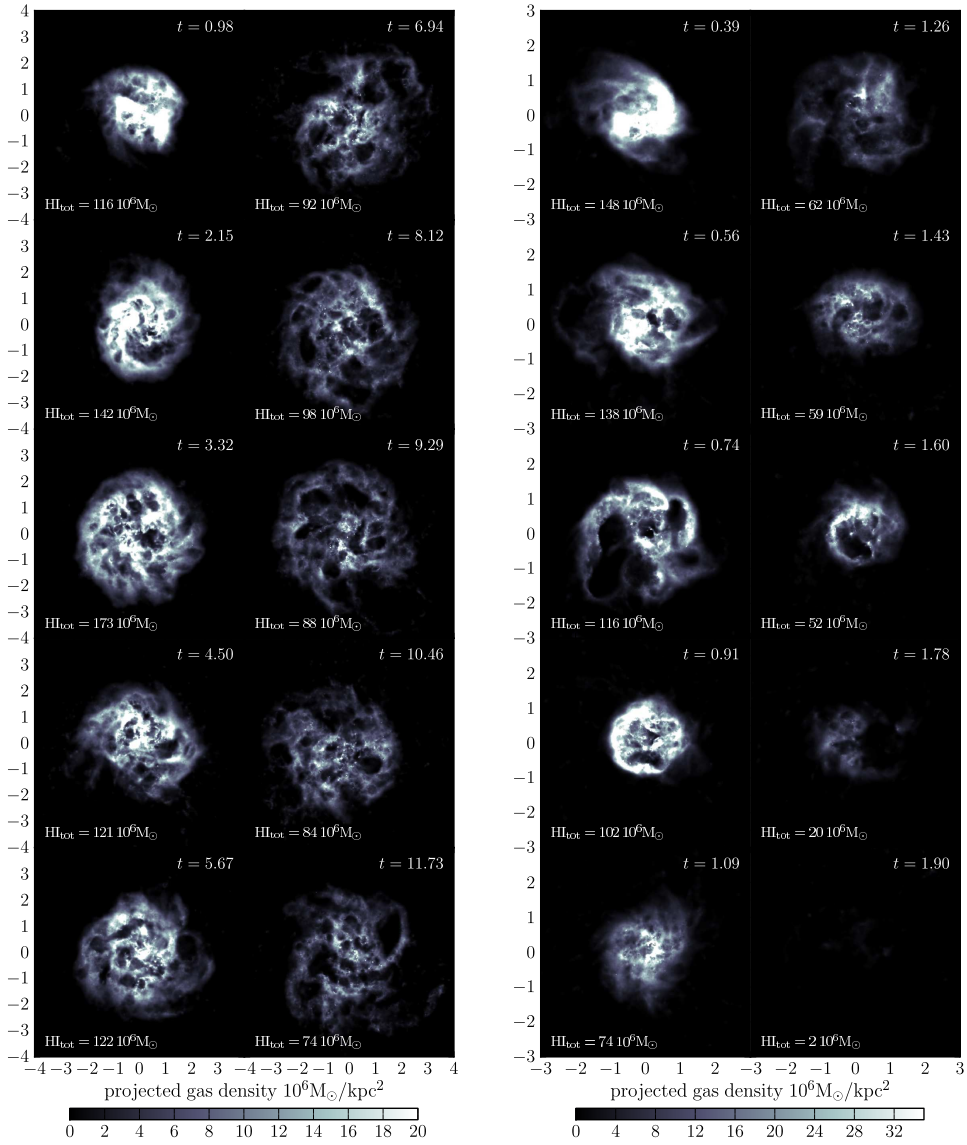
**Figure 5.6:** Density maps of the neutral gas in the high-resolution . Left is Z4refrot_HR, right is Z12fullrot_HR. Density of the neutral gas is color coded according to the color bar on the respective figures, which have different ranges. The same sequence of snapshots is shown as in Figure 5.5.

However, solely selecting these ionized gas particles will still represent interstellar gas in different astrophysical phases, which can be seen directly in the last frames of the series in Figure 5.8. On the one hand, there are quite sharply defined bright dots visible, mostly in the central regions, but also a much vaguer and more extended gaseous structure on the other hand. Adding extra selections on gas density - above $10^{-24}\,\mathrm{g/cm^3}$ or below $10^{-25}\,\mathrm{g/cm^3}$, dubbed "high" and "low" density - will enable us to distinguish between
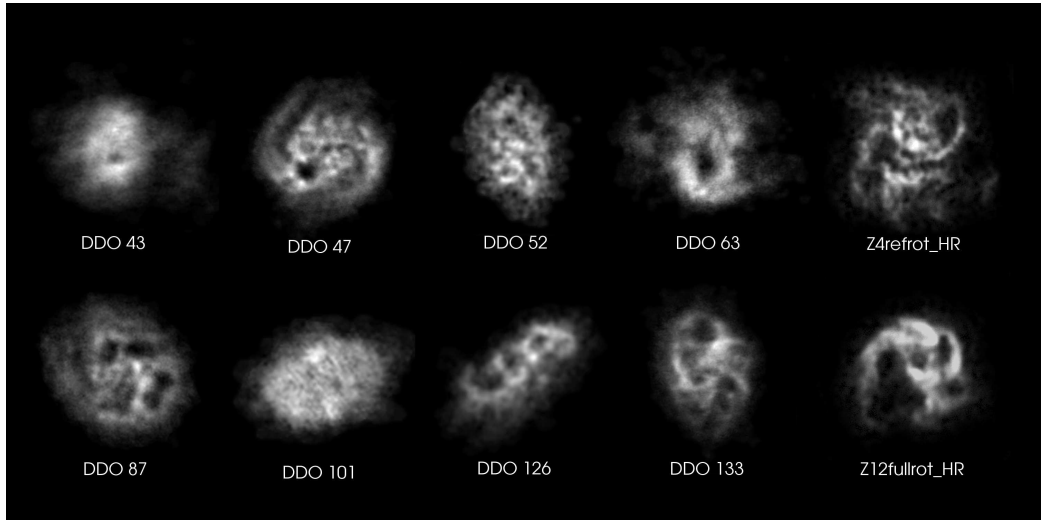
**Figure 5.7:** HI maps of our selection of dwarf galaxies from the Little Things sample (Hunter *et al.*, 2012) that is listed in Table 5.2 (image sizes are not to any absolute or relative scale). The two rightmost images are simulation snapshots taken from, respectively, Z4refrot_HR (snapshot at 11.73 Gyr) and Z12fullrot_HR (snapshot at 0.74 Gyr) (see Figure 5.6). A Gaussian filter and some random noise have been applied to the simulated images to make them into mock observations, and visually comparable to the real observations.

the two. In Figures 5.9 and 5.10 the same range of snapshots is used as in Figure 5.6 for making images of the highly ionized gas during the evolution of, respectively, the Z4refrot_HR and Z12fullrot_HR simulations. These have been separated in a low density component and a high density component. The high density component is always found in very small-scale structures (the dots), and represents the dense ionized gas which is around newly born star particles, before this star particle had enough time to disperse the dense gas clump it originated in by stellar feedback. The low density component (the vaguer structure) is much more extended, and represents ionized gas in more advanced stages of stellar feedback. The bright central features, that are actually inside the stellar body of the dwarf galaxy, are the result of several supernova events combining their force to blow local bubbles in the ISM, and they can generally be seen to correlate very well with the dark voids in the neutral gas (this forms nice "inverted" images of the ones in Figure 5.6, with previous dark neutral voids now filled with bright ionized blobs). The features on the outskirts are further along the feedback evolution, and are formed when the former feedback bubbles migrate out of the stellar body, are deformed by shear, and form outward expanding shells of ionized gas.
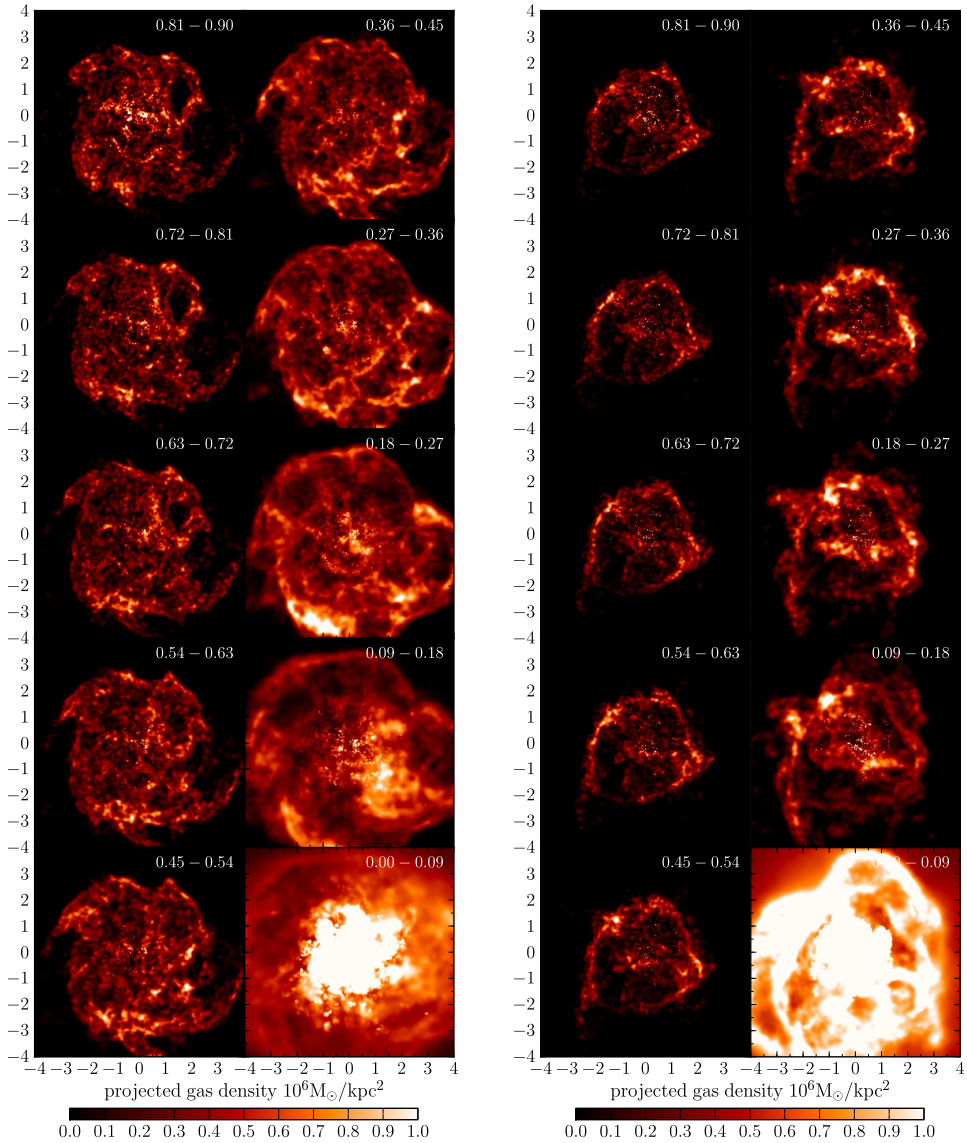
**Figure 5.8:** Map of different ionized gas ranges in our high-resolution models mentioned in Table 5.2. Left is Z4refrot_HR (snapshot at 11.73 Gyr), right is Z12fullrot_HR (snapshot at 0.74 Gyr). Density of the ionized gas is color coded according to the color bar on the respective figures. From top to bottom in the columns, gas particles have been selected with neutral fractions from [0.81-0.9] down to [0-0.09], which is indicated on each frame.

### 5.2.4   Power spectrum

A more quantitative way of comparing the spatial structure of the neutral gas component in our simulations, that we imaged in Section 5.2, with observations, is to calculate their power spectrum. This is a way to directly check whether the relative strengths of
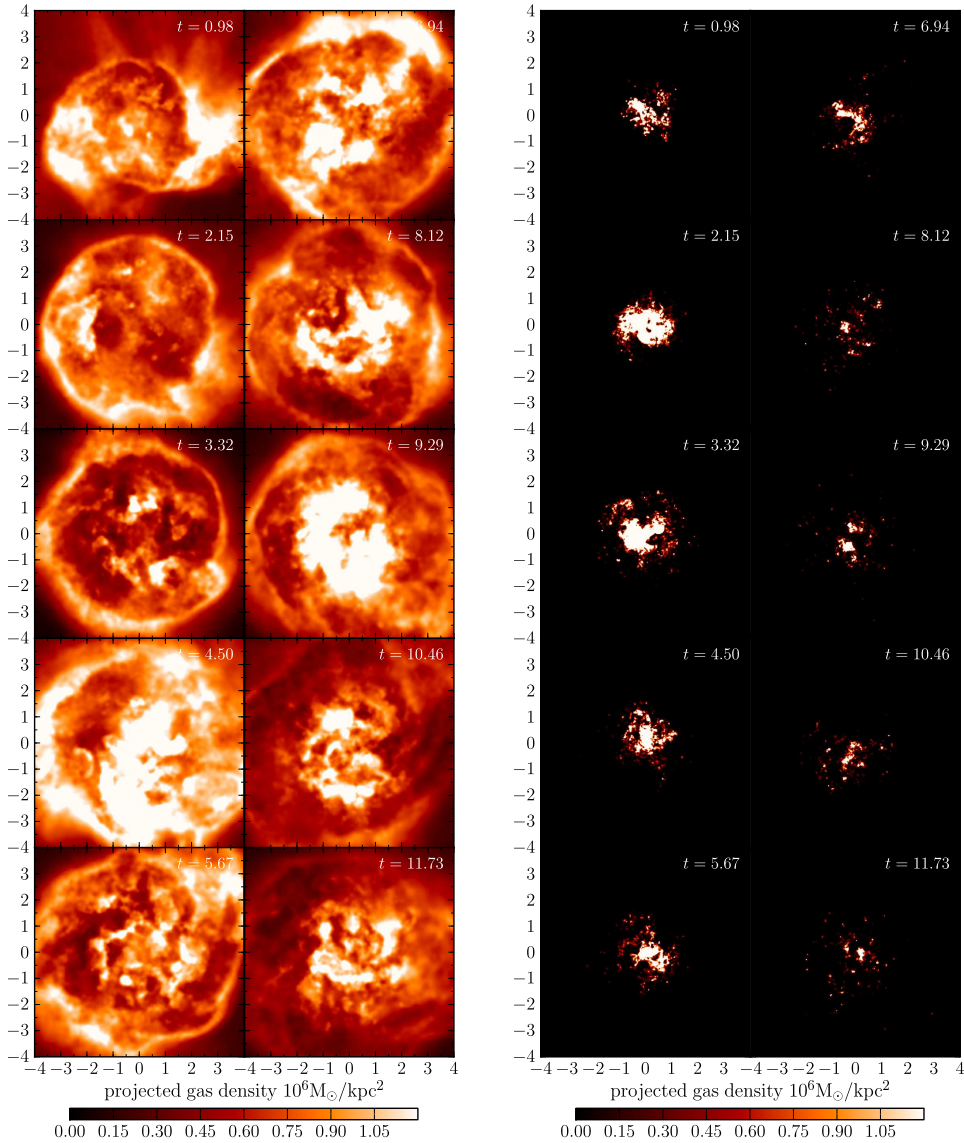
**Figure 5.9:** Ionized gas imaging of the same range of snapshots as in Figure 5.5, from simulation
Z4refrot_HR (see Figure 5.8). Selected gas particles have neutral fractions of 0.1 or
lower, with extra cuts on gas density: the left series shows the "low" density (below
$10^{-25}\,\mathrm{g/cm^3}$), while the right series shows the "high" density (above $10^{-24}\,\mathrm{g/cm^3}$).

the formed structures on different spatial scales in the neutral gas are realistic. The 1-
dimensional power spectrum is derived directly from the generated 2-dimensional images,
which are density maps of the neutral gas, in the following way:

- the 2D image is converted to its 2D Fourier transform in wavelength space

- to be able to get to a 1-dimensional power spectrum, we combine the two wavelength-
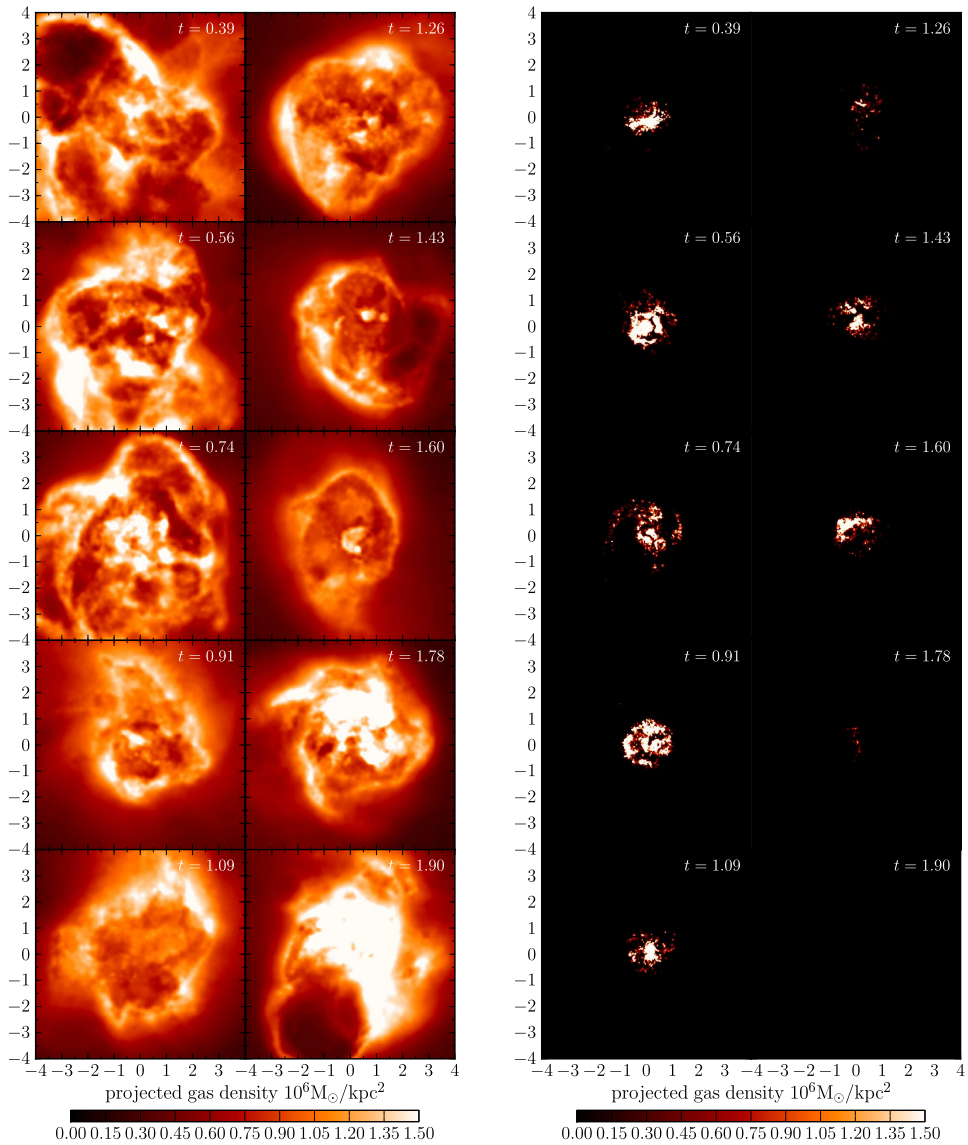
**Figure 5.10:** Ionized gas imaging of the same range of snapshots as in Figure 5.5, from simulation
Z12fullrot_HR (see Figure 5.8). Selected gas particles have neutral fractions of 0.1
or lower, with extra cuts on gas density. Left are the low density images, right the
high density images.

dimensions $\lambda_x$ and $\lambda_y$ to one $\lambda$, by taking $\lambda = \sqrt{\lambda_x^2 + \lambda_y^2}$

- this means that when we construct the power spectrum by binning the power in the
  $\lambda$ dimension, we are summing and averaging the power over circular annuli in the
  2D Fourier-transformed wavelength space.

This gives us a spectrum of the strength of the contribution of each wavelength - or structural scale - to the total spatial structure of the neutral gas in these images. The exact same procedure is also used to process observational images of the HI gas in dwarf galaxies, and in order to provide more equivalent conditions under which to compare the simulated images with the observations, we can alter the former by

- adding a Gaussian smoothing filter to the image to mimick observational seeing,

- employing a lower cutoff to the gas density value, under which the values are set to 0.

In Figure 5.11 the Fourier transforms and power spectra are shown of our high-resolution simulations, as well as for a selection of observed dwarf galaxies from the Little Things sample. The power spectra of the neutral gas in the simulations are seen to correspond very well to those of the HI gas in the observed dwarf galaxies, with very similar shapes and slopes. This means that the structures in the neutral gas and their intensities are comparable to those in observations, providing a solid quantitative benchmark for our dwarf galaxy models.

## 5.3   Line and continuum emission

Besides the neutral fraction of gas particles in Section 5.2, we can also derive emission flux tables from the knowledge of the chemical composition and ionization balance of the interstellar gas. These work with the same 5-parameter format as the cooling, heating, and neutral fraction tables, and the post-processing routines in our analysis software are therefore very similar to those developed for the neutral fraction analysis.

Theoretically speaking, almost any specific emission line or continuum emission can be calculated in this way. At the moment of writing, the following implemented tables are available:

- $H\alpha$ line emission,

- CII (157.7 micron) line emission,

The most straightforward way to use these tools in comparisons between simulations and observations is again by direct imaging. For this we produce standard SPH-rendered images, this time mapping the emission fluxes of all gas particles in the different lines/regions instead of the density of a selection of them, and compare these to observed images in the same wavelength regions, if available.

There are however also additional methods to compare the emission flux predictions from our chemical framework to reality, which are more quantitative and provide more insight into the general astrophysical behaviour of our models. Both the abovementioned $H\alpha$ and CII lines are traditional, often used "star formation rate indicators" for ongoing star formation in gas-rich galaxies. Investigating the relation between the evolution of the total emission in these lines and that of the star formation rate in our simulations, and comparing them with the observed trends, will provide a test on both
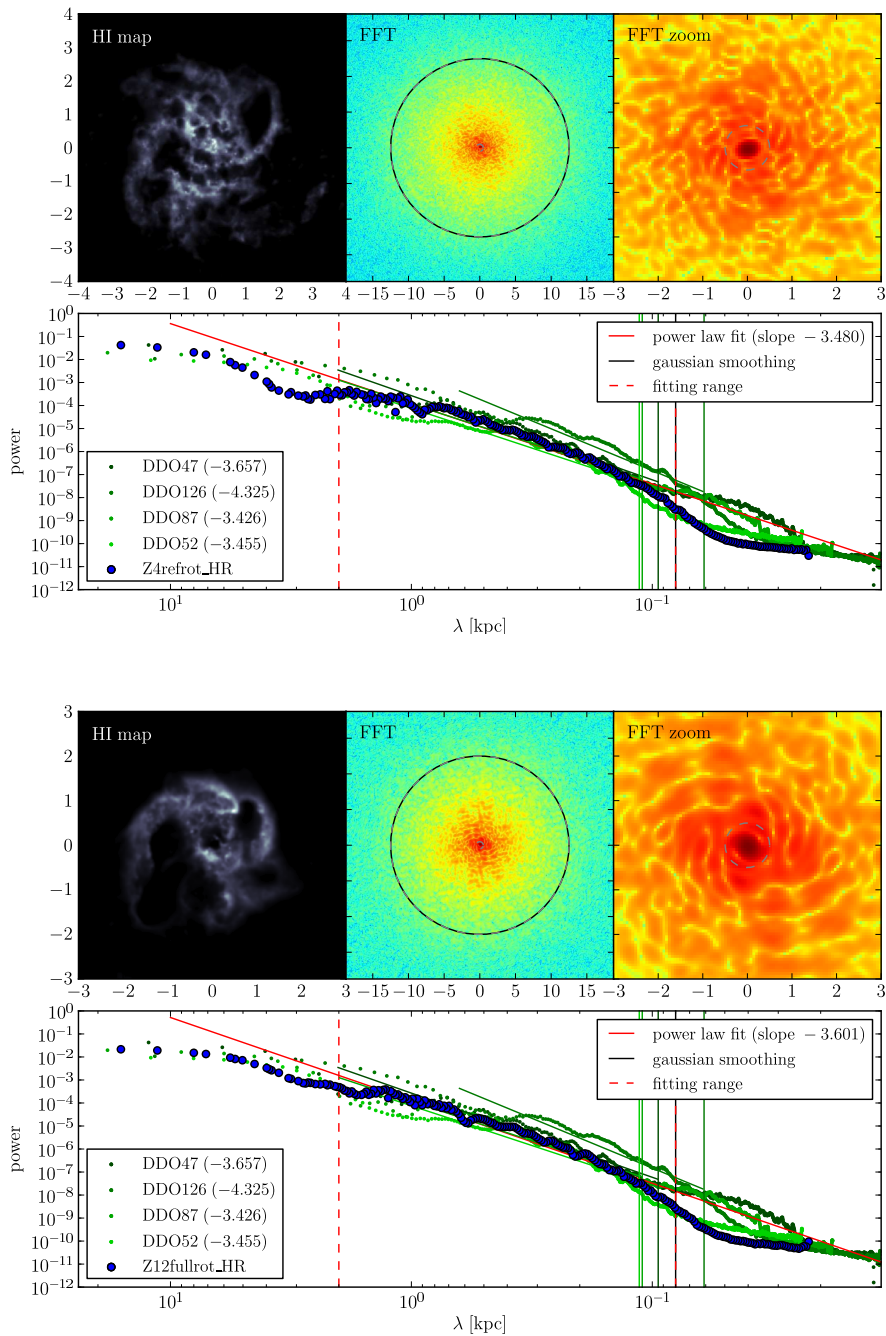
**Figure 5.11:** Neutral gas maps, 2D Fourier transforms, and the derived power spectra of
Z4refrot_HR (top plots, snapshot at 11.73 Gyr) and Z12fullrot_HR (bottom plots,
snapshot at 0.74 Gyr). A power law is fitted to the power spectrum, its slope is
indicated in the legend. Power spectra of dwarf galaxies from the Little Things
sample (Table 5.2, Figure 5.7) are also plotted, with vertical lines indicating their
respective seeing length scales, and power laws fitted to the spectra (slopes are in
the legend). The axes on the neutral gas map are in kiloparsec, and for the FFT
plots in wavelength numbers.

- the well-functioning of the astrophysical prescriptions in our dwarf galaxy models, to indicate whether our star formation factory is working properly and is producing the radiations it needs to produce, in the right quantities as in observed systems,

- the validity of using those two emission lines as star formation rate indicators in the first place - when is the correct time and place to do so and when not.

For the imaging analyses in this section, we use the same high-resolution reruns of our simulations and the same observed objects that we used in Section 5.2 for investigating the neutral fraction (see Table 5.2 for a summary of the observations and simulations).

### 5.3.1 Observations

The observational data we use to compare the H$\alpha$ imaging of our simulated dwarf galaxies with are taken from Hunter & Elmegreen (2004), and is the same selection of objects that we used before for the neutral gas analysis (see Table 5.2 for the list of objects, and their total H$\alpha$ luminosities). This data is made available through the LITTLE THINGS website. CII imaging, on the other hand, is not readily available in the literature, especially for dwarf galaxies. At best one can find CII contour maps of low spatial resolution, as for instance for the LMC and IC 10 in Israel $et~al.$ (1996), Madden $et~al.$ (1997), and Israel & Maloney (2011).

To investigate these emissions as star formation rate tracers, we only need values for the total emission of dwarf galaxies in these lines, which are easier to come by. In Kennicutt (1998) we find an observed relation between the H$\alpha$ fluxes of galaxies and their estimated star formation rates, while in Karachentsev & Kaisina (2013)[2] we find H$\alpha$ fluxes and independently derived star formation rates (from FUV flux) for a large sample of nearby galaxies with which we can compare our models (Makarov, private communication). From De Looze (2013) we use data on the total CII emissions and the star formation rates from resolved observations of dwarf galaxies to compare our models with.

### 5.3.2 Imaging

#### 5.3.2.1 H$\alpha$

Figure 5.12 shows a sequence of snapshots of our high-resolution simulations, imaged in the H$\alpha$ emission line. The structures seen in these images are very similar to those in the images of the high-density ionized gas in Figures 5.9 and 5.10 (almost one-to-one in several cases), indicating it is only produced in sufficiently dense, hot, and ionized regions in the ISM. Therefore it is a reasonably good tracer for recent star formation (for which it is also widely used in observations), which can be verified when comparing to the recently formed stars in Figure 5.5, and as we already hinted on in earlier research (Section 3.3.3). H$\alpha$, however, does not trace all newly formed stars, or not all equally well. It requires the star (particle) to already having sufficiently heated and ionized its surrounding dense

---

[2]http://www.sao.ru/lv/lvgdb/

gas, but not yet dispersed it significantly. This is why the tracing of newly formed stars by Hα is quite good in the more central and more dense regions in the gas, but much less so in the outer, and less dense regions (comparing Figure 5.5 with Figure 5.12). The environment in which the star is formed influences how quickly it will be able to disperse the surrounding dense gas clump out of which it formed.

A comparison with observations is made in Figure 5.13, where we show the Hα images of the selection of observed dwarf galaxies from the Little Things survey (Table 5.2, images from Hunter & Elmegreen 2004). Again we produced mock observations of our two high-resolution simulations for an as-direct-as-possible visual comparison. These have been generated by adding a bias value to the simulated Hα map, applying a Gaussian filter, and adding random noise. The similarity of the simulations with the observations is striking, although the vaguer emission structure in the background is somewhat stronger in the simulations than in the observations, which could be due to observational limitations such as a detection limit. The general look and behaviour of the Hα emission images in real dwarf galaxies is nicely reproduced in our simulated dwarf galaxies.

#### 5.3.2.2    CII

CII images of the same sequence of snapshots as before can be found in Figure 5.14. Although similar structures are seen as in the Hα emission, the CII emission is less confined to the high-density highly-ionized regions, and is more extended. Therefore it traces the newly formed stars better than Hα, in the sense that nearly all star particles plotted in Figure 5.5 can be seen to have a correlating bright structure in the CII image in Figure 5.14. The downside is that it also traces dense gas in general to a certain degree, because of the relatively low ionization potential of carbon, which is indicated by the fact that the general gas structure from the same snapshot in Figure 5.5 is quite recognizable in the CII emission images. This is much less clear in the Hα emission, which is much more confined to discrete small-scale regions. So besides the bright star-forming clumps, it shows considerable background emission. In some cases it can be seen to trace dense clumps that have not formed a star particle yet, but might be about to form a star particle in the next time steps. In a sense CII therefore traces both *recent* and *future* star formation.

As mentioned before, comparing the CII imaging to observations is not really possible, due to the few and low-resolution data that is available in this wavelength. We can only compare the total fluxes of our simulations with the observations, which we do in Section 5.3.3.

### 5.3.3    Emission fluxes as star formation rate indicators

Aside from the imaging in the previous sections, we can also simply use the total values of the model's radiation in these emission lines, and their connection to the current star formation rate. Since they are both well-known and often used star formation rate indicators, and there are no resolution issues, there is plenty of observational data to compare them with, unlike with the imaging. This will then also provide solid quantitative checks

**Figure 5.12:** Imaging of our high resolution models in the Hα emission line, with the same sequence of snapshots as in the previous figures. Left is Z4refrot_HR, right is Z12fullrot_HR, with the Hα flux color coded according to the color bar.

on these calculations, and the sub-grid astrophysical cycle in our models in general. In Figures 5.15 and 5.16 the evolution over time is plotted of the star formation rate and both emissions in our high-resolution models, as well as the former one versus the latter two. In this second type of plot, the whole data array is plotted, while giving the data points a color depending on the time to be able to see the evolution in time, together with observed galaxies/relations to compare with. A side note here is that Z12fullrot_HR has been run with much more snapshots than Z4refrot_HR. This means that we can follow the
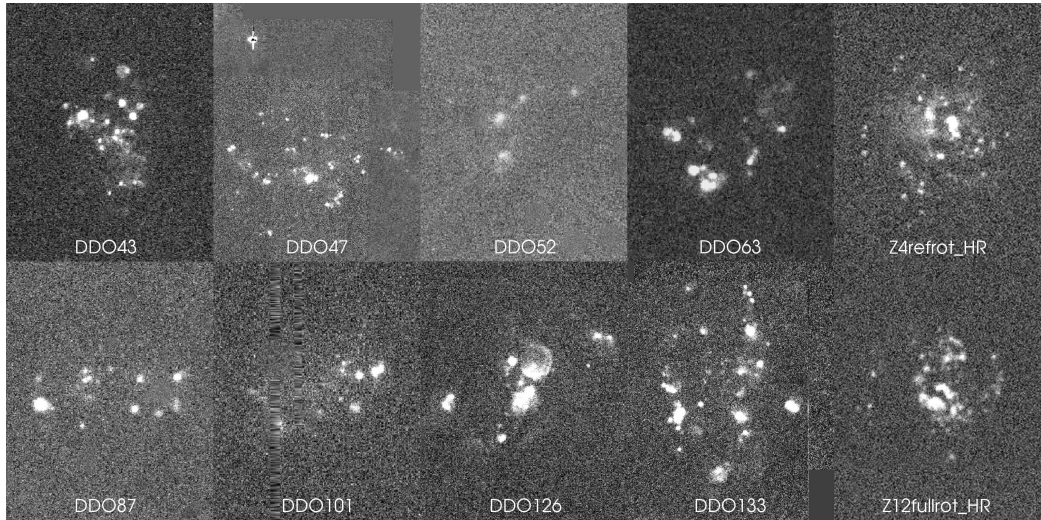
**Figure 5.13:** Hα maps of our selection of dwarf galaxies from the Little Things sample (Hunter *et al.*, 2012) (Hunter & Elmegreen, 2004) that is listed in Table 5.2 (image sizes are not to any absolute or relative scale). The two rightmost images are simulation snapshots taken from, respectively, Z4refrot_HR (snapshot at 11.73 Gyr) and Z12fullrot_HR (snapshot at 0.74 Gyr) (see Figure 5.12). A bias, a Gaussian filter, and some random noise have been applied to the simulated images to make them into mock observations, and visually comparable to the real observations.

evolution of the former in much higher time detail and resolve the small-scale peaks and lulls in the SFR, while the evolution of the latter is much more averaged in time. The data points of Z12fullrot_HR will therefore show more spread and reach to much lower SFRs, while Z4refrot_HR's evolution will be much more localized on the plot. Two things that can be immediately noted from Figures 5.15 and 5.16 are that, in both simulations, the Hα emission is about one order of magnitude *off* the relation derived from observations, while the CII emission compares *very* well to the observed trend in dwarf galaxies.

#### 5.3.3.1 Hα

The Hα emission appears to reach high values from almost the moment star formation begins, there is no buildup necessary at all, after which it gradually decreases throughout the evolution. This can be seen on the SFR-emission plots, where the model reaches its most upper-right position at the very beginning of the simulation (with an emission value that is more than an order of magnitude higher than the observational relation), and gradually moves down and left on the plot, on average, and approaches the observed relation. From our models we could therefore conclude that dwarf galaxies seem to obey to an SFR-Hα relation with a *slightly* flatter slope than the one from Kennicutt (1998), which was not derived from dwarf galaxies. However, they also lie outside the spread of the data points from Karachentsev & Kaisina (2013), which have independent SFR
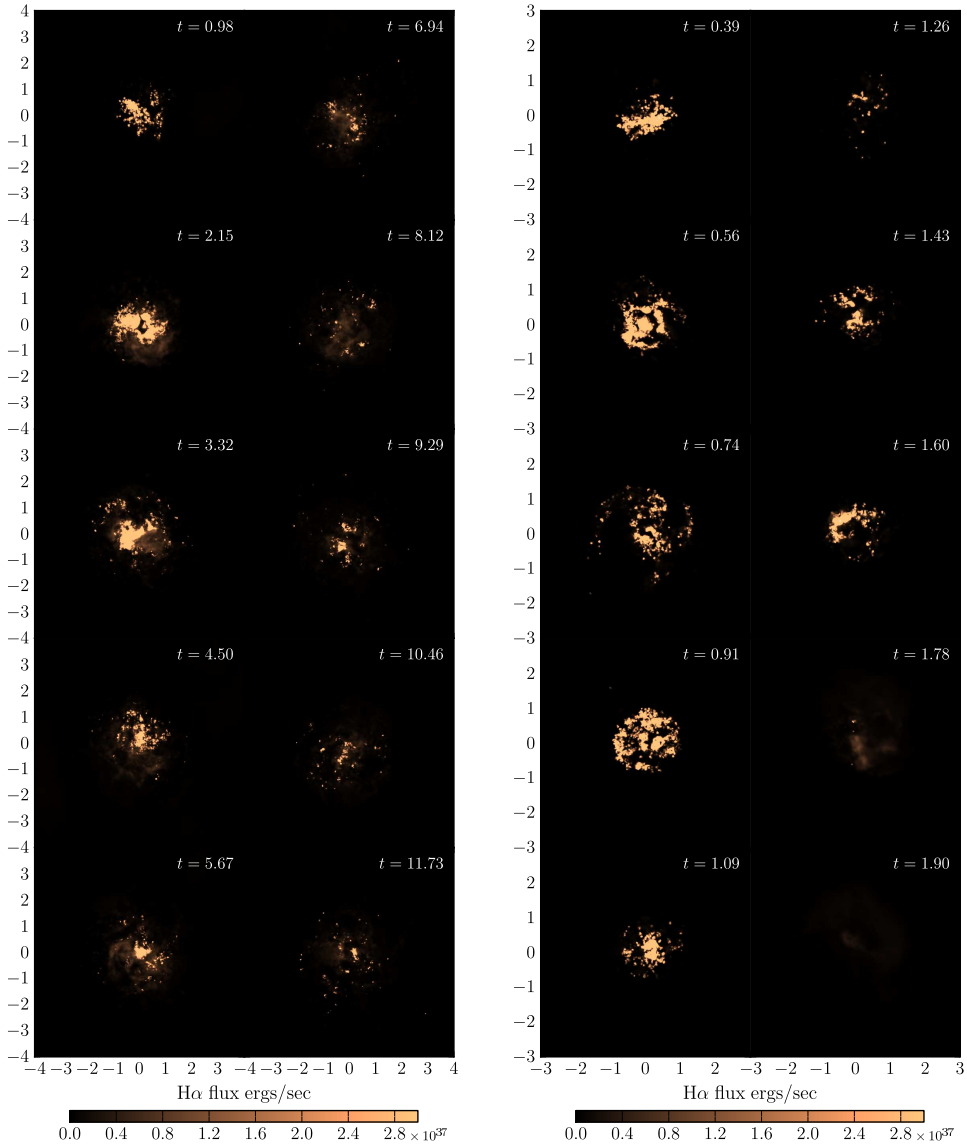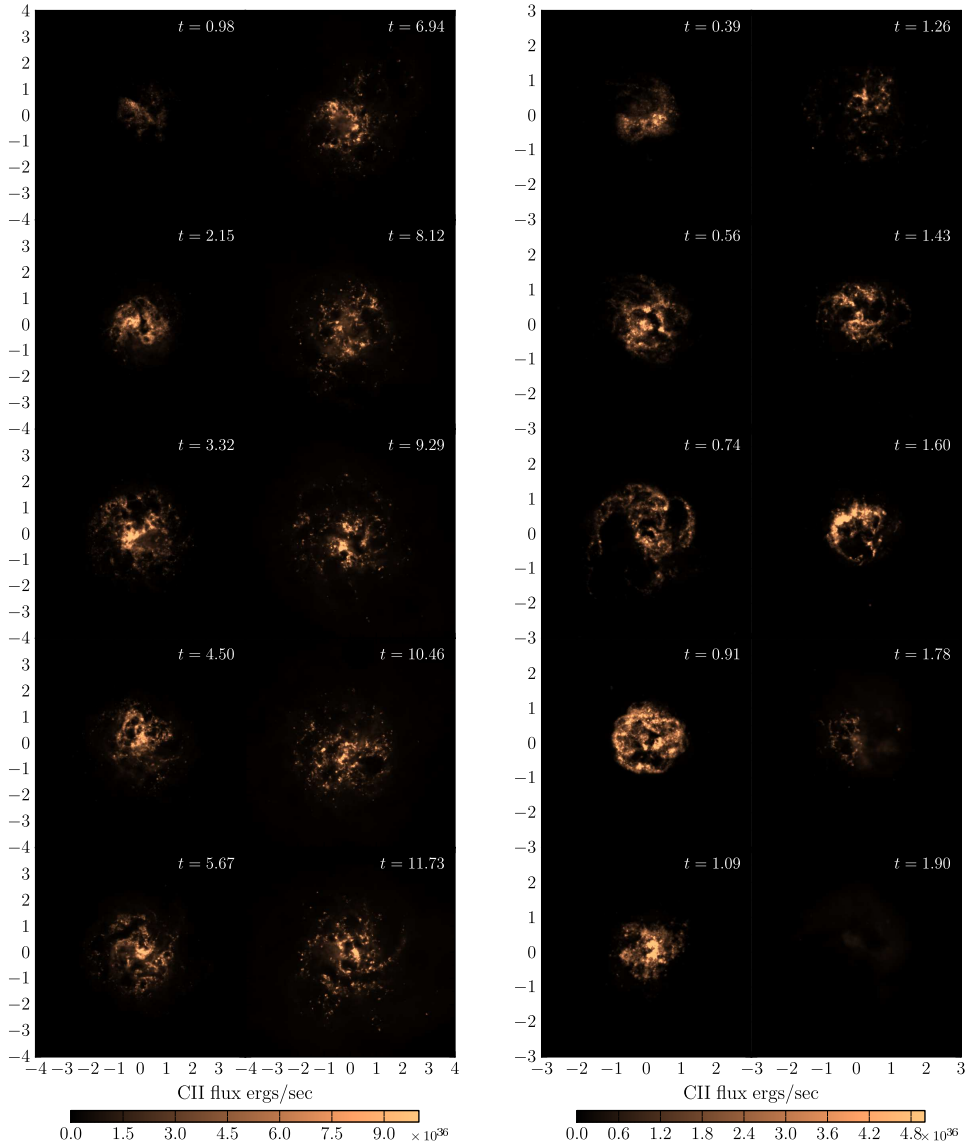
**Figure 5.14:** Imaging of our high resolution models in the CII emission line, with the same sequence of snapshots as in the previous figures. Left is Z4refrot_HR, right is Z12fullrot_HR, with the CII flux color coded according to the color bar.

measurements, and the values for the total H$\alpha$ emission that are shown in Table 5.2 seem to be about an order of magnitude higher than the values of the observed dwarf galaxies. This discrepancy could be due to resolution effects, because our star particles are in effect stellar populations. In real life the HII regions are closely located around newly born stars, while in simulations the whole stellar population spreads its feedback over the neighbouring gas particles according to the SPH smoothing kernel, in a sense making an artificially large HII region around it that emits an excess of H$\alpha$ radiation.

Dust, which is not accounted for in our simulations, could also contribute to lowering the Hα flux. We also note that, whatever the actual relation is, the spread that our models show on it is relatively large, compared to CII emission, in any case making it a not very accurate star formation tracer.

### 5.3.3.2  CII

The CII emission does need to build up, because it needs metals to be produced in the ISM before it can begin being an effective cooling line for the gas. In the evolution plots it can be seen that the CII emission gradually rises during roughly the first quarter of the model's star formation period, while on the SFR-emission plots the model gradually approaches the observational trend, in Z12fullrot_HR in "loops" that successively flatten along the observed slope. Once it reaches this, it either converges to a definite point on the relation (in the case of Z4refrot_HR), or it moves up and down along the relation, reproducing the same slope (in the case of Z12fullrot_HR) - the difference being due to the difference in time resolution of the two simulations, as mentioned before. From this we can conclude that, on the one hand, during star formation the ISM in our simulations produces exactly the radiation that it is expected to produce and with the correct behaviour. On the other hand, from the evolution of our models, we also conclude that CII can only be used as a reliable star formation tracer when the dwarf galaxy has built up enough metals for the CII line to become efficient. Once its efficiency saturates, however, it appears a very reliable indicator for current star formation in a star-forming dwarf galaxy, with a relatively low spread on the relation (compared to Hα).
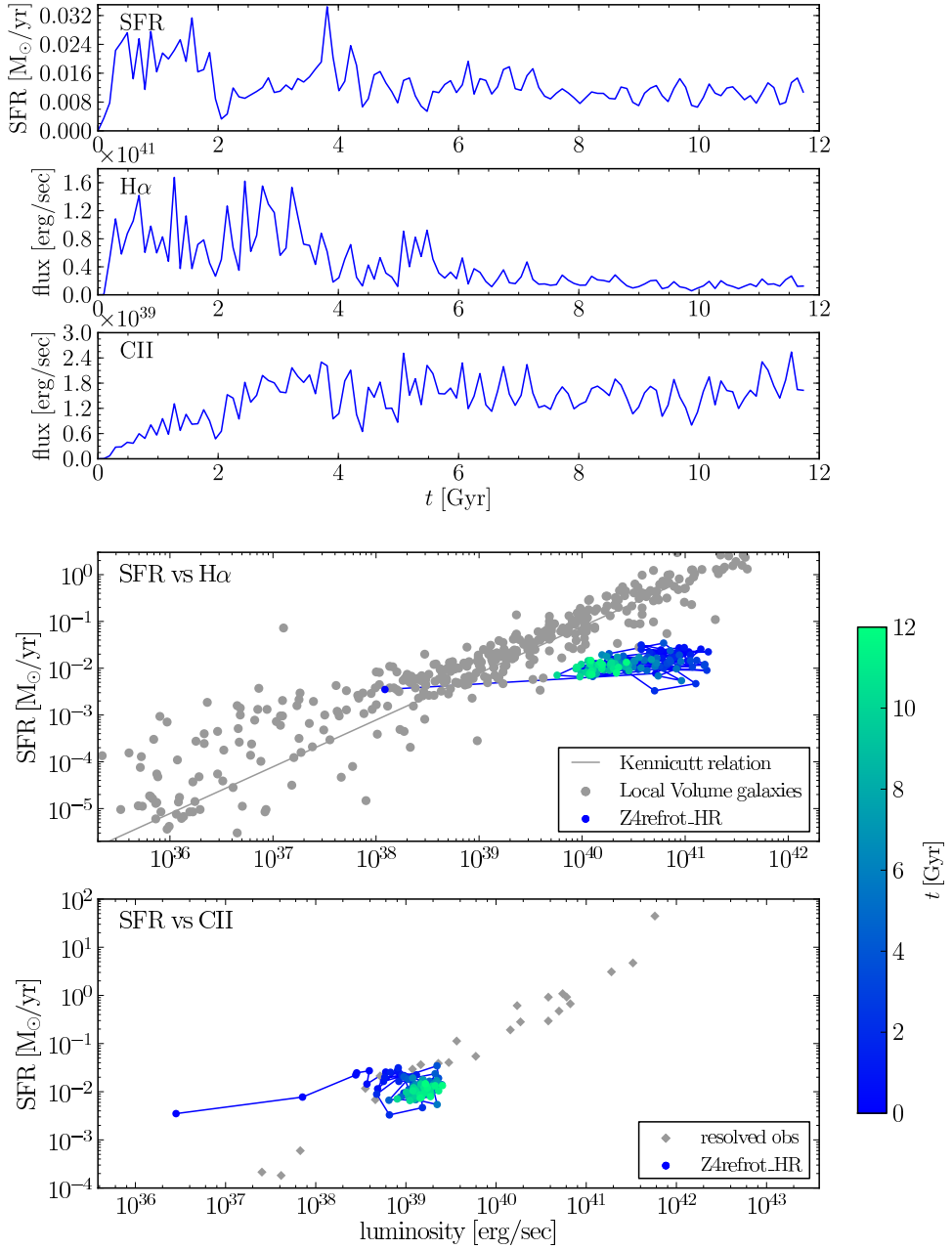
**Figure 5.15:** Upper panels show the evolution of the SFR, and the Hα and CII emissions during the run of Z4refrot_HR, our high-resolution reference simulation with the old 3D cooling that starts at redshift 4.3. On the lower two panels these evolutions are shown in plots of the SFR versus the two emissions. The color denotes the time in the evolution according to the color bar on the right, and the grey dots/lines are observations they are compared with (Hα relation from Kennicutt 1998, Hα-SFR data from Karachentsev & Kaisina 2013, CII-SFR data from De Looze 2013).
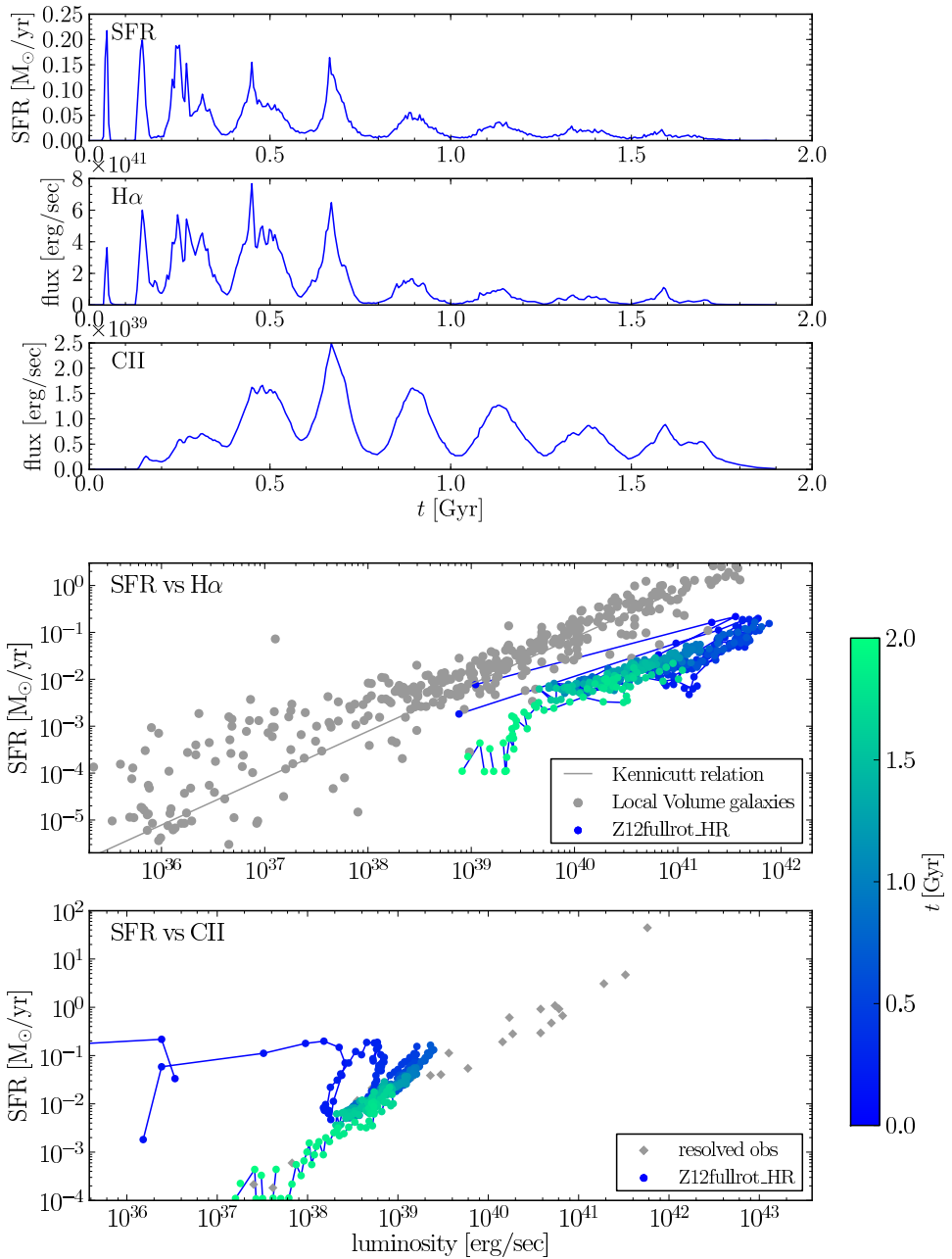
**Figure 5.16:** Similar plot as Figure 5.15, but now for Z12fullrot_HR, our high-resolution reference simulation with the new 5D cooling and heating that starts at redshift 12. The color mapping has been rescaled to a time range between 0 and 2 Gyr, since this model only forms stars in that period.

# 6
# Summary

*Understanding star formation is one of the oldest and most important questions in galactic astrophysics* - from the conditions under which an individual star is born out of a dense gas cloud, over the spatial, chemical and temporal distributions of stellar populations, to the global modes in which bulk star formation proceeds in galaxies. In all these matters, dwarf galaxies in particular provide a very useful tool for investigating the astrophysical mechanisms behind the phenomena, both in the observational and the theoretical realm. Their modest dimensions and masses make gravity a less dictating factor during their formation and evolution, but instead allow for other physical processes to be more strongly expressed in their behaviour. This sensitivity, to their internal properties as well as their environment, can provide us with vital clues on the fundamental issues of star formation and galaxy formation.

Observationally, they are the closest galactic objects outside of our own Galaxy, and boast some of the best and deepest observational data available. Numerically, they can be simulated with high spatial and physical detail, at relatively low computational cost. Mainly this latter property is exploited in this thesis research.

## Virtual dwarf galaxy models

The tools at our disposal are N-body/SPH dwarf galaxy models, which we employ as galactic laboratories to experiment in. We simulate the formation and evolution of dwarf galaxies, and try to explain the astrophysical processes in observations. These models encompass the primordial ingredients (gas and dark matter), as well as self-consistent pre-

scriptions for the astrophysical processes that transform them into virtual dwarf galaxies (cooling, star formation, feedback). Improving and expanding their physical and computational performance is a continuous effort alongside the astronomical research done with them.

The modifications made to the models during this research mainly focused on improving the star formation scheme, to go from the classical "old" low density threshold for star formation of $0.1\,\mathrm{amu/cm^3}$ (LDT) to the "new" high density threshold of $100\,\mathrm{amu/cm^3}$ (HDT). However, since this parameter strongly affects the physical behaviour of the gas, it entails much more extensive modifications than just dialing up this value, in order to produce realistic dwarf galaxies that accord with the observed scaling relations. To reach these high densities, the interstellar gas in our simulations needs to be able to cool below $10^4\,\mathrm{K}$ to form cold, high density clumps that will be the cradles of star formation. On the other hand, to battle these high densities in the clumps and produce dwarf galaxies that are not too concentrated, the efficiency of the supernova feedback needs to be increased so that these high density clumps can be dispersed again after having formed star(particle)s. Furthermore, for rotating dwarf galaxies to form stars in this scheme, it appears the initial setup of the gas already needs to be centrally concentrated to a certain degree (with e.g. a pseudo-isothermal profile), and they should receive their initial rotation with a profile that goes to 0 in the center (e.g. and arctangens-shaped profile).

We call this the "HDT-scheme" for star formation, that provides a *much more detailed representation of star formation in a simulated interstellar medium (ISM) by producing cold, dense, star forming clouds*, than using the classical low density threshold value. It is also characterized by shorter star formation timescales and lower stellar masses produced by the models.

# The role of angular momentum

The total mass of a dwarf galaxy is one of the most important parameters to determine its evolution. It will mainly dictate the amount of stars that is formed, and therefore determine the galaxy's position on the scaling relations. The specific modes of star formation in a dwarf galaxy are however not solely set by its total mass. In this context we are specifically interested in the effects that angular momentum has on the behaviour and evolution of our dwarf galaxy models.

We find in our simulations that *angular momentum is an important second parameter of dwarf galaxy evolution, which differentiates between different star formation modes*:

- In non-rotating models the gas collapses very centrally, creating a strong centralized star formation event and subsequent strong supernova feedback, that causes a temporary global blowout of gas - after which the gas cools again and the process repeats. This creates a bursty and centralized star formation mode, that also gets more centralized over subsequent bursts.

- When rotating, however, the gas does not readily fall to the center but spirals around,

making star formation much more extended over a larger area. The supernovae are now also not very concentrated, and only combine locally to blow away gas to low density bubbles, instead of causing gas blowout on a global scale. This leads to a continuous and spatially extended star formation mode, that does not shrink to the center over time.

These star formation modes, in turn, have their consequences for the *spatial distribution of metals in the stellar populations*:

- A bursty, centralized star formation mode will naturally enrich the central regions more than the outskirts of a dwarf galaxy, and therefore give rise to negative radial stellar metallicity gradients - meaning the average metallicity of stellar particles decreases with increasing radius from the center.

- A continuous, extended star formation mode will equally enrich the whole galaxy, and cause flat radial stellar metallicity profiles across the entire galaxy body.

This "centrifugal barrier mechanism" is at least qualitatively reminiscent of the blue compact dwarf (BCD) - dwarf irregular (dIrr) dichotomy, where our rotating models show and explain all the characteristic properties of the latter. It also provides a nice and plausible explanation for the combinations of metallicity profiles and rotation that is seen in observations.

# The properties of metallicity gradients

We focus further on the evolution of the radial stellar metallicity gradients themselves that are formed in our non-rotating dwarf galaxy models. They compare or scale well to observed gradients of Local Group dwarf spheroidal galaxies (dSph), showing realistic slopes, shapes, and absolute metallicities.

*The bursty, centralized star formation modes are found to gradually build up the metallicity gradients.* Each star formation episode by itself is strongly centrally concentrated, enriching the center more than the outer regions, and subsequent star formation episodes also generally become more centrally concentrated, adding their own contribution to the overall gradient. Between star formation episodes there are no signs of the metallicity gradient weakening. Even when truncating the star formation completely at a certain point during the simulation, by an idealized instant gas stripping event, *the gradients appear to be very robust and easily survive several gigayears* on their own.

We look further into the underlying stellar orbits, in particular to how strongly they statistically diverge from their average original radius where the star(particle) was born. We find that these *"orbital displacements" are very limited in all our dwarf galaxy models*, of the order of only fractions of the half light radius ($<0.5$) over time-spans of 5 to 10 Gyr. In the dwarf galaxy regime there do not seem to be any radically orbit-changing processes at work, such as the radial migration process that is active in massive disc galaxies, where stars are scattered off major spiral structures. These structures are absent in our dwarf

galaxies, so that only the much milder dynamical heating is able to change stellar orbits over time, by turbulent gas motions and scattering of stars off dense gas clumps. These dynamical features of the stellar body allow a long-term survival of population gradients in dwarf galaxies.

Although the orbital displacements are generally very limited, the density threshold for star formation is found to have a significant influence. Compared to the LDT, the HDT scheme for star formation produces high density, cold, star forming clumps in the ISM - which will cause a stronger dynamical heating of the stellar body in our dwarf galaxy models. The LDT simulations actually barely show any dynamical heating at all, while the HDT simulations do show a clear dynamical footprint of this heating, albeit limited in absolute terms.

# Chemical framework

In the current state of our models we have at our disposal a newly developed full chemical framework. At the basis of it is a calculation scheme to determine the chemical composition and ionization equilibrium of the interstellar gas in our simulations, from a limited number of global properties of the gas particles. This allows for calculating practically every desired property of the physical state of the gas.

The main supplied features of this chemical framework that we implemented in our dwarf galaxy simulations, are fully self-consistent radiative cooling and heating tables that take all relevant radiative processes into account, as well as the UV background, the interstellar radiation field, and shielding effects. During runtime, these tables are interpolated on with a general $N$-dimensional interpolator, to determine the energy input and output of a gas particle through radiative processes. When running such simulations of our dwarf galaxy models, the radiation fields pump a considerable amount of energy into the ISM, significantly dispersing it. To keep the models on the scaling relations, this requires us to dial the feedback efficiency down again to more realistic values. It is now easier for supernovae to disperse the cold, dense gas clumps after they formed stars. Starting simulations after the epoch of reionization will subject the models to a strong UV background from the very beginning, causing a significant decrease in the produced amount of stellar mass. When gas is blown to lower densities it cannot shield itself anymore and will be fully bathed in the background radiation, making it virtually impossible to cool again and reach densities high enough for star formation. Starting simulations before the epoch of reionization, however, significantly decreases the effect of radiative heating. There is only the interstellar radiation field present, and most of the stellar mass of the dwarf galaxy models is anyway formed before reionization and the UV background start playing a role.

Additional features of the chemical framework that we implemented to use in post-processing of the simulated ISM include the calculation of

- the neutral fraction of gas particles, enabling us to select gas on the basis of their relative amount of neutral or ionized gas. Imaging the gas with neutral fractions of

0.95 and above compares well with observed HI images of gas-rich dwarf galaxies - both visually, in mock observations, and more quantitatively by the total neutral gas mass and our calculations of the power spectrum of structures of both the simulated and observed images. Imaging the simulated gas selected in the more ionized ranges, with an additional selection on gas density, allows us to clearly identify the different astrophysical phases of the gas. We can separately image the dense but highly ionized HII regions around newly born stars which are heated by supernova, and the more dilute ionized gas in more advanced stages of stellar feedback, filling supernova-blown voids in the galaxy and subsequently extending beyond the stellar body in giant shells of expelled ionized gas.

- emission fluxes of gas particles, in any emission line or wavelength range such as H$\alpha$ and CII. Imaging these gives good visual comparisons to observational images, and the ratios of total emission values to the star formation rate of the model provides us with tests on both our models, and the appropriateness of specific emissions as star formation rate tracers. Our models are seen to exhibit realistic astrophysical behaviour, and indicate that H$\alpha$ is not a very good star formation rate indicator due to the big spread - while CII, after enough metals have been produced, does appear to be a very reliable star formation rate tracer.

## Visualisations

An important part of numerical research and analysis in astronomy is visualizing the results. We do this for our dwarf galaxy models in the first place in the "standard" ways of SPH-rendering and scatter plots, but we also expanded our tools to other ways of visualizing. We are now able to present our models with 3D rendering packages, and a ray-tracing code that produces very realistic-looking artificially observed images of the simulated ISM. Both can also be used in stereo mode, both with the classical anaglyph stereo method (with the red-and-blue glasses), and the current full-color Dolby 3D Stereo system.

# 7

# Nederlandstalige samenvatting

*Het begrijpen van stervorming is een van de oudste en belangrijkste vragen van extragalactische astrofysica* - gaande van de specifieke omstandigheden waaronder een individuele ster gevormd wordt uit een dichte gaswolk, over de ruimtelijke, chemische en tijdelijke verdeling van stellaire populaties, tot de globale modes waarin massale stervorming zich voortplant in galaxieën. In al deze zaken zijn dwerggalaxieën een zeer nuttig werktuig om de astrofysische mechanismes achter de fenomenen te onderzoeken, zowel in het observationele als het theoretische domein. Hun bescheiden afmetingen en massas maken van de zwaartekracht een minder overheersende factor tijdens hun vorming en evolutie, en geeft andere fysische processen de kans tot uiting te komen in hun gedrag. Deze gevoeligheid, voor zowel hun interne eigenschappen als hun omgeving, kan ons waardevolle hints verschaffen over de fundamentele kwesties van stervorming en galaxievorming.

Observationeel gezien, zijn ze de dichtstbijzijnde galactische objecten buiten onze eigen Melkweg, en beschikken ze over sommige van de beste en diepste observationele data die beschikbaar zijn. Numeriek gezien, kunnen ze gesimuleerd worden met hoog ruimtelijk en fysisch detail, tegen een relatief lage computationele kost. Vooral deze laatste eigenschap is uitgebuit in dit thesisonderzoek.

## Virtuele dwerggalaxiemodellen

De werktuigen die ons ter beschikking staan zijn N-body/SPH dwerggalaxiemodellen, die we gebruiken als galactische laboratoria om in te experimenteren. We simuleren er hun vorming en evolutie mee, en proberen de astrofysische processen in observaties te

verklaren. Deze omvatten zowel de primordiale ingrediënten (gas en donkere materie), als zelf-consistente voorschriften voor de astrofysische processen die deze transformeren in virtuele dwerggalaxieën (koeling, stervorming, feedback). Het verbeteren en uitbreiden van hun fysische en computationele prestaties is een voortdurende inspanning die geleverd wordt langszij het astronomische onderzoek dat ermee verricht wordt.

De verbeteringen die gedurende dit onderzoek tot stand zijn gekomen richtten zich vooral op het verbeteren van het *stervormingsschema*, om van de klassieke "oude" lage dichtheids-drempelwaarde voor stervorming $0.1 \, \mathrm{amu/cm^3}$ (LDT) over te gaan naar de "nieuwe" hoge waarde van $100 \, \mathrm{amu/cm^3}$ (HDT). Maar aangezien deze parameter het fysische gedrag van het gas sterk beïnvloedt, zal dit echter veel meer verregaande aanpassingen met zich mee-brengen dan gewoon de waarde verhogen, teneinde nog steeds dwerggalaxieën te produc-eren die voldoen aan de schalingsrelaties. Om deze hoge dichtheden te bereiken, moet het interstellair gas in onze simulaties de mogelijkheid hebben om te koelen tot beneden $10^4 \, \mathrm{K}$ om koude, hoge-dichtheids wolken te vormen die de wieg zullen vormen van toekomstige stervorming. Aan de andere kant, om deze hoge dichtheden te kunnen bevechten binnen die wolken, en dwerggalaxieën te produceren die niet te geconcentreerd zijn, moet de ef-ficiëntie van de supernova feedback verhoogd worden zodat de wolken terug uiteengedreven kunnen worden nadat ze ster(deeltjes) gevormd hebben. Verder blijkt dat het vormen van sterren in roterende dwerggalaxieën vereist dat het gas initiëel al met een zekere centrale concentratie moet opgesteld worden (met bijvoorbeeld een pseudo-isotherm profiel), en dat ze hun initiële rotatie zouden moeten ontvangen met een profiel dat naar 0 gaat in het centrum (bijvoorbeeld een boogtangens-vormig profiel).

Dit noemen we het "HDT-schema" voor stervorming, dat een *veel gedetailleerdere voorstelling is van stervorming in een gesimuleerd interstellair medium (ISM) door het produceren van koude, dichte, stervormende wolken*, dan de klassieke lage waarde van de dichtheidsdrem-pel. Deze modellen hebben ook karakteristiek een kortere tijdsschaal voor stervorming, en produceren lagere stellaire massas.

# De rol van draaimoment

De totale massa van een dwerggalaxie is een van de belangrijkste parameters die zijn evolutie bepalen. Het zal hoofdzakelijk vastleggen hoeveel sterren er gevormd worden, en bepaalt daarmee de positie van de galaxie op de schalingsrelaties. De specifieke *modes van stervorming* in een dwerggalaxie zijn echter *niet* enkel en alleen vastgesteld door zijn totale massa. In deze context zijn we specifiek geïnteresseerd in de effecten die het draaimoment heeft op het gedrag en de evolutie van onze dwerggalaxiemodellen.

We vinden in onze simulaties dat het *draaimoment een belangrijke tweede parameter is in dwerggalaxie-evolutie, die differentieert tussen verschillende stervormingsmodes*:

- In niet-roterende modellen stort het gas heel centraal in, creëert sterke geconcen-treerde stervorming en bijgevolg sterke supernova feedback, die een tijdelijke maar globale uitstoot van gas veroorzaakt - waarna het gas opnieuw koelt en het pro-ces zich herhaald. Dit veroorzaakt een *zeer gecentraliseerde stervormingsmode met*

*opeenvolgende uitbarstingen (="bursty").*

- Waneer er echter rotatie aanwezig is, zal het gas niet rechtstreeks instorten maar eerder rondom spiraleren, hetgeen de stervorming over een groter gebied uitsmeert. De supernovae zijn bijgevolg ook niet erg geconcentreerd, en combineren hun krachten op een meer lokaal vlak waarbij ze gas wegblazen tot lage-dichtheids bubbels, in plaats van gasuitstoot op een globale schaal te veroorzaken. Dit leidt tot een *continue en ruimtelijk uitgespreide stervormingsmode, die niet krimpt over verloop van tijd.*

Deze stervormingsmodes hebben op hun beurt hun gevolgen voor de *ruimtelijke verdeling van metalen in de stellaire populaties*:

- Een bursty, gecentralizeerde stervormingsmode zal op natuurlijke wijze de centrale gebieden meer verrijken dan de buitenste regionen van een dwerggalaxie, en daardoor aanleiding geven tot *negatieve radiële stellaire gradiënten* - wat betekent dat de gemiddelde metalliciteit van de sterdeeltjes daalt met toenemende afstand tot het centrum.

- Een continue, uitgespreidde stervormingsmode zal de hele galaxie op gelijkmatige manier verrijken, en veroorzaakt een *vlak radiëel stellair metalliciteitsprofiel* over het hele galactische lichaam.

Deze "centrifugaalbarrière" doet kwalitatief denken aan de tweespalt tussen blauwe compacte dwergen (BCD) en onregelmatige dwergen (dIrr), waarbij onze roterende modellen alle karakteristieke kenmerken vertonen van deze laatste. Het levert ook een goede en plausibele verklaring voor de combinaties van metalliciteitsprofielen en rotatie die voorkomt in observaties.

# De eigenschappen van metalliciteitsgradiënten

We focussen ons verder op de *evolutie van de radiële stellaire metalliciteitsprofielen* zelf, die gevormd worden in onze niet-roterende dwerggalaxiemodellen. Ze vergelijken of schalen zich goed in verhouding met waargenomen gradiënten van sferoïdale dwerggalaxiën (dSph) in de Lokale Groep, en vertonen realistische hellingen, vormen, en absolute metalliciteitswaarden.

De bursty, gecentralizeerde stervormingsmodes blijken *stelselmatig de metalliciteitsgradiënten op te bouwen*. Elke periode van stervorming is op zichzelf al centraal geconcentreerd, waarbij deze het centrum meer verrijkt dan de buitenste gebieden, en de opeenvolgende stervormingsperiodes worden ook steeds meer en meer geconcentreerd, waarbij ze hun bijdrage toevoegen aan het totale gradiënt. Tussen afzonderlijke stervormingsperiodes is er geen teken van verzwakking in het metalliciteitsgradiënt. Zelfs wanneer de stervorming volledig wordt stopgezet op een bepaald punt in de simulatie, door een geïdealizeerd en instantaan strippen van het gas, blijken de gradiënten zeer robuust en *overleven ze gemakkelijk verschillende gigajaren* op zichzelf.

We kijken hierbij verder naar de onderliggende stellaire banen, en dan vooral naar hoe sterk, statistisch gezien, ze afwijken van de originele radius waar het sterdeeltje werd geboren. We vinden dat deze *"orbitale verplaatsingen" zeer beperkt zijn* in *al* onze dwerggalaxiemodellen, en slechts fracties bedragen van de halflichtstraal (<0.5), over tijdsspannes van 5 tot 10 gigajaar. In het dwerg-regime lijken er geen processen aan het werk te zijn die de banen radicaal veranderen, zoals het radiële migratieproces dat actief is in massieve schijfgalaxieën, waar sterren verstrooid worden door grote spiraalstructuren. Deze structuren zijn niet aanwezig in onze dwerggalaxiemodellen, zodat enkel het veel mildere *dynamisch verhittingsproces* in staat is om de stellaire banen te veranderen over verloop van tijd, door turbulente gasbewegingen en verstrooien van sterren door dichte gaswolken. Deze dynamische eigenschappen van het stellaire lichaam *laten toe dat populatiegradiënten op lange termijn kunnen overleven in dwerggalaxieën.*

Hoewel de orbitale verplaatsingen over het algmeen zeer beperkt zijn, vinden we wel dat de dichtheidsdrempel voor stervorming een duidelijke invloed heeft. Vergeleken met de LDT, produceert het HDT schema voor stervorming koude, hoge-dichtheids wolken in het ISM - hetgeen een sterkere dynamische verhitting van het stellaire lichaam teweeg zal brengen in onze dwerggalaxiemodellen. Het LDT scheme vertoont zelfs nauwelijks enige dynamische verhitting, terwijl de HDT simulaties wel een duidelijke dynamiche voetafdruk vertonen van deze verhitting, hoewel het in absolute termen beperkt blijft.

# Chemisch kader

In de huidige staat van onze modellen hebben we een recent ontwikkeld *chemisch kaderwerk* tot onze beschikking. Aan de basis ervan ligt een berekeningsschema om de totale chemische samenstelling en het ionisatie-evenwicht te berekenen van het interstellaire gas in onze simulaties, gebruik makende van slechts een beperkt aantal globale eigenschappen van de gasdeeltjes. Dit laat toe praktisch elke eigenschap van de fysische toestand van het gas te berekenen.

De belangrijkste functionaliteit van dit chemisch kaderwerk die we hebben geïmplementeerd in onze dwergalaxiesimulaties, zijn *volledig zelf-consistente radiatieve koelings- en verhittingstabellen*, die alle relevante radiatieve processen in rekening brengen, alsook de UV achtergrondstraling, het interstellair stralingsveld, en afschermings-effecten. Tijdens de simulaties wordt er geïnterpoleerd op deze tabellen met een algemene $N$-dimensionale interpolator, om de input en output van energie door radiatieve processen te bepalen. Wanneer we zulke simulaties lopen van onze dwerggalaxiemodellen, pompen de stralingsvelden een stevige hoeveelheid energie in het ISM, die daardoor merkelijk uiteengedreven wordt. Om de modellen in lijn te houden met de schalingsrelaties, moeten we de feedback efficientie terug verlagen tot meer realistische waarden. Het is nu gemakkelijker voor supernovae om de koude, dichte gaswolken terug uiteen te drijven nadat ze sterren hebben gevormd. Als we de simulaties starten *na het tijdperk van reionisatie* zullen ze onderhevig zijn aan een sterke UV achtergrondstraling van in het begin, hetgeen een *significante verlaging veroorzaakt in de totale geproduceerde stermassa.* Als het gas tot lage dichthe-

den uiteengeblazen wordt kan het zichzelf niet meer afschermen, en zal het volledig baden in de achtergrondstralingen, waardoor het praktisch onmogelijk wordt om nog terug te koelen en dichtheden te bereiken die hoog genoeg zijn voor stervorming. Starten we de simulaties *voor het tijdperk van reionisatie*, dan zal het *effect* van de radiatieve verhitting sterk *verminderen.* Enkel het interstellair stralingsveld is aanwezig, en het grootste deel van de stellaire massa wordt gevormd voordat reionizatie en de UV achtergrond een rol beginnen spelen.

Bijkomende functionaliteiten van het chemische kaderwerk die we geïmplementeerd hebben om te gebruiken in het post-processen van het gesimuleerde ISM omvatten de bereking van

- de *neutrale fractie* van gasdeeltjes, die ons in staat stellen om gas te selecteren op basis van de relatieve hoeveelheid aan neutraal of geïoniseerd gas. Beelden gemaakt van het gas met een neutrale fractie van 0.95 of hoger kunnen goed vergeleken worden met waargenomen beelden van het HI gas van gasrijke dwerggalaxieën. Dit zowel *visueel*, met imitatie-waarnemingen, als meer kwantitatief door de totale massa aan neutraal gas en onze berekeningen van het *power spectrum van de structuur* in zowel de gesimuleerde als geobserveerde beelden. Als we beelden maken van het geïoniseerde gas kunnen we een extra selectie opleggen aan de gasdichtheid, zodat we duidelijk onderscheid kunnen maken tussen de verschillende astrofysische fases van het gas. We kunnen afzonderlijk beelden maken van zowel de dichte maar sterk geionizeerde gebieden rond pasgeboren sterren die verhit zijn door supernova, als van het meer diffuse geionizeerde gas in meer vergevorderde stadia van stellaire feedback, dat de door supernovae geblazen gaten vult in de galaxie en zich vervolgens uitstrekt tot voorbij het stellaire lichaam in enorme schillen van uitgestoten geïoniseerd gas.

- de *emissie flux* van gasdeeltjes, in eender welke emissie lijn of golflengtegebied zoals $H\alpha$ en CII. Beelden maken van deze emissies levert goede vergelijkingen met geobserveerde beelden, en de verhoudingen van de totale emissiewaarden tot de sterke van stervorming levert ons goede tests voor zowel onze modellen, als de toepasselijkheid van specifieke emissies als stervormingstracers. Onze modellen vertonen realistisch astrofysisch gedrag, en geven aan dat $H\alpha$ geen erg goede stervormingstracer is door de grote spreiding - terwijl CII, nadat voldoende metalen zijn geproduceerd, wel een betrouwbare stervormingstracer blijkt te zijn.

## Visualizaties

Een belangrijk onderdeel van numeriek onderzoek en analyse in de astronomie is het visualizeren van de resultaten. We doen dit voor onze dwerggalaxiemodellen in de eerste plaats op de "standaard" manier van SPH-rendering en scatter plots, maar we hebben onze werktuigen ook uitgebreid naar andere visualizatiemanieren. We zijn nu in staat onze modellen te tonen met 3D-rendering paketten, en een ray-tracing code die zeer realistisch uitziende artificiële observatiebeelden produceert van het gesimuleerde ISM. Beide kunnen

ook gebruikt worden in stereo-modus, zowel op de klassieke anaglyph stereo methode (met de rood-blauwe brillen), en het huidige Dolby 3D stereo systeem in volledige kleur.

# 8

## Outlook

Many ideas have popped up in my head in the (sparse) moments of clarity during the course of the last four years - some which were forgotten as quickly as they came, others that were remembered, but too stupid to survive the slightest scrutiny, and then some that unfortunately never made it into fruition... An outlook.

## More simulations

The main keyword in an outlook is of course always "more simulations". Since we are getting a better understanding of the internal mechanisms and parameters that drive our idealized models in isolated simulations, the logical next step is to place them in more realistic environments and try to form them in more cosmologically motivated ways.

Efforts on the cosmological formation of dwarf galaxies are already underway in the department, by forming dwarf galaxies through merger trees drawn from the Millennium simulations. Related to my thesis research, I am interested in putting the dwarf galaxy models on orbits around a Milky-Way-like potential, and to study individual merger events between dwarf galaxies - if possible with additional ram-pressure stripping processes. Both cases are to extend my current research, and see what effects these external influences have on the metallicity profiles, rotation of the stellar body, and star formation (modes) in general. This would produce more realistically simulated dwarf galaxies that alleviate much of the biased effects of the idealized setup we use. This will make them better suited to directly compare to observations, since they would have undergone gas stripping events and gravitational interactions such as the real galaxies have.

It would also be interesting to investigate the flattening distribution of simulated dwarf galaxies, for instance by producing a large set of individual merger simulations, with realistic distributions for the parameters of the merger event configuration, and compare them to the available observed flattening distributions.

# Better simulations

An important second keyword in an outlook is "better simulations". Since galaxy formation models like this are basically a big collection of approximations, often one on top of the other, we should always take great interest and care in improving those approximations and make them as realistic as possible.

With the novel chemical framework, of which I presented the first implementations and results in this thesis, and the development of new hydrodynamical prescriptions that include ionization effects, we are at the onset of extensive improvements and a wide range of new possibilities for the dwarf galaxy models. This can mean new physical processes that are accounted for during runtime (realistic cooling and heating, ionized gas, molecular gas,...), which could make things computationally more costly, but much more interesting and physically detailed. In post-processing of the simulation output there are also vast possibilities for sophisticated analysis methods, such as the neutral and ionized fraction of the gas, its emission flux in different emission lines and ranges,... These functionalities have the potential to take the humble dwarf galaxy models to a whole new, astrophysically sophisticated level.

Among the wilder but more concrete ideas is the suggestion to decouple the mass resolution of stellar particles from the mass resolution of the gas particles. For the simulated ISM it will always be interesting to go to higher resolutions, but decreasing the resolution of the stellar particles to much below 1000 solar masses will create unrealistic situations with the stellar populations they are supposed to represent. The suggestion is to not convert gas particles into star particles, but to create star particles from mass taken from a region of gas particles that satisfies certain conditions.

# Better equipment

On the technical side, the Hyplot analysis package is due for a thorough restructuring. Many of the analysis functionalities, scripts, and visualization tools that I developed or used during this research would be very useful to be integrated into the main program, and many archaic remnants should be rewritten or removed.

For the visualizations, the current scripts that I have written to produce 2D, 3D, and stereo animations with, using the Mayavi and Splotch tools could definitely benefit from a proper rewrite to become more flexible and user-friendly. Our research group's (and my personal) current interests in stereo 3D equipment (Dolby Stereo projecting system, Nvidia 3D vision graphical cards and 3D desktop screens) will also require extensive redevelopment of the Hyplot package, in order to take full advantage of these capabilities.

# A

# Scripts and codes

Throughout the years, an certain amount of scripting and coding of all kinds has been amassed in this PhD work, some which might be of use to others. For ease of use, and limit the amount of paper used in printing, this technical appendix section concerning the scripts and codes that have been used for the research presented in this thesis consists of a series of very brief descriptions, while the well-documented scripts can be found online in all their completeness, at `https://github.ugent.be/jschroye/astroScripts`.

## A.1 Analysis

Firstly, many of the scientific results have been achieved with the usage scripts to analyze the simulation output, mostly using the HYPLOT package to interact directly with the simulation data or the standard summary files. A collection of the most useful among them:

- `coolingCurveTest.py`:
  Plot the evolution of the cooling strength of one particle throughout the simulation. Particle data that is plotted needs to have been extracted with the extractParticles method of a CDataBlock. The tabulated cooling curves can be plotted in a second frame for comparison.

- `dynamicalTime.py`:
  Plot the evolution of the dynamical time and total mass within a certain region, for a set of simulations. Dynamical time can be calculated within fixed radius, within the

final half-light radius of each simulation, or within the evolving half-light radius of each simulation. It is calculated separately for the gas and dark matter component, and for the total content.

- `galaxyEvolution.py`:
  Plot the evolution of a list of global snapshot quantities (that are available in the standard HYPLOT summary files) in one overview, for a set of simulations. Script automatically arranges subplots according to the desired number of columns.

- `particleEvolution.py`:
  Plot the evolution of a single particle from a simulation. Any particle data that has been extracted with the extractParticles methode can be plotted, and the particle's orbit can be plotted in 3D with the `mplot3d` module available for MatPlotLib.

- `powerSpectrum_simulations.py`:
  Calculate and plot the power spectrum of structure in the neutral gas of a simulation (see Section 5.2.4 and Figure 5.11). A rendered image of the selected neutral gas is made with HYPLOT as in `neutralFraction_imaging.py`, its 2D Fourier transform is calculated with SciPy, and both images are displayed in smaller subplots on the top of the final figure. From the Fourier transform the power spectrum is derived, and displayed in a large subplot on the bottom of the figure. Observed power spectra can be overplotted as well, by calling the `powerSpectrum_observations.py` script - which is pickled for speed, so it only needs to be called the first time. The original neutral gas image can be modified with a Gaussian filter, random noise, and a lower cut on intensity, to mimic observational circumstances and better reproduce the shape of the observational power spectra. The scales of the observational or simulated seeing/smoothing are indicated, and a linear fit is made to the power spectrum in log-log space. The total HI/neutral gas mass can be derived from the original image.

- `powerSpectrum_observations.py`:
  Calculate the power spectrum of structure from HI observations (e.g. from Little Things), similarly to `powerSpectrum_simulations.py`. Necessary data are the distance to the objects, and the beam sizes or seeing. The calculated power spectra, all useful information, and fits to the spectrum, are stored in an object so that it can be pickled and extracted by other scripts calling this one.

- `profileGenerator.py`:
  Extensive module/class to generate and post-process profiles, as an extension to the built-in profiling functionality in HYPLOT. It can be given a set of simulations, together with a set or range of snapshots to profiles for each simulation. It will produce all profiles by calling HYPLOT, and store the CProfile C++ objects in a dictionary. These arrays of profiles can then be post-processed by averaging/stacking over time (running average over different snapshots), and by averaging/stacking over space (the `XYaveraging` method makes the same profile for the positive and negative

$x$ and $y$ axes in a single snapshot, and stacks these 4 profiles). The profile dictionary can be pickled and saved for later re-use, by replacing the C++ CProfile instances with PProfile Python-wrappers. All profiles, or a selection of them, can be shown on either a 2D or 3D plot. See the first paragraphs of Section 4.4 and Figures 4.6, 4.7, 4.9, and 4.10.

- `rotationCurves.py`:
  Plot the rotation curves of the stellar (or other) component, for a set of simulations. Can be collected in one plot, or in separate subplots showing the individual rotation curve's evolution with a desired time interval. Fits can be made to the rotation curves using a "universal" rotation curve function, and maximal rotation velocity is determined.

- `scalingRelations.py`:
  Plot scaling relations of any quantity against any quantity for a set of simulations, and combine any desired number of those in one overview frame, where subplots are automatically arranged according to the desired number of columns. All available observational data will automatically be added to each scaling relation.

- `SFHistogram.py`:
  Plot the evolution of the radial star formation density for a set of simulations in one overview. Script automatically arranges subplots according to the desired number of columns.

- `SFR_FFT.py`:
  Plot the evolution of the star formation conditions and calculate its Fourier transform, for comparing two sets of simulations. Image is divided in 3 columns, the left 2 show the FFT of the star formation rate evolution for the 2 sets, the rightmost column shows the star formation rate for both.

- `SFR_tracers.py`:
  Plot the evolution of the star formation rate and the total emission in H$\alpha$ and CII, together with two plots where the evolutions of the emissions are plotted versus star formation rate to see how they trace it. Time is colorcoded, observational SFR tracer data is overplotted. Emission evolution data for a specific simulation is pickled at first use, to speed up further plotting.

- `stellarMigration.py`:
  Extensive script to plot the statistical deviation over time of stellar particles from their original birth radius (see the first paragraphs of Section 4.5 an Figures 4.13, 4.14, 4.15, and 4.16). The orbit data of individual stellar particles need to have been extracted from the snapshots with the extractParticles method, and as many of them as possible or manageable. The measured difference between current and birth radius can be in absolute or signed form, and as radius or as distance to the $z$ axis. Contains several methods to remove suspicious or unwanted particles from the

statistics, or bins containing too few particles. The script can pickle the structure containing all the read-in particle data to speed up replotting.

- `surfaceBrightnessProf.py`:
  Plot the surface brightness profiles of sets of simulations, the profiles having been calculated beforehand by the standard HYPLOT analysis. Fits to the profiles can also be plotted.

- `variance.py`:
  Plot the statistical variance of a set of simulations, for a list of desired quantities that are available in the standard HYPLOT summary files. Ideally used for a set of similar, but differently seeded simulations.

## A.2   Imaging

During this thesis I spent a considerable amount of time on different ways of visualizing the dwarf galaxy models. These include 2D visualizations, such as standard SPH image rendering and also post-processing of simulation snapshots, in this section. A list of (possibly) useful scripts:

- `imaging.py`:
  General script for basic imaging of simulation snapshots. Uses the standard HYPLOT routines to plot the SPH-rendered gas density using a specified color scale, and overplotted stellar particles (if desired) which can be restricted to specific populations (limiting quantity can be chosen freely). A small inset frame can be plotted over the main frame to show a scatter plot of particles, for quantities of choice. Complete star formation history can also be plotted in a separate frame, with an indicator to show the current position in the evolution.

- `CII_imaging.py`:
  Specific script to image CII emission from the interstellar gas in simulations. HY-PLOT's built-in post-processing modules are used to interpolate on 5-dimensional tables and calculate the CII flux for each gas particle, which is the quantity which is then used in the standard rendering routines to produce the image. See Section 5.3 and Figure 5.14.

- `Halpha_imaging.py`:
  Specific script to image $H\alpha$ emission from the interstellar gas in simulations. HY-PLOT's built-in post-processing modules are used to interpolate on 5-dimensional tables and calculate the $H\alpha$ flux for each gas particle, which is the quantity which is then used in the standard rendering routines to produce the image. See Section 5.3 and Figure 5.12.

- `Halpha_mock_observations.py`:
  Produce mock-observational $H\alpha$ images of the interstellar gas in simulations for

a direct visual comparison to observations. Generates an Hα image as in Halpha_imaging.py, where now several observational effects can be imitated and tweaked to make the image *look very much like* an observation. Gaussian filtering can be added as seeing, random numbers as instrumental noise, added value as a bias, and a lower cut on the values which are shown. See Section 5.3 and Figure 5.13.

- `neutralFraction_imaging.py`:
  Specific script to image the neutral interstellar gas in simulations. HYPLOT's built-in post-processing modules are used to interpolate on 5-dimensional tables and calculate the neutral fraction for each gas particle. Only particles with a high enough neutral fraction (usually above 0.95) are selected, and these are then used in a standard density rendering image. The image thus shows the projected density of the neutral (approximately HI) gas. See Section 5.2 and Figure 5.6.

- `ionizedFraction_imaging.py`:
  Specific script to image the ionized interstellar gas in simulations. HYPLOT's built-in post-processing modules are used to interpolate on 5-dimensional tables and calculate the neutral fraction for each gas particle. Particles with a specified neutral fraction (usually any range below 0.9) are selected, and these are then used in a standard density rendering image. The image thus shows the projected density of the ionized gas in the range of choice. See Section 5.2 and Figures 5.8, 5.9, and 5.10.

- `neutraFraction_mock_observations.py`:
  Produce mock-observational HI images of the interstellar gas in simulations for a direct visual comparison to observations. Generates an HI image as in neutralFraction_imaging.py, where now several observational effects can be imitated and tweaked to make the image *look very much like* an observation. Gaussian filtering can be added as seeing, two levels of random numbers (one as the astrophysical interference of any kind that radiation might encounter on its way to us, the other as instrumental noise), added value as a bias, and a lower cut on the values which are shown. See Section 5.2 and Figure 5.7.

- `BmIcolor.py`:
  Produces a color image (example here is B-I) of the stellar body in a range of snapshots, by producing gridded images in two luminosity bands with HYPLOT, converting these to magnitudes, and subtracting them. A Gaussian filter can be added to the image to simulate seeing. A second frame can be plotted with the rendered gas density and desired stellar populations.

## A.3   Animations

Even more time I spent on visualizing the dwarf galaxy models *in motion*, at first also in 2D, but soon expanding the horizons to 3D visualizations (using 3D rendering and ray

tracing packages), and stereo visualizations (in red-and-blue anaglyph mode, but also full-color Dolby stereo). Since these work very well for presenting the models to a variety of audiences, and the many possibilities for 3D animations, extensive Python modules have been written to control every aspect of the animation.

- `animation2D.py`:
  Similarly to `imaging.py`, a script to set up a standard animation with rendered gas density and stellar populations. Can render both "face-on" and "edge-on" projections in two frames side by side, or the same projection for two different simulations.

- `animation3D_class.py`:
  Extensive class to actively generate a 3D animation using 3D rendering package Mayavi. One has control over the timing, the camera movement, any aspect on the elements that are shown, stereo mode, etc...

- `animation3D_scenario.py`:
  Example "scenario" for a Mayavi animation using the `animation3D_class.py` script.

- `animationSplotch_geometryGenerator.py`:
  Extensive class to generate a geometry file for an animation using ray-tracing tool Splotch. The end result is a file containing the consecutive positions of the camera, positions of the focus point (lookat point), and direction of "up" (sky vector), together with the number of the snapshot to load (fidx). This can be read by Splotch, by directing the Splotch parameter file to it.

- `animationSplotch_scenario.py`:
  Example "scenario" to generate a geometry file for a Splotch animation, using the `animationSplotch_geometryGenerator.py` script.

- `animationSplotch.par`:
  Example parameter file for Splotch. It sets the snapshots, describes which elements are shown and how, links to the geometry file to be used, sets the stereo mode, and the directory to output to.

## A.4    Miscellaneous

And, for lack of a consistent category, *the rest*...

- `recenter_snapshots.py`:
  Simple script that reads in a simulation snapshot, re-centers it on the center of mass, and writes this snapshot out again. Can come in handy for visualizing with Splotch, since the models can sometimes drift from the original center of the coordinate system.

- `remove_particles.py`:
  Reads in a simulation snapshot, removes particles on any desired criterion, and writes

the snapshot out again. Handy to select e.g. neutral or ionized gas to image with Splotch.

- `renumber_frames.sh`:
  Short shell-script to renumber batches of files, such as snapshots or images. Useful for switching from e.g. a 3-digit numeric format to a 4-digit one.

- `combineStereo.py`:
  combines left and right images into a stereo image format of choice (red-cyan anaglyph, side-by-side, over-under). Executes this on all files in "left" and "right" directories, outputs to "stereo" directory, and combines the latter into a movie file with Mencoder.

- `makevid`:
  Alias command to generate a movie file from a series of images with Mencoder.

# References

C. Alard (2001). Metallicity gradients in the Sagittarius dwarf spheroidal Galaxy. A&A, 377:389–395.

A. Aparicio, C. Gallart, C. Chiosi & G. Bertelli (1996). Model Color-Magnitude Diagrams for Hubble Space Telescope Observations of Local Group Dwarf Galaxies. ApJ, 469:L97.

M. L. Balogh, J. F. Navarro & S. L. Morris (2000). The Origin of Star Formation Gradients in Rich Galaxy Clusters. ApJ, 540:113–121.

F. D. Barazza & B. Binggeli (2002). A metallicity-flattening relation for dwarf elliptical galaxies. A&A, 394:L15–L18.

F. D. Barazza, B. Binggeli & H. Jerjen (2002). More evidence for hidden spiral and bar features in bright early-type dwarf galaxies. A&A, 391:823–831.

J. Barnes & P. Hut (1986). A hierarchical O(N log N) force-calculation algorithm. Nature, 324:446–449.

G. Battaglia, M. Rejkuba, E. Tolstoy, M. J. Irwin & G. Beccari (2012). A wide-area view of the Phoenix dwarf galaxy from Very Large Telescope/FORS imaging. MNRAS, 424:1113–1131.

G. Battaglia, E. Tolstoy, A. Helmi, M. Irwin, P. Parisi, V. Hill & P. Jablonka (2011). Study of the Sextans dwarf spheroidal galaxy from the DART Ca II triplet survey. MNRAS, 411:1013–1034.

G. Battaglia, E. Tolstoy, A. Helmi, M. J. Irwin, B. Letarte, P. Jablonka, V. Hill, K. A. Venn, M. D. Shetrone, N. Arimoto, F. Primas, A. Kaufer, P. Francois, T. Szeifert, T. Abel & K. Sadakane (2006). The DART imaging and CaT survey of the Fornax dwarf spheroidal galaxy. A&A, 459:423–440.

K. Bekki & Y. Shioya (1999). Stellar Populations in Gas-rich Galaxy Mergers. II. Feedback Effects of Type IA and Type II Supernovae. ApJ, 513:108–127.

V. Belokurov (2013). Galactic Archaeology. The dwarfs that survived and perished. *ArXiv e-prints*.

R. Bender, D. Burstein & S. M. Faber (1992). Dynamically hot galaxies. I - Structural properties. ApJ, 399:462–477.

E. J. Bernard, A. Aparicio, C. Gallart, C. P. Padilla-Torres & M. Panniello (2007). Stellar Content and Recent Star Formation History of the Local Group Dwarf Irregular Galaxy IC 1613. AJ, 134:1124–1132.

E. J. Bernard, C. Gallart, M. Monelli, A. Aparicio, S. Cassisi, E. D. Skillman, P. B. Stetson, A. A. Cole, I. Drozdovsky, S. L. Hidalgo, M. Mateo & E. Tolstoy (2008). The ACS LCID Project: RR Lyrae Stars as Tracers of Old Population Gradients in the Isolated Dwarf Spheroidal Galaxy Tucana. ApJ, 678:L21–L24.

G. Besla, N. Kallivayalil, L. Hernquist, R. P. van der Marel, T. J. Cox & D. Kereš (2012). The role of dwarf galaxy interactions in shaping the Magellanic System and implications for Magellanic Irregulars. MNRAS, 421:2109–2138.

B. Binggeli & C. C. Popescu (1995). Dwarf galaxies in the Virgo cluster. III. Flattening distributions. A&A, 298:63.

B. Binggeli, C. C. Popescu & G. A. Tammann (1993). The kinematics of the Virgo cluster revisited. A&AS, 98:275–296.

B. Binggeli, G. A. Tammann & A. Sandage (1987). Studies of the Virgo cluster. VI - Morphological and kinematical structure of the Virgo cluster. AJ, 94:251–277.

L. G. Book, Y.-H. Chu & R. A. Gruendl (2008). Structure of Supergiant Shells in the Large Magellanic Cloud. ApJS, 175:165–178.

A. Boselli, S. Boissier, L. Cortese & G. Gavazzi (2008). The Origin of Dwarf Ellipticals in the Virgo Cluster. ApJ, 674:742–767.

D. Burstein, R. Bender, S. Faber & R. Nolthenius (1997). Global Relationships Among the Physical Properties of Stellar Systems. AJ, 114:1365.

P. Buyle, S. De Rijcke, D. Michielsen, M. Baes & H. Dejonghe (2005). The HI content of Fornax dwarf elliptical galaxies: FCC032 and FCC336. MNRAS, 360:853–858.

N. Caldwell (1999). Surface Brightness Profiles of Three New Dwarf Spheroidal Companions to M31. AJ, 118:1230–1234.

I. V. Chilingarian (2009). Evolution of dwarf early-type galaxies - I. Spatially resolved stellar populations and internal kinematics of Virgo cluster dE/dS0 galaxies. MNRAS, 394:1229–1248.

M.-R. L. Cioni (2009). The metallicity gradient as a tracer of history and structure: the Magellanic Clouds and M33 galaxies. A&A, 506:1137–1146.

A. Cloet-Osselaer, S. De Rijcke, J. Schroyen & V. Dury (2012). The degeneracy between star formation parameters in dwarf galaxy simulations and the $M_{star}$-$M_{halo}$ relation. MNRAS, 423:735–745.

C. J. Conselice, K. O'Neil, J. S. Gallagher & R. F. G. Wyse (2003). Galaxy Populations and Evolution in Clusters. IV. Deep H I Observations of Dwarf Elliptical Galaxies in the Virgo Cluster. ApJ, 591:167–184.

S. Côté, C. Carignan & K. C. Freeman (2000). The Various Kinematics of Dwarf Irregular Galaxies in Nearby Groups and Their Dark Matter Distributions. AJ, 120:3027–3059.

S. Côté, A. Draginda, E. D. Skillman & B. W. Miller (2009). Star Formation in Dwarf Galaxies of the Nearby Centaurus a Group. AJ, 138:1037–1061.

D. Crnojević, E. K. Grebel & A. Koch (2010). A close look at the Centaurus A group of galaxies. I. Metallicity distribution functions and population gradients in early-type dwarfs. A&A, 516:A85.

L. P. David, W. Forman & C. Jones (1990). The evolution of the interstellar medium in elliptical galaxies. I - The early wind phase. ApJ, 359:29–41.

W. J. G. de Blok (2010). The Core-Cusp Problem. *Advances in Astronomy*, 2010.

I. De Looze (2013). Star formation tracers.

I. de Looze, M. Baes, S. Zibetti, J. Fritz, L. Cortese, J. I. Davies, J. Verstappen, G. J. Bendo, S. Bianchi, M. Clemens, D. J. Bomans, A. Boselli, E. Corbelli, A. Dariush, S. di Serego Alighieri, D. Fadda, D. A. Garcia-Appadoo, G. Gavazzi, C. Giovanardi, M. Grossi, T. M. Hughes, L. K. Hunt, A. P. Jones, S. Madden, D. Pierini, M. Pohlen, S. Sabatini, M. W. L. Smith, C. Vlahakis & E. M. Xilouris (2010). The Herschel Virgo Cluster Survey . VII. Dust in cluster dwarf elliptical galaxies. A&A, 518:L54.

S. De Rijcke, H. Dejonghe, W. W. Zeilinger & G. K. T. Hau (2003a). Embedded disks in Fornax dwarf elliptical galaxies. A&A, 400:119–125.

S. de Rijcke, D. Michielsen, H. Dejonghe, W. W. Zeilinger & G. K. T. Hau (2005). Formation and evolution of dwarf elliptical galaxies. I. Structural and kinematical properties. A&A, 438:491–505.

S. de Rijcke, S. J. Penny, C. J. Conselice, S. Valcke & E. V. Held (2009). Hubble Space Telescope survey of the Perseus cluster - II. Photometric scaling relations in different environments. MNRAS, 393:798–807.

S. De Rijcke, J. Schroyen, B. Vandenbroucke, J. Decroos, N. Jachowicz, A. Cloet-Osselaer & M. Koleva (2013). New composition dependent cooling and heating curves for galaxy evolution simulations. MNRAS.

S. De Rijcke, W. W. Zeilinger, H. Dejonghe & G. K. T. Hau (2003b). Evidence for a warm interstellar medium in the Fornax dwarf ellipticals FCC046 and FCC207. MNRAS, 339:225–234.

D. S. De Young & J. S. Gallagher, III (1990). Selective loss of metals from low-mass galaxies. ApJ, 356:L15–L19.

D. S. De Young & T. M. Heckman (1994). The effect of central starbursts on the interstellar medium of dwarf galaxies. ApJ, 431:598–603.

H. Dejonghe & T. de Zeeuw (1988). Analytic axisymmetric galaxy models with three integrals of motion. ApJ, 333:90–129.

A. Dekel & J. Silk (1986). The origin of dwarf galaxies, cold dark matter, and biased galaxy formation. ApJ, 303:39–55.

M. den Brok, R. F. Peletier, E. A. Valentijn, M. Balcells, D. Carter, P. Erwin, H. C. Ferguson, P. Goudfrooij, A. W. Graham, D. Hammer, J. R. Lucey, N. Trentham, R. Guzmán, C. Hoyos, G. Verdoes Kleijn, S. Jogee, A. M. Karick, I. Marinova, M. Mouhcine & T. Weinzirl (2011). The HST/ACS Coma Cluster Survey - VI. Colour gradients in giant and dwarf early-type galaxies. MNRAS, 414:3052–3070.

K. P. Dere, E. Landi, P. R. Young, G. Del Zanna, M. Landini & H. E. Mason (2009). CHIANTI - an atomic database for emission lines. IX. Ionization rates, recombination rates, ionization equilibria for the elements hydrogen through zinc and updated atomic data. A&A, 498:915–929.

R. C. Dohm-Palmer, E. D. Skillman, M. Mateo, A. Saha, A. Dolphin, E. Tolstoy, J. S. Gallagher & A. A. Cole (2002). Deep Hubble Space Telescope Imaging of Sextans A. I. The Spatially Resolved Recent Star Formation History. AJ, 123:813–831.

A. Dolphin (1997). A new method to determine star formation histories of nearby galaxies. NewA, 2:397–409.

A. E. Dolphin (2002). Numerical methods of star formation history measurement and applications to seven dwarf spheroidals. MNRAS, 332:91–108.

A. E. Dolphin, D. R. Weisz, E. D. Skillman & J. A. Holtzman (2005). Star Formation Histories of Local Group Dwarf Galaxies. ArXiv Astrophysics e-prints.

P.-A. Duc, F. Bournaud & M. Boquien (2007). Tidal dwarf galaxies as laboratories of star formation and cosmology. In B. G. Elmegreen & J. Palous, editors, IAU Symposium, volume 237 of IAU Symposium, pp. 323–330.

R. J. Dufour & W. V. Harlow (1977). Abundances in 10 H II regions in the Small Magellanic Cloud. ApJ, 216:706–712.

C.-A. Faucher-Giguère, A. Lidz, M. Zaldarriaga & L. Hernquist (2009). A New Calculation of the Ionizing Background Spectrum and the Effects of He II Reionization. ApJ, 703:1416–1443.

H. C. Ferguson & B. Binggeli (1994). Dwarf elliptical galaxies. A&A Rev., 6:67–122.

A. Ferrara & E. Tolstoy (2000). The role of stellar feedback and dark matter in the evolution of dwarf galaxies. MNRAS, 313:291–309.

W. Forman & C. Jones (1982). X-ray-imaging observations of clusters of galaxies. ARA&A, 20:547–585.

M. Geha, P. Guhathakurta & R. P. van der Marel (2003). Internal Dynamics, Structure, and Formation of Dwarf Elliptical Galaxies. II. Rotating versus Nonrotating Dwarfs. AJ, 126:1794–1810.

G. Gentile, P. Salucci, U. Klein, D. Vergani & P. Kalberla (2004). The cored distribution of dark matter in spiral galaxies. MNRAS, 351:903–922.

B. K. Gibson, K. Pilkington, C. B. Brook, G. S. Stinson & J. Bailin (2013). Constraining Sub-Grid Physics with High-Redshift Spatially-Resolved Metallicity Distributions. *ArXiv e-prints*.

R. A. Gingold & J. J. Monaghan (1977). Smoothed particle hydrodynamics - Theory and application to non-spherical stars. MNRAS, 181:375–389.

F. Governato, C. Brook, L. Mayer, A. Brooks, G. Rhee, J. Wadsley, P. Jonsson, B. Willman, G. Stinson, T. Quinn & P. Madau (2010). Bulgeless dwarf galaxies and dark matter cores from supernova-driven outflows. Nature, 463:203–206.

A. W. Graham, H. Jerjen & R. Guzmán (2003). Hubble Space Telescope Detection of Spiral Structure in Two Coma Cluster Dwarf Galaxies. AJ, 126:1787–1793.

E. K. Grebel (1999). Evolutionary Histories of Dwarf Galaxies in the Local Group. In P. Whitelock & R. Cannon, editors, *The Stellar Content of Local Group Galaxies*, volume 192 of *IAU Symposium*, p. 17.

E. K. Grebel, J. S. Gallagher, III & D. Harbeck (2003). The Progenitors of Dwarf Spheroidal Galaxies. AJ, 125:1926–1939.

J. E. Gunn & J. R. Gott, III (1972). On the Infall of Matter Into Clusters of Galaxies and Some Effects on Their Evolution. ApJ, 176:1.

D. Harbeck, E. K. Grebel, J. Holtzman, P. Guhathakurta, W. Brandner, D. Geisler, A. Sarajedini, A. Dolphin, D. Hurley-Keller & M. Mateo (2001). Population Gradients in Local Group Dwarf Spheroidal Galaxies. AJ, 122:3092–3105.

L. Hernández-Martínez, M. Peña, L. Carigi & J. García-Rojas (2009). Chemical behavior of the dwarf irregular galaxy NGC6822. Its PN and HII region abundances. A&A, 505:1027–1039.

L. Hernquist & N. Katz (1989). TREESPH - A unification of SPH with the hierarchical tree method. ApJS, 70:419–446.

P. F. Hopkins, T. J. Cox, S. N. Dutta, L. Hernquist, J. Kormendy & T. R. Lauer (2009). Dissipation and Extra Light in Galactic Nuclei. II. "Cusp" Ellipticals. ApJS, 181:135–182.

D. A. Hunter & B. G. Elmegreen (2004). Star Formation Properties of a Large Sample of Irregular Galaxies. AJ, 128:2170–2205.

D. A. Hunter & B. G. Elmegreen (2006). Broadband Imaging of a Large Sample of Irregular Galaxies. ApJS, 162:49–79.

D. A. Hunter, D. Ficut-Vicas, T. Ashley, E. Brinks, P. Cigan, B. G. Elmegreen, V. Heesen, K. A. Herrmann, M. Johnson, S.-H. Oh, M. P. Rupen, A. Schruba, C. E. Simpson, F. Walter, D. J. Westpfahl, L. M. Young & H.-X. Zhang (2012). Little Things. AJ, 144:134.

M. Irwin & D. Hatzidimitriou (1995). Structural parameters for the Galactic dwarf spheroidals. MNRAS, 277:1354–1378.

M. J. Irwin, V. Belokurov, N. W. Evans, E. V. Ryan-Weber, J. T. A. de Jong, S. Koposov, D. B. Zucker, S. T. Hodgkin, G. Gilmore, P. Prema, L. Hebb, A. Begum, M. Fellhauer, P. C. Hewett, R. C. Kennicutt, Jr., M. I. Wilkinson, D. M. Bramich, S. Vidrih, H.-W. Rix, T. C. Beers, J. C. Barentine, H. Brewington, M. Harvanek, J. Krzesinski, D. Long, A. Nitta & S. A. Snedden (2007). Discovery of an Unusual Dwarf Galaxy in the Outskirts of the Milky Way. ApJ, 656:L13–L16.

F. P. Israel & P. R. Maloney (2011). $C^+$ emission from the Magellanic Clouds. II. [C II] maps of star-forming regions LMC-N 11, SMC-N 66, and several others. A&A, 531:A19.

F. P. Israel, P. R. Maloney, N. Geis, F. Herrmann, S. C. Madden, A. Poglitsch & G. J. Stacey (1996). C + Emission from the Magellanic Clouds. I. The Bright H II Region Complexes N159 and N160. ApJ, 465:738.

H. Jerjen, A. Kalnajs & B. Binggeli (2000). IC3328: A "dwarf elliptical galaxy" with spiral structure. A&A, 358:845–849.

S. S. Kaisin, I. D. Karachentsev & S. Ravindranath (2012). H$\alpha$ survey of nearby dwarf galaxies. MNRAS, 425:2083–2098.

I. D. Karachentsev & E. I. Kaisina (2013). Star formation properties in the Local Volume galaxies via $H\alpha$ and FUV fluxes. *ArXiv e-prints*.

N. Katz, D. H. Weinberg & L. Hernquist (1996). Cosmological Simulations with TreeSPH. ApJS, 105:19.

A. Kaufer, K. A. Venn, E. Tolstoy, C. Pinte & R.-P. Kudritzki (2004). First Stellar Abundances in the Dwarf Irregular Galaxy Sextans A. AJ, 127:2723–2737.

T. Kaufmann, C. Wheeler & J. S. Bullock (2007). On the morphologies, gas fractions, and star formation rates of small galaxies. MNRAS, 382:1187–1195.

D. Kawata & J. S. Mulchaey (2008). Strangulation in Galaxy Groups. ApJ, 672:L103–L106.

R. C. Kennicutt, Jr. (1998). Star Formation in Galaxies Along the Hubble Sequence. ARA&A, 36:189–232.

S. Kim, M. A. Dopita, L. Staveley-Smith & M. S. Bessell (1999). H I Shells in the Large Magellanic Cloud. AJ, 118:2797–2823.

S. Kim, L. Staveley-Smith, M. A. Dopita, R. J. Sault, K. C. Freeman, Y. Lee & Y. . Chu (2005). A Neutral Hydrogen Survey of the Large Magellanic Cloud: Aperture Synthesis and Multibeam Data Combined. *ArXiv Astrophysics e-prints*.

E. N. Kirby, J. G. Cohen & M. Bellazzini (2012). The Dynamics and Metallicity Distribution of the Distant Dwarf Galaxy VV124. ApJ, 751:46.

E. N. Kirby, G. A. Lanfranchi, J. D. Simon, J. G. Cohen & P. Guhathakurta (2011). Multi-element Abundance Measurements from Medium-resolution Spectra. III. Metallicity Distributions of Milky Way Dwarf Satellite Galaxies. ApJ, 727:78.

J. T. Kleyna, M. I. Wilkinson, N. W. Evans & G. Gilmore (2005). Ursa Major: A Missing Low-Mass CDM Halo? ApJ, 630:L141–L144.

H. A. Kobulnicky & E. D. Skillman (1997). Elemental Abundance Variations and Chemical Enrichment from Massive Stars in Starbursts. II. NGC 1569. ApJ, 489:636.

M. Koleva, A. Bouchard, P. Prugniel, S. De Rijcke & I. Vauglin (2013). The transmutation of dwarf galaxies: stellar populations. MNRAS, 428:2949–2965.

M. Koleva, S. de Rijcke, P. Prugniel, W. W. Zeilinger & D. Michielsen (2009). Formation and evolution of dwarf elliptical galaxies - II. Spatially resolved star formation histories. MNRAS, 396:2133–2151.

M. Koleva, P. Prugniel, S. de Rijcke & W. W. Zeilinger (2011). Age and metallicity gradients in early-type galaxies: a dwarf-to-giant sequence. MNRAS, 417:1643–1671.

M. R. Krumholz (2012). Star Formation in Atomic Gas. ApJ, 759:9.

D. Kunth, S. Maurogordato & L. Vigroux (1988). CCD observations of blue compact galaxies - A mixed bag of morphological types. A&A, 204:10–20.

R. B. Larson, B. M. Tinsley & C. N. Caldwell (1980). The evolution of disk galaxies and the origin of S0 galaxies. ApJ, 237:692–707.

J. R. D. Lépine, I. A. Acharova & Y. N. Mishurov (2003). Corotation, Stellar Wandering, and Fine Structure of the Galactic Abundance Pattern. ApJ, 589:210–216.

S. Lianou, E. K. Grebel & A. Koch (2010). Dwarf spheroidals in the M 81 group - Metallicity distribution functions and population gradients. A&A, 521:A43.

D. N. C. Lin & S. M. Faber (1983). Some implications of nonluminous matter in dwarf spheroidal galaxies. ApJ, 266:L21–L25.

T. Lisker, K. Glatt, P. Westera & E. K. Grebel (2006). Virgo Cluster Early-Type Dwarf Galaxies with the Sloan Digital Sky Survey. II. Early-Type Dwarfs with Central Star Formation. AJ, 132:2432–2452.

S. R. Loebman, R. Roškar, V. P. Debattista, Ž. Ivezić, T. R. Quinn & J. Wadsley (2011). The Genesis of the Milky Way's Thick Disk Via Stellar Migration. ApJ, 737:8.

E. L. Łokas, S. Kazantzidis & L. Mayer (2011). Evolutionary Tracks of Tidally Stirred Disky Dwarf Galaxies. ApJ, 739:46.

E. L. Lokas, K. Kowalczyk & S. Kazantzidis (2012). Stellar populations in tidally stirred dwarf galaxies. *ArXiv e-prints*.

L. B. Lucy (1977). A numerical approach to the testing of the fission hypothesis. AJ, 82:1013–1024.

M.-M. Mac Low & A. Ferrara (1999). Starburst-driven Mass Loss from Dwarf Galaxies: Efficiency and Metal Ejection. ApJ, 513:142–155.

S. C. Madden, A. Poglitsch, N. Geis, G. J. Stacey & C. H. Townes (1997). [C ii] 158 Micron Observations of IC 10: Evidence for Hidden Molecular Hydrogen in Irregular Galaxies. ApJ, 483:200.

U. Maio, K. Dolag, B. Ciardi & L. Tornatore (2007). Metal and molecule cooling in simulations of structure formation. MNRAS, 379:963–973.

A. Marcolini, F. Brighenti & A. D'Ercole (2003). Three-dimensional simulations of the interstellar medium in dwarf galaxies - I. Ram pressure stripping. MNRAS, 345:1329–1339.

D. Martínez-Delgado, J. Peñarrubia, R. J. Gabany, I. Trujillo, S. R. Majewski & M. Pohlen (2008). The Ghost of a Dwarf Galaxy: Fossils of the Hierarchical Formation of the Nearby Spiral Galaxy NGC 5907. ApJ, 689:184–193.

J. Masegosa, M. Moles & A. del Olmo (1991). Spatial inhomogeneities in giant extragalactic H II regions. A&A, 249:505–517.

M. L. Mateo (1998). Dwarf Galaxies of the Local Group. ARA&A, 36:435–506.

L. Mayer, F. Governato, M. Colpi, B. Moore, T. Quinn, J. Wadsley, J. Stadel & G. Lake (2001a). The Metamorphosis of Tidally Stirred Dwarf Galaxies. ApJ, 559:754–784.

L. Mayer, F. Governato, M. Colpi, B. Moore, T. Quinn, J. Wadsley, J. Stadel & G. Lake (2001b). Tidal Stirring and the Origin of Dwarf Spheroidals in the Local Group. ApJ, 547:L123–L127.

L. Mayer, C. Mastropietro, J. Wadsley, J. Stadel & B. Moore (2006). Simultaneous ram pressure and tidal stripping; how dwarf spheroidals lost their gas. MNRAS, 369:1021–1038.

A. W. McConnachie, N. Arimoto & M. Irwin (2007). Deconstructing dwarf galaxies: a Suprime-Cam survey of Andromeda II. MNRAS, 379:379–392.

A. W. McConnachie & M. J. Irwin (2006). Structural properties of the M31 dwarf spheroidal galaxies. MNRAS, 365:1263–1276.

R. McCray & M. Kafatos (1987). Supershells and propagating star formation. ApJ, 317:190–196.

K. B. W. McQuinn, E. D. Skillman, J. M. Cannon, J. Dalcanton, A. Dolphin, S. Hidalgo-Rodríguez, J. Holtzman, D. Stark, D. Weisz & B. Williams (2010). The Nature of Starbursts. II. The Duration of Starbursts in Dwarf Galaxies. ApJ, 724:49–58.

D. Michielsen, M. Koleva, P. Prugniel, W. W. Zeilinger, S. De Rijcke, H. Dejonghe, A. Pasquali, I. Ferreras & V. P. Debattista (2007). Toward a Solution for the Ca II Triplet Puzzle: Results from Dwarf Elliptical Galaxies. ApJ, 670:L101–L104.

S. Mieske, M. Hilker, L. Infante & C. Mendes de Oliveira (2007). The early-type dwarf galaxy population of the Fornax cluster. A&A, 463:503–512.

S. Mieske, M. Hilker, A. Jordán, L. Infante, M. Kissler-Patig, M. Rejkuba, T. Richtler, P. Côté, H. Baumgardt, M. J. West, L. Ferrarese & E. W. Peng (2008). The nature of UCDs: Internal dynamics from an expanded sample and homogeneous database. A&A, 487:921–935.

J. J. Monaghan (1992). Smoothed particle hydrodynamics. ARA&A, 30:543–574.

M. Monelli, E. J. Bernard, C. Gallart, G. Fiorentino, I. Drozdovsky, A. Aparicio, G. Bono, S. Cassisi, E. D. Skillman & P. B. Stetson (2012). Variable stars in the Cetus dwarf spheroidal galaxy: population gradients and connections with the star formation history. MNRAS, 422:89–105.

B. Moore, N. Katz, G. Lake, A. Dressler & A. Oemler (1996). Galaxy harassment and the evolution of clusters of galaxies. Nature, 379:613–616.

B. Moore, G. Lake & N. Katz (1998). Morphological Transformation from Galaxy Harassment. ApJ, 495:139.

M. Nagashima & Y. Yoshii (2004). Hierarchical Formation of Galaxies with Dynamical Response to Supernova-Induced Gas Removal. ApJ, 610:23–44.

J. F. Navarro, C. S. Frenk & S. D. M. White (1996). The Structure of Cold Dark Matter Halos. ApJ, 462:563.

J. F. Navarro, C. S. Frenk & S. D. M. White (1997). A Universal Density Profile from Hierarchical Clustering. ApJ, 490:493.

J. P. Ostriker & M. A. Hausman (1977). Cannibalism among the galaxies - Dynamically produced evolution of cluster luminosity functions. ApJ, 217:L125–L129.

J. P. Ostriker & S. D. Tremaine (1975). Another evolutionary correction to the luminosity of giant galaxies. ApJ, 202:L113–L117.

B. E. J. Pagel, M. G. Edmunds, R. A. E. Fosbury & B. L. Webster (1978). A survey of chemical compositions of H II regions in the Magellanic Clouds. MNRAS, 184:569–592.

R. F. Peletier & D. M. Christodoulou (1993). A photometric and dynamical study of the Helix galaxy NGC 2685. AJ, 105:1378–1391.

F. I. Pelupessy, P. P. van der Werf & V. Icke (2004). Periodic bursts of star formation in irregular galaxies. A&A, 422:55–64.

S. J. Penny, C. J. Conselice, S. de Rijcke & E. V. Held (2009). Hubble Space Telescope survey of the Perseus Cluster - I. The structure and dark matter content of cluster dwarf spheroidals. MNRAS, 393:1054–1062.

R. C. Peterson & N. Caldwell (1993). Stellar velocity dispersions of dwarf elliptical galaxies. AJ, 105:1411–1419.

A. Pipino, A. D'Ercole, C. Chiappini & F. Matteucci (2010). Abundance gradient slopes versus mass in spheroids: predictions by monolithic models. MNRAS, 407:1347–1359.

Y. Revaz & P. Jablonka (2012). The dynamical and chemical evolution of dwarf spheroidal galaxies with GEAR. A&A, 538:A82.

Y. Revaz, P. Jablonka, T. Sawala, V. Hill, B. Letarte, M. Irwin, G. Battaglia, A. Helmi, M. D. Shetrone, E. Tolstoy & K. A. Venn (2009). The dynamical and chemical evolution of dwarf spheroidal galaxies. A&A, 501:189–206.

K. L. Rhode, J. J. Salzer, D. J. Westpfahl & L. A. Radice (1999). A Test of the Standard Hypothesis for the Origin of the H I Holes in Holmberg II. AJ, 118:323–336.

E. Roediger, R. P. Kraft, W. R. Forman, P. E. J. Nulsen & E. Churazov (2013). Kelvin-Helmholtz Instabilities at the Sloshing Cold Fronts in the Virgo Cluster as a Measure for the Effective Intracluster Medium Viscosity. ApJ, 764:60.

R. Roškar, V. P. Debattista, T. R. Quinn & J. Wadsley (2012). Radial migration in disc galaxies - I. Transient spiral structure and dynamics. MNRAS, 426:2089–2106.

R. Roškar, V. P. Debattista, G. S. Stinson, T. R. Quinn, T. Kaufmann & J. Wadsley (2008). Beyond Inside-Out Growth: Formation and Evolution of Disk Outskirts. ApJ, 675:L65–L68.

S. Roychowdhury, J. N. Chengalur, A. Begum & I. D. Karachentsev (2010). Thick gas discs in faint dwarf galaxies. MNRAS, 404:L60–L63.

E. E. Salpeter (1955). The Luminosity Function and Stellar Evolution. ApJ, 121:161.

R. Sánchez-Janssen, J. Méndez-Abreu & J. A. L. Aguerri (2010). Thin discs, thick dwarfs and the effects of stellar feedback. MNRAS, 406:L65–L69.

I. Saviane, E. V. Held & G. Piotto (1996). CCD photometry of the Tucana dwarf galaxy. A&A, 315:40–51.

T. Sawala, Q. Guo, C. Scannapieco, A. Jenkins & S. White (2011). What is the (dark) matter with dwarf galaxies? MNRAS, 413:659–668.

T. Sawala, C. Scannapieco, U. Maio & S. White (2010). Formation of isolated dwarf galaxies with feedback. MNRAS, 402:1599–1613.

M. Schmidt (1959). The Rate of Star Formation. ApJ, 129:243.

R. Schönrich & J. Binney (2009). Origin and structure of the Galactic disc(s). MNRAS, 399:1145–1156.

J. Schroyen, S. De Rijcke, M. Koleva, A. Cloet-Osselaer & B. Vandenbroucke (2013). Stellar orbits and the survival of metallicity gradients in simulated dwarf galaxies. MNRAS.

J. Schroyen, S. de Rijcke, S. Valcke, A. Cloet-Osselaer & H. Dejonghe (2011). Simulations of the formation and evolution of isolated dwarf galaxies - II. Angular momentum as a second parameter. MNRAS, 416:601–617.

J. A. Sellwood (1983). Quiet starts for galaxy simulations. *Journal of Computational Physics*, 50:337–359.

J. A. Sellwood & J. J. Binney (2002). Radial mixing in galactic discs. MNRAS, 336:785–796.

S. Shen, J. Wadsley & G. Stinson (2010). The enrichment of the intergalactic medium with adiabatic feedback - I. Metal cooling and metal diffusion. MNRAS, 407:1581–1596.

J. D. Simon & M. Geha (2007). The Kinematics of the Ultra-faint Milky Way Satellites: Solving the Missing Satellite Problem. ApJ, 670:313–331.

E. D. Skillman (2005). Star formation histories in local group dwarf galaxies [review article]. *NewAR*, 49:453–460.

A. V. Smith Castelli, L. P. Bassino, T. Richtler, S. A. Cellone, C. Aruta & L. Infante (2008). Galaxy populations in the Antlia cluster - I. Photometric properties of early-type galaxies. MNRAS, 386:2311–2322.

D. N. Spergel, R. Bean, O. Doré, M. R. Nolta, C. L. Bennett, J. Dunkley, G. Hinshaw, N. Jarosik, E. Komatsu, L. Page, H. V. Peiris, L. Verde, M. Halpern, R. S. Hill, A. Kogut, M. Limon, S. S. Meyer, N. Odegard, G. S. Tucker, J. L. Weiland, E. Wollack & E. L. Wright (2007). Three-Year Wilkinson Microwave Anisotropy Probe (WMAP) Observations: Implications for Cosmology. ApJS, 170:377–408.

L. Spitzer, Jr. & M. Schwarzschild (1953). The Possible Influence of Interstellar Clouds on Stellar Velocities. II. ApJ, 118:106.

V. Springel (2005). The cosmological simulation code GADGET-2. MNRAS, 364:1105–
1134.

V. Springel, S. D. M. White, A. Jenkins, C. S. Frenk, N. Yoshida, L. Gao, J. Navarro,
R. Thacker, D. Croton, J. Helly, J. A. Peacock, S. Cole, P. Thomas, H. Couchman,
A. Evrard, J. Colberg & F. Pearce (2005). Simulations of the formation, evolution and
clustering of galaxies and quasars. Nature, 435:629–636.

L. Staveley-Smith, R. D. Davies & T. D. Kinman (1992). H I and optical observations of
dwarf galaxies. MNRAS, 258:334–346.

S. G. Stewart, M. N. Fanelli, G. G. Byrd, J. K. Hill, D. J. Westpfahl, K.-P. Cheng,
R. W. O'Connell, M. S. Roberts, S. G. Neff, A. M. Smith & T. P. Stecher (2000). Star
Formation Triggering Mechanisms in Dwarf Galaxies: The Far-Ultraviolet, H$\alpha$, and H
I Morphology of Holmberg II. ApJ, 529:201–218.

G. Stinson, A. Seth, N. Katz, J. Wadsley, F. Governato & T. Quinn (2006). Star forma-
tion and feedback in smoothed particle hydrodynamic simulations - I. Isolated galaxies.
MNRAS, 373:1074–1090.

G. S. Stinson, J. J. Dalcanton, T. Quinn, S. M. Gogarten, T. Kaufmann & J. Wadsley
(2009). Feedback and the formation of dwarf galaxy stellar haloes. MNRAS, 395:1455–
1466.

G. S. Stinson, J. J. Dalcanton, T. Quinn, T. Kaufmann & J. Wadsley (2007). Breathing
in Low-Mass Galaxies: A Study of Episodic Star Formation. ApJ, 667:170–175.

L. E. Strigari, S. M. Koushiappas, J. S. Bullock & M. Kaplinghat (2007). Precise con-
straints on the dark matter content of MilkyWay dwarf galaxies for gamma-ray experi-
ments. Phys. Rev. D, 75(8):083526.

E.-C. Sung, C. Han, B. S. Ryden, R. J. Patterson, M.-S. Chun, H.-I. Kim, W.-B. Lee
& D.-J. Kim (1998). The Intrinsic Shapes of Low Surface Brightness Dwarf Irregular
Galaxies and Comparison to Other Types of Dwarf Galaxies. ApJ, 505:199–206.

R. S. Sutherland & M. A. Dopita (1993). Cooling functions for low-density astrophysical
plasmas. ApJS, 88:253–327.

E. Tolstoy, V. Hill & M. Tosi (2009). Star-Formation Histories, Abundances, and Kine-
matics of Dwarf Galaxies in the Local Group. ARA&A, 47:371–425.

E. Tolstoy, M. J. Irwin, A. Helmi, G. Battaglia, P. Jablonka, V. Hill, K. A. Venn, M. D.
Shetrone, B. Letarte, A. A. Cole, F. Primas, P. Francois, N. Arimoto, K. Sadakane,
A. Kaufer, T. Szeifert & T. Abel (2004). Two Distinct Ancient Components in the
Sculptor Dwarf Spheroidal Galaxy: First Results from the Dwarf Abundances and Ra-
dial Velocities Team. ApJ, 617:L119–L122.

E. Tolstoy & A. Saha (1996). The Interpretation of Color-Magnitude Diagrams through
Numerical Simulation and Bayesian Inference. ApJ, 462:672.

M. Tosi (2007). Star Formation Histories of Resolved Stellar Populations: In and Beyond the Local Group. In A. Vallenari, R. Tantalo, L. Portinari & A. Moretti, editors, *From Stars to Galaxies: Building the Pieces to Build Up the Universe*, volume 374 of *Astronomical Society of the Pacific Conference Series*, p. 221.

M. Tosi, L. Greggio, G. Marconi & P. Focardi (1991). Star formation in dwarf irregular galaxies - Sextans B. AJ, 102:951–974.

C. Travaglio, W. Hillebrandt, M. Reinecke & F.-K. Thielemann (2004). Nucleosynthesis in multi-dimensional SN Ia explosions. A&A, 425:1029–1040.

T. Tsujimoto, K. Nomoto, Y. Yoshii, M. Hashimoto, S. Yanagida & F.-K. Thielemann (1995). Relative frequencies of Type Ia and Type II supernovae in the chemical evolution of the Galaxy, LMC and SMC. MNRAS, 277:945–958.

S. Valcke (2010). Simulations of isolated and interacting dwarf galaxies - comparing virtual stellar systems with reality. *PhD Thesis.*

S. Valcke, S. de Rijcke & H. Dejonghe (2008). Simulations of the formation and evolution of isolated dwarf galaxies. MNRAS, 389:1111–1126.

S. Valcke, S. de Rijcke, E. Rödiger & H. Dejonghe (2010). Kelvin-Helmholtz instabilities in smoothed particle hydrodynamics. MNRAS, 408:71–86.

E. Van Hese, M. Baes & H. Dejonghe (2009). The Dynamical Structure of Dark Matter Halos with Universal Properties. ApJ, 690:1280–1291.

L. van Zee (2002). Comparison of Star Formation Modes in Normal Dwarf Irregulars and BCDs (Invited). In E. K. Grebel & W. Brandner, editors, *Modes of Star Formation and the Origin of Field Populations*, volume 285 of *Astronomical Society of the Pacific Conference Series*, p. 333.

L. van Zee, J. J. Salzer & E. D. Skillman (2001). Kinematic Constraints on Evolutionary Scenarios for Blue Compact Dwarf Galaxies. I. Neutral Gas Dynamics. AJ, 122:121–139.

L. van Zee, E. D. Skillman & M. P. Haynes (2004). Rotationally Supported Virgo Cluster Dwarf Elliptical Galaxies: Stripped Dwarf Irregular Galaxies? AJ, 128:121–136.

B. Vandenbroucke, S. De Rijcke, J. Schroyen & N. Jachowicz (2013). Physics of a partially ionized gas relevant to galaxy formation simulations – the ionization potential energy reservoir. *ArXiv e-prints.*

A. Vazdekis, E. Casuso, R. F. Peletier & J. E. Beckman (1996). A New Chemo-evolutionary Population Synthesis Model for Early-Type Galaxies. I. Theoretical Basis. ApJS, 106:307.

M. G. Walker, M. Mateo, E. W. Olszewski, O. Y. Gnedin, X. Wang, B. Sen & M. Woodroofe (2007). Velocity Dispersion Profiles of Seven Dwarf Spheroidal Galaxies. ApJ, 667:L53–L56.

M. G. Walker, M. Mateo, E. W. Olszewski, J. Peñarrubia, N. Wyn Evans & G. Gilmore (2010). Erratum: "A Universal Mass Profile For Dwarf Spheroidal Galaxies?" (2009, ApJ, 704, 1274). ApJ, 710:886–890.

F. Walter, E. Brinks, W. J. G. de Blok, F. Bigiel, R. C. Kennicutt, Jr., M. D. Thornley & A. Leroy (2008). THINGS: The H I Nearby Galaxy Survey. AJ, 136:2563–2647.

R. Weaver, R. McCray, J. Castor, P. Shapiro & R. Moore (1977). Interstellar bubbles. II - Structure and evolution. ApJ, 218:377–395.

R. H. Wechsler, J. S. Bullock, J. R. Primack, A. V. Kravtsov & A. Dekel (2002). Concentrations of Dark Halos from Their Assembly Histories. ApJ, 568:52–70.

D. R. Weisz, E. D. Skillman, J. M. Cannon, A. E. Dolphin, R. C. Kennicutt, Jr., J. Lee & F. Walter (2008). The Recent Star Formation Histories of M81 Group Dwarf Irregular Galaxies. ApJ, 689:160–183.

D. R. Weisz, E. D. Skillman, J. M. Cannon, A. E. Dolphin, R. C. Kennicutt, Jr., J. Lee & F. Walter (2009). Does Stellar Feedback Create H I Holes? A Hubble Space Telescope/Very Large Array Study of Holmberg II. ApJ, 704:1538–1569.

M. I. Wilkinson, J. T. Kleyna, N. W. Evans, G. F. Gilmore, M. J. Irwin & E. K. Grebel (2004). Kinematically Cold Populations at Large Radii in the Draco and Ursa Minor Dwarf Spheroidal Galaxies. ApJ, 611:L21–L24.

Y. Yoshii & N. Arimoto (1987). Spheroidal systems as a one-parameter family of mass at their birth. A&A, 188:13–23.

D. B. Zucker, A. Y. Kniazev, D. Martínez-Delgado, E. F. Bell, H.-W. Rix, E. K. Grebel, J. A. Holtzman, R. A. M. Walterbos, C. M. Rockosi, D. G. York, J. C. Barentine, H. Brewington, J. Brinkmann, M. Harvanek, S. J. Kleinman, J. Krzesinski, D. Long, E. H. Neilsen, Jr., A. Nitta & S. A. Snedden (2007). Andromeda X, a New Dwarf Spheroidal Satellite of M31: Photometry. ApJ, 659:L21–L24.